UNIVERSITY OF SOUTHAMPTON

FACULTY OF NATURAL AND ENVIRONMENTAL SCIENCES

SCHOOL OF CHEMISTRY

The design and synthesis of near infra-red absorbing inorganic pigments

by

Adam Carl Keates

Thesis for the degree of Doctor of Philosophy

November 2014

UNIVERSITY OF SOUTHAMPTON

ABSTRACT

FACULTY OF NATURAL AND ENVIRONMENTAL SCIENCES

SCHOOL OF CHEMISTRY

Doctor of Philosophy

THE DESIGN AND SYNTHESIS OF NEAR INFRA-RED ABSORBING INORGANIC PIGMENTS

Adam Carl Keates

Materials which exhibit strong absorption in the Near Infra-Red (NIR) region have applications as laser-marking pigments, IR filters in photovoltaics and CCD detectors, medical imaging devices and absorbing coatings in solar thermal collectors. New NIR absorbing materials based on iron (II) and copper (II) frameworks have been designed using knowledge of predicted d-energy levels and associated transitions. Materials from this class have been synthesised and characterised in terms of structure and optical properties

A family of 13 iron phosphates and fluorophosphates have been obtained using hydrofluorothermal routes and characterised using single crystal X-ray diffraction. These materials show a variety of structural elements with one-, two- and three-dimensional connectivity. For example $RbFe_3(PO_3F)_2(PO_2(OH)_2)F_2$ has a framework structure consisting of face-sharing FeO_4F_2 octahedra linked by PO_3F tetrahedra, which are orientated such that the fluoride are terminal and line inter-framework space. This includes the first example of a hydrothermally synthesised iron chlorofluorophosphate, $(NH_4)_2Fe^{(II)}Fe^{(III)}(PO_3F)_2FCl_{2,}$ which contains sheets of $Fe^{II}O_2Cl_4$ octahedra linked together by edge-sharing chloride and chains of $Fe^{III}O_4F_2$ octahedra *trans* linked by μ^2-bridging fluoride.

UV/Vis/NIR spectra have been collected for 49 compounds and correlations between structure and NIR absorbing properties have been derived. A trend in ligand fields across the series SiO_4, PO_4 SO_4 determined SiO_4 showing the weakest ligand field making compounds with this ligand most suitable for NIR absorbing applications. Eight of the most promising materials have been tested for their laser-marking properties using a Nd:YAG laser at Merck, Darmstadt. The effect of particles size on the optical and laser-marking properties has been investigated using $K_2FeP_2O_7$ as an example. The decrease in particle size caused a red-shift in the absorbance maxima, and produced a well dispersed pigment within the test polymer matrix. Out of these eight compounds, Cu_2PO_4OH and Cu_4PO_4O exhibited laser-marking properties comparable to other commercial Merck NIR absorbing pigments.

Table of Contents

List of Tables

List of Figures

Declaration of Authorship

I, Adam Carl Keates declare that this thesis entitled ‘The design and synthesis of near infra-red absorbing inorganic pigments’ and the work presented in it are my own and has been generated by me as the result of my own original research. I confirm that:

- This work was done wholly or mainly while in candidature for a research degree at this University;
- Where any part of this thesis has previously been submitted for a degree or any other qualification at this University or any other institution, this has been clearly stated;
- Where I have consulted the published work of others, this is always clearly attributed;
- Where I have quoted from the work of others, the source is always given. With the exception of such quotations, this thesis is entirely my own work;
- I have acknowledged all main sources of help;
- Where the thesis is based on work done by myself jointly with others, I have made clear exactly what was done by others and what I have contributed myself;

Signed: ....

Date:...

The work was performed exclusively by the author, with the following exception: the investigations into the laser-marking results presented in Chapter 5 were carried out by colleagues from Merck, Darmstadt.

Acknowledgements

This work was undertaken with the financial support of Merck and the University of Southampton. This thesis would not have been possible without the support of many people. I would like to express my sincere gratitude to:

- My industrial supervisors from Merck, Dr. Fredrick Koenig, Dr. Slyke Klein and Rod Riddle, who offered support and feedback throughout my studies.
- My supervisor, Prof. Mark Weller for his invaluable guidance, advice and expertise during my PhD.
- Dr Robert Raja, who allowed me to continue my studies within his research group at the University of Southampton.
- Members of Raja and Weller groups, both past and present, for all the banter and good times.
- All friends and family, in particular my parents for their support, understanding and reassurance over the last four years.
- Finally the author would like to acknowledge the heroic effort of William Roszczk for proof reading.

List of Publications

Work discussed in this thesis has been published in the following papers:

Keates, A. C.; Armstrong, A. J. and Weller, M. T., Iron Fluorophosphates, *Dalt. Trans.*, **2013**, *42(30):* 10715-10724.

Keates, A. C.; Wang, Q. and Weller, M. T., Synthesis and structural characterisation of iron(II) and copper(II) diphosphates containing flattened metal oxotetrahedra, *J. S. S. Chem*, **2014**, *210 (1)*: 10-14

Chapter 1 Introduction

Inorganic materials chemistry is an area of interest due to its wide range of possible and actual applications, including pigments, catalysts, ion-exchange materials, high-temperature superconductors and battery materials. To meet the ever-growing demand for these applications, novel materials are required possessing either new properties or improvements on existing properties. Therefore, the synthesis of new functional inorganic materials still remains a highly-desired research goal.

These applications result from the physical and chemical properties of the materials, which in turn arise from their crystal structure. The rich structural diversity of inorganic materials results in three-dimensional frameworks (3D), two-dimensional layers (2D), one-dimensional chains (1D) and clusters (0D). The structure of framework materials can be described in terms of linked polyhedra, which include tetrahedra, octahedra, and trigonal bipyramid etc. These polyhedra can be linked through corner-, edge- or face-sharing interactions to construct the crystal structure of a material. This means it is possible to design inorganic materials through manipulation of their crystal structure for specific applications.

1.1 Designing NIR absorbing pigments

Colour arises from inorganic materials due to partially filled d-orbitals of transition metals; it is possible to promote an electron from the highest-occupied molecular orbital (HOMO) to the lowest-unoccupied molecular orbital (LUMO) by absorption of a photon of electromagnetic radiation having an appropriate energy. Electromagnetic radiation in the visible region of the spectrum often possesses the appropriate energy for such transitions; hence the colour of 3d metal complexes arises from d-d transitions. The energy difference for d-d transitions, ΔE, is inversely related to the wavelength of the light:

$$\Delta E = \frac{hc}{\lambda}$$

Equation 1.1

For electronic transitions to occur in the NIR, the energy levels involved (typically HOMO and LUMO) need to be separated by approximately 0.5 to 1.5 eV (780 to 2500 nm); this is a relatively low energy in comparison with those that exist in most materials and compounds. These low energy separations can be found in some highly-conjugated organic π-systems, such as phthalocyanine, but also in some inorganic compounds with partially-occupied d orbitals, and this thesis will focus on the latter.

The intensity and position of the absorption band, within 3d transition metal complexes, depends on a variety of factors. The energy difference between the energy levels, ΔE, can be affected by: geometry of ligands around the metal, bond distances and the nature of the ligand. By using Crystal-Field theory and applying the ligand-orbital repulsion model, it is possible to construct energy level diagrams for a range of different geometries **(**Figure 1-1**)**

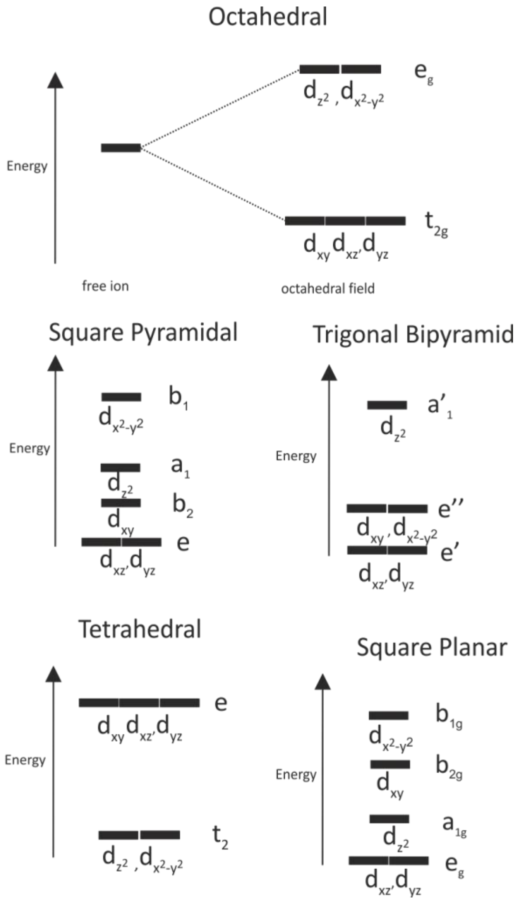

Figure 1-1 - Energy level diagram for different geometries

Simple theory predicts that $\Delta_{tet} = 4/9\ \Delta_{oct}$ and $\Delta_{SP} = 1.3\ \Delta_{oct,}$ however this only applies for complexes with the same metal and ligands with similar metal-ligand (M-L) bond lengths.[1] Ligand-field theory, which is an application of MO theory, provides a more substantial framework for understanding the effect of the ligand on ΔE. This is normally called the spectrochemical series, with ligands arranged in order of increasing ΔE:

$$\mathrm{I^- < Br^- < S^{2-} < Cl^- < NO_3^- < F^- < OH^- < C_2O_4^{2-} < H_2O < NH_3 < CH_3 < en < CO}$$

This series is based on the electron donor/acceptor properties of the ligands, and can be explained by using MO diagrams (Figure 1-2). There are three main types of ligand: σ-donor, σ-donor/ π-donor and σ-donor/ π-acceptor. σ-donor ligands (CH_3^-, H^-, NH_3^-) are located in the middle of the spectrochemical series: all ligands have σ-donor properties, but not all have the free orbitals for π-bonding. For an octahedral complex there are six M-L bonds, where each of the ligand orbitals is located along the M-L axis. Six of the metal orbitals have appropriate symmetry to interact with the ligand set, therefore a set of six bonding and six anti-bonding MO are formed (Figure 1-2). There is no combination of ligand σ orbitals that has the symmetry of the t_{2g} orbitals, so the t_{2g} set of orbitals is non-bonding for these types of ligands. Ligands that have empty π-orbitals, such as CO, are able to overlap with the t_{2g} orbitals of the metal centre, because they have the correct symmetry. As a result of this bonding interaction, the metal is donating electron density back to the ligands in a process called back bonding, hence π acceptors form a very strong M-L bond. This back bonding process stabilises the t_{2g} orbitals and therefore increases the ΔE (Figure 1-2). Ligands such as OR- and X- can donate lone pairs of electrons to the t_{2g} orbitals of the metal centre. This π-donation will result in the destabilisation of the t_{2g} orbitals, due to the repulsion between the lone pair electrons, and the t_{2g} orbitals hence weaken M-L bonds and reduce the ΔE.

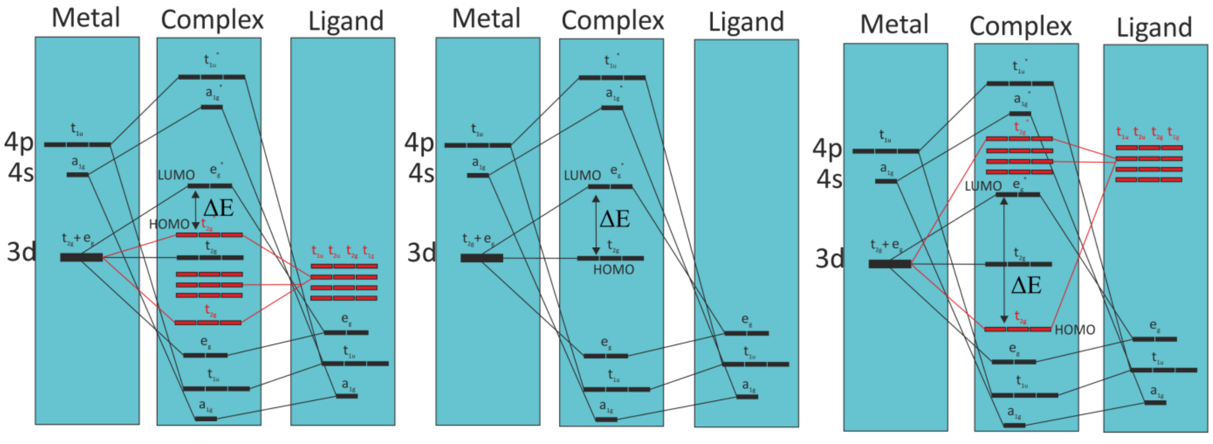

π-donor

σ-bonding

π-acceptor

Figure 1-2 - Energy level diagram for ligand field theory

Bond distances between the transition metal and ligands can influence the value of ΔE; if R is the metal-ligand inter-atomic distance and Q is the charge on the ligands, then ΔE can be expressed as:[2]

$$\Delta E \sim \frac{Q(r)^4}{(R)^5}$$

Equation 1.2

Where r is the mean value of the radius of a d-orbital, this value is approximately constant for ions of similar valance in the same transition metal series.

Therefore if the bond length is increased, this will decrease ΔE and will shift the absorbance peak to higher wavelengths. This equation can be related to the oxidation number and metal ion choice, which influence the M-L bond lengths. The variation with oxidation numbers reflects the smaller size of more highly-charged ions and the consequent smaller M-L distances, increasing ΔE. Moving down the group improves M-L bonding due the more expanded 4d and 5d orbitals, compared with the compact 3d orbitals, which increases ΔE.

The intensities of absorbance peaks for 3d transition metal are determined by spectroscopic selection rules: these are summarised in Table 1.1. For a spin allowed transition, there must not be a change in the spin angular momentum, i.e. $\Delta S=0$, all d-d transitions are spin allowed.

The Laporte selection rule states that *in a centrosymmetric molecule or ion, the only allowed transitions are those accompanied by a change in parity* [3]. Therefore transitions between g→g and u→u are forbidden: hence s-s, p-p, d-d and f-f transitions are forbidden, whereas s-p, p-d, and d-f transitions are allowed. The Laporte rule only applies to centrosymmetric molecules so does not apply to tetrahedral, square pyramidal and trigonal bipyramidal geometries. However, the Laporte rule can be relaxed for centrosymmetric geometries, such as octahedral and square planar, by distortion imposed by the ligand environment and through p-d mixing/hybridisation of orbitals.

Table 1.1 - Summary of absorbance selection rules

Band type	Intensity ($dm^{-3}mol^{-1}cm^{-1}$)
Spin forbidden	<1
Laporte- allowed	ca. 250
Laporte- forbidden	200-100
Symmetry allowed	10000-50000

Coloured transitions can also occur from charge-transfer (CT) bands: these arise from the movement of electrons between orbitals that are predominantly ligand in character, and orbitals that are predominantly metal in character. The transition is classified as ligand-to-metal charge-transfer transitions (LMCT) if the migration of the electron is from the ligand to the metal, and *vice versa* for metal-to-ligand charge-transfer (MLCT). CT bands can also occur between elements with multiple oxidation states - this is called inter-valance charge-transfer (IVCT). The colour arises from the transfer of an electron from a nearly-localised donor site to an adjacent acceptor site; where both donor and acceptor metal ions possess more than one accessible oxidation state. Several factors affect this IVCT, most notably the nature of the donor/ acceptor metal ions and the bridging ligand. A good example is Prussian Blue, $KFe[Fe(CN)_6]$, which contains Fe in both 2+ and 3+ oxidation states.

Therefore by manipulating the geometry, ligand type and bond distances, it is possible to tune the absorption bands of transition metal frameworks, and shift d-d transitions into the desired NIR region of the electromagnetic spectrum.

1.2 NIR radiation

Typically, d-d transitions occur within the visible region (400 to 750 nm) of the electromagnetic spectrum (Figure 1-3). However, in the Near-InfraRed (NIR) (750 to 3000 nm) region, this type of radiation occurs in a different part of the spectrum.

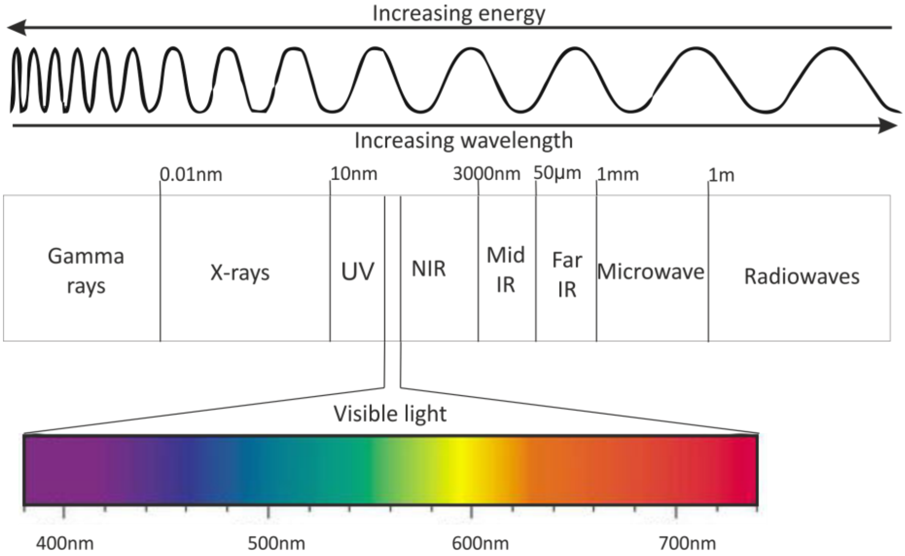

Figure 1-3 - Diagram of electromagnetic spectrum

Radiation from different regions of the electromagnetic spectrum interacts with molecules/matter in the same way: reflection, absorption, scattering and diffraction. However, the varying energies of these regions affect molecules in different ways, and this can be used to characterise materials, as summarised in Table 1.2.

Table 1.2 - Summary of electromagnetic radiation effect on molecules and their applications

Type of Radiation	Effect on Molecule	Type of Spectroscopy
Gamma	Atomic nuclei excitation	Mossbauer
X-rays	Core electron excitation	X-ray absorbance
Visible/UV	Outer electron excitation	Absorbance
Infrared	Molecular vibrations	Vibrational
Microwave	Molecular rotations	Raman
Radiowaves	Proton spin	NMR

The NIR region of the spectrum is between the visible and the mid-IR: as a result, NIR radiation can induce both molecular vibrations and outer electron excitation. The most prominent bands occurring in the NIR region are related to overtone and combination bands of fundamental IR vibrations of -XH (Where X= C, N, S and O) functional groups.[4] Overtone bands arise from transitions between vibrational states of $\Delta\nu = 2$ or 3. Combination bands arise from the addition of asymmetric, symmetric and bending modes in the mid-IR region. For example, the dominant NIR bands for water occur at 1938 nm (a combined bending and asymmetric stretching mode) and 1440 nm (an overtone of the symmetric stretching mode), with a weaker band at 2175 nm (second overtone of the bending mode).[5]

NIR radiation also forms an important and significant part in the solar spectrum that reaches the earth’s surface (Figure 1-4). Figure 1-4 indicates the solar spectrum contains approximately 45 % of its energy in the visible region, with 5 % in the ultraviolet and 50 % in the NIR. Most of the solar NIR radiation is effectively wasted and is considered harmful, as it is not needed by plants for photosynthesis and generates heat in the Earth’s atmosphere.

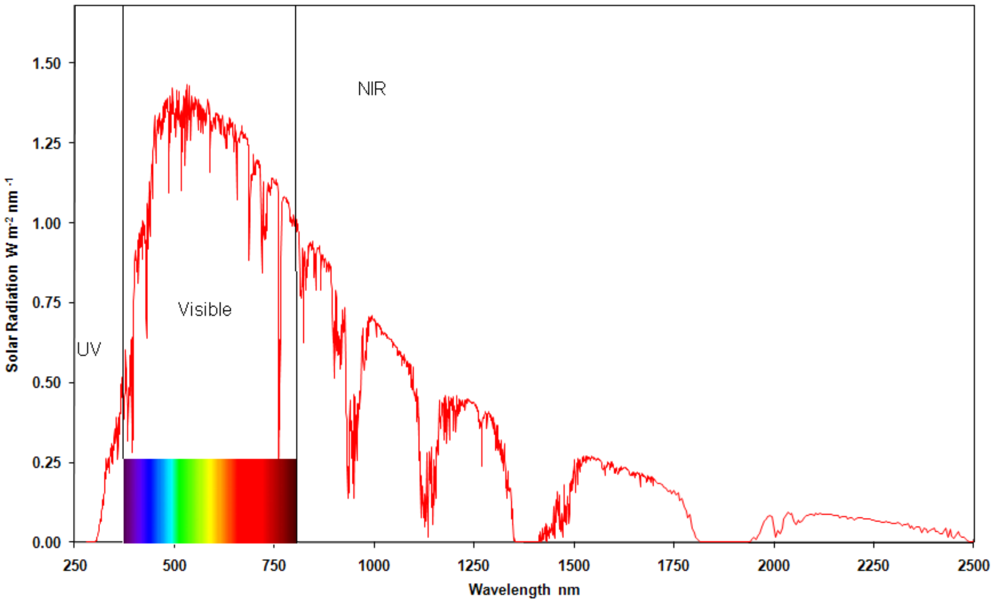

Figure 1-4 - Solar spectrum at Earth's surface

If this radiation could be harvested, through photovoltaic cells, or absorbed to reduce heat gain in the atmosphere through solar water heaters, this would be beneficial. The types of applications that utilise NIR energy have been described below.

Laser-marking

Laser-marking systems using different lasers may be used to mark an almost endless list of materials including metals, plastics, ceramics, glass, wood and leather, as well as painted surfaces. Laser-marking can be used for the labelling of manufactured goods, most commonly in the form of an alphanumeric code imprinted on the surface to indicate the date of manufacture, best-before or serial number, for example (Figure 1-5). This is important for security and quality control reasons. Laser-marking can potentially have many advantages when compared to conventional ink printing processes and labelling, including: indelible marking; high resolution capability; variability of substrate being marked; non-contact; lower overhead cost; fast cycle time; lower piece cost; reduction of consumables cost; reduced risk of forgery; reduction and/or elimination of surface pre-treatments; no curing time; reduction and/or elimination of inks and solvents; reduced environmental impact; and reduced maintenance.[6]

Figure 1-5-Current applications for laser-marking pigments

Lasers can interact with materials in a number of different ways depending on the type of marking that is desired and the type of laser used. There are two main types of lasers that are used in industry for marking applications: solid-state lasers (SSLs) such as neodymium doped crystals (Nd:YAG, Nd:YVO$_4$), and gas lasers such as carbon dioxide.[7] Each of these lasers has an output wavelength in different parts of the electromagnetic spectrum. SSLs have an fundamental wavelength of 1064 nm, but through frequency doubling or tripling, 532 nm and 355 nm outputs can be achieved and CO$_2$ lasers have an output at 10.6 μm.

Each wavelength interacts with materials to a different degree of suitability: generally speaking, the wavelength of Nd:YAG lasers couples better with metals, and the wavelength of CO$_2$ lasers couples better with non-metals.[7] However this project will only focus on the interaction with non-metal materials such as polymers. UV wavelengths such as 532 nm and 355 nm react with polymers photochemically to produce a bleaching effect; this is known as “cold marking”. NIR and Far-IR wavelengths such as 1064 nm and 10.6 μm react thermochemically and can be used for ablation, carbonisation, engraving and foaming marking.[8]

There are two main methods for the marking of plastics: beam-steered and mask. Both types of methods react with the plastic, as described above, but differ in the method used to project the laser beam and create the marking image. Each of these methods have their own advantages and disadvantages, and Figure 1.6 contains schematic diagrams for each of the methods.

A beam-steered laser marker allows the greatest degree of flexibility and image manipulation, and the correct system can virtually replicate any graphic image. To create the mark image with a beam-steered system, two mirrors mounted on computer-controlled galvanometers direct the laser beam across the target surface, much like a pencil on paper. Each galvanometer-controlled mirror provides one axis of beam motion in the marking field. The beam is projected through a flat-field lens assembly, which focuses the laser light to achieve the highest power density possible on the marking substrate. In this mode the laser requires multiple pulses to get the desired image marked onto the substrate.

A mask or stencil marking system sacrifices image quality and some versatility in return for significantly increased marking speed, because the image can be created in a single laser pulse. The marking image is created by projecting the laser beam through a mask, normally copper [7], of the desired image, and refocusing the beam on the marking substrate (see Figure 1-6).

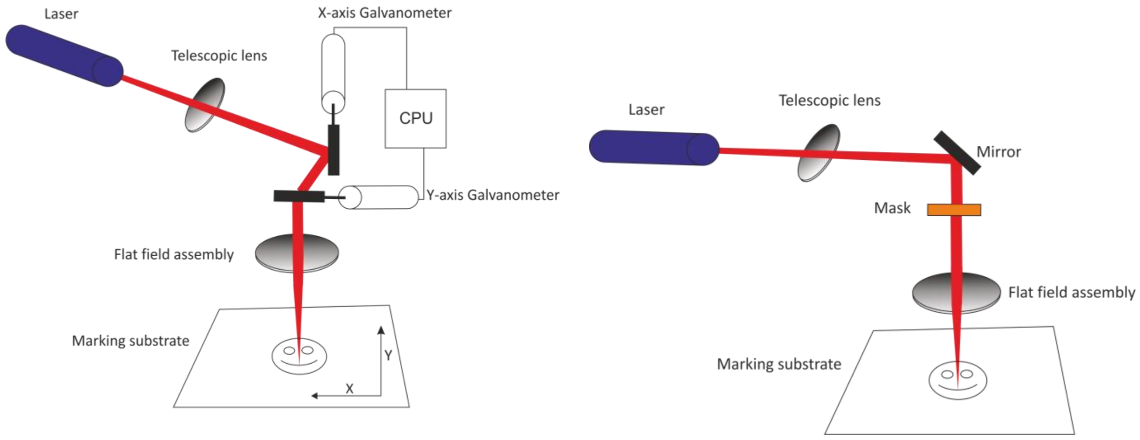

Figure 1-6 - Schematic diagram of (a) beam-steered and (b) mask laser-marking processes

A beam-steered system can provide detailed images and deeper marking, but a mask system can mark much faster. However, both systems provide a better combination of speed, permanence, and imaging flexibility than other marking techniques presently available.[8]

Each application is unique relative to the plastic substrate composition and colour, marking quality, speed, laser efficiency, type of marking, and total system costs. This means that the selection of laser type and system is strongly dependant on application.

The type of laser system that has been used in this project, and by Merck, is a beam-steered Nd:YAG laser. Beam-steered Nd:YAG lasers are popular in the laser-marking industry due to their power, performance and versatility. These lasers produce a wavelength at 1064 nm and depending on the colour of the substrate, some plastics (acrylonitrile butadiene styrene is one example) can yield an average quality laser mark without the need for chemical additives. However, most non-pigmented (natural) plastics and pigmented (white, black, blue, green, red, etc.) plastics are not laser-markable, or are only slightly laser-markable if such plastics are not activated with a laser material additive.

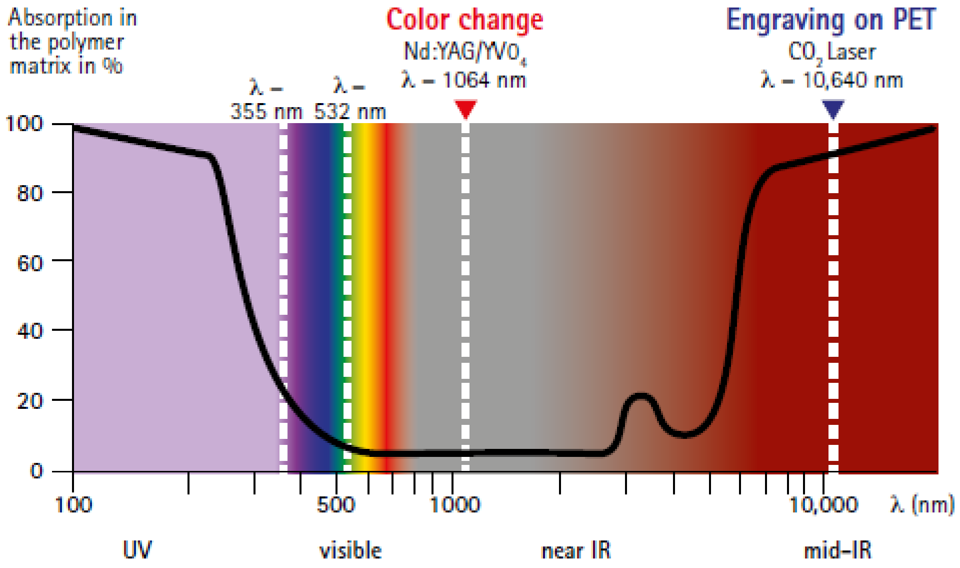

Figure 1-7 - Absorption spectrum of Polyethylene terephthalate [9]

When an additive is radiated under the Nd:YAG laser beam, the radiant energy is absorbed and converted to thermal energy. This increase in thermal energy can cause two main types of laser-marking (Figure 1-8); first, a charring process occurs when the energy absorbed raises the temperature of the surrounding material - this is high enough to cause thermal degradation of the polymer. This can result in burning of the polymer in the presence of oxygen, but with a limited supply of oxygen the charring of the polymer forms a black or dark-on-light marking. Second, a foaming process occurs when the local temperature of the surrounding polymer is sufficiently high that the polymer generates gases. The hot gases are surrounded by molten polymer and expand to form bubbles; the bubbles can scatter light in a way that results in white or light-on-dark marking.

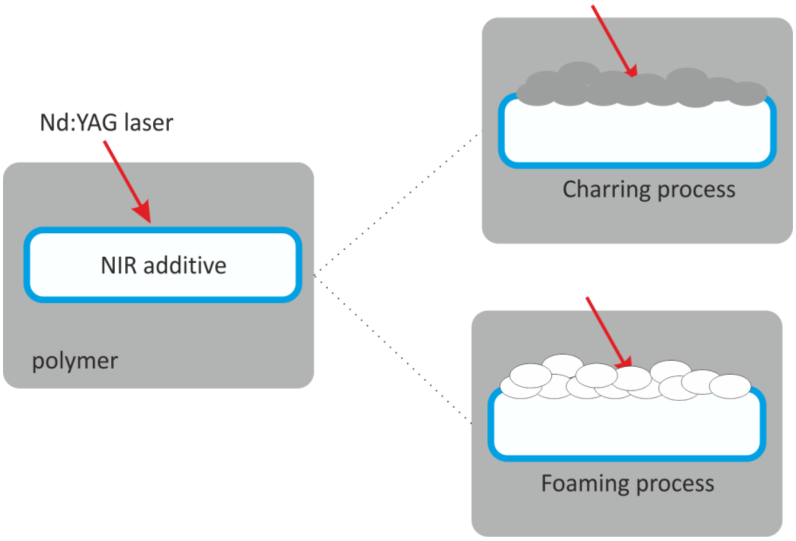

Figure 1-8 - Different laser-marking processes

There are already examples of inorganic pigments that are currently being used as NIR absorbers for laser-marking applications. U.S. Pat. No. 4,816,374 (Lecomte)[10] discloses the use of antimony oxide as a laser-marking material in polyurethane plastics in order to make ear tags for livestock animals. The use of Bismith-based pigments of the formula $Bi_xM_yO_z$ (U.S. Pat. No. 6,503,316 ,Sakoske *et al*.)[11] - where M is at least one metal selected from: Zn; Ti; Fe; Cu; Al; Zr; P; Sn; Sr; Si; Y; Nb; La; Ta; Pr; Ca; Mg; Mo; W; Sb; Ba; and Ce - have very high IR reflectance and show good marking on polyurethane substrates. Patent No. 2010105735 A1 (Elder *et al*.)[12] describes suitable absorbers for laser-marking of plastics which contain at least one metal compound and at least one reducing agent. These include carbon black, conductive pigments such as antimony, Sb/Sn mixed oxides such as Sb_2O_3, $(Sn,Sb)O_2$ and with $(Sn\ Sb)O_2$-coated mica flakes, and iron compounds such as magnetite, molybdenum disulphide and molybdenum oxide. It is important that there is direct and intimate contact between the metal compound and reducing agent; this is done through coating. These platelet-shaped pigments are commercially available under the trademark Iriodin ® from Merck KGaA.

However, it is not preferred to use heavy metals such as antimony in thermoplastic compounds for health and safety reasons, and some of these compounds have strong absorbance in the visible region, which can change the colour of the polymer matrix. Therefore development into materials that are “transparent” in the visible region with high absorbance with Nd:YAG lasers are desirable. Patent No. 2010105735 A1 (Elder *et al*.)[12] describes transparent or semi-transparent substrates such as sheet silicates, finely-divided metal particles (such as tin, iron or aluminium), dyes, copper phosphate/ basic copper phosphate, hydrated copper pyrophosphate and copper hydroxide phosphates, with promising laser-marking potential.

Solar water heaters

Solar Water Heaters (SWHs) are referred to by a number of different names such as: Solar Hot Water Panels, Solar Hot Water Collectors, Solar Thermal Panels or Solar Thermal Collectors; all of these terms describe the same device. SWHs are currently being used to provide hot water and heating to domestic households all over the world. This energy is free, environmentally friendly and reliable.

SWHs are already cost-competitive with fossil fuels or electric boilers in sunny countries. China has by far the most SWH capacity, due to low costs and government support, and the EU is the second largest market, with the majority of installations located in the south and Germany. Falling costs and increasing efficiencies will soon make SWHs economically attractive for a broader range of climates. As a result, global capacity is forecast to double to 975 gigawatt thermal (GWth) by 2030.[13]

A SWH absorbs solar radiation, converts it into heat, and transfers this heat to a fluid (usually air, water, or antifreeze) flowing through the collector. The solar energy collected is carried from the circulating fluid by copper risers either directly to the hot water or to a thermal energy storage tank. An energy efficient solar collector should absorb incident solar radiation, convert it to thermal energy and deliver the thermal energy to a heat transfer medium with minimum losses at each step.[14]

There are two main types of SWHs: stationary and sun tracking collectors. Both of these types have numerous variations in the way the solar radiation is collected, however the process and basic principle described above remains the same. Therefore each individual variation will not be discussed in this thesis: for a comprehensive review on SWH types and applications, the author recommends Kalogirou [15] and references within.

However the most common type of SWH, a flat-plate collector, will be discussed in more detail (Figure 1-9). A typical flat-plate collector consist of a transparently-glazed, normally toughened glass because it can transmit as much as 90 % of the incoming short-wave solar irradiation while transmitting virtually none of the long-wave radiation emitted outward by the absorber plate [15]. Below the glazing is a blackened absorber plate that absorbs as much solar radiation as possible and converts it to heat: this will be discussed in more detail below. The heat is transferred to the transport fluid in copper risers - these are made from copper due to its excellent thermal conductivity properties – and the heated fluid is then carried away in the header tube for storage or use. Insulation is used to reduce the heat loss from the back and sides of the device, while the casing is made from aluminium to provide rigidity.

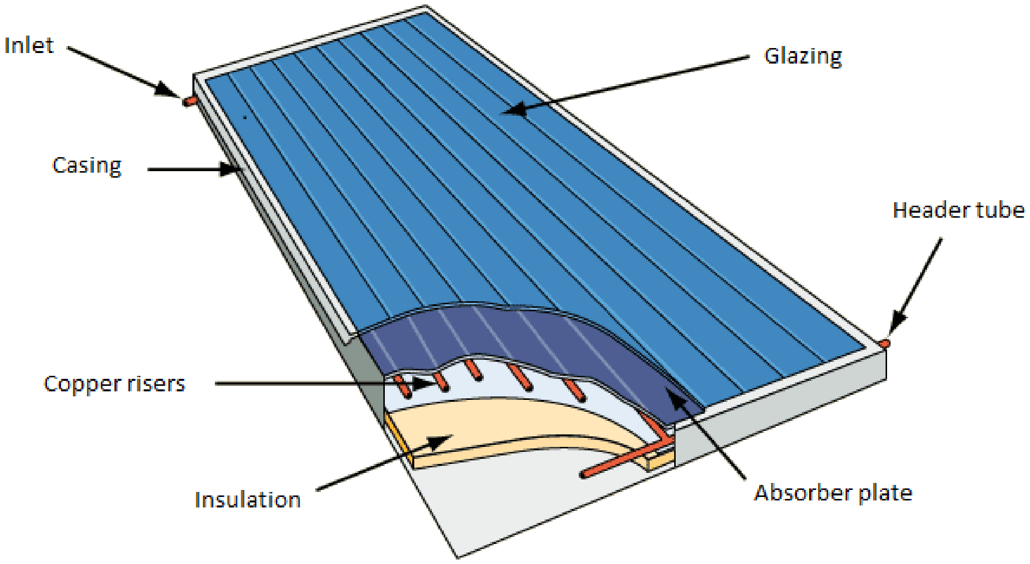

Figure 1-9 - Schematic of solar water heater [14]

The absorber plate is a key component of the SWH; it absorbs the energy from sunlight and converts it into heat: the more efficient the absorber plate, the greater the collector‘s output. There are two main types of absorber plate materials: selective and non-selective coatings. Current non-selective materials that are being used within the absorber plates are normally black or very dark materials. One of the issues facing non-selective coatings arises from re-radiating heat to the surroundings, because the temperature of the absorber surface is above ambient temperature. This loss mechanism is a function of the heat radiation of the surface for long-wavelength radiation. The dilemma is that many coatings that enhance the absorption of sunlight also enhance the long-wavelength radiation loss from the surface.

Aims to reduce this long-wavelength temperature loss have led to the development of spectrally selective coatings (SSCs). These materials have high absorbance within the solar spectrum (Figure 1-4) and high reflectivity above 2500 nm.

Various SSCs have been designed based upon the following concepts: (i) intrinsic absorbers; (ii) semiconductor-metal tandem or absorber-reflector tandem; (iii) multi-layer absorbers; (iv) metal-dielectric composite/cermet; (v) textured surfaces; and (vi) selectively solar-transmitting coating on a blackbody absorber or heat mirrors.

(i) Intrinsic absorbers use a material with intrinsic properties, which results in the desired spectral selectivity. Intrinsic solar-selective properties are found in transition metals and semiconductors. However, both need to be greatly modified through structural and compositional changes, or the addition of an anti-reflective layer, to serve as an intrinsic absorber (e.g. HfC [16], metallic W [17]).

(ii) Semiconductor-metal tandems absorb short wavelength radiation by having semiconductors with bandgaps, from ~0.5 eV (2500 nm) to 1.26 eV (1000 nm), combined with metal layers to provide low thermal emittance (e.g. PbS/Al [18]).

(iii) Multilayer absorbers use multiple reflections between dielectric and semi-transparent reflective (typically metal) layers to absorb light and can be tailored to be efficient selective absorbers (e.g. Al_2O_3/ Mo/Al_2O_3 [19]).

(iv) Metal-dielectric composites/cermets consist of fine metal particles in a dielectric or ceramic host material. Cermets have a highly-absorbing coating in the solar region (i.e., black) that is transparent in the IR, deposited onto a highly IR-reflective metal substrate (e.g. Al_2O_3-Ni [20]).

(v) Textured surfaces can produce high solar absorbance by multiple reflections among needle-like, dendritic, or porous microstructures (e.g. Textured Ni, Cu and Stainless steel [21]).

(vi) Selectively solar-transmitting coatings on a blackbody-like absorber are also used but are typically used in low-temperature applications. The selective solar-transmitting coating can be a highly-doped semiconductor (e.g. In_2SO_3:Sn:MgF_2) over an absorber (e.g. black enamel) with a proven long-term durability [22].

For a full review of mid-to-high temperature SSCs, the author would recommend Selvakumar *et al* [23], Kenndy [24] and references within, as both review papers provide detailed explanations of the different types of SSCs with numerous examples. The absorbance and reflectivity data for all the examples are also included, as well as data for commercial materials currently being employed in SWHs.

However, the absorbance of selective coatings is seldom as high as for non-selective coatings, and a trade-off must be made based on whether the increased high-temperature performance overshadows the reduced low-temperature performance and expense of the selective coating [25].

Photovoltaic cells

Photovoltaic cells (PV) are used to generate electricity from sunlight. Crystalline silicon is the dominant material in the production of PV cells, as it is nontoxic and abundant. Most PV cells today are made from silicon, and therefore from one semiconductor material with one band-gap. The band-gap of Si is in the region of about 600 to 1100 nm. Hence these Si-based PV cells do not use the full solar spectrum (Figure 1-4. Photons which have energies below the band-gap are not absorbed and photons which exceed the band-gap are converted into heat, and are therefore lost as well. The use of multi-junction solar cells, where semiconductors with different energy band-gaps extract power from their respective portions of the solar spectrum, leads to higher overall solar power conversion efficiencies. Therefore there is a need for a material that absorbs strongly and broadly over 1000 to 1800 nm.

There have already been attempts to create these multi-junction solar cells through dye-sensitised TiO_2 cells and Organic PhotoVoltaic cells (OPV). TiO_2 cells have a band-gap of 3 to 3.2 eV; this means that they absorb strongly in the UV region of the spectrum; from Figure 1-4, we can see this is only a small portion of the solar spectrum. Therefore, research into dye-synthesised TiO_2 cells looks to maximise the amount of the solar spectrum absorbed. These cells are mainly combined with quantum dots such as PbS and CdS [26], CdTe and CuIn(As)Se [27]etc. These cells have high efficiencies but use highly toxic materials of low natural abundance. OPV cells have also been developed for the absorption of NIR radiation; these consist of two organic layers made of different organic semiconductors, one with an electron-donor character and the other with an electron-acceptor character. These organic semiconductors have highly conjugated π-systems, such as Buckminsterfullerene (C_{60}) and metal-complexed phthalocyanines.[28] The advantages of OPV are that organic materials are abundantly available, and the production costs are low compared to inorganic PV cells. However, a drawback of the current OPV cells is that their efficiency is significantly lower than that for an inorganic PV cell. OPV cells also have lower lifetimes due to exposure to UV radiation, oxygen and moisture, which causes photo-oxidative reactions that limits their stability over time.[29]

This same principle of having two materials that absorb over different regions of the solar spectrum can also be beneficial to reduce the heating of current PV cells. Heating of silicon-based PV cells can lead to a decrease in the output power and conversion efficiency due to [30]:

- Increase of the thermal lattice vibrations, leading to electron-phonon scattering;
- Decrease of charge carrier mobility;
- Reduction of the p–n junction built-in voltage and junction ability to separate electrons from holes in the photogenerated pairs.

It is therefore beneficial to remove this heat from PV cells, so they can operate under optimum temperature conditions. It is possible and desirable to collect both electrical and thermal energy from solar radiation in the same unit; this would be much cheaper than buying two separate units. These types of system are called photovoltaic-thermal (PV/T) or hybrid systems. A PV/T is basically a flat plate collector with the solar cells directly over the absorber plate. However PV/T collectors will not be discussed in detail, as the desired properties of the materials required for these applications are the same as for PV and SWHs. For reviews on PV/T, the author recommends Zondag [31] and references within, which provide a historical background and some aspects of manufacturing, market potential and different designs. There is also a paper from Ibrahim *et al* [32], which discusses the recent advances in flat plate PV/T collectors.

NIR imaging

NIR imaging is a promising approach for medical imaging because it's non-invasive and provides real-time data and high-resolution images. NIR imaging (700 nm to 1000 nm) has been dedicated immense attention owing to the low absorption from organisms and tissues in the NIR spectral range, which can minimise background interference and improve tissue depth penetration and image sensitivity.[33]

Current compounds used for NIR imaging can be separated into two categories: inorganic and organic molecules. Inorganic NIR molecules are mainly associated with quantum dots [34, 35] and gold/carbon nanoparticles.[36] Biological applications of these inorganic molecules have been slowed down due to several fundamental problems, such as possible toxicity and technical barriers arising from poor reproducibility. Organic NIR dyes are mainly centred on cyanine, Squaraine, Phthalocyanines and porphyrin derivatives.[33] These are very attractive candidates for imaging because of the availability for covalent or non-covalent conjugation with cancer-targeted organic and biological molecules [33]. Therefore these dyes can be used to detect specific types of cancer, however these dyes do not have as strong NIR absorbance as inorganic molecules. These types of compounds can be used for the treatment of cancers through photodynamic therapy [33].

1.3 Candidate materials

Candidate materials need to be cheap, chemically stable and have low/zero toxicity. In order to manipulate the position of the absorbance band into the NIR, the transition metal will be required to have an absorbance peak towards the red part of the spectrum (i.e. blue or colourless compounds): these complexes will require less manipulation. Therefore, to determine which transition metal complex has an absorbance peak in the red part of the spectrum, a selection of hexaaqua 3d transition metal complexes were analysed (Figure 1-10). Hexaaqua complexes were selected due to the positon of water ligands in the spectrochemical series, changing the ligand type to stronger π-donors will result in a red shift in the absorbance spectrum. The results of this preliminary screening indicate that Cu (II) and Fe (II) have absorbance close to the NIR region; therefore these complexes have been selected for further analysis.

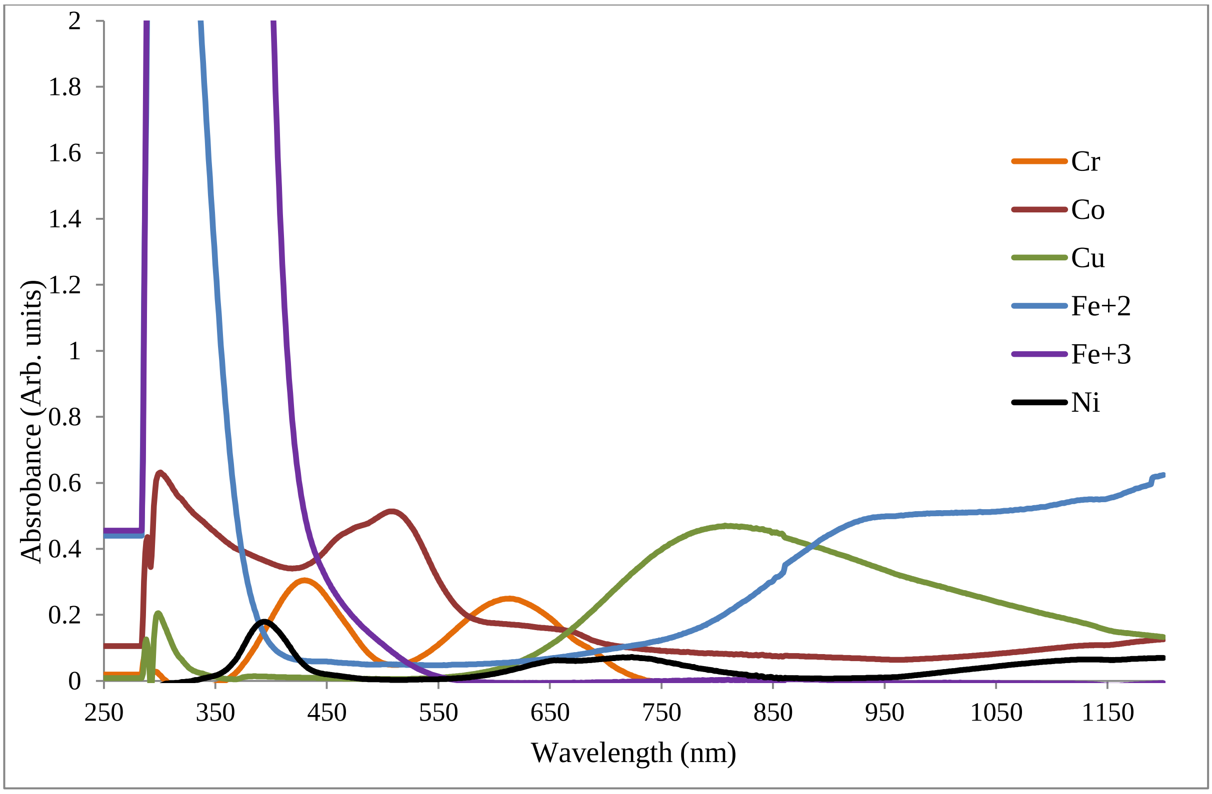

Figure 1-10 - Absorbance spectrum of a selection of 3d transition metal hexaaqua complexes

The chemical and thermal stability of TM complexes are generally less when compared to TM frameworks. Iron and copper compounds have formed a variety of different framework structures, and have numerous applications related to their unique physical properties.

1.4 Framework materials

Framework materials are of interest due to their wide range of possible and actual applications, including catalysts, pigments, ion-exchange, magnetic and battery materials. The structure of framework materials can be described in terms of linked polyhedra, which include tetrahedra, octahedra, trigonal bipyramids etc. These polyhedra can be linked through corner-, edge- or face-sharing to construct the crystal structure of the material. Depending on how these polyhedra are linked can lead to a range of dimensionalities such as 0D clusters, 1D chains, 2D layers and 3D frameworks.

The first framework materials discovered were naturally occurring aluminosilicate zeolites: these structures contain corner-sharing SiO_4 and AlO_4 tetrahedra. There are over 200 different zeolite structure types discovered to date.[37] Microporous aluminosilicates have shape and size specific channels or pores, and can be represented by the general formula $[A^{n+}]_{x/n}[SiO_2]_x[AlO_2]_{1-x} \bullet yH_2O$; the counter cations (A) and water are located within these channels/pores. All of these zeolites are based upon strict corner-sharing SiO_4 and AlO_4 tetrahedra, where Loeweinstein’s rule states that Al-O-Al linkages are forbidden within zeolitic frameworks.[38] The Si/Al ratio can range from a minimum of 1 to infinity: where a value of one gives rise to strictly alternating Si-O-Al linkages, any value greater than one allows structures to contain Si-O-Si linkages. A range of 3D zeolite frameworks can be formed through secondary building units (SBUs) which are comprised of corner sharing TO_4 tetrahedra (T=Al, Si) (Figure 1-10). For example, 4- and 6-rings combine to form β-cages: these cages are present in numerous zeolites, such as sodalite (Figure 1-11).

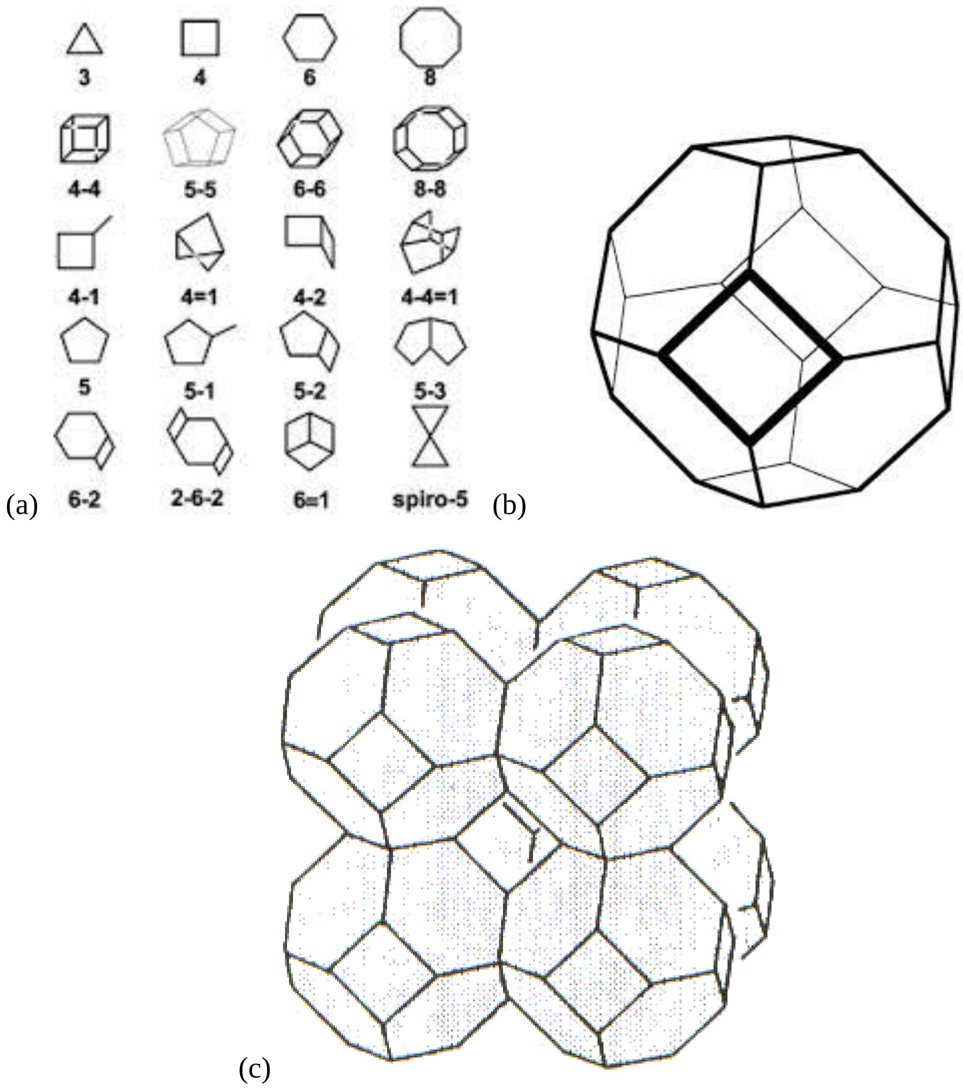

Figure 1-11 - (a) The secondary building units (SBUs) present in zeolite structures; (b) β-cage formed from 4- and 6-ring SBUs; (c) the structure of Sodalite comprised solely of linked β-cages.

The way in which these SBUs are connected is related to the porosity of the zeolite. Pore sizes range from about 2.5 Å in the case of sodalities (SOD) to about 10 Å in so-called UTD-1 (University of Texas, Dallas), which has a 14-ring channel.[39] These varying pore sizes give rise to excellent ion-exchange properties in the hydrated state, and catalytic properties exhibited in their dehydrated forms. Some of the most common applications are provided in Table 1.3.

Table 1.3 - Common industrial applications of zeolites[40]

Process	**Application**
Ion-exchange with hydrated zeolites	detergency (e.g. zeolites Na-A and Na-P) water softeners animal feeds radioactive waste remediation (e.g. Cs, Sr with clinoptilolite)
Molecular sieving with dehydrated zeolites	air separation (N_2 from O_2 with Li-LSX) drying agents (e.g. double glazing, air conditioning) sulphur removal from natural gas separation of HFCs (CFC substitutes)
Catalysis with dehydrated zeolites	catalytic cracking (gasoline production)-zeolite-Y derivatives xylene isomerization (for polyesters)-H-ZSM-5 butene isomerization-H-FER methanol to gasoline-H-ZSM-5 phenol to hydroquinone- titanosilicates denox reactions-Cu-ZSM-5, Co-FER

Following the extensive development of synthetic zeolites, research has gradually shifted towards new families of 3D frameworks. Flanigen and co-workers at Union Carbide Corporation discovered a new generation of microporous materials, aluminophosphate (AlPOs), at the beginning of the 1980s.[41] AlPO structures have the general formula $[(AlO_2)_x(PO_2)_x]\bullet yH_2O$, consisting of strictly alternating aluminate and phosphate tetrahedra, via Al-O-P linkages. Unlike zeolites, the synthesis of AlPOs typically occurs in acidic conditions, with an amine or quaternary ammonium salt added to act as a templating or structure-directing agent. Calcination of AlPOs is used to remove organic components and create open framework materials. A number of AlPOs are isostructural with zeolites: AlPO-17 with erionite/offretite, AlPO-20 with sodalite, and AlPO-24 with analcime. However, new structural motifs not present in zeolites have also been discovered, such as AlPO-5 [41] and VPI-5 [42] (Figure 1-12).

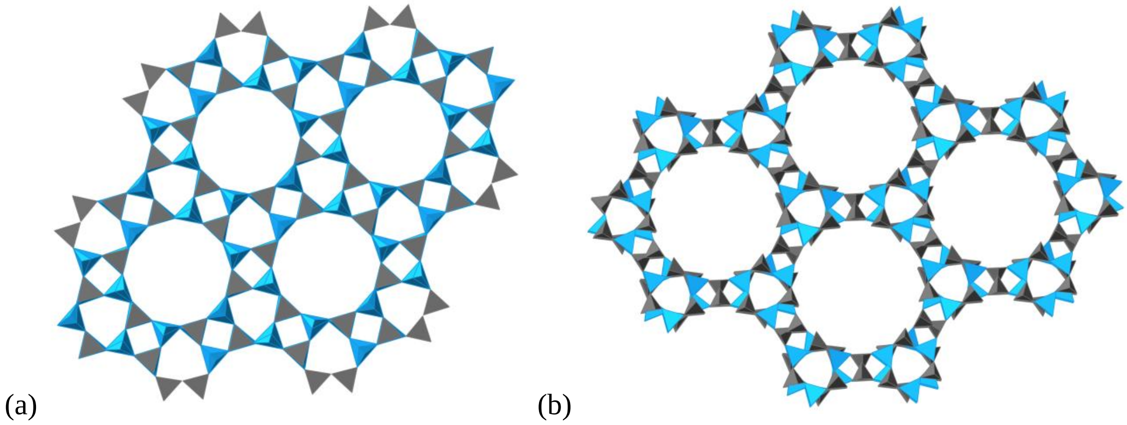

Figure 1-12 - Structure of (a) AlPO-5 and (b) VPI-5, viewed along the c-axis. Water molecules and organic templates have been removed for clarity. Al tetrahedra in light blue and P tetrahedra in grey

This work was further extended through the substitution of aluminium for an isoelectric species, gallium (GaPOs). Most of the early work on GaPOs produced isostructural materials previously reported for AlPO frameworks such as AlPO-12, -21, and -25.[43] These compounds were synthesised solvothermally using a specific structure directing agent (SDA) with a gel containing Ga_2O_3-P_2O_5-$40H_2O$. However further work led to unique structures for GaPO frameworks - $[HNEt_3]$ $Ga_9P_9O_{36}OH$ is gallophosphate with an open framework containing channels along the (001) and (010) planes which accommodate the triethylamine template. This structure also contains three types of gallium centres: two are tetrahedral, and the third is in distorted trigonal bipyramidal geometry. These AlPO and GaPO materials differ from zeolites due to the presence of non-tetrahedral polyhedra within the framework. Both Al and Ga can be found in higher coordination numbers (5-6) normally situated in trigonal bipyridmal and octahedral geometries.[44, 45] Examples include AlPO-12, -15 and -21 (Figure 1-13). Another important discovery was provided by Guth and Kessler, who introduced the fluoride method in the synthesis of zeolitic materials.[46] Fluoride anions at low concentrations have been found to act as mineralisers in the formation of framework materials [47], and provide a catalytic role where fluoride anions are required for phase formation, but are not necessarily present in the final structure [48], whilst at higher concentrations, fluoride may be incorporated into the structures by substitution with framework oxygen atoms, or through bridging Al/Ga sites, therefore increasing coordination numbers. For example, fluoride stabilises the formation of double 4-rings (D4R), with the fluoride anion encapsulated in the cage. The most famous member is cloverite, a GaPO solely comprised of F-containing D4R cages, with a 3D channel system with 13.2 Å pore size.[49] Fluoride anions have been reported in terminal and bridging sites within the Mu-*n*, ULM-*n* and MIL-*n* phases. The layered structure of Mu-35 [50] displays terminal Ga-F and bridging Ga-F-Ga bonds, and is built from GaO_5F,GaO_4F_2 octahedra and

HPO_4, PO_4 tetrahedra. The terminal fluoride anions are orientated into extra-framework space, forming H-bonding interactions with the organic amine within the layer (Figure 1-14). The ULM-*n* [51] series shows numerous examples of fluoride bridging, resulting in the formation of more complex SBUs, which include tetramers, (Ga_2P_2), hexamers (Ga_3P_3) and octomers (D4R). The tetrameric units are constructed from two Ga-polyhedra linked through an F-atom, either corner- or edge-sharing, and two phosphate tetrahedra. The tetrameric unit is present within the ULM-1structure. Hexameric units are comprised of a central Ga-octahedron, linked through F to two Ga-trigonal bipyramids, with the three Ga-polyhedra capped by three phosphate tetrahedra. This hexameric unit is present within the ULM-3,-4 and-5 structures. For a full review on the fluoride method application to microporous materials, the author would recommend Loiseau *et al* [52] and Kessler *et al*.[47]

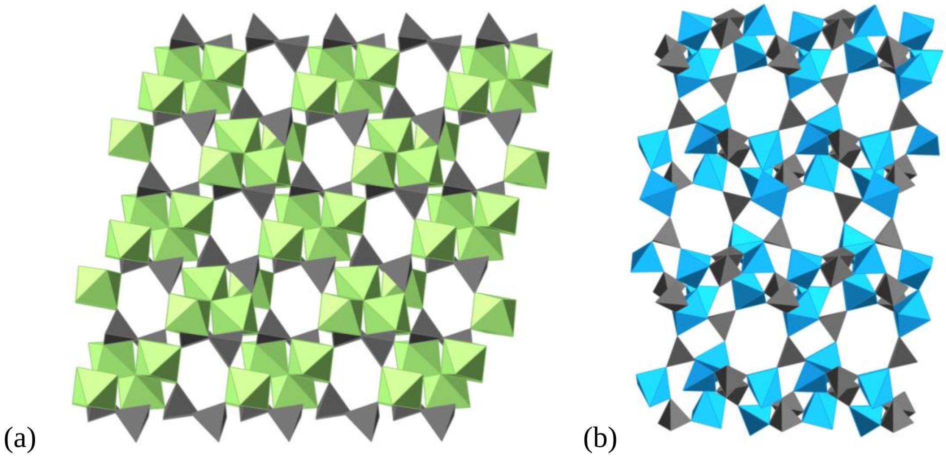

Figure 1-13 - Structure of (a) GaPO-15 viewed along the b-axis. (b) AlPO-21, viewed along the (101) direction. Ga octahedra in light green, Al tetrahedra in light blue and P tetrahedra in grey

Further investigations have been performed to modify the chemical properties of AlPO materials by incorporation of elements with different valences. This led to the synthesis of several new series of materials, in particular silicoaluminophosphates (SAPO-n),[53] metalaluminiophosphates (MAPO-n) and metalsilicoaluminophosphates (MAPSO-n) [54]: where M are divalent cations that are able to adopt tetrahedral coordination (E.g. M= Mg, Mn, Fe, Co and Zn). The combination of different transition metal species (Fe, Co and Mn) in the AlPO-5 framework has resulted in a catalyst which is selective in the oxidation of cyclohexane to cyclohexanone and cyclohexanol,[55] whilst Mg, Zn, Co-containing MAPO-18 frameworks have shown promising activity for methanol conversion to light olefins.[56]

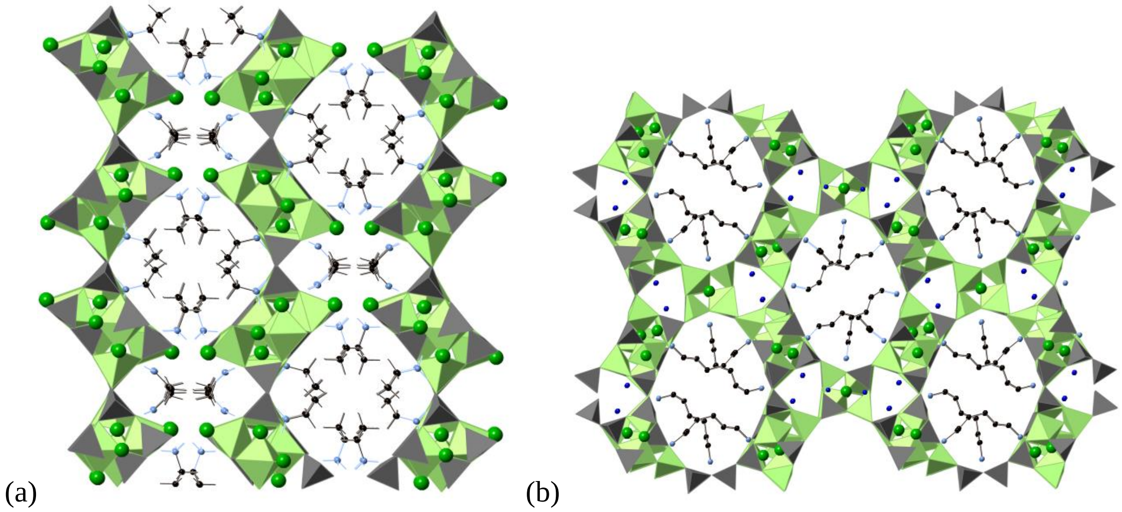

Figure 1-14 – Structures of (a) Mu-35 viewed along the b-axis (b) ULM-5 viewed along the a-axis. Ga polyhedra in light green and P tetrahedra in grey, F atoms are green spheres, C atoms are black spheres and N atoms are light blue spheres

Following the successful introduction of transition metals into AlPO frameworks, and the discovery of framework materials with coordination numbers larger than four, a large amount of research was attempted to synthesise transition metal frameworks. The variable oxidation state and flexible coordination preferences of transition metals mean that a wide range of material compositions and structures can arise in materials formed of linked polyhedra, especially when compared with aluminosilicate chemistry.

There is a wealth of literature related to the formation of new transition metal frameworks, which extends beyond the range of this thesis. For more information on other transition metal frameworks, the author recommends a review by Natarajan *et al* and references within.[57] This paper contains information not only on phosphate frameworks, but expands into other tetrahedral anions such as sulphate and arsenates.

This thesis will focus on copper and iron frameworks due to the desirable optical properties described earlier (Figure 1-10). The following section will describe a selection of copper and iron frameworks and their potential and actual applications, which extend beyond the ion exchange and catalytic properties described previously.

Iron frameworks

The phosphate ligand combines with over 30 elements to form phosphate minerals. Approximately 45 % of the known phosphate minerals contain ferric or ferrous ions as a major component.[58] Therefore iron phosphates are among the most important materials besides silicates and aluminates.

The blue mineral vivianite ($Fe_3(PO_4)_2{\bullet}8H_2O$) was used as a pigment in Europe around 10 AD.[59] Vivianite is an unstable iron phosphate mineral with variable iron (II/III) content that is completely colourless when containing solely iron (II), and that, if exposed to oxygen, will over time oxidise into blue and eventually brown compounds with higher iron (III) content. The structure of vivianite (Figure 1-15) contains layers of iron octahedra and phosphate tetrahedra. These layers consist of edge-sharing dimers of Fe octahedra ($Fe_2O_6(H_2O)_4$) and $FeO_2(H_2O)_4$, which are linked through P tetrahedra along the *a*-axis. The blue colour arises from the inter-valence charge transfers (IVCT) between iron ions, filling dimers of edge-sharing octahedra in the crystal structure.

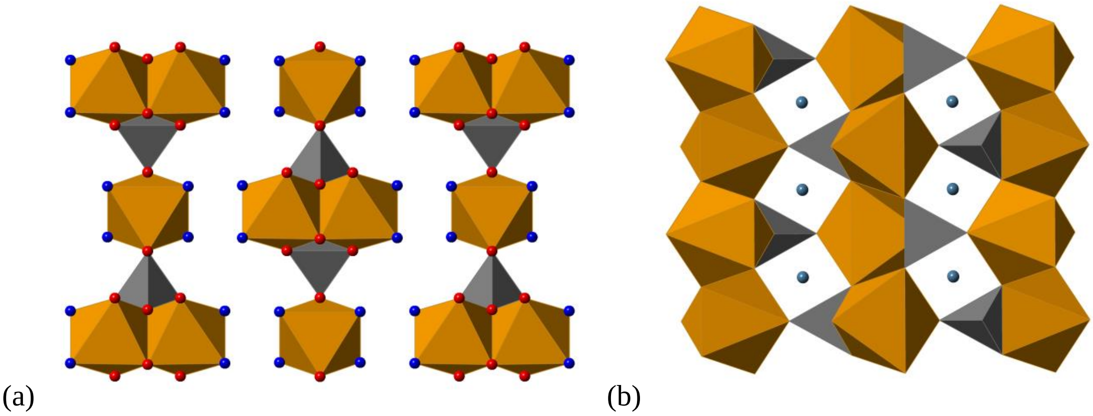
(a) (b)

Figure 1-15 - Structure of (a) Vivianite and (b) $LiFePO_4$ viewed along c-axis. Fe polyhedra in orange, P tetrahedra in grey, O atoms are red spheres, water ligands are dark blue spheres and Li atoms are turquoise spheres

Another iron phosphate mineral, $LiFePO_4$, has been extensively studied as a host compound from which Li ions can be inserted/extracted reversibly.[60-64] The hosts are transition metal (TM) compounds with a redox couple (or an M-3d band) that accepts/donates electrons that charge compensate for inserted/extracted Li ions. The structure of $LiFePO_4$ contains edge-sharing FeO_6 octahedra and PO_4 tetrahedra to form a 3D framework containing channels along the *b* and *c*-axes occupied by Li cations (Figure 1-15). During lithium-ion extraction and insertion, the active material undergoes a two-phase transition between $LiFePO_4$ and $FePO_4$. $LiFePO_4$ is now commercialised as the active cathode element of a new generation of lithium-ion batteries. This material was recognised as a very promising candidate for that purpose by Padhi *et al* [62] because it is low cost, non-toxic, and has a remarkable thermal stability. $LiFePO_4$ has a theoretical capacity of 170 mAh g^{-1} and a flat voltage profile at 3.55 V versus a lithium metal anode, which enables it to substitute for the toxic and expensive $LiCoO_2$ material employed in lithium-ion batteries.[65]

Compounds based on the 3D structure of NASICON have been studied as host materials: the general formula is $A_nFe_2(XO_4)_3$ (where A= Li and Na, X= As, P and S).[66, 67] The structure is comprised of corner-sharing FeO_6 and XO_4 polyhedra, which form a framework with large diffusion channels containing A cations (Figure 1-16). A difference of 0.8 eV between the redox energies in the isostructural NASICON frameworks of $Li_3Fe_2(PO_4)_3$ and $Li_2Fe_2(SO_4)_3$ can be attributed to the inductive effect; the oxygen forming a stronger bond within SO_4 than in PO_4 tetrahedra.[67]

Lithium iron silicates have also attracted attention as potential host materials in lithium batteries.[68] Li_2FeSiO_4 contains layers of alternating corner-sharing FeO_4 and SiO_4 tetrahedra, where the Li cations are located in between the layers (Figure 1-16). The theoretical capacity of ~160 mAh g^{-1}, and the abundance of raw materials, have enhanced lithium iron silicates' potential to become cathode materials of choice for large-scale battery applications.

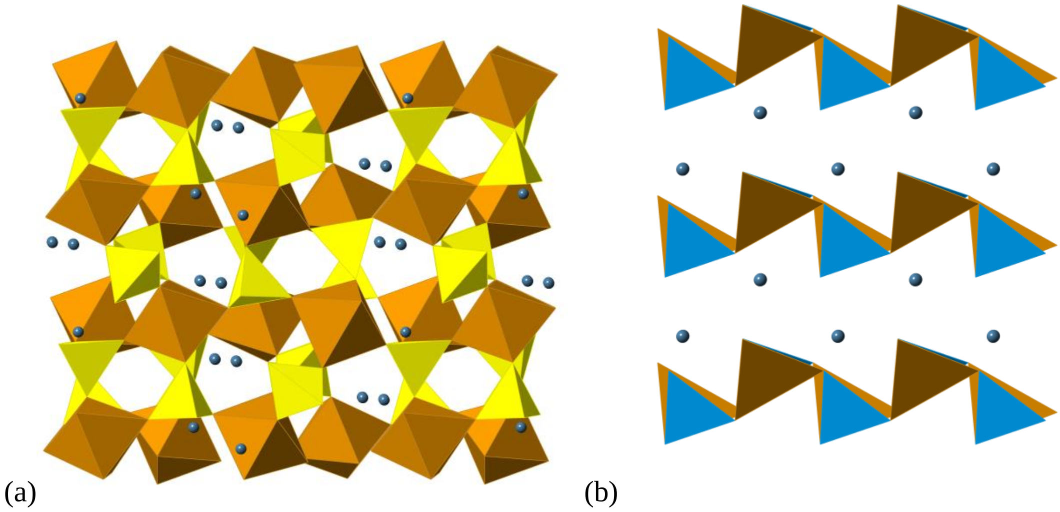

Figure 1-16 – Structures of (a) $Li_2Fe(SO_4)_3$ viewed along c-axis and (b) Li_2FeSiO_4 viewed along a-axis. Fe polyhedra in orange, S tetrahedra in yellow, S tetrahedra in light blue and Li atoms are turquoise spheres

Iron frameworks are also of interest for their catalytic properties, since the doping of Fe into AlPO-5 frameworks.[55] Iron phosphates have shown potential catalytic properties for the selective oxidative dehydrogenation of isobutyric acid into methacrylic acid.[69, 70] The reaction requires the Fe centres to change their oxidation state during the course of the reaction, and lattice oxygens to extract protons from the substrate.[71] One of the most active and selective phases for methacrylic acid formation is α-$Fe_3(P_2O_7)_2$. This structure consists of trimers of face-sharing FeO_6 octahedra linked together by diphosphate units creating a dense 3D framework Figure 1-17). The presence of these trimers should allow easier electron transfer during the catalytic process.

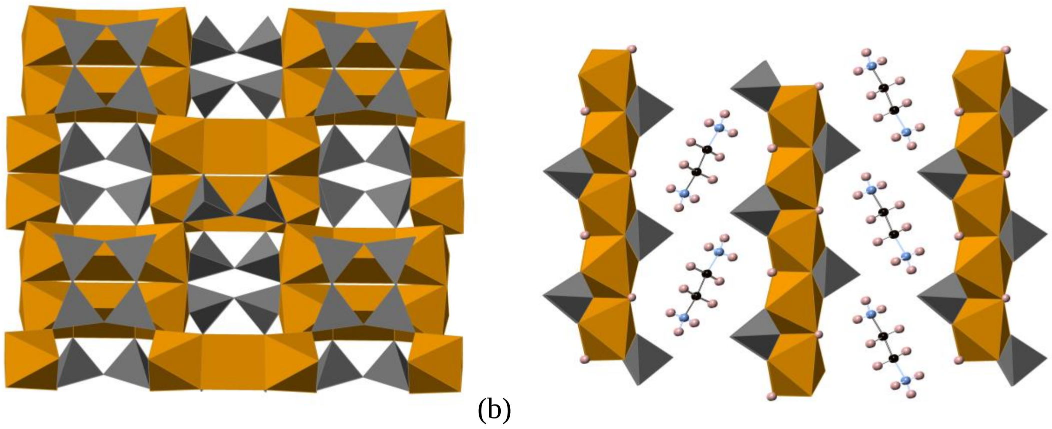
(a) (b)

Figure 1-17 –Structures of (a) $Fe_3(P_2O_7)_2$ and (b) $[En]_{0.5}Fe(PO_4)(OH)$ viewed along the a-axis. Fe polyhedra in orange, P tetrahedra in grey H atoms are pink spheres, C atoms are black spheres and N atoms are light blue spheres

Efforts have been made to synthesise open-framework materials containing solely iron and phosphate polyhedra: one of the first of these was by Cavellec *et al*.[72] (Figure 1-17b). $[En]_{0.5}Fe(PO_4)(OH)$ was synthesised hydrothermally using the $FeO(OH)$-H_3PO_4-HF-en-H_2O (en = ethylenediamine) as starting materials, with the aim to synthesise iron fluorophosphates with open frameworks. The fluoride containing compounds are described in the iron fluorophosphate section.

Another notable series was generated by Lii *et al*.[73] The materials were synthesised hydrothermally by heating iron chlorides or nitrates, amines, and phosphoric acid in appropriate proportions in water or a mixture of water and organic solvents in Teflon-lined autoclaves, at temperatures ranging from 110 to 180 °C for several days. This series produced 10 novel, organically-templated iron phosphate materials with varying degrees of dimensionality and iron oxidation states. An example from this series, $[H_3N(CH_2)_3NH_3]Fe_2O(PO_4)_2$, consists of Fe_4O_{16} clusters formed from four FeO_5 trigonal bipyramids, which are linked into two-dimensional sheets through phosphate tetrahedra, with the protonated organic template located between the sheets (Figure 1-18). The cluster contains a dimer of edge-sharing trigonal bipyramids, which are further linked at the corners of the other two trigonal bipyramids. Unfortunately, these compounds were not truly porous because thermal treatment to remove the organic template resulted in structural collapse, limiting the potential of these materials for catalytic applications.

However, these materials do exhibit some interesting magnetic properties arising from superexchange and/or supersuperexchange interactions.

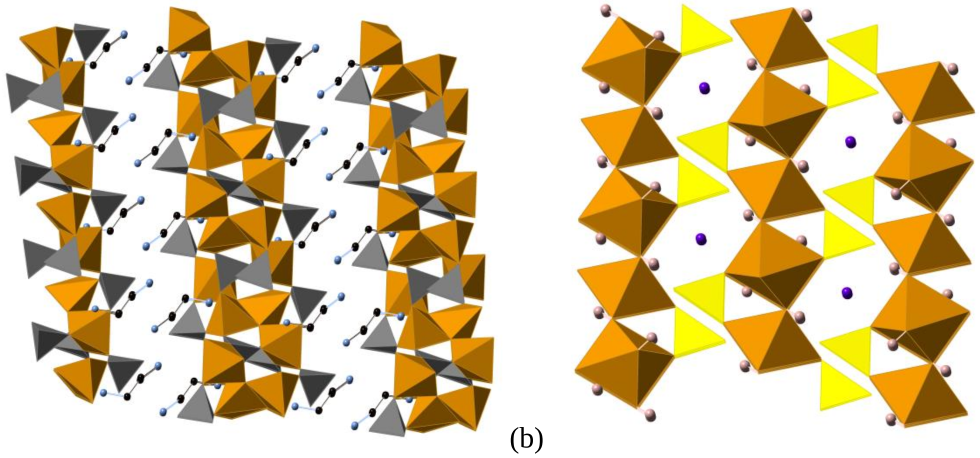
(a) (b)

Figure 1-18 - Structure of (a) $[H_3N(CH_2)_3NH_3]Fe_2O(PO_4)_2$ and (b) $K_2Fe_3(SO_4)_2(OH)_6$ viewed along a-axis. Fe polyhedra in orange, P tetrahedra in grey, S tetrahedra in yellow, H atoms are pink spheres, C atoms are black sphere, K atoms are purple spheres and N atoms are light blue spheres

A large number of iron framework materials have been investigated in the literature regarding their magnetic properties, and a selection of examples are provided below.

The iron sulphate framework $K_2Fe_3(SO_4)_2(OH)_6$ belongs to the jarosite family, and exhibits a kagomé lattice.[74] The kagomé lattice is an example of a geometric magnetically-frustrated system. The structure of jarosite contains $FeO_2(OH)_4$ octahedra, which are linked through μ^2-bridging OH to form infinite Fe-OH-Fe-OH-Fe…. chains (Figure 1-18b). The kagomé lattice is formed in the *ab* plane, which is separated from adjacent kagomé planes by K and SO_4 ions, resulting in a layered structure. The magnetic susceptibility was found to follow a Curie-Weiss law with a negative Weiss temperature $\Theta_p \sim -700$ K, indicating antiferromagnetic interactions.[75]

$NaFe_2(PO_4)(HPO_4)$ is built up from alternate FeO_4 and PO_4 tetrahedra linked via vertex-sharing oxygen atoms (μ^2 and μ^3) forming S-shaped layers with Na cations located in inter-layer space [76] (Figure 1-19a). The vertex linkages of FeO_4 and PO_4 tetrahedra form a cage-building unit that consists of two three-membered rings, four four-membered rings, and two six-membered rings. The magnetic properties of this material arise from Fe-O-Fe superexchange pathways, which result in a negative Weiss temperature ($\Theta \sim -45.7$ K), confirming the existence of antiferromagnetic interactions.[76]

The ferrous chain silicate $CaFeSi_2O_6$ exhibits, as do virtually all iron-rich silicates, a magnetic phase transition from a disordered (paramagnetic) to an ordered antiferromagnetic state at low temperatures.[77] The structure consists of chains of edge-sharing Fe-octahedra along *c*-axis with neighbouring chains linked by silicate tetrahedra: these linkages create six membered rings containing Ca cations (Figure 1-19b). The magnetic interaction within the FeO_6 chains is ferromagnetic, whereas the interaction between neighbouring chains is antiferromagnetic and distinctly weaker than the ferromagnetic intra-chain interaction.[77]

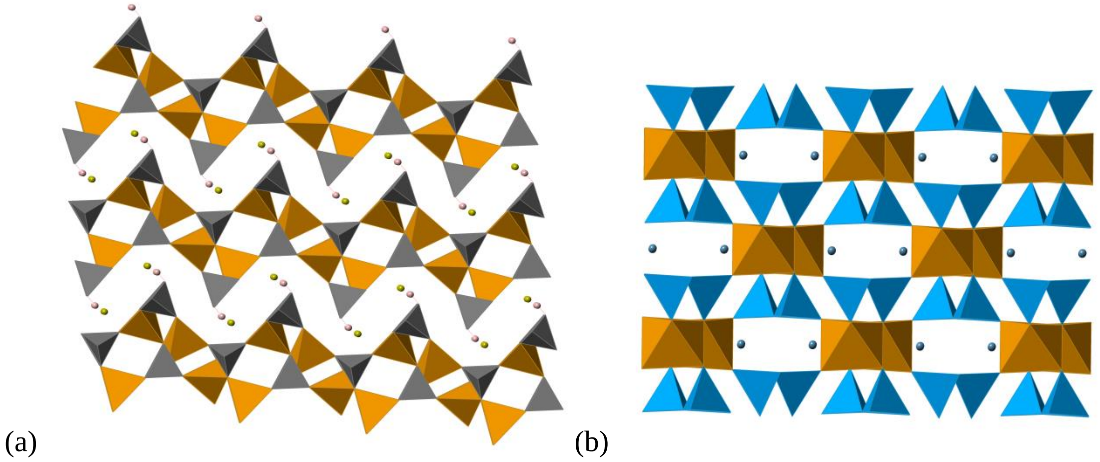

Figure 1-19 - Structure of $NaFe(PO_4)(HPO_4)$ viewed along the a-axis and (b) $CaFeSi_2O_6$ viewed along the c-axis. Fe polyhedra in orange, P tetrahedra in grey, Si tetrahedra in light blue, H atoms are pink spheres and Ca atoms are turquoise spheres

Whilst attempting to make a number of iron frameworks that contained oxygen and fluoride ligands, a variety of fluoride containing iron phosphate materials - iron fluorophosphates - were synthesised solvothermally. The applications of these materials extend beyond the scope of this PhD, but are of interest for their unique electrochemical and magnetic properties. [40]

Iron fluorophosphates

Iron-based materials adopting structures formed by linking the metal centres through tetrahedral oxopolyhedra, such as PO_4, SiO_4 and SO_4, are of considerable interest due to their potential and actual applications. Further compositional, and therefore structural, variability beyond oxopolyhedral anions can be achieved by the introduction of additional anionic species, such as a halide (X^-), into a material. The addition of F^- into a solvothermal reaction mixture at low concentrations generally acts as a mineralising agent [47], while at moderate and higher molar concentrations it is more likely to be incorporated into the product material.

There are examples of fluoride containing iron phosphate frameworks - iron fluorophosphates - in the mineral kingdom. These will not be discussed in this review, and the focus will be on synthetic iron fluorophosphates, with particular attention paid to the unique structural features that arise due to the inclusion of fluoride into the structure.

Early work on iron fluorophosphates was performed in the hydrothermal synthesis laboratory of the institute of crystallography, in the USSR. The work from this laboratory has described numerous alkali metal templated frameworks from the MF-iron oxide-$(NH_4)_2HPO_4$-H_2O system (where M= Li, Na, K, Cs and iron oxide = FeO, Fe_2O_3). All of these compounds were synthesised under high temperature and pressure hydrothermal conditions (T = 400 °C, P =1000 atm).

The first of these compounds to come out of this work was Fe_2PO_4F in 1978 [78]; it is the synthetic and pure iron version of the mineral triplite. The structure of Fe_2PO_4F contains two different iron octahedral, both of which have FeO_4F_2 composition. These iron octahedra are linked through edge- and face-sharing μ^3-O and μ^4-F bridging ligands. These two types of linkages occur along all the crystallographic directions, and create a dense 3D framework. It is also possible to substitute different transition metals onto one of the metal sites. $FeCoPO_4F$ was synthesised under mild hydrothermal conditions (180 °C for 6 days), using a $FeCl_3$: $CoCl_2$: H_3PO_4: NH_4F: $NH_2(CH_2)_3NH_2$: H_2O system.[79]

$KFePO_4F$ [80] was synthesised using the same KF-Fe_2O_3-$(NH_4)_2HPO_4$-H_2O system as Fe_2PO_4F, and is isostructural with $KTiOPO_4$ (KTP) (Figure 1-20a). The FeO_4F_2 octahedra in $KFePO_4F$ form zig-zag chains which are linked through alternating *cis, trans* μ^2- bridging F, and run along [001] and [0-11] planes. These chains are linked through PO_4 tetrahedra to form stacks, with the potassium cations located within pores created by six membered rings (3x PO_4, 3x FeO_4F_2), which run along the *c*-axis.

Li and Na templated structures have been synthesised by this group including tavorite, $LiFePO_4(OH,F)$; followed by $Na_3Fe_2(PO_4)_2(OH)_2F$ [81]; and a fully fluorinated version, $Na_3Fe_2(PO_4)_2F_3$ (Figure 1-20b).[82] The magnetic properties and phase changes of this fully fluorinated material has been studied by Le Mein *et al.*[83] From a thermal point of view, three phase changes have been evidenced: namely the γ, β, and α forms (from low to high temperature). The magnetic properties of this material indicate 3D antiferromagnetic ordering where T_N= 62(2) K and θ_p = -239 (15) K.

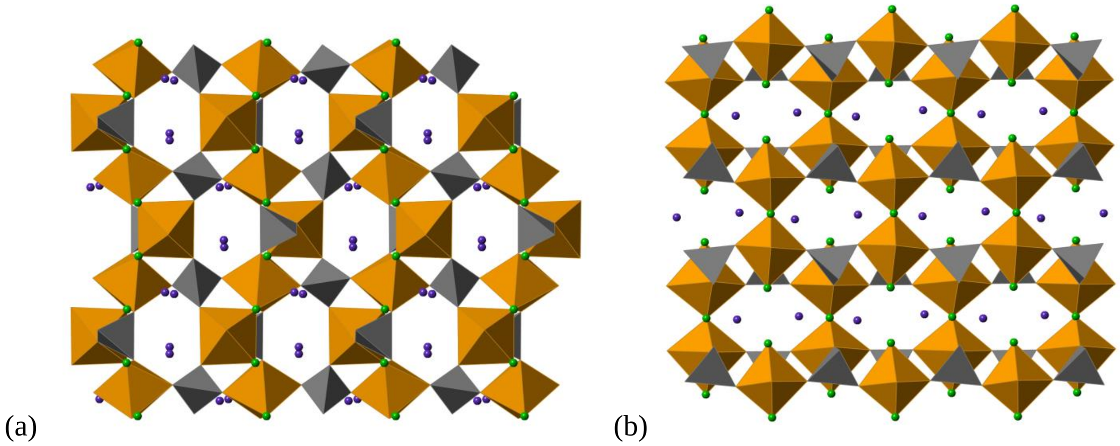

Figure 1-20-Structures of (a) $KFePO_4F$ viewed along c-axis (b) $Na_3Fe_2(PO_4)_2F_3$ viewed down a-axis. Fe polyhedra in orange, P tetrahedra in grey, F atoms are green spheres and Na atoms are purple spheres

During this early work, the first iron fluorodiphosphate, $K_2Fe_2(P_2O_7)F_{2,}$[84] was synthesised. $K_2Fe_2(P_2O_7)F_2$ contains zigzag chains of edge-sharing FeO_4F_2 octahedra along the (001) direction. These chains are linked by pyrophosphate groups along the (100) and (010) direction to form a 3D framework. Potassium cations are located in pores that run along the (110) direction. The main original feature of this new pyrofluorophosphate is the mixed (O, F) nature of the shared edge.

A Cs-containing mixed valance iron fluorophosphate, $Cs_8Fe^{3+}{}_8Fe^{2+}{}_7\,F_{10}(PO_4)_{12}$ [85], was grown in the hydrothermal system $CsF\text{-}Fe_2O_3\text{-}(NH_4)_2HPO_4\text{-}H_2O$. The structure contains three types of Fe polyhedra (octahedra, tetrahedra and square pyramids) which share vertices, mostly μ^2- bridging F, to form 2D layers approximately parallel to the [120] plane. These layers are linked by PO_4 tetrahedra to form a 3D framework; with Cs atoms occupying spaces.

There is little information regarding the possible applications and properties of these materials in this early work. It was not until 1994 when Loiseau *et al* [86] synthesised NH_4FePO_4F, which is isotopic with $KFePO_4F$, that the magnetic properties of iron fluorophosphates were investigated. The iron octahedra chains along the (001) and (0-11) planes, and represent the only two directions within which long-range magnetic superexchange interactions can occur via 180° Fe-F-Fe pathways.[86] Due to the 180 ° magnetic superexchange pathway, strong antiferromagnetic interactions would be expected [87]; this was confirmed by the negative value obtained from the magnetic susceptibility measurements ($\theta_p = -227(10)$ K). The Néel temperature of this compound was higher ($T_N = 45(2)$ K) compared to other 1D antiferromagnetic fluorides ($T_N = 10$ K). This would indicate that there is some significant 3D magnetic ordering, and that magnetic interactions do not occur solely through Fe-F-Fe pathways.[86]

The research from the Férey group led to the ULM-series (for University of Le Mans) in 1996, which comprised of a range of organically-templated iron fluorophosphates.[88] The ULM-series was synthesised by mild hydrothermal conditions (110 to 180 °C), under autogenous pressure, in the presence of organic templating agents. The iron source used was either Fe_2O_3 or FeO(OH), in the presence of HF and phosphoric acid, where the Fe/P ratio was close to unity. In this work they describe common structural building units (SBU) (Figure 1-21) found within the ULM-series and the magnetic properties of these materials. The materials produced have an open framework but are not porous. All the attempts to remove the protonated amines templates by thermal treatment, with the aim of generating real porous materials, led to the collapse of the structures.[88] The reason for this structural collapse is due to the acidic synthetic conditions. These lead to protonation of the amines, which induces strong template-framework interactions that are destroyed by heating, leading generally to amorphous phases.[88]

The ULM-series has already been reviewed in detail by Cheetham *et al* [40] and Riou-Cavellec *et al* [88]. The work from the ULM-series is summarised in Table 1.4.

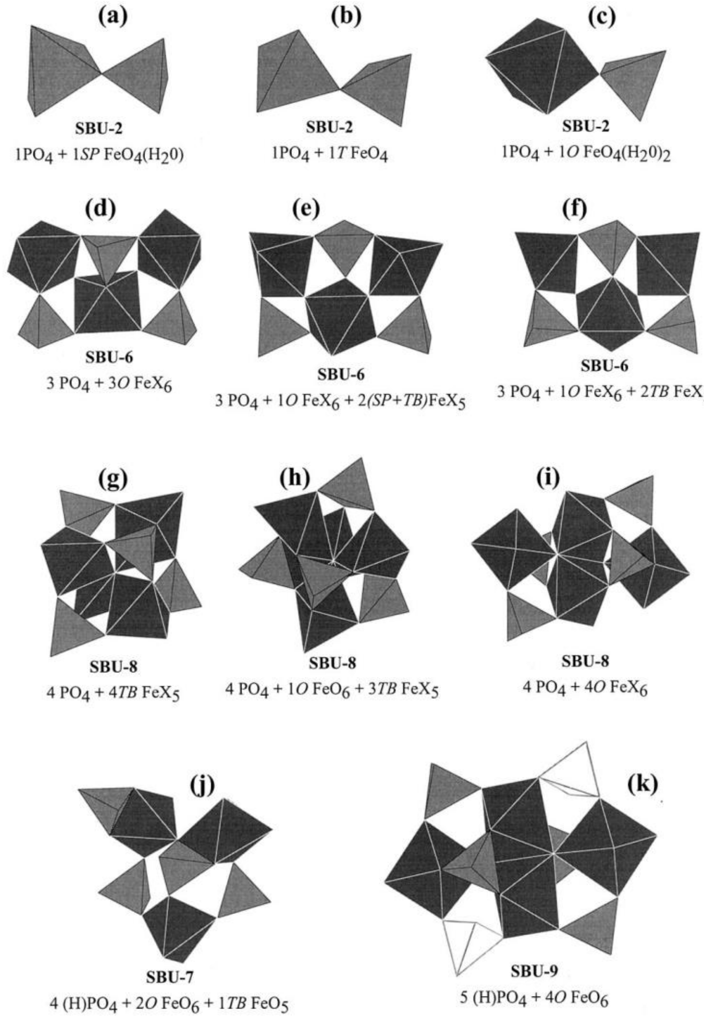

Figure 1-21 - representation of the different SBUs encountered in ULM-Series [88]. Meaning of the labels in italics: O (Octahedra), SP (Square planar), TB (Trigonal bipyramid), T (Tetrahedra). Empty tetrahedra of SBU-9 correspond to sites with half multiplicity.

Table 1.4 - Summary of iron ULM-series

ULM series no.	Chemical formula	Main structural features	Magnetic properties		Ref
			Θ_P (K)± 10	T_N (K)± 1	
3	[H_2-1,4 diaminobutane] $Fe_3(PO_4)_3F_2$	SBU-6 hexamer is based on two trigonal bipyramids, FeO_4F, one octahedron, $FeO_4F_{2,}$ and three PO_4 tetrahedra. The three Fe polyhedra are linked μ^2-bridging fluorine atoms and thus form ferric trimers, $Fe_3O_{12}F_2$. These trimers are connected by phosphates and create a porous 3D structure.	-196	38	89
4	$[CH_3NH_3]_2$ $Fe_3(PO_4)_3F_2$• H_2O	Built up from same SBU-6 as ULM-3, the 3D connection between ferric trimers and PO_4 tetrahedra generate ten-membered tunnels in the [010] direction, in which methylamine and water molecules are located, and eight-membered channels along [100].	-135	25	90
10	[H-ethylenediamine] $Fe^{2+}Fe^{3+}F_2(HPO_4)_2$ (H_2O)	The 2D layers are built up from Fe^{2+} and Fe^{3+} in octahedral coordination. $Fe^{2+}O_2F_2(H_2O)_2$ and $Fe^{3+}O_4F_2$ octahedra are alternatively connected by their trans fluorine vertices and form chains in the [110] direction. These chains are connected to one another by HPO4, tetrahedral unit, in such a way that the OH groups are orientated toward in layer-space.	-133	28	91
11	[ethylenediamine] $FeF(HPO_4)$	2D layered compound with FeO_3F_2N octahedra, since the amine is part of the coordination polyhedra, these octahedra	N/A	N/A	92

		form chains linked by μ^2- *trans* bridging fluoride along [010]. These chains are connected to one another via HPO_4 tetrahedra, whose terminal OH groups point alternatively up and down within the layer.			
12	[H_2-DABCO] $Fe_4(PO_4)F_4(H_2O)_3$	Contains SBU-6 and SBU-2, where the hexamer is built up by three Fe in octahedral coordination: a central FeO_4F_2 and two external $FeO_4F(H_2O)$ octahedra. The dimer is formed by the corner sharing of a PO_4 tetrahedron and an iron square pyramid, $FeO_4(H_2O)$. The water molecules are terminal in the three iron polyhedra.	-110	11	93
14	[H_2-1,3 diaminopropane] $FeF(HPO_4)_2$• xH_2O	1D structure built up from infinite $[FeF(HPO_4)_2]^{2-}$ chains running along the [100] direction. The chain is built up from a central core constituted by FeO_4F_2 octahedra linked by μ^2- *trans* bridging fluoride. The HPO4 tetrahedra are orientated in such a way that the OH group is terminal.	-130	10	94
15	[H_2-1,3 diaminopropane] $Fe_4F_3(PO_4)$ $(HPO_4)_4(H_2O)_4$	3D framework built up from corrugated planes of Fe octahedra and HPO_4 tetrahedra which consist of (i) infinite chains and (ii) dimers. The infinite chains of FeO_4F_2 octahedra are linked via μ^2- *trans* bridging fluorides in the [001] direction. The dimers are formed by $FeO_4F(H_2O)$ octahedra linked by corner-sharing fluorine atoms. The planes are connected to each other through PO_4 tetrahedra and produce large ovoid 16-membered rings channels running along [001], in which diprotonated 1,3-diaminopropane and water molecules are encapsulated.	-250	22	95

19	[H_2-DABCO] $Fe_4(PO_4)F_4$	Dehydration of ULM-12 at 260°C yields ULM-19, which also contains SBU-6 and SBU-2 units. Here however, due to the loss of water molecules, the hexamer is built up from central FeO_4F_2 octahedra; square pyramid, FeO_4F, and a trigonal bipyramid, FeO_4F. The dimer is now constituted of PO_4 and FeO_4 tetrahedra.	-228	9	96

Continuing on from the ULM-series, Le Meins *et al* looked at the hydrothermal synthesis at higher temperature and pressure using the B-Fe-P-O-H-F system (where B = Sr and Ba). It was shown that by varying the HF/H_3PO_4 ratio it is possible to form different fluorinated species. When no HF was added, $B_2Fe_2(HPO_4)(PO_4)_2F_2$ [97] is the primary phase; if the ratio between HF and H_3PO_4 reaches unity, $BFePO_4F_2$ is formed.[98]

$B_2Fe_2(HPO_4)(PO_4)_2F_2$ consists of FeO_5F octahedra that are connected to each other via bridging phosphate groups to form a 2D layered structure. The fluorine atom on the Fe octahedra and the OH on the P tetrahedra are terminal and orientated toward the inter-layer space; this inter-layer space is occupied by B^{2+} cations.

$BFePO_4F_2$, Figure 1-22, is also a 2D layered structure which contains FeO_2F_4 and FeO_4F_2 octahedra that are linked through *trans* μ^2- bridging fluoride to form chains that run along the (001) direction. These chains are linked via PO_4 tetrahedra to generate layers. One of the oxygen’s on the phosphate tetrahedra is terminal, and lines the layers along with fluoride atoms on the FeO_2F_4 octahedra. The magnetic measurements of this material indicate strong antiferromagnetic superexchanges, where $T_N = 52$ K and $\theta_P = -217(10)$ K. Both $B_2Fe_2(HPO_4)(PO_4)_2F_2$ and $BFePO_4F_2$ form 2D layers due to the large cation size of Sr and Ba. Most of the work up to 1995 focused on the magnetic properties of iron fluorophosphates. It was not until 2007 that the electrochemical properties of these materials were tested. The success of $LiFePO_4$ as a positive electrode material has led to lots of research into the improvement of iron phosphate battery materials. The inclusion of fluoride causes an inductive effect, which increases the ionicity of the bonding around the metal, and thus raises the potential of the transition metal ion redox couple.[62] The work from Ellis *et al* was the first to test iron fluorophosphate materials as battery materials.[99] The compound tested was A_2FePO_4F (where A = Li and Na) (Figure 1-22b). This is a 2D layered compound consisting of face-sharing FeO_4F_2 octahedra connected via μ^2-bridging F atoms to form chains, which are joined by PO_4 tetrahedra with Na and Li located in the inter-layer space. The average charge potential of A_2FePO_4F was 3.6 V (vs Li metal electrode) and on cycling is similar to that of $LiFePO_4$ (3.55 V).[99]

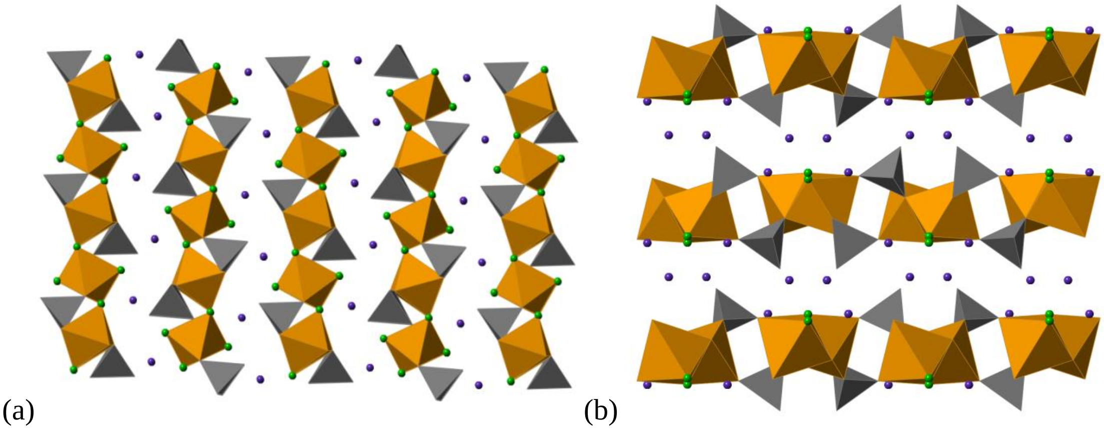
(a) (b)

Figure 1-22 – Structures of (a) $BFePO_4F_2$ and (b) A_2FePO_4F viewed along the a-axis. Fe polyhedra in orange, P tetrahedra in grey, F atoms are green spheres and B/A atoms are purple spheres

However, examples of materials combining both oxo-tetrahedra and high levels of fluoride anions in a framework material are still comparatively rare, though reported examples include templated fluoro-vanadyl-hydrogenarsenates [100] and cerium fluoride-arsenate frameworks.[101] To ensure significant levels of fluoride incorporation into new material types, a new synthetic technique was developed with a reaction medium with a high F:O molar ratio - hydrofluorothermal synthesis - by Armstrong *et al*.[102] In this work there were approximately 50 amine and alkali metal-templated, copper, cobalt, manganese and iron fluorophosphate compounds synthesised. Examples of materials produced through this method include $(NH_4)_3Fe_4F_9(PO_4)_2$ (Figure 1-23), which is constructed from four FeO_2F_4 octahedra linked into tetrahedral units which then link further to form chains along the (100) direction; these chains are cross-linked through PO_4 units into a 3D network defining channels containing the ammonium cations. $(CH_3NH_3)FeFPO_4$ (Figure 1-23), was also produced, and consists of slightly corrugated infinite chains of *cis* and *trans* μ^2-bridged FeO_4F_2 octahedra via F atoms along the (010) direction and are cross-linked by PO_4 tetrahedra to form a 3D channel system containing methylammonium cations. This hydrofluorothermal work has been significantly expanded with papers describing new Cu [103], Mn [104] and Co [105] fluorophosphate frameworks. A paper containing iron fluorophosphates has been published,[106] which contains a combination of compounds from Armstrong *et al* [102] and from the work described in Chapter 3.

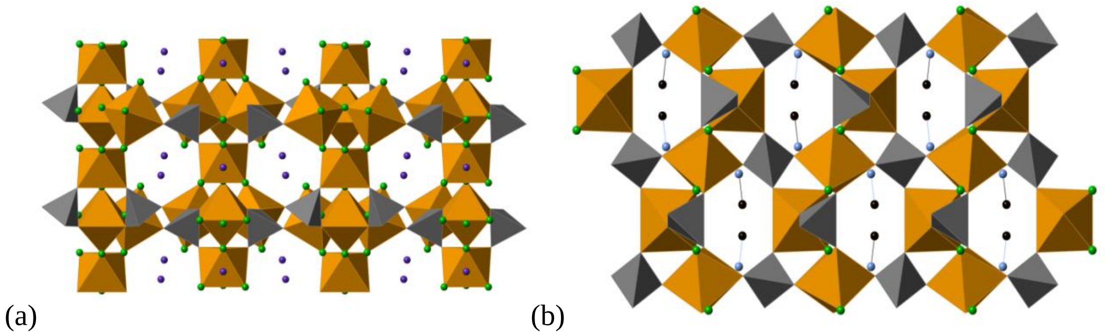

Figure 1-23 – Structures of (a) $(NH_4)_3Fe_4F_9(PO_4)_2$viewed along the (101) direction and (b) $(CH_3NH_3)FeFPO_4$ viewed along the c-axis. Fe polyhedra in orange, P tetrahedra in grey, F atoms are green spheres, C atoms are black sphere and N atoms are light blue spheres.

The main interest in iron fluorophosphates concerns their magnetic and electrochemical properties but with limited research into their catalytic properties, probably due to the lack of porosity. Iron fluorophosphates open the way to a new class of open-framework solids that combine well-known sieving properties with magnetic properties; these might be used for magnetic separation if the ordering temperatures reached are sufficiently high.[40]

Copper frameworks

Structures comprised solely of copper and oxopolyhedra are much desired due to the multiple oxidation states and coordination polyhedra possible for copper centres. The doping of copper into open-framework systems, such as AlPOs and zeolites, has been shown to increase catalytic activity in comparison to undoped parent frameworks. The catalytic activity for the reduction of nitric-oxide by Cu-ZSM-5,[107] and oxidation of organic compounds by Cu-MCM-41,[108] arises from the redox chemistry of the copper species present.

A range of open-framework copper silicates have been produced using hydrothermal techniques under conditions comparable to those used in classical zeolite synthesis. The series of nanoporous copper silicates are designated as CuSH-*nA*, where *n* is a framework type number and *A* represents the extra-framework cations.[109] The structures contain 8- ,10- or 12-ring channel systems which are filled by alkali metal cations and water molecules.

CuSH-1Na- (Figure 1-24a) is comprised of silicate double layers and $CuO_4(H_2O)_2$ octahedra that define straight 12-ring channels, analogous to those found in LTL-type zeolite.[110] The silicate double layer contains 12-ring channels of tetrahedra that run along the (001) direction and have an aperture of 7.3 x 4.4 Å, and 8-ringchannels along the (011) and $(01\bar{1})$ directions with an aperture of 3.8 x 2.5 Å. The structure of CuSH-2Na contains double chains of SiO_4 tetrahedra that are interlinked by CuO_5 square-based pyramids to form a 3D framework

(Figure 1-24b). The 3D framework is traversed by a 1D system of eight ring channels that are filled by sodium ions and water molecules.

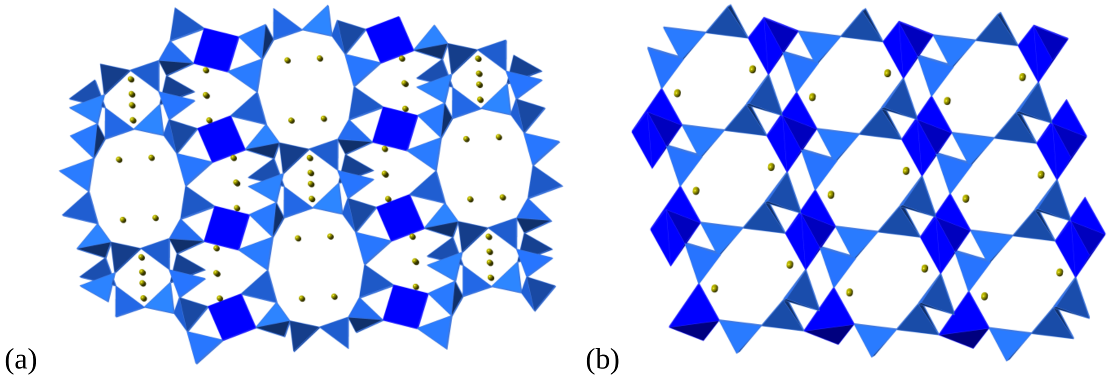
(a) (b)

Figure 1-24 – Structure of (a) CuSH-1Na viewed along the a-axis and (b) CuSH-2Na viewed along the b-axis. Cu polyhedra in dark blue, Si tetrahedra in light blue, Na atoms are yellow spheres and water has been removed for clarity.

High temperature synthetic techniques have been used in copper framework synthesis and are still predominantly utilised. One of the first open-framework copper phosphate materials to be synthesised was monoclinic $KCuPO_4$, in 1980 by Shoemaker *et al*;[111] a low temperature orthorhombic structure was formed hydrothermally by Effenburger in 1984.[112] Monoclinic $KCuPO_4$ is comprised of square planes (CuO_4) and square-based pyramids (CuO_5) linked through PO_4 tetrahedra to form a 3D porous framework, with K cations within the channels (Figure 1-25).[113] A similar 3D framework with the formula $RbCuPO_4$ was found to have the ABW-zeolite structure with alternating corner-sharing CuO_4 and PO_4 tetrahedra, where Rb cations occupy the inter-framework channels [114] (Figure 1-25).

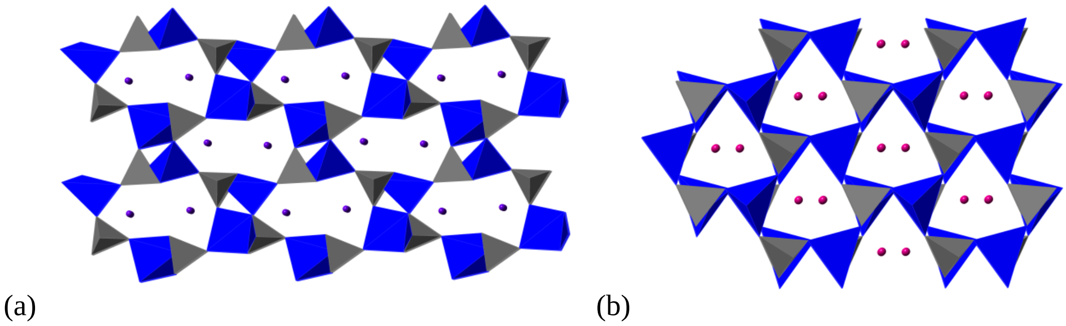
(a) (b)

Figure 1-25 - Structure of (a) $KCuPO_4$ and (b) $RbCuPO_4$ viewed along the c-axis. Cu polyhedra in dark blue, P tetrahedra in grey, K atoms are purple spheres and Rb atoms are dark pink spheres

The layered copper silicates cuprorivaite ($CaCuSi_4O_{10}$) and effenbergerite ($BaCuSi_4O_{10}$) are naturally occurring silicate sheet minerals.[115, 116] Cuprorivaite (Egyptian Blue) and effenbergerite (Hans Blue) have been used as blue pigments since ancient times.[59] The structures are composed of rings containing four SiO_4 tetrahedra, $[Si_4O_{10}]$ which are capped at either end by square-planar copper centres. This forms double copper silicate layers which are separated by alkali-earth cations in a distorted cubic geometry (Figure 1-26).

Han Purple ($BaCuSi_2O_6$) contains a similar structural motif to the other copper silicate sheet compounds described above. However it is composed of Si_2O_6 rings, which are also capped by square planar copper centres. The smaller rings result in the copper centres being separated by ~2.8 Å, resulting in the formation of Cu-Cu bonds. The formation of the Cu-Cu bond gives this compound its distinct colour, and reduces the stability of this pigment, Figure 1-26.

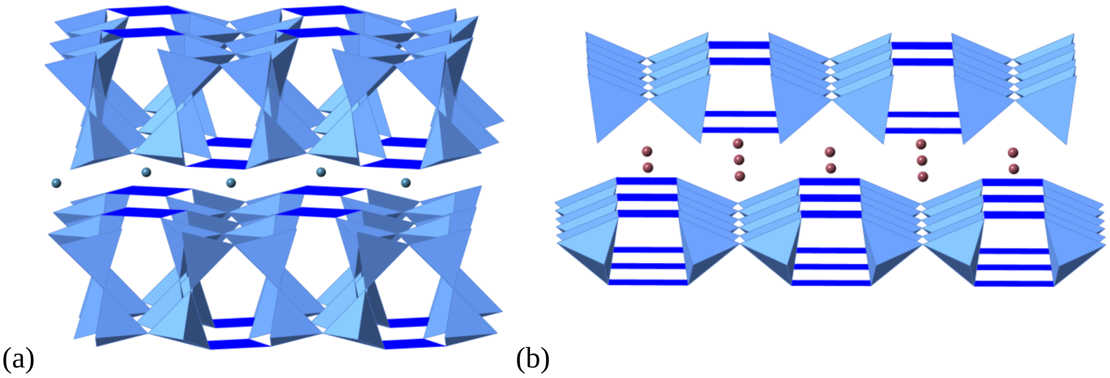
(a) (b)

Figure 1-26 - Structure of (a) Egyptian blue and (b) Han Purple viewed along the b-axis. Cu polyhedra in dark blue, Si tetrahedra in light blue, Ca atoms are turquoise spheres and Ba atoms are light pink spheres

Copper compounds have been of interest for their magnetic properties since the discovery of the Ya-Ba-Cu-O superconductors.[117] A large number of copper phosphates have been reported in the literature that exhibit interesting magnetic properties.[118-123] For example, $BCuP_2O_7$ (B = Ca; Sr, and Pb) contains CuO_5 square pyramids that are linked though diphosphate groups to from a 3D framework with channels along the *b* and *c*-axes containing B cations (Figure 1-27).[118] The Cu framework forms 1D zig-zag chains, where the Cu centres in the 1D chain are connected with each other through one PO_4 group. The magnetic specific heat exhibited one broad maximum due to short-range magnetic ordering, which is characteristic of quasi-1D systems.

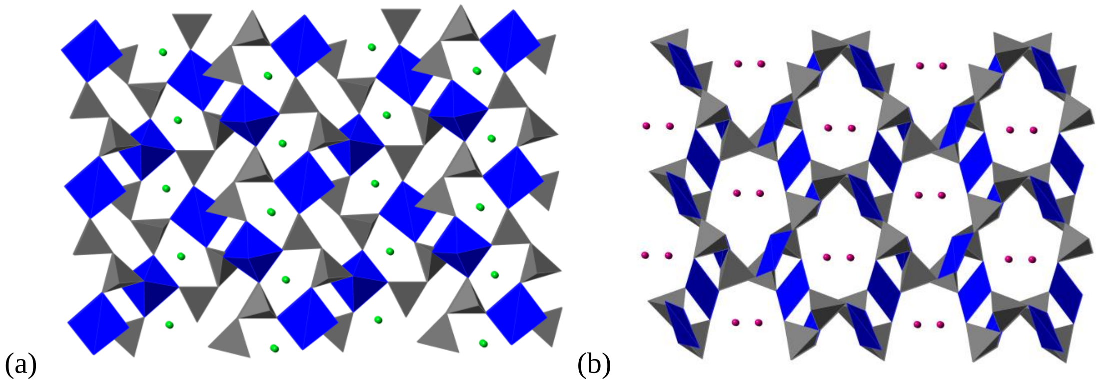

Figure 1-27 - Structure of (a) $BCuP_2O_7$ and (b) $CsCu_3P_4O_{12}$ viewed along c-axis. Cu polyhedra in dark blue, P tetrahedra in grey, B atoms are light green spheres and Cs atoms are dark pink spheres

$Cs_2Cu_3P_4O_{14}$ [123] contains alternating square-planar (CuO_4) and diphosphate units which share vertex O atoms.to form a 1D channel structure along the *c*-axis where the Cs cations reside (Figure 1-27). The magnetic properties of this material are derived from the three CuO_4 units which are stacked in a staggered configuration and separated by ~3.4 Å. This gives rise to a weak ferromagnetic transition at T_c =14 K.

Most of the research related to copper sulphate frameworks are centred on the synthesis and characterisation of mineral materials.[124-127] An example of this relates to Kröhnkite type chains observed within $A_2Cu(SO_4)_2{\bullet}2H_2O$, where A = Na and K.[128] The chains are comprised of sulphate tetrahedra and copper octahedra (CuO_4 ($2H_2O$)) extending along the *c*-axis (Figure 1-28); these chains are linked together by seven coordinate A atoms. The Cu octahedra show typical Jahn-Teller distortion with four short planar bonds and two elongated axial bonds.

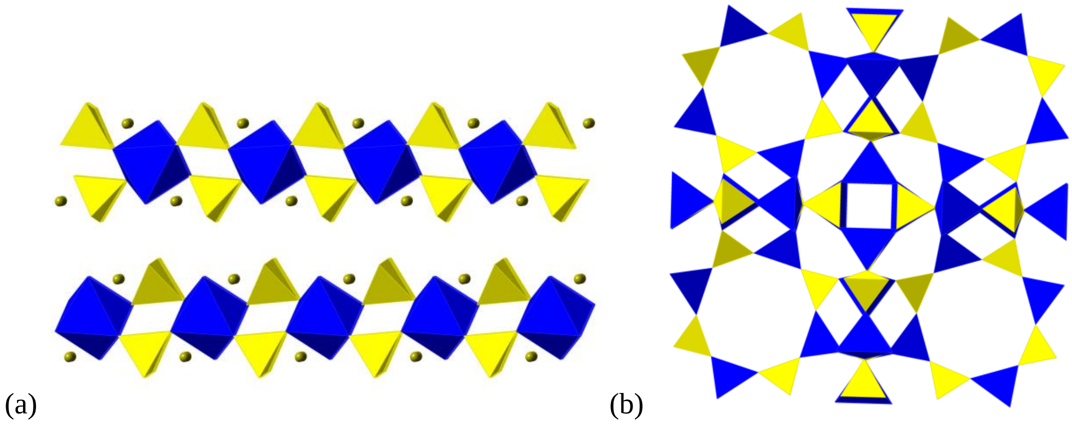

Figure 1-28 –Structure of (a) Kröhnkite chain and (b) $[Cu_{12}(SO_4)_{12}(3H_2O)]{\bullet}H_2O$ viewed along the a-axis. Cu polyhedra in dark blue, S tetrahedra in yellow, A atoms are yellow spheres and water has been removed for clarity.

The majority of transition sulphates are water-soluble, indicating water molecules are the most competitive ligand with the sulphate groups in bonding to metal cations. Water molecules are framework-terminating species, which normally leads to lower dimensionality of frameworks such as the Kröhnkite type chains. However, a 3D copper sulphate framework with the formula $[Cu_{12}(SO_4)_{12}(3H_2O)]•H_2O$ contains sulphate and copper tetrahedra linked similar to the LTA framework type[129] The structure (Figure 1-28) contains β-cages connected by double-4-rings to create large nine-membered rings and features unique tetra-dentate bridging sulphate ions.

1.5 Scope of the work

The reviews of current iron and copper frameworks highlight the lack of research into the optical properties of these materials, specifically in terms of their potential for NIR absorbance. The aim of this thesis is to create a library of iron and copper frameworks, and determine their NIR absorbance, with the prospect of developing structural-property relationships.

Initial work to build this library focussed on using hydrothermal techniques to synthesise new materials, which included fluoride to add further structural diversity. The result of this initial work is provided in Chapter 3, which describes the structures of 13 iron fluorophosphate compounds and provides insight into the unique structural feature that arose due to fluoride inclusion.

A range of iron and copper materials were then synthesised using more conventional synthetic techniques, such as solid state methods. The effects of the geometry and ligand environment on the optical properties of these materials were investigated and presented in Chapter 4 respectively.

Materials containing a strong absorbance around 1064 nm have been selected as candidates for Nd:YAG laser-marking trials, the results of which are presented in Chapter 5.

Chapter 2 Experimental Techniques

A wide range of experimental techniques have been utilised to synthesise and characterise desired materials. The main synthetic techniques employed are centred-on solid-state and solvothermal methods. Compounds have been primarily characterised using non-destructive X-ray diffraction methods, such as Powder X-ray Diffraction (PXD) and Single crystal X-ray Diffraction (SXD).

SXD was used to carry out characterisation of unknown crystal structures, and as such was the primary method for identifying solvothermal reaction products. PXD was used in the identification of any powdered products, as well as in the determination of sample phase purity. Powdered products are commonly formed by solid-state synthesis.

Once the structure and phase purity had been confirmed by X-ray diffraction, the optical properties of these materials were tested using an UV/Vis/NIR spectrometer. Scanning electron microscopy (SEM), in combination with energy dispersive X-ray analysis (EDX), was used to observe crystal and particle morphologies, whilst probing the chemical composition of samples. Thermogravimetric analysis (TGA) was used to determine the thermal stability of reaction products and investigate possible intrinsic changes due to heating.

Bond valence (BV) calculations were employed primarily to distinguish between sites where the scattering power proved to be ambiguous. BV calculations were also employed to check charges on the iron centres and remaining structure, thus confirming the structural formulae.

2.1 Synthetic methods

Solid State methods

Solid state or high temperature reactions are a very common method for the preparation of polycrystalline materials, which involves heating solid starting materials over an extended period. Reaction, even at high temperatures, is slow and typically takes several days, as the energies involved in breaking down the structures - by overcoming the lattice enthalpies and diffusing the ions through the solid structures over significant distances - are very high.[3]

The types of starting materials that are used during solid state synthesis are typically oxides. In reactions between oxides the most mobile ions are normally cations, as these are usually smaller than the oxide ions, and it is these ions that diffuse though the reaction mixture to form new phases.[130]

The rate limiting step in solid state reactions is the diffusion of ions; increasing the temperature will speed up the mobility of the various ions. However, raising the temperature can also cause

the mixture of solids to melt and the ions to become highly mobile; cooling a molten mixture does not normally yield the desired phase in pure form. Temperature is not the only factor that can improve the rate of reaction. It is also possible to increase the number of reactive crystal interfaces and to reduce the diffusion distance between starting materials. This can be achieved by reducing the particle sizes (i.e increasing the surface area) and by pelletising the material. Grinding of the starting materials, by hand with a pestle and mortar or mechanically via ball-milling, will aid the homogenous distribution of the starting materials. Pelletising the material, normally carried out with a hydrolytic press, will reduced the inter-particle void space (i.e. diffusion distance), producing many more interfaces over which the reaction can take place.[130]
In a typical synthesis the solid starting materials are weighed out in stoichiometric amounts (Equation 2.1), and the types of starting materials that are used are normally metal oxides. It is more common to use a chemical precursor that will decompose, with the loss of a gaseous species, to generate fine, highly reactive oxide species that reduce reaction times. The main types of precursors are carbonates, nitrates, oxalates and hydroxides. Another advantage of using chemical precursors are that they are normally air stable, while metal oxides are hygroscopic and absorb CO_2 from the air. After the reaction mixture has been thoroughly ground and pelletised, the mixture is placed into crucibles which are constructed using inert materials such as high density alumina, gold or platinum. The samples are then fired to the desired temperature; in general the complete reaction can be achieved if the reaction temperature reaches two-thirds of the melting point of one of the solid reactants.[131]
Unfortunately, the formation of the product tends to reduce the area of contact between reactants, therefore reducing the rate of reaction. To combat this, the reaction mixture is normally reground at regular intervals during the heating cycle.
The reaction environment may need to be controlled if a desired oxidation state is required or if one of the reaction components is volatile. Solid state reactions can be carried out under controlled atmospheres using a tube furnace, where gas can be passed over the reaction mixture during heating. For example, to produce Iron (II) materials a reductive (H_2/N_2) or protective (Argon, N_2) atmosphere is required to prevent oxidation. Sealed tube reactions were performed under vacuum to reduce the loss of volatile reaction components; this loss can lead to impure products.[130]

$$\mathrm{Fe_2O_3 + 2(NH_4)_2HPO_4 \rightarrow 2FePO4 + 4NH_3 \uparrow + 3H_2O \uparrow}$$

Equation 2.1

The reaction can be monitored at different stages by using PXD; it is also possible to use Variable Temperature PXD (VT-PXD) to look at the reaction *in-situ.*

Hydrothermal /Solvothermal synthesis

The term hydrothermal/solvothermal usually refers to any heterogeneous reaction in the presence of aqueous solvent and/or mineralisers under high pressure and temperature conditions to dissolve and recrystallize materials that are relatively insoluble under normal conditions.[132] A mineraliser acts as a catalyst and aids the solubility of the starting materials. The most common types include hydroxide and fluoride ions. The fluoride route has the advantage of allowing a greater range of pH values, whereas the hydroxide route is limited to alkaline pH values. It is more common to use the term solvothermal synthesis as it encompasses a broader set of solvents than hydrothermal.

The solvothermal technique, in contrast to other conventional techniques, such as solid state and sol-gel methods, offers several advantages. Compounds that contain elements with oxidation states that are difficult to obtain can be synthesised in a closed solvothermal system. Synthesis of metastable compounds is possible, as the overall free energy change for hydrothermal synthesis is usually quite small, therefore the outcome is most frequently kinetically controlled.[133] During solvothermal synthesis the solvent, normally water, will be subjected to sufficient temperature and pressure, to allow the solvent to become supercritical. Under supercritical conditions, the solvent can act as a gas and liquid, and this enables very fast ion mobility, and therefore only a short reaction time is needed: typically a few days. Solid state and sol-gel methods by comparison could take a matter of weeks.

There are also some disadvantages to the solvothermal method, namely limited control of product formed, difficulty in obtaining a single phase, and poor crystal quality. A wide variety of factors can affect the final product: pH, temperature, pressure, time, and the ratio/order of the starting materials. Therefore a trial-and-error process is required until the correct formula is found, however this can also be an advantage, as once the correct formula has been found, a slight variation in one of the factors above can give a wide range of materials.

The mechanism that occurs during solvothermal synthesis is not fully understood: there is a review paper by Cundy et al [134] that summaries the different theories. A general mechanism that solvothermal reactions will proceed through is given below and depicted in Figure 2-1:

a) Primary amorphous phase - the point at which the starting materials are mixed, and a gel is formed.
b) Secondary amorphous phase - after some time (shorter at elevated temperatures) regions of order will start to form, but not the framework lattice itself.
c) Crystalline product - In the final stages of the reaction, if an ordered area reaches a critical nuclear size a nucleation event will occur, and a crystalline product will start to form.

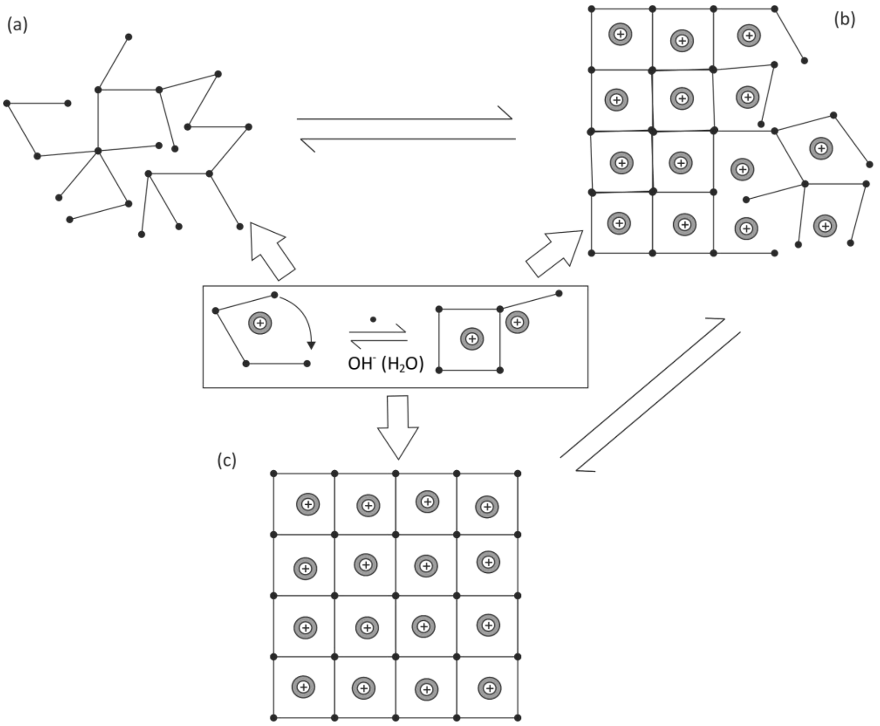

Figure 2-1- Generalised mechanism for solvothermal synthesis. (a) Primary amorphous phase, (b) Secondary amorphous phase, (c) Crystalline product formed. (Central insert) Cation templating of framework

Figure 2-2 shows the 23 mL PTFE (Polytetrafluoroethylene, Teflon®) lined, stainless steel Parr™ autoclave used to perform solvothermal experiments. The PTFE liners are ideal for our applications; they are an inert material and therefore can be used under strongly acidic or alkaline conditions. There are a few limitations of PTFE that are undesirable: under high temperature and pressure PTFE has a significant creep effect, therefore maintaining a tight seal becomes more difficult. PTFE is also a porous material; this can cause leeching of materials from the liner into the reaction mixture, and vapour migration into the liner walls cannot be avoided. From these limitations the absolute maximum working temperature and pressure is 250 °C and 1800 psig, respectively.

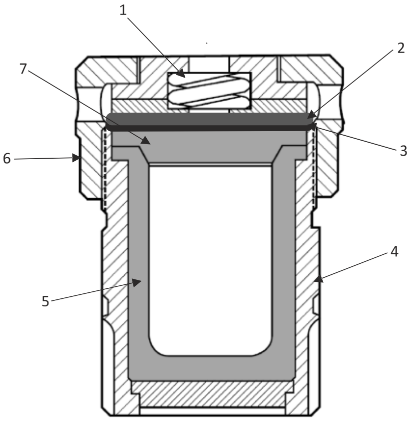

Figure 2-2- Indicating the type of hydrothermal bomb used in this project. (1) Screw-loaded seal - maintains constant pressure on the liner seal. (2) Corrosion disc - protects the Rupture disc from corrosive vapour. (3) Rupture disc - protects the bomb/operator from hazards of bomb explosion. (4) Stainless steel metal jacket. (5) Thick-walled Teflon® liner. (6)Bomb cap - Screw top. (7)Teflon liner lid - made with a broad, flanged closure to enable higher temperature synthesis.

2.2 Characterisation Techniques

These synthetic techniques produce crystalline materials which were characterised using X-ray diffraction techniques. Under standard synthetic conditions, most of the materials produced contained very small crystallites; therefore the primary characterisation technique employed was powder X-ray diffraction (PXD). However, solvothermal synthesis can yield single crystals of sufficient size and quality to characterise new materials fully using single crystal X-ray diffraction (SXD).

X-ray Diffraction

X-rays were discovered in 1896 by Wilhelm Röntgen and can interact with matter in a way similar to light. X-rays can be scattered with no loss of energy (scattered radiation), scattered with a small loss of energy (Compton radiation) or be absorbed by atoms. To obtain structural information from X-ray diffraction we are only interested in scattered radiation. X-rays are scattered in various directions by atom electrons within a crystalline material.

This scattering behaviour was first realised in 1912 from the work of Max von Laue, Paul Knipping and Walter Friedrich, who observed the first powder X-ray diffraction pattern of zinc blende. This demonstrated for the first time the ability of crystals to act as X-ray diffraction gratings, reflecting only at certain allowed directions, similar to visible light.

A crystalline material can be defined as a regular repetition of ordered molecules in 3D space. The simplest portion, which is repeated by translation and shows its full symmetry, is defined as the unit cell, Figure 2-3.

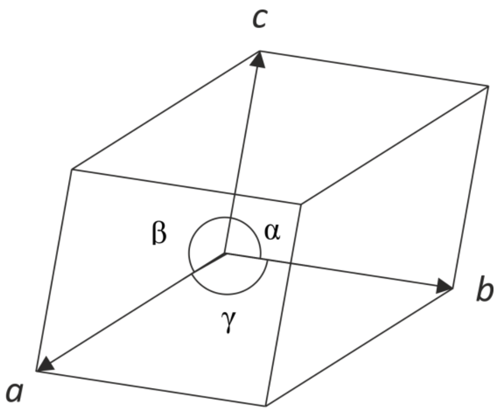

Figure 2-3 - Unit cell defined by lattice parameters a, b, c and α, β and γ

The different types of unit cells are better characterised by determining the number of lattice points belonging to them; this takes into account that points on faces, sides and on corners are only partially shared by a given cell.[135] This gives rise to four lattice types: Primitive (P) has 1 lattice point; Body-centred (I for Innenzentrierte) has 2 lattice points; Face-centred (F) 4 lattice points; and Base-Centred (C) 2 lattice points. By combining the seven crystal systems with the four lattice types, 14 Bravais lattice types are possible: this establishes a connection between the external crystalline form/shape and the internal molecular/atomic arrangements (Table 2.1).[136] Symmetry elements are used to relate lattice points to each other and fall under two categories: point and translational symmetry elements. These are required to describe all the possible patterns which arise by combining motifs of different symmetries with their appropriate Bravais lattice types.[136] Each Bravais lattice can be described by point group symmetry elements, which describe the rotational and reflection symmetry within the unit cell (such as centres of symmetry, mirror planes and inversion axes): this gives rise to 32 point groups (Table 2.1). These 32 point groups can be further divided into 230 space groups, which describe all symmetry elements within the unit cell, and include translational symmetry elements such as screw axes and glide planes.

The simplest example is the triclinic crystal system which, due to the asymmetry of the unit cell, can only be a primitive lattice type, with the only possible additional symmetry being a centre of inversion. The resulting space groups available for a triclinic unit cell are therefore $P1$ and $P\bar{1}$.

Table 2.1- Crystallographic table

Unit cell dimensions	Crystal system	Bravais Lattice types	Point groups
a=b=c, α=β=γ=90°	Cubic	P,I,F	$23, m\bar{3}, 432, \bar{4}3m, m\bar{3}m$
a=b≠c, α=β=γ=90°	Tetragonal	P,I	4, $\bar{4}$, 4/m, 422, 4mm, $\bar{4}$2m, 4/mmm
a≠b≠c, α=β=γ=90°	Orthorhombic	P,C,I,F	$mmm, mm2, 222$
a≠b≠c, α=γ=90°, β≠90°	Monoclinic	P,C	$2, m, 2/m$
a≠b≠c, α≠β≠γ≠90°	Triclinic	P	$1, \bar{1}$
a=b=c, α=β=90°, γ=120°	Hexagonal	P	$6, \bar{6}, 6/m, 622, 6mm, \bar{6}2m, 6/mmm$
a=b=c, α=β=γ	Trigonal/ Rhombohedral	P/R	$3, \bar{3}, 32, 3m, \bar{3}m$

Atoms within a crystalline material can be envisaged as an ordered array of scattering centres, which are related to each other in three dimensions, by translational symmetry, to form lattice planes. Treating X-ray diffraction as a series of reflecting planes has enabled, through the work of Laue [137] and W.L Bragg [138] , the use of X-rays to determine crystalline structures. Laue treated the diffracting crystalline material as a three-dimensional diffraction grating; this gives rise to three expressions, which require a large number of variables to be determined. A much simpler explanation was provided by Bragg. He assumed that a crystalline material is made up of a series of reflecting/diffracting planes (Figure 2-4).

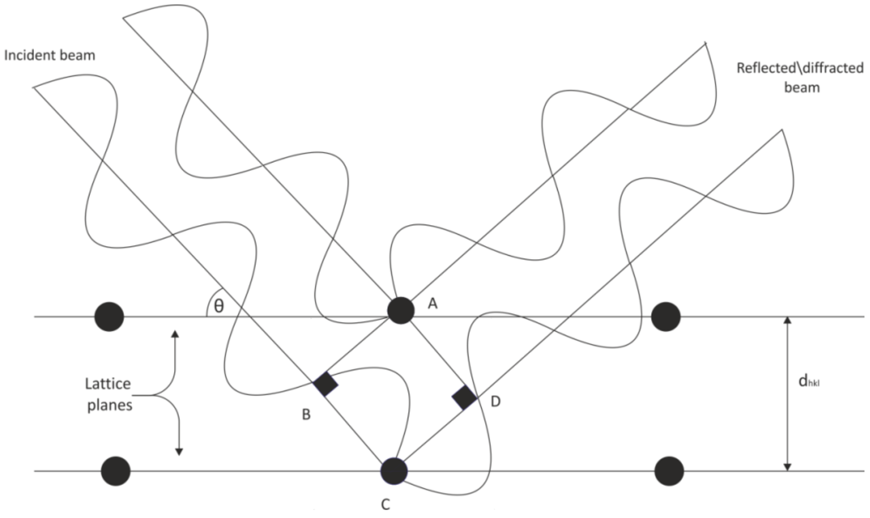

Figure 2-4 - Depicting Bragg's law

When the incident X-ray beam scatters from lattice points A and C from parallel lattice planes, this will produce an *in phase* (constructive interference) diffracted/reflected set of X-ray beams, if the additional distance travelled to point C is an integral number of wavelengths (nλ). This relationship gives rise to the expression known as Bragg's equation (Equation 2.2)

$$\text{Path difference = BC+CD=}\ \boldsymbol{n\lambda = 2d_{hkl}\sin\theta}$$

Equation 2.2

Where n is an integer, λ is the X-ray wavelength, d_{hkl} is the d-spacing, and θ is the angle of incident beam.

For a primitive lattice type, scattering can be observed from all *hkl* values. However, destructive interference can arise due to systemic absences, leading to certain values of *h,k* and *l* that will not be observed in an X-ray diffraction pattern. Systemic absences occur when Bragg's law is not satisfied, which are related to the Bravais lattice type and translational symmetry elements. Examples of the rule for allowed reflections for specific Bravais lattice types include $h + k + l = 2n$ for body-centred systems, and h, k, l must be all odd or all even for the system to be face-centred (for a full list of systemic absences see Fundamentals of crystallography 2nd edition page 175).[135] By noting the systematic absences for an observed X-ray diffraction pattern, it is possible to deduce the crystal system and reduce the number of possible space groups for a given unit cell.

The relationship between the d-spacing and the lattice parameter is dependent on the crystal system and can be determined by trigonometry; the expressions for selected crystal systems are given in Table 2.2.

Table 2.2-Expression for d-spacings in selected crystal systems

Crystal system	Expression for d_{hkl}
Cubic	$\frac{1}{d^2}=\frac{h^2+k^2+\ l^2}{a^2}$
Tetragonal	$\frac{1}{d^2}=\frac{h^2+k^2}{a^2}+\frac{l^2}{c^2}$
Orthorhombic	$\frac{1}{d^2}=\frac{h^2}{a^2}+\frac{k^2}{b^2}+\frac{l^2}{c^2}$
Monoclinic	$\frac{1}{d^2}=\frac{1}{\sin^2\beta}\left(\frac{h^2}{a^2}+\frac{k^2\sin^2\beta}{b^2}+\frac{l^2}{c^2}-\frac{2hl\cos\beta}{ac}\right)$

By combining the Bragg equation (Equation 2.2) with the expressions for d_{hkl} (Table 2.2) and eliminating d_{hkl}, it is possible to relate the lattice parameters and diffraction angle θ. Equation 2.3 shows an example for a cubic system:

$$\sin^2\theta=\frac{\lambda^2}{4a^2}(h^2+k^2+l^2)$$

Equation 2.3

This relationship allows structural information to be obtained from X-ray diffraction patterns. The determination of further structural information, such as atom positions/types, from powder X-ray diffraction data, is problematic due to peak overlap. The greater quantity of data collected from single crystal X-ray diffraction provides a powerful tool for structure determination of unknown materials. Single crystal diffraction data is collected as diffraction spots, the intensities of which are related to specific atoms. The occurrence of diffraction spots can be explained by using Ewald's sphere, shown in Figure 2-5.

The crystal to be studied is positioned at the centre of a sphere with radius 1/λ, (where λ is the wavelength of electromagnetic radiation) Ewald's sphere. If the incident X-ray beam is unaffected by the crystal, (i.e. passing straight through), it has the lattice point (000) on the surface of the Ewald's sphere. This lattice point (000) is defined as the origin of reciprocal space; other diffraction spots arise from lattice planes (hkl), which form a reciprocal lattice with dimensions 1/a, 1/b and 1/c. The Bragg equation (Equation 2.2) is satisfied if the diffraction spots lie upon the surface of the sphere, a distance of $1/d_{hkl}$ from the (000) lattice point. Rotation of the crystal allows further diffraction spots to intercept the surface of Ewald's sphere, allowing for the full structural characterisation of the crystal. The fraction of Ewald's sphere that needs to be collected, in order to obtain full data completeness, is dependent on the symmetry of the unit cell. Increasing the symmetry within the unit cell reduces the quantity of data required. For example, a centre of inversion, $\bar{1}$, halves the required sphere surface, whilst a point group of 4/*mmm* requires only a sixteenth of the sphere surface for full structural characterisation.

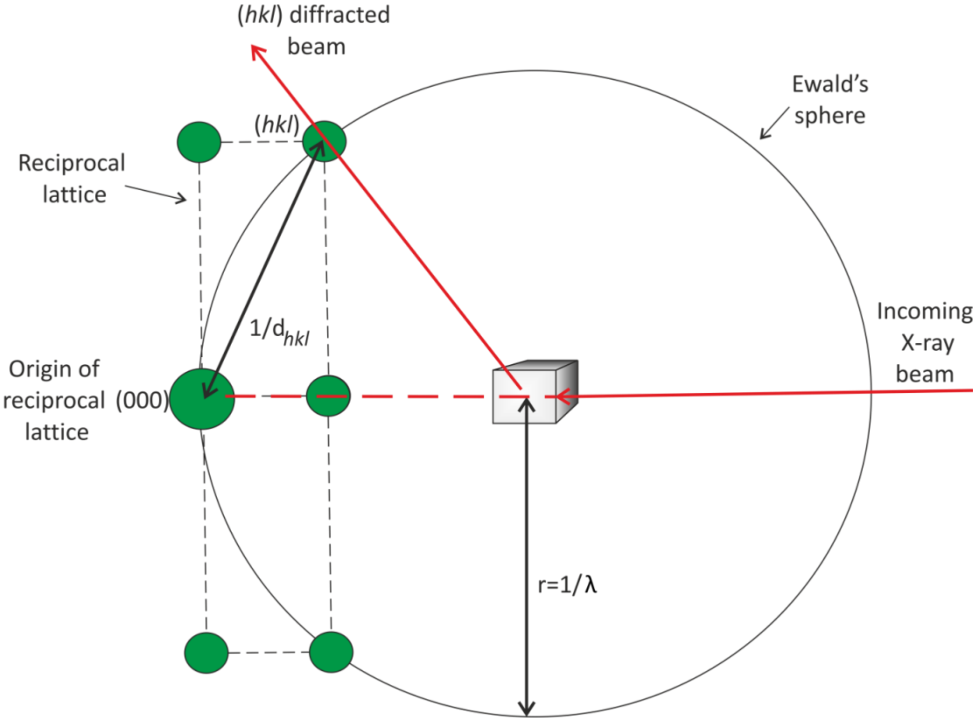

Figure 2-5 - Diagram of Ewald's sphere

Single crystal diffraction (SXD) there is a single crystal that will adopt a single orientation, which will give rise to a set of discrete spots (or reflections) from the d-spacings of the crystallite. Therefore interpretation of the geometry and intensities of the diffracted beams can lead to a full description of the crystal structure at atomic resolution.

Crystal structure determination is a two-part process: (a) the determination of the size and shape of the unit cell from the geometry of the diffraction pattern; and (b) the determination of the lattice type and distribution of the atoms in the structure from the (relative) intensities of the diffraction spots.[136] The determination of the unit cell is very simple as it is related to the diffraction angle (2θ) as shown in Equation 2.3 for a cubic system. So far each spot has been treated as having equal scattering power, but this is not the case, as X-rays are scattered by electrons in atoms and the scattering power is related to the number of electrons, hence this is different for each element. In order to solve part (b), the amplitude of the scattering from a reflection plane with Miller indices (hkl) and the phase angle of the scattered wave, must be determined: this is expressed as a complex number and known as the structure factor, F_{hkl}:

$$F_{(hkl)} = |F(hkl)| \times \exp[i\phi(hkl)]$$

Equation 2.4

Where $|F(hkl)|$is the amplitude of the wave and $\exp[i\phi(hkl)]$ is the phase angle.

The intensities of the diffraction pattern and the arrangement of the atoms in the unit cell of the crystal structure are related to each other by Fourier transformation (FT). The diffraction pattern is the FT of the electron density, and the electron density is the reverse FT of the diffraction pattern.[139] The FT for the diffraction pattern is given below:

$$F(hkl) = \int_{cell} \rho(xyz) \times exp[2\pi i(hx + ky + lz)]dV$$

Equation 2.5

Where the structure factor for each reflection (hkl) is given by electron density at each point in the unit cell ,$\rho(xyz)$, multiplying by a phase wave shift relative to the unit cell origin, $exp[2\pi i(hx + ky + lz)]$, and integrating these values over the whole cell volume.

The electron density is the reverse FT of the diffraction pattern, because the diffraction pattern consists of discrete reflections, this FT is a summation not an integral:[139]

$$\rho(xyz) = \frac{1}{V}\sum_{hkl} |F(hkl)| \times \exp[i\phi(hkl)] \times exp[-2\pi i(hx + ky + lz)]$$

Equation 2.6

Where $\frac{1}{V}$ is a necessary for unit correction, all other terms are same as above. The electron density, which originally generates the diffraction pattern, is the summation of all the diffracted beams, with their correct amplitude and phases.[139] The electron density map will help to locate the positions of atoms within the unit cell by using the reverse FT above, where all the other values are known except the phase. Phase information is lost because the intensities recorded are proportional to the square of the structure factor ($F_{(hkl)}^2$). The square of a complex number always gives a real number, hence information about the phase angles is lost, and this is referred to as the phase problem. If the phases of the dominant reflections can be determined, this may help determine the phases of the other reflections. To work out the phases using trail-error to thousands of waves is an impossible task, hence a need to determine a trail structure: there are two main methods used; Patterson (Heavy atom) and direct methods.

The Patterson method sets all the phases equal to zero (i.e. all in phase) and uses the square of the amplitudes ($|F_O(hkl)|^2$), given in Equation 2.6. This produces a Patterson map which shows where the atoms lie relative to each other, not relative to the unit cell origin, which is what is desired. It is possible to find a set of atomic coordinates for the heavy atoms which are responsible for the larger peaks; this can be used as the trial structure.

$$P(xyz) = \frac{1}{V}\sum_{h,k,l}|F_o(hkl)|^2 \times exp[-2\pi i(hx + ky + lz)]$$

Equation 2.7

Patterson peaks have similar shapes to electron density peaks but are about twice as broad; therefore atoms with similar atomic numbers cannot be distinguished using this method, ergo the need for direct methods that works for equal atom structures.

Direct methods try to derive the structure factor phases directly from the observed amplitude through probabilistic relationships. The electron density is the reverse FT of the diffraction pattern, therefore the addition of sets of waves produce the electron density distribution. The electron density is everywhere and positive or zero and it is also composed of discrete locations (i.e. where atoms are located). These factors reduce the number of ways that waves can be added together and by using trial-and-error methods, phases can be calculated. Direct methods select the most intense reflections as these contribute most to the electron density FT (Equation 2.6), and determine the probable relationships among their phases. The most promising calculate phases (φ_C) are then put into the FT cycle described below.

Once the trial structure has been obtained either through Patterson or direct methods, the coordinates from the trial structure can be used to generate a diffraction pattern using a forward FT (Equation 2.5). This gives rise to a calculated structure factor (F_c), and this contains both information on the amplitude ($|F_c|$) and the calculated phase (φ_C). For each observed intensity (F_o) there is a calculated equivalent (F_c); if the trial structure is partially correct there will be some resemblance between the calculated and observed diffraction patterns, and this gives a residual factor (R-factor) below:

$$R_1 = \frac{\sum \left||F_o| - |F_c|\right|}{\sum |F_o|}$$

Equation 2.8

For a completed structure this R-factor should be <10%. Another useful, more accurate R-factor includes the weights of each reflection (w) and the square of the structure factor; this gives the weighted R-value:

$$wR_2 = \sqrt{\frac{\sum \left(w(F_0^2 - F_c^2)\right)^2}{\sum w(F_0^2)^2}}$$

Equation 2.9

Even though the weighted R-value is more statistically meaningful, it is still common to use the unweighted R_1 value to assess the quality of a structural model.

This calculated phase (φ_C) can be used in combination with the observed amplitude (F_o) to create a new model structure by using the electron density equation, Equation 2.6. This should show the existing electron density map, together with additional unassigned atoms. By including the newly-located atoms in another FT cycle, this should get a better estimate of the phases. Thus the newly-calculated pattern ($|F_c|$) will closely resemble the observed diffraction pattern ($|F_o|$), hence the R-factor will be lower. Further FT cycles can be performed until all atomic positions are revealed and the R-factor will reach a minimum.

In order to reveal these atomic positions, a series of factors must be taken into account. Firstly, the correct crystal system and space group need to be ascertained. This is done computationally by taking into account the systemic absences of the diffraction pattern. When a suitable crystal system and space group have been selected, it is possible to start assigning atom positions. To build a structure, a combination of spot intensity and bond distances are used. The heaviest atoms are normally assigned first because these generate the most intense diffraction spots. Once all the heaviest atoms have been assigned it is possible, depending on the quality of the SXD data, to locate smaller atoms such as hydrogen and lithium. To determine if the atoms have been assigned correctly, a combination of R-factors and atomic displacement parameters (ADP) can be utilised. If atoms have been incorrectly assigned this is reflected in the thermal parameters - if the atom has too much electron density (i.e. too heavy) this will cause the thermal parameters to be orders of magnitude lower compared to equivalent correctly-assigned sites.

Single crystal data has been collected on two different types of diffractometers, both of which contain the same set-up shown in Figure 2-6. The old system was a Bruker-Nonius Kappa CCD diffractometer with a rotating anode and a molybdenum target (K_α= 0.71703 Å). The beam was focused with confocal focusing mirrors. Diffraction data was collected using a 72 x72 mm Kappa CCD detector. All of the data sets were collected at low temperature (120 K) via an Oxford Cryosystems system.

The new single crystal diffractometer use a FR-E+ SuperBright Molybdenum X-Ray generator producing a highly focused beam (70μm). The setup is completed with an AFC12 goniometer and an enhanced sensitivity Saturn 724+ 18bit CCD detector. Data is routinely collected at 100 K with the aid of an Oxford Cryosystems system.

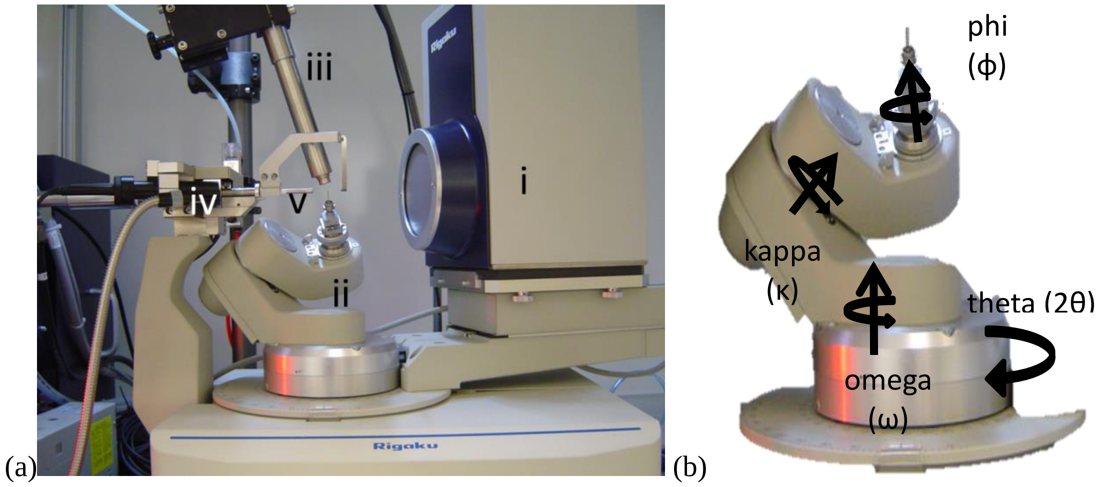

Figure 2-6 - (a) Rigaku FR-E+ Very high Flux diffractometer, (i) CCD detector (ii) goniometer (iii) cryostream (iv) positioning camera (v) X-ray beam. (b) Right: close up of 4 circle goniometer

A typical procedure includes selecting a suitable crystal, which is then mounted onto a pip; the pip is then aligned to the X-ray beam. A series of approximately 15 images are collected, which can be used to determine the unit cell and crystal quality. The crystal quality depends on the shape and intensity of diffraction spots. If the diffraction spots are doubled this implies a twinned crystal, whilst blurred spots are indicative of disorder within the crystal and poor intensity can be overcome with longer scan times.

Once images of sufficient quality are obtained, the d*TREK software suite,[140] within CrystalClear-SM Expert 2.0 r5, [141] processes the images and suggests possible unit cells. This is refined by the user before searching for unit cells of higher symmetry. When the unit cell has been determined, the parameters are compared to the ICSD database to establish if the material is novel. Once novelty has been established a full collection is undertaken, where the number of frames (i.e. fraction of Ewald's sphere) required to obtain a data completeness of 100 % is calculated by d*TREK.

On completion of data collection, the images were integrated and corrected for absorption, both through using the FS-Process software suites.[142] This data was refined using the Wingx package [143], using SHELXL-97 refinement suite.[144]

As stated above, the scattering of X-rays by a crystalline material is related to the structure and symmetry. Therefore each material will produce a unique pattern in terms of the position of the observed reflections and the peak intensities. Hence powder X-ray diffraction (PXD) is a useful technique for the identification of unknown compounds and phase purity.

A polycrystalline material will contain a larger number of crystallites. Each will adopt a random orientation and all of these crystallites will obey the Bragg equation and produce diffraction maxima at certain angles. This will give rise to a cone of diffraction, where each cone consists of a set of closely-spaced dots from the d-spacings of individual crystallites.

In order to determine the position (i.e. the diffraction angle, 2θ) and intensity of these diffraction cones, a powder X-ray diffractometer is used (see Figure 2-7).

During this project, two types of powder diffractometer have been used: a Siemens D5000 and a Bruker D8. A schematic for both of these diffractometers is shown in Figure 2-7; they use monochromatic copper $K_{\alpha 1}$ radiation (λ=1.5406 Å), produced from a copper anode, coupled with a germanium single crystal monochromator. There are a range of diaphragms that collimated the monochromatic X-ray beam, and the aperture and scattered-radiation diaphragms are set at 2 mm, with the detector diaphragm set to 0.2 mm. The collimated, monochromatic X-ray beam interacts with the sample, which is normally mounted on a Perspex, silica or aluminium sample holder, and the scattered radiation is measured using a scintillation counter. The sample is rotated at an angle θ; the detector is moved around the measuring circle to ensure the diffraction angle is 2θ. The incident beam, sample and detector are designed according to Bragg Brentano geometry, this allows for the diffracted beam to be focused onto the detector.

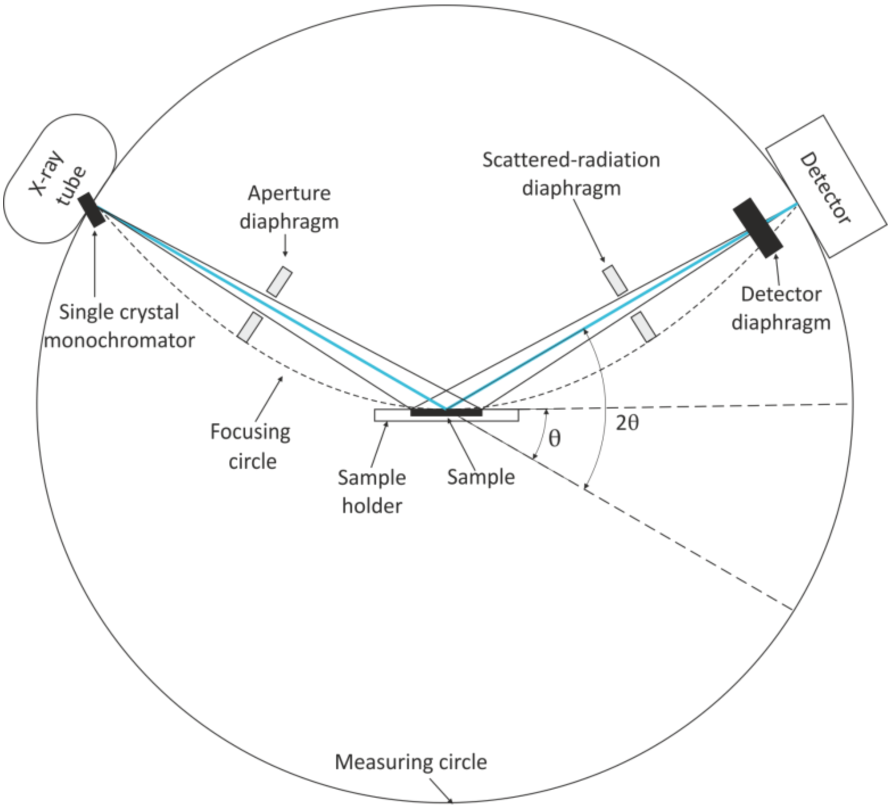

Figure 2-7 - Schematic diagram of D5000 and D8 powder diffractometers: the solid lines represent X-ray beams

The Bruker D8 diffractometer was used to carry out variable temperature powder X-ray diffraction (VT-PXD) experiments, utilising an Anton-Paar HTK-1200 furnace stage. This allowed diffraction patterns to be collected up to a temperature of 1200 °C and under different environments, such as vacuum and various flowing gases. The sample stage is permeable to X-rays through the use of Kapton polyimide windows, which are used due to their low X-ray absorption and scattering properties.

The data was collected typically over the 2θ range 5-60 °: these diffraction patterns were analysed using the Diffrac^{plus} evaluation program (Eva) [145] and compared to the International Centre for Diffraction Data (ICDD) database. Further structure analysis on unknown compounds was performed using the Rietveld method.

Structural information can be obtained from powder patterns using the Rietveld method. This method requires a trial structure. The trial structure needs to be an appropriate model and is determined by comparison with known structures and their diffraction pattern. This is usually obtained from a crystallographic information file (cif).

The refinement aims to minimise the difference between the trial and calculated structure by using a least squares refinement. To perform this refinement a number of structural, positional, profile and instrument factors need to be varied. The procedure below describes the typical refinement process, and includes the most important refinement variables:

1. Need to add trial structure from cif file, experimental powder data (Histogram) , and instrument file
2. Refine unit cell parameters
3. Refine background and scale factor
4. Refine zero-point error
5. Refine Gaussian and Lorentzian peak shape parameters
6. Refine atom positions
7. Refinement of thermal parameters
8. Preferred orientation and micro absorption (if present)

A set of reliability factors (R-factors) quantitatively assess the agreement between the experimental and calculated profiles. These included: for the profile (R_p), weighted profile (R_{wp}), Bragg (R_B), expected (R_E) and goodness of fit (Gof). The most useful are:

$$R_{wp} = \sqrt{\frac{\sum w_i (y_{io} - y_{ic})^2}{\sum w_i y_{io}^2}}$$

Equation 2.10

$$R_E = \sqrt{\frac{(N - P + C)}{\sum w_i y_{io}^2}}$$

Equation 2.11

Where y_{io} is the intensity observed at the ith step in the step scanned powder diffraction pattern, $y_{ic}$is that calculated, and the weight w_i, N is the number of observations [*i.e.* of y_{io}], P is the number of parameters adjusted, and C is the number of constraints imposed. The goodness of fit can be expressed in terms of R_{wp} and R_E as given by χ^2:

$$Gof = \chi^2 = \frac{\sum w_i (y_{io} - y_{ic})^2}{N - P + C} = \left(\frac{R_{wp}}{R_E}\right)^2$$

Equation 2.12

For a good fit χ^2 should approach unity, and the difference line between the calculated and experimental patterns should be flat or consistent with background noise. The most meaningful values for the determination of the refinement are R_{wp} and χ^2 since they show the numerator being minimised.

The Rietveld refinements were performed using the computer package General Structure Analysis System (GSAS) [146] using the EXPGUI suite.[147]

UV/Visible/Near Infra-Red spectroscopy

UV/Visible/Near Infra-Red spectroscopy (UV/Vis/NIR) uses photons in the range of 150-3000 nm. In this region of the electromagnetic spectrum, molecules undergo outer electron excitation and transitions.

There are two different types of mode through which the absorbance of a molecule can be determined: either transmission or diffuse reflectance mode. For both of these methods, the way that light can interact with the sample is key. When light comes into contact with the sample, it can be reflected, scattered and absorbed by the sample, similar to X-rays. Reflection of the light is not an issue, as the fraction of reflected light can be eliminated through reference measurement with the same material. Therefore only scattering and absorbing interactions affect the intensity if the light passes through the sample (transmitted light).

In transmission mode the intensity of transmitted light is measured and compared to the intensity of light in the incident beam. This is the application of the *Beer-Lambert* law, which relates the absorbance to the concentration of the absorber and path length (Equation 2.13)

$$A = -\log\left(\frac{I}{I_0}\right) = \varepsilon \cdot c \cdot L$$

Equation 2.13

Where A = Absorbance, I_0= the intensity of the incident beam, I = the transmitted intensity, ε =molar absorption coefficient, c =the concentration of the absorber, and L =path length.

This mode is particularly useful for when scattering is negligible, as with molecules dispersed in solution: however scattering is considerable for solids, and this means transmission of the sample is very low.

If scattering in the sample is high, it is possible to use this scattered light to obtain the absorbance using diffuse reflectance mode.

In diffuse reflectance mode, the randomly-oriented crystals in a powder reflect light in different directions. To obtain the absorbance from diffuse reflectance the *Kubelka-Munk* (K-M) model is used; the K-M model is based on several assumptions:[148]

1. The sample is modelled as an infinite sheet with finite thickness, so there are no boundary effects.
2. All intensities are assumed to be perfectly diffuse.
3. The only interactions of light with the sample are scattering and absorption; polarisation and fluorescence are ignored.
4. The particles making up the layer must be much smaller than the total thickness.
5. No external or internal surface reflections occur.
6. The absorption and scattering coefficients are constant whatever the thickness of layer is.

Figure 2-8 depicts the assumptions of the K-M model. Due to the infinite sheet approximation, only the thickness (L) is included in the equations. The incident, transmitted and reflected intensities are all assumed to be perfectly diffuse, and are assigned two directions: upwards(J) or downwards (I).[148] The reflecting sample (R) is placed into contact with an opaque substrate with a known reflectance (R_g). The sample is split into a series of layers of equal thickness (x); these layers are separated by a distance of dx, and each layer receives a flux traveling downward (i_x) and flux traveling upward (j_x).

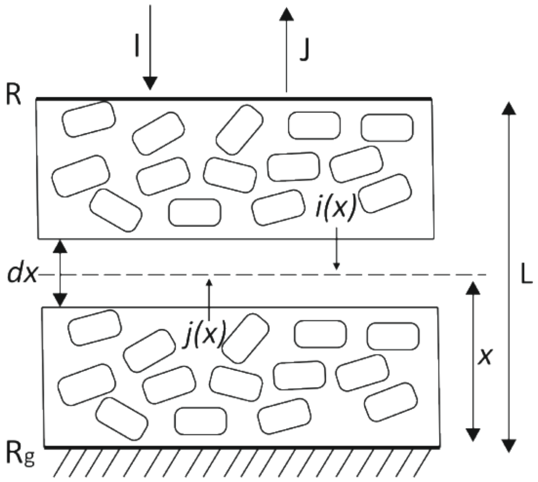

Figure 2-8- Light path of the K-M model

Light can only be scattered or absorbed, therefore the rate of flux in the upward and downward directions can be described by first order differential equations:

$$\frac{\mathrm{dJ}}{\mathrm{dx}} = -\mathrm{KJ} - \mathrm{SJ} + \mathrm{SI}$$

Equation 2.14

$$\frac{\mathrm{dI}}{\mathrm{dx}} = -\mathrm{KI} - \mathrm{SI} + \mathrm{SJ}$$

Equation 2.15

Where K = Absorption coefficient and S = Scattering coefficient.

Equation 2.14 and Equation 2.15 are two differential equations with flux terms, I and J: it is then possible to define the reflectance factor (R) in terms of the flux by:

$$\mathrm{R} = \frac{\mathrm{J}}{\mathrm{I_0}}$$

Equation 2.16

Where $I_0 = I$ and I_0 = the intensity of the incident beam.

The reflectance is therefore dependant on four parameters of the system, S, K, L and R_g. By using a limiting case where there is infinite layer thickness $(L \to \infty)$; this corresponds to a layer that is so thick that it is effectively opaque and therefore hides the substrate completely $(R_g \to 0)$. Therefore the system is only dependant on S and K: in such systems, the Kubelka-Munk function applies:

$$\frac{\mathrm{K}}{\mathrm{S}} = \frac{(1 - \mathrm{R}_\infty)^{\,2}}{2\mathrm{R}_\infty}$$

Equation 2.17

Solving Equation 2.17 in terms of R_∞ gives a useful expression in terms of the absorption and scattering factors:

$$\mathrm{R}_\infty = 1 + \frac{\mathrm{K}}{\mathrm{S}} - \sqrt{\frac{\mathrm{K}^2}{\mathrm{S}^2} + 2\frac{\mathrm{K}}{\mathrm{S}}}$$

Equation 2.18

Where $R_\infty$is the reflectance for an infinitely thick sample.

With this assumption, the reflectance is related to the ratio between the absorption and scattering coefficients By collecting the diffuse reflectance the scattering is lost, and therefore the absorbance is directly proportional to the reflectance.

To obtain the absorbance properties of the materials, a Perkin-Elmer Lambda 19 UV/Vis/NIR spectrometer has been used. The data was collected in the range between 200-2500 nm.

Figure 2-9 shows a simplified schematic and light path within the spectrometer. There are two different radiation sources: a deuterium lamp and a halogen lamp, which cover the range of the spectrometer. For operation in the Vis/NIR, mirror 1(M1) reflects radiation from the halogen lamp onto mirror 2 (M2). If UV light is desired, M1 is raised and radiation from the deuterium lamp reflects off M2. Radiation from the respective source lamp is then reflected through a slit assembly to the monochromator, where it is reflected off a UV/Vis or NIR grating: the rotational position of the grating selects a segment of the spectrum, therefore providing near-monochromatic radiation. The incident beam is split into two, one passing through the sample, and the other through the reference ($BaSO_4$). The radiation passes alternatively through the sample and reference and is reflected onto the appropriate detector. A photomultiplier is used in the UV/Vis range, while a PbS detector is used in the NIR range. The integration sphere measures reflectance from the reference and sample cells.

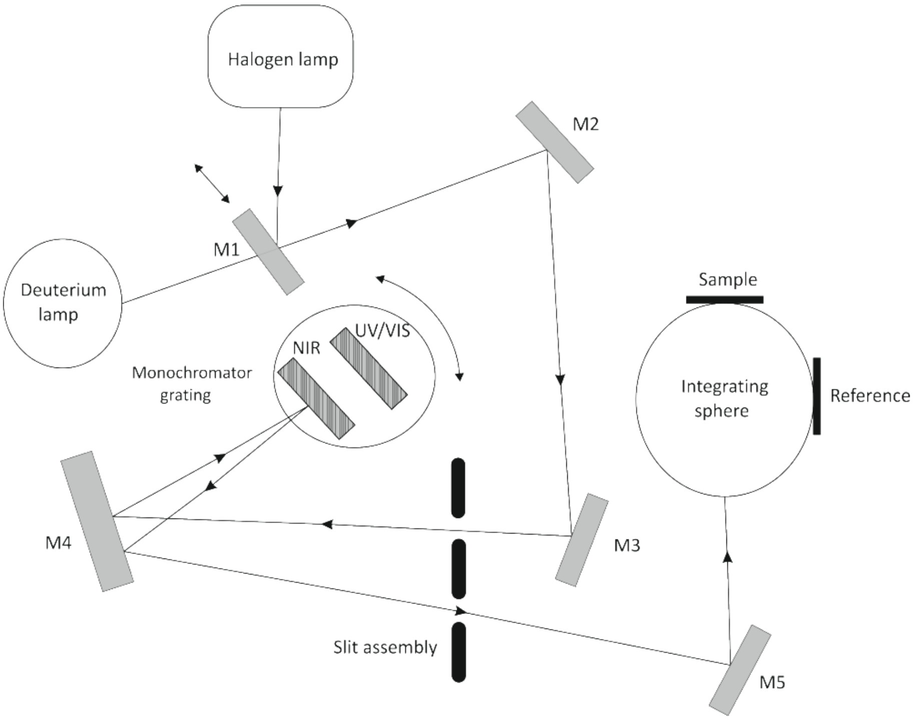

Figure 2-9 - Schematic diagram and light path of a UV/Vis/NIR spectrometer

Scanning electron microscopy

Scanning electron microscopy (SEM) allows for the observation and characterisation of materials on a nanometre to micrometre scale. A Philips XL-30 ESEM fitted with an Oxford Instruments Inca Energy 300 Energy-Dispersive X-ray Spectrometry analysis system was used and a typical schematic is shown in Figure 2-10. The types of signal produced from the interaction of the electron beam with the sample include secondary electrons, back-scattered electrons, characteristic X-rays, and other photons of various energies.[149] The imaging signals of the greatest interest are the secondary and backscattered electrons. Backscattering arises from elastic scattering of the electron beam and is element dependent, with heavy elements being stronger backscatters than lighter elements. This produces a contrast dependent on chemical composition, allowing imaging of the distribution of different species within the sample. Secondary electrons are loosely-bound outer shell electrons from the sample atoms, which during inelastic scattering of beam electrons are ejected from the atom. The combined effect of elastic and inelastic scattering processes is to distribute the beam electrons over a “three-dimensional” interaction volume.[149]

In SEM, characteristic X-rays are emitted as a result of electron bombardment; the energy of the emitted X-rays is characteristic of the element from which it is originates. The detection of these X-rays, through the use of energy dispersive X-ray spectroscopy (EDX), yields both qualitative identification and semi-quantitative elemental analysis. However EDX has difficulties in detecting lighter elements, due to the low energy of the emitted X-rays and resolution of elements with similar X-ray energies, such as O and F, which is due to peak overlap.

SEM requires a conducting surface; this prevents the sample becoming negatively charged when scanned by the electron beam, which would cause scanning faults and other image artefacts. Samples in this study were non-conducting and uncoated, therefore an environmental scanning electron microscope (ESEM) was utilised. An ESEM uses water vapour to neutralise the charging effect and amplify the secondary electron signal. However the additional gases within the sample chamber reduce the spatial resolution of the emitted X-rays: nonetheless, it is still of use for elemental analysis.

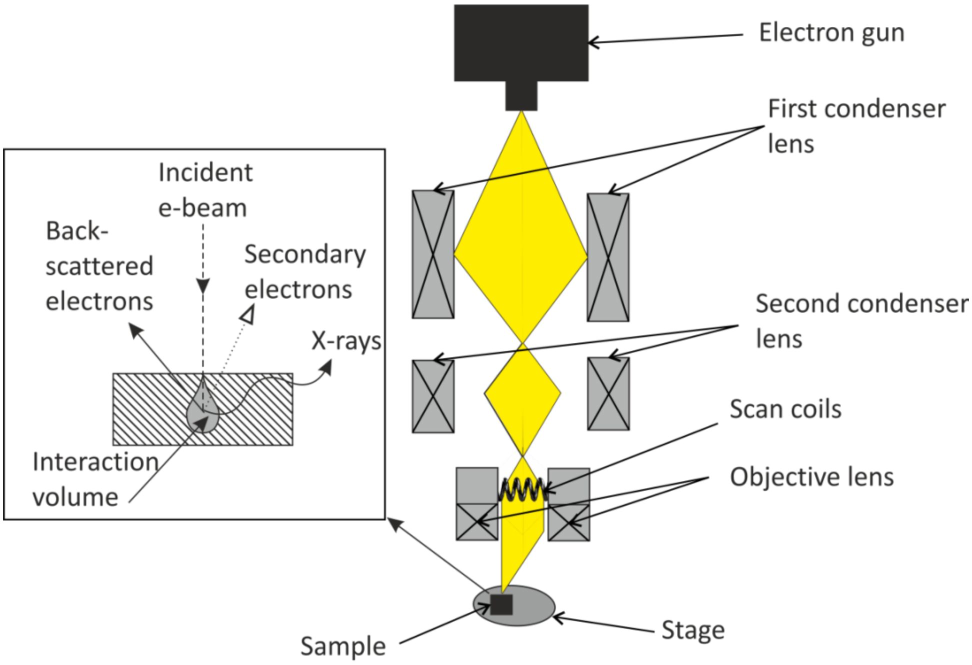

Figure 2-10 - Schematic diagram for SEM, with insert indicating e-beam interaction with sample

Thermogravimetric analysis

Thermogravimetric analysis (TGA) measures the change in a weight of a sample as it is heated, cooled or held at a constant temperature. This technique is mainly used to determine the thermal stability of framework samples and can indicate loss of species, such as water, ammonia and organic templates. This loss is shown by calculating the mass lost as a percentage and comparing the value to the expected loss from the sample's stoichiometric formula.

Differential thermal analysis (DTA) is often performed simultaneously with TGA and measures thermal events taking place with the sample. This is done by comparison with a reference, typically alumina powder, which is stable over a high temperature range. The temperatures of the reference and sample should be identical unless a thermal event takes place, when the sample temperature increases faster than that of the reference: this indicates an exothermic event, and *vice versa* in the case of an endothermic event. Typical thermal events include melting/crystallisation, decomposition and phase changes.

Throughout this project TGA has been collected in combination with DTA, using a Polymer Laboratories PL-STA 1500 simultaneous thermal analysis system. A schematic of this apparatus is shown in Figure 2-11. For typical data collection, a sample with mass 10 - 20 mg was heated from room temperature to 600 °C at 2 °C per minute, with data points collected every two seconds.

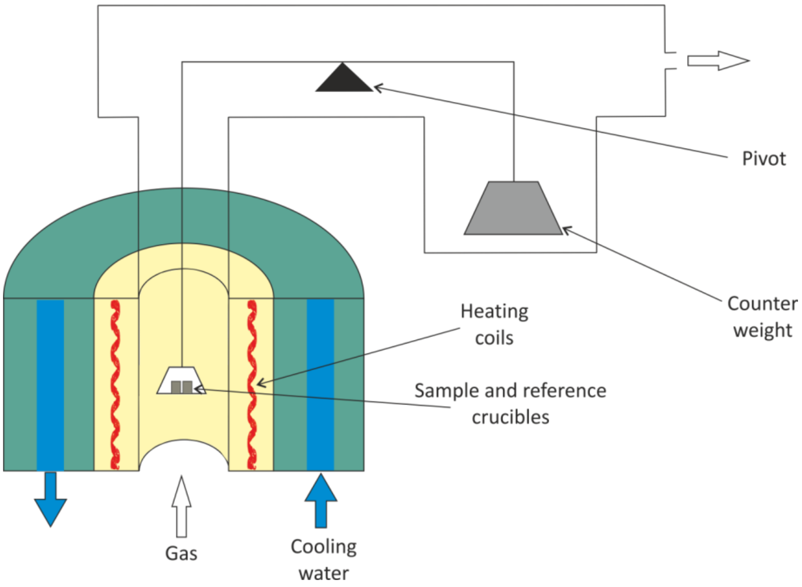

Figure 2-11 - Schematic diagram for thermogravimetric analysis

Bond Valence calculations

Bond Valance (BV) calculations were carried out on all new materials in order to determine the correct assignment from the SXD data and to confirm charge balancing. These calculations were performed using Equation 2.19 and Equation 2.20. One of the main purposes for using BV calculations was to differentiate between O/F, by readily distinguishing sites with 2−/ 1− charges respectively. BV calculations were also performed to determine the oxidation state of iron present in these compounds.

$$V = \sum v_i$$

Equation 2.19

$$v_i = exp\left(\frac{R_0 - R_i}{b}\right)$$

Equation 2.20

Where V is the valancy of the atom and v_i is the sum of individual bond valances surrounding the atom, R_i is the observed bond length [150], and R_0 is the tabulated bond length and is a constant b = 0.37 Å.[151]

Chapter 3 Iron fluorophosphates

The main aim of the project was to synthesise iron (II) fluorophosphates hydrothermally. However, during the course of this study a large number of new iron (III) and mixed valence iron species have been formed.

A number of iron fluorophosphate materials have been previously synthesised and reported in literature. However, examples of materials combining both oxo-tetrahedra and high levels of fluoride anions in a framework material are still comparatively rare. To ensure significant levels of incorporation of fluoride into new material types, the use of a reaction medium with a high F:O molar ratio is essential. Recently it has been found that by using transition metal (TM) fluoride salts as a F source and HPF_6 as a phosphorus and F source, it is possible to attain these high F:O ratios.[101, 102] This high ratio is further enhanced by the addition of counter cation fluoride salts, normally those of alkali metals. However, protonated amine templates can also be used as counter cations and lead to new templated iron fluorophosphate structures. Amine templates are usually protonated due to highly acidic synthetic conditions, and can play three distinct roles: templating, structure directing, and space filling. Space filling is the most common and is a process in which the amines exclude solvent molecules; therefore enhancing framework-amine interactions leading to increased thermodynamic stability.[57]

A summary of the use of TM fluoride salts to synthesise mid- to late first row transition metal fluorophosphates has been published.[102] Work carried out in this research has focused on the use of FeF_2 as a starting material and varying the phosphorus source and counter ions. This has led to the range of iron-based fluorophosphates, synthesised and characterised, to be extended considerably.

These materials were synthesised hydrothermally using a 23 mL Parr™ hydrothermal bomb as depicted in Figure 2-2. A typical procedure involves mixing the starting materials within the Teflon® autoclave liner and sealing the bomb in a stainless steel container. These hydrothermal bombs were then transferred to an oven, where the heating temperature and duration are varied, some of these conditions are provided in Table 3.1. After the reaction has completed, the products were collected by washing with deionised water and vacuum filtering, and these products were then dried overnight at 80 °C. Once dried, the sample is visually checked, under a polarisable microscope, for the presence of suitable single crystals. If the crystals have sufficient quality they are characterised by SXD; if not, samples are ground and analysed using PXD. This section describes the structures of new iron fluorophosphate materials that have been synthesised using the hydrofluorothermal technique. The observed trends in compositional and structural features for these iron-based materials produced are also analysed and discussed. Crystallographic information files (CIFs) for the successful reactions, shown in Table 3.1, are included as appendices.

Table 3.1 - Reaction conditions for iron fluorophosphates

Starting materials	Reaction conditions	Crystal morphology and phase purity	Product(s)	Section in Thesis
FeF_2 (0.05g, 0.533 mmol), H_3PO_4 (85 % wt, 0.10 mL, 1.456 mmol) and NH_4F (0.08g, 2.160 mmol).	175 °C, 48 h	Colour needles, pure phase	$(NH_4)_3Fe(PO_3F)_2F_2$	0 (**I**)
$(NH_4)_2Fe(SO_4)_2$•$6H_2O$ (0.05g, 0.128 mmol), H_3PO_4 (85 % wt, 0.10 mL, 1.456 mmol) and NaF (0.08g, 1.905 mmol)	175 °C, 12 h	Pink needles ~70 % crystalline phase, remainder unknown impurity	$M_2FeF_2[H(HPO_4)_2]$	3.2 (**II**)
FeF_2 (0.137g, 1.460 mmol), H_3PO_4 (85 % wt, 0.10 mL, 1.456 mmol), KF (0.08g, 1.377 mmol) and deionised water (1mL)	175 °C, 48 h	~70 % crystalline phase, remainder unknown impurity		K analogue previously reported [152]
FeF_2 (0.05g, 0.533 mmol), H_3PO_4 (85 % wt, 0.10 mL, 1.456 mmol) and 1,2 dianilinoethane (0.025g, 0.118 mmol)	125 °C, 24 h	Brown needles, ~80 % crystalline phase, remainder amorphous impurity	$[H_2\text{-1,2dianilinoethane}]_{0.5}$ $FeF(PO_2(OH,F)_2(PO_3,F,OH)$•$0.42H_2O$	3.3 (**III**)
FeF_2 (0.05g, 0.533 mmol), HPF_6 (65 % wt, 0.16 mL, 1.176 mmol) and piperazine (0.0991g, 1.15 mmol).	175 °C, 72h	Colourless plates, ~70 % crystalline phase, remainder unknown impurity	$[H_2\text{-Piperazine}]$ $FeF_2(PO_3F)(PO_2FOH)$	3.4 (**IV**)

FeF_2 (0.08g, 0.824 mmol), H_3PO_4 (85 % wt, 0.10 mL, 1.456 mmol), ethylenediamine (0.08mL, 1.15 mmol) and deionised water (1.8mL).	180 °C, 72 h	Colourless plates, ~50 % crystalline phase, remainder unknown impurity	[H_2-Ethlyenediamine] $Fe^{(II)}Fe^{(III)}(HPO_4)(PO_4)F_2(H_2O)_2$	3.5 (**V**)
FeF_2 (0.1g, 1.066 mmol),HPF_6 (65 % wt, 0.34 mL, 2.352 mmol) and piperazine (0.0991g, 1.15 mmol).	125 °C, 96 h	Yellow plates, ~10 % crystalline phase, remainder unknown impurity	[H_2-Piperazine]$_4$ $Fe_4(PO_3F,OH)_6(PO_2(F,OH)_2)_8$	3.6 (**VI**)
FeF_2 (0.1g, 1.066 mmol), H_3PO_4 (85% wt, 0.20 mL, 2.912 mmol) and NaF (0.06g, 1.429 mmol)	175 °C, 48 h	~70 % crystalline phase, remainder unknown impurity	$NaFeP_2O_7$	3.7 (**VII**)
FeF_2 (0.05g, 0.533 mmol), H_3PO_4 (85 % wt, 0.10 mL, 1.456 mmol) and NaOH (50% wt., 0.1mL, 1.890 mmol).	175 °C, 48 h	~70 % crystalline phase, remainder unknown impurity	$NaFe(HPO_4)_2$	3.8 (**VIII**)
FeF_2 (0.05g, 0.533 mmol), H_3PO_4 (85 % wt, 0.10 mL, 1.456 mmol) and CaF_2 (0.08g, 1.025 mmol)	175 °C, 96 h	Colourless blocks, ~70% crystalline phase, remainder CaF_2 impurity	$Fe_2(PO_3F)_3$	3.9 (**IX**)
FeF_2 (0.137g, 1.460 mmol), H_3PO_4 (85 % wt, 0.10 mL, 1.456 mmol) and KF (0.08g, 1.377 mmol)	175 °C, 48 h	Pink plates, ~70% crystalline phase, remainder	$KFe_2(PO_2F_2)(PO_3F)_2F_2$	3.10 (**X**)

		unknown impurity		
FeF_2 (0.05g, 0.533 mmol), CuF_2 (0.05g, 0.492 mmol), HPF_6 (65 % wt, 0.16 mL, 1.176 mmol) and NaOH (50 % wt., 0.05mL, 0.945 mmol).	225 °C, 48 h	Colourless plates, ~60 % crystalline phase, remainder unknown impurity	$NaFe(PO_3F)_2$	3.11 (**XI**)
FeF_2 (0.05g, 0.533 mmol), H_3PO_4 (85 % wt, 0.10 mL, 1.456 mmol) and RbF (0.08g, 0.766 mmol)	175 °C, 12 h	Pink needles, ~40% crystalline phase, remainder unknown impurity	$RbFe^{(II)}_3(PO_3F)(PO_2(F,OH)_2)F_2$	3.12 (**XII**)
FeF_2 (0.05g, 0.533 mmol), H_3PO_4 (85 % wt, 0.10 mL, 1.456 mmol) , NH_4F (0.03g, 0.810 mmol) and hydrochloric acid (37%wt, 0.08mL, 0.960 mmol).	175 °C, 48 h	Colourless plate, ~30% crystalline phase, remainder unknown impurity	$(NH_4)_2Fe^{(II)}Fe^{(III)}(PO_3F)_2FCl_2$	3.13 (**XIII**)
$FePO_4 \cdot 4H_2O$ (0.053g, 0.238 mmol) + H_3PO_4 (85 % wt, 0.10 mL, 1.456 mmol)+ $LiOH \cdot H_2O$ (0.05g, 1.190 mmol)	175 °C, 48 h	Colourless blocks, minor phase	$Li_2Fe(PO_4)(HPO_4)$	Jinxiao *et al* [153]
FeF_2 (0.05g, 0.533 mmol), H_3PO_4 (85 % wt, 0.10 mL, 1.456 mmol) and NH_4OH solution (30 % wt, 0.03mL, 0.471 mmol)	175 °C, 48 h	Minor phase of colourless blocks	$NH_4Fe(HPO_4)_2$	Isostructural with Rb+ compound, Lesage *et al* [154]

FeO (0.1g, 1.392 mmol), P_2O_5 (0.07g, 0.493 mmol), KOH (45 % wt, 0.1mL, 1.170 mmol) and H_2O (2mL)	175 °C, 48 h	Minor phase of colourless blocks	$Fe^{(III)}_2Fe^{(II)}_{1.5}(PO_4)(PO_4)_2$	Duan *et al* [155]
FeF_2 (0.1g, 1.066 mmol), H_3PO_4 (85 % wt, 0.20 mL, 2.912 mmol), NaF (0.08g, 1.905 mmol) and Zn (0.05g, 0.765 mmol)	175 °C, 48 h	Minor phase of colourless blocks	$NaFe^{(II)}_2(PO_4)(HPO_4)$	Zhao *et al* [76]
FeF_2 (0.09g), H_3PO_4 (85 % wt, 0.10 mL, 1.456 mmol) and 1,2 dianilinoethane (0.05g, 2.216 mmol)	175 °C, 48 h	Minor phase of pink needles	Fe_2PO_4F	Yakubovich *et al* [78]
FeF_2 (0.05g, 0.533 mmol), HPF_6 (65 % wt, 0.16 mL, 1.176 mmol) + DABCO (0.13g, 1.15 mmol)	175 °C, 48 h	Pure phase of yellow plates	$(H_2\text{-DABCO})Fe(PO_3F)F_3$	Armstrong *et al* [102]

3.1 Compound I- $(NH_4)_3Fe(PO_3F,OH)_2F_2$

$(NH_4)_3Fe(PO_3F)_2F_2$ (Compound **I**) crystallised as colourless needles of sizes 0.06 x 0.06 x 0.02 mm^3, and has a monoclinic unit cell with space group $P2_1/m$. A summary of the crystallographic data is provided in Table 3.2. Compound **I** contains a one-dimensional chain structural unit; these chains are constructed of four membered rings formed from two Fe-centred octahedra and two phosphate-centred tetrahedra, with key bond lengths given in Table 3.3. Polyhedra are linked through oxygen, with the fluoride ions of the *trans*-FeO_4F_2 octahedra and the F/OH groups of the phosphate tetrahedra orientated towards the inter-chain space. Chains are formed by the use of *trans* edges of the FeO_4 square planes (of the FeO_4F_2 octahedra) in adjacent four-membered rings. The chains in Compound **I** run along the *b*-axis, Figure 3-1. The inter-chain space is occupied by NH_4 cations and forms NH-----O/F hydrogen-bonding interactions to the chains ranging from 2.074-2.666Å, (Figure 3-1).

Table 3.2- Crystallographic data for Compound I

Cell axes *a,b,c* (Å)	7.899 (3)	5.185 (2)	12.410 (4)
Cell angles *α,β,γ* (deg)	90	103.937 (3)	90
Empirical formula	$H_{12}F_4FeN_3O_6P_2$	**Z**	2
Formula weight ($gmol^{-1}$)	332.92	**Cell volume ($Å^3$)**	493.40 (3)
Temperature	120K	**Density (gcm^{-3})**	2.315
Crystal system	Monoclinic	**R_1 (all)**	0.068
Space group	$P2_1/m$	**wR_2 (all)**	0.123
Crystal appearance	Colourless needles	**R_1 (obs)**	0.056
Crystal size (mm)	0.06 x 0.025 x 0.005	**wR_2 (obs)**	0.114
		Goof	1.063

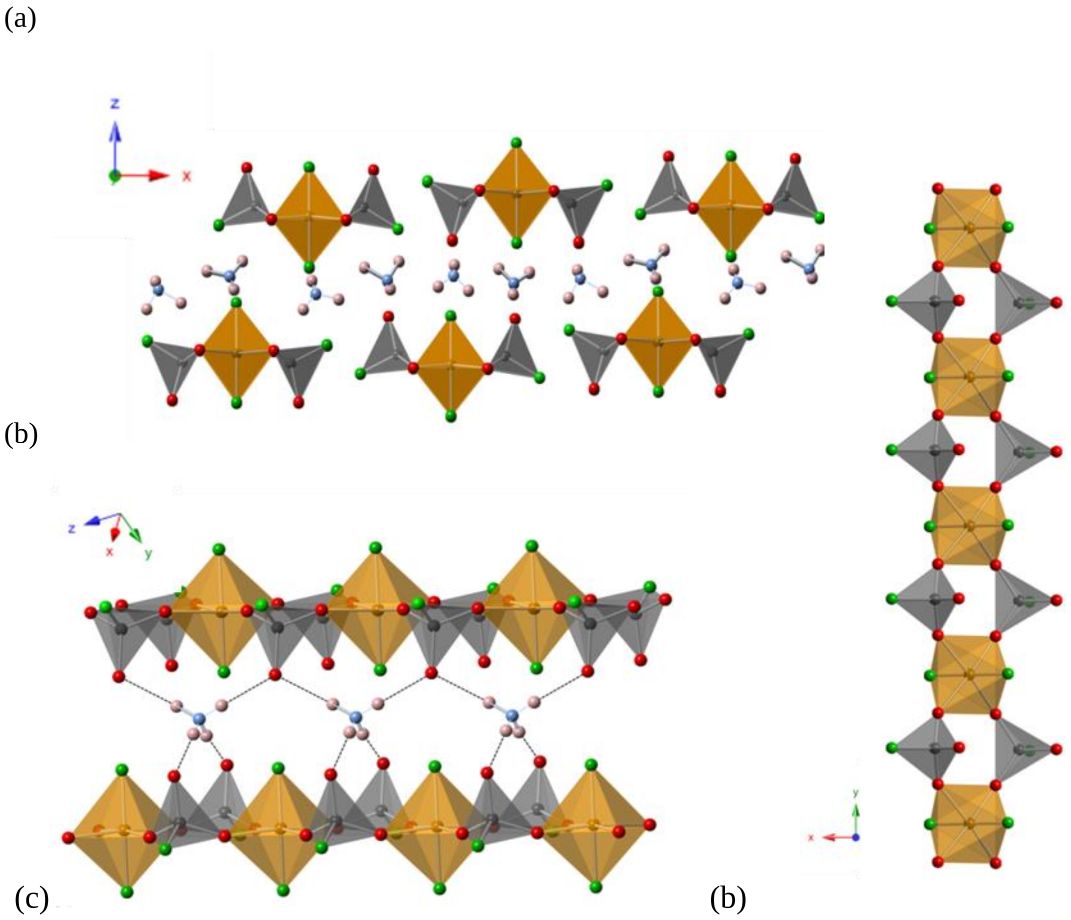

Figure 3-1 –(a) Structure of compound I viewed along the b-axis, (b) Chain structure of Compound I and (c) Hydrogen bonding between the NH_4 cations and framework oxygen atoms. Hydrogen bonding is represented by dashed black lines. Fe polyhedra in orange, P tetrahedra in grey, O atoms are red spheres, F atoms are green spheres, N atoms are light blue spheres and H atoms are light pink spheres

Each phosphate tetrahedra has two vertices that does not bridge to iron octahedral units, but is orientated into inter-chain space. For charge balancing purposes, one of these two vertices must have a 1^- charge, either as hydroxide or fluoride anions; the other terminal vertex will have a 2^- charge. These sites can be assigned with examination of the anisotropic temperature factors, bond valence calculations and bond lengths. From Table 3.3, terminal bond lengths are longer (1.50-1.56 Å) compared to bridging sites (1.485 Å), and the degree of this elongation depends on the type of terminal species. Significant elongation can be attributed to vertices having a 1^- charge (1.564 Å) and minor elongation 2^- charge (1.505 Å). The ADP values of these terminal sites did not change dramatically when assigned as either oxygen or fluoride. However, examination of the bond valence calculations for the terminated phosphate vertices, as shown in

Table 3.4, show a lack of bond valency when refined as oxide anions, in contrast to values approaching the correct bond valency when refined as fluoride anions. However, the contribution of H-bonding is ignored in the BV calculation and can lead to lower values than expected. The valence of the H---X (acceptor) bond can be well determined because the valence is not sensitive to small uncertainties in bond length.[151] The low BV values for O3 (1.62) and O6 (1.77) can be explained due to the strong H-bonding to the amine template. The correlation between bond valance and bond length has been studied for a range of acceptor atoms.[151] There are 2 x O6----H-N interactions with a bond distance around 2 Å: this will increase the BV by roughly 0.34, leading to a BV value closer to the expected value. For O3-----H-N, there are 6 bonds between 2.6-2.9 Å - this will increase the BV value by ~0.36, resulting in a BV value the same as the expected value.

Table 3.3 - Key bond lengths in Compound I

Bond	Bond length (Å)	Bond	Bond length (Å)
Fe1-F1*	1.952 (5)	P2-O3*	1.498 (6)
Fe1-F2*	1.882 (5)	P2-F4*	1.562 (6)
Fe1-O1	1.971 (6)	P3-O10	1.484 (6)
Fe1-O10	1.976 (6)	P3-O6*	1.511 (5)
P2-O1	1.485 (6)	P3-F3*	1.565 (4)

*Terminal bonds

Table 3.4 - Bond valence calculations for terminal phosphate vertices in Compound I

Atom label	Bond valence (O^{2-})	Bond valence (F^{-})	Assignment
F3	1.25	0.96	P-F
F4	1.27	0.98	P-F
O3	1.62	1.15	P-O
O6	1.77	1.30	P-O

Thermogravimetric analysis of Compound **I** (Figure 3-2) showed mass loss at ~200 °C equivalent to 1 mole of NH_3. On heating above 350 °C rapid mass loss is observed consistent with structural collapse. The IR spectrum of this compound shows three distinct peaks between 3200-2850 cm^{-1} which are related to the N-H stretches associated with the presence of ammonium. There are no peaks at higher wavelengths suggesting there are no O-H stretches, therefore it is likely that the terminal species on the phosphate tetrahedra are fluoride atoms.

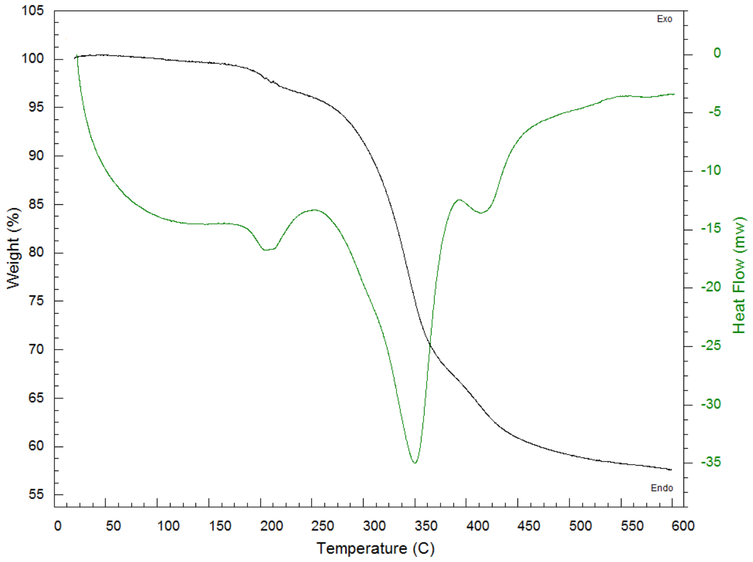

Figure 3-2-TGA plot for Compound I. Mass loss and DTA were recorded as a function of temperature, black and green lines respectively.

3.2 Compound II- $Na_2FeF_2[H(HPO_4)_2]$

Compound **II** crystallised as pink needles of size 0.025 x 0.025 x 0.05 mm^3, with a monoclinic unit cell in the space group $P2_1/c$: a summary of the crystallographic data is provided in Table 3.5. The potassium analogue compound **II** has been reported previously [152].Compound **II** contains the same chain structure as shown in Figure 3-1, however differences in the structures of compounds **I** and **II** derive from the method of chain packing. This arises from the varying size and coordination preferences of the charge–balancing counter ions that occupy the inter-chain space. Chains form along the a-axis and are comprised of octahedral iron centres, FeO_4F_2, and HPO_4 tetrahedron with a disordered H-atom position with 50 % occupancy to form $PO_2(OH)_2$ tetrahedra (Figure 3-3). Compound **II** displays elongation of terminal vertices on phosphate tetrahedra (Table 3.6), where the average of μ^2- bridging O sites in compound **II** are 1.508 Å compared to 1.571 Å for terminal vertices.

The inter-chain space is occupied by Na^+ cations, which are located in a 7-coordinate (NaF_2O_5) trigonal prismatic geometry. A comparison of the ionic radii for NH_4^+ (1.45 Å) and Na^+ (0.95 Å) indicates the differences in chain-packing. In compound **I** the Fe-chains are all roughly parallel to each other, whereas in compound **II** the Fe-chains are rotated to allow the smaller Na species to occupy the space between chains and the formation of H-bonding between phosphate tetrahedra. The distance between terminal oxygen in compound **II** is 2.41 Å: this short distance allows for the formation of H-bonds. The distance between terminal vertices in compound **I** is much larger - 3.10 Å - therefore no intermolecular H-bonding can occur between phosphate tetrahedra. This supports the argument that the terminal species for compound **I** are fluoride not hydroxide.

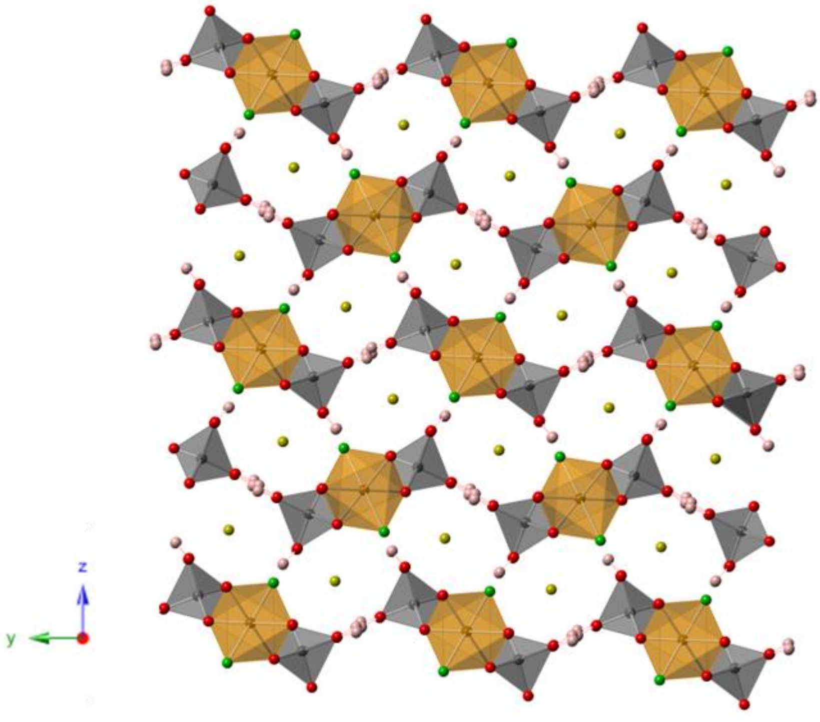

Figure 3-3 – Structure of Compound II viewed along the a-axis. Fe polyhedra in orange, P tetrahedra in grey, O atoms are red spheres, F atoms are green spheres and H atoms are light pink spheres

Table 3.5 - Crystallographic data for Compound II

Cell axes *a,b,c* (Å)	4.627 (4)	8.060 (5)	10.218 (6)
Cell angles *α,β,γ* (deg)	90	91.014 (4)	90

Empirical formula	$H_3F_2FeNa_2O_8P_2$	**Z**	2
Formula weight (gmol^{-1})	332.79	**Cell volume (Å^3)**	381.10 (5)
Temperature	120 K	**Density (gcm^{-3})**	2.900
Crystal system	Monoclinic	**R_1 (all)**	0.092
Space group	$P2_1/c$	**wR_2 (all)**	0.192
Crystal appearance	Pink Needles	**R_1 (obs)**	0.064
Crystal size (mm)	0.05 x 0.025 x 0.025	**wR_2 (obs)**	0.173
		Goof	1.133

Table 3.6 - Key bond lengths in compound II

Bond	Bond length (Å)	Bond	Bond length (Å)
Fe1-F1*	1.919 (6)	P1-O2*	1.550 (6)
Fe1-O3	2.010 (7)	P1-O3	1.504 (7)
Fe1-O1	2.031 (6)	P1-O4*	1.591 (7)
P1-O1	1.511 (7)		

*Terminal bonds

3.3 Compound III- (H_2- 1,2 dianilinoethane) $Fe(HPO_4)(PO_2(OH)_2)F$ •$0.42H_2O$

Compound **III** crystallised as brown needles of sizes 0.05 x 0.025 x 0.025 mm^3 in the orthorhombic space group *Pccn*. One of these brown needle crystals was selected for SXD, and a summary of the crystallographic information can be found in Table 3.7. The structure consists of chains of FeO_4F_2 octahedra produced by *trans*-linking μ^2-bridging F atoms. Assignment of the fluoride site (F1) occurred as oxygen yielded non-positive or very small ADP values; reassignment of this scattering power as fluoride produced similar ADP values for all anion sites, as well as a reduction in data-fitting residual values. Each pair of adjacent octahedra are further doubly bridged by the edges of two PO_3OH and $PO_2(OH)_2$ tetrahedra, forming three membered rings (Figure 3-4). There are two crystallographically different phosphate tetrehdra, both containing two bridging vertices and two terminal vertices. However, for charge-balancing purposes, one of these terminal vertices must have a 2^- charge and the remaining vertices a 1^- charge; either as fluoride or hydroxide. Examination of the bond lengths (Table 3.8) gives an indication as to which terminal vertex will have a 2^- charge: normally terminal vertices are elongated compared to μ^2- bridging O sites. However as seen in compound **I**, a terminal vertex with a 2^- charge has similar bond lengths to bridging sites. In compound **III**, the P1-O7 bond is terminal and has a shortened bond length (1.494 Å) compared to the other terminal vertices (1.554 Å). Therefore it was determined that P1 contains terminal vertices of 2^- and 1^- charge. The nature of the 1^- charge was assigned as oxide, as this leads to similar ADP values for all anions and a reduction in the residual fitting factors. It was also possible to locate the hydrogen atoms associated with the hydroxide groups using Fourier difference maps. The chains run along the crystallographic *c*-lattice direction, with diprotonated 1.2-dianilinoethane and water occupying the inter-chain space and forming hydrogen-bonding interactions (N-H....O/F) that range from 1.606-2.832 Å (Figure 3-4).

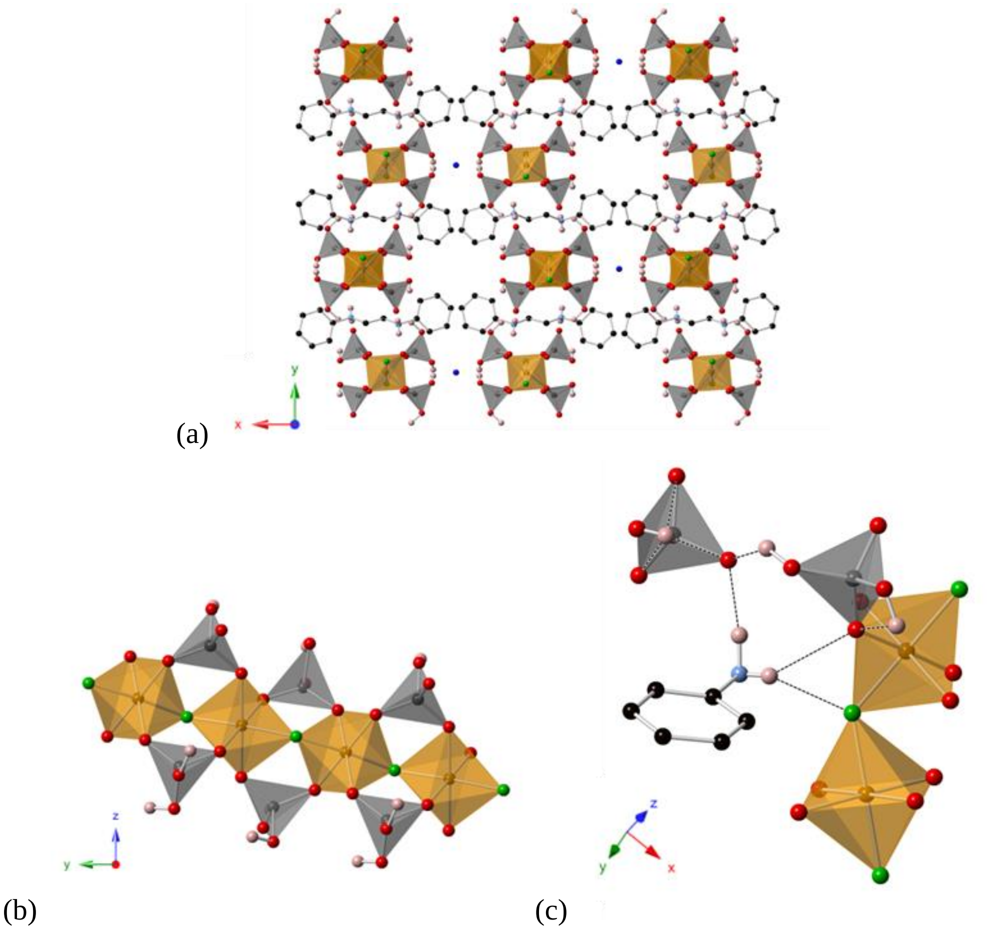

Figure 3-4 – The structure of compound III: (a) viewed along the c-axis; (b) showing trans-linked FeO_4F_2 chains running along the c-axis and (c) H-bonding around protonated nitrogen. Hydrogen bonding is represented by dashed black line. Fe polyhedra in orange, P tetrahedra in grey, O atoms are red spheres, F atoms are green spheres, N atoms are light blue spheres and H atoms are light pink spheres

Table 3.7 - Crystallographic data for Compound III

Cell axes *a,b,c* (Å)	15.453 (2)	24.217 (3)	7.166 (10)
Cell angles *α,β,γ* (deg)	90	90	90
Empirical formula	$C_{14}H_{26}F_2Fe_2N_2O_{16.84}P_4$	**Z**	4
Formula weight ($gmol^{-1}$)	765.36	**Cell volume ($Å^3$)**	2681.8(6)
Temperature	100 K	**Density (gcm^{-3})**	1.896
Crystal system	Orthorhombic	**R_1 (all)**	0.147
Space group	*Pccn*	***w*R_2 (all)**	0.194
Crystal appearance	Colourless Plate	**R_1 (obs)**	0.079
Crystal size (mm)	0.05 x 0.025 x 0.025	***w*R_2 (obs)**	0.162
		Goof	1.029

Table 3.8 - Key bond lengths in compound III

Bond	Bond length (Å)	Bond	Bond length (Å)
Fe1-O1	1.963 (2)	P1-O2	1.486 (2)
Fe1-O7	1.965 (2)	P1-O1	1.487 (2)
Fe1-O5	1.965 (2)	P1-O7*	1.494 (2)
Fe1-F1	1.974 (3)	P1-O3*	1.582 (2)
Fe1-F1	1.977 (3)	P2-O8	1.494 (2)
Fe1-O8	1.994 (2)	P2-O5	1.504 (2)
		P2-O6*	1.540 (2)
		P2-O4*	1.541 (2)

*Terminal bonds

3.4 Compound IV- [H_2-Piperazine]$FeF_2(PO_3F)(HPO_3F)$

[H_2-Piperazine]$FeF_2(PO_3F)(HPO_3F)$ (**IV**) crystallised as colourless plates of size ~0.25 x 0.05 x 0.025 mm^3, and adopted a monoclinic unit cell with the space group *C*2/*c*. A colourless plate crystal was selected for SXD: the summary of the crystallographic information can be found in Table 3.9, with key bond lengths provided in Table 3.10. The structure consists of sheets of FeO_4F_2 octahedra, linked together by HPO_3F tetrahedra, in the *ab*-plane, with diprotonated piperazine cations located between the sheets. As with the other structures, all of the F atoms are terminal and orientated into inter-layer space (Figure 3-5). Assignment of oxygen on fluoride sites (F1 and F2) led to non-positive ADP values. Looking at the bond lengths (Table 3.10) indicates that terminal fluoride sites on Fe octahedra are significantly shorter (1.925 Å) compared to bridging sites (1.995 Å). This is in stark contrast to terminal bond lengths on phosphate tetrahedra, which are elongated (1.535 Å) in comparison to equivalent bridging sites (1.502 Å). The sheets are comprised of eight-membered rings that contain four FeO_4F_2 octahedra and four HPO_3F tetrahedra, and are stabilised by hydrogen-bonding interactions between HPO_3F and PO_3F tetrahedra with a typical O-O distance of 2.5 Å (Figure 3-5). The sheets are further stabilised by hydrogen-bonding interactions to the diprotonated piperazine ranging from 1.709-2.840 Å (Figure 3-5).

Table 3.9 - Crystallographic data for Compound IV

Cell axes *a,b,c* (Å)	9.204 (11)	9.041 (12)	14.309 (2)
Cell angles *α,β,γ* (deg)	90	102.54 (7)	90
Empirical formula	$C_4H_{13}F_4FeN_2O_6P_2$	**Z**	4
Formula weight (gmol^{-1})	378.95	**Cell volume (Å^3)**	1162.3(3)
Temperature	100 K	**Density (gcm^{-3})**	2.166
Crystal system	Monoclinic	**R_1 (all)**	0.036
Space group	*C*2/*c*	**wR_2 (all)**	0.082
Crystal appearance	Brown plates	**R_1 (obs)**	0.029
Crystal size (mm)	0.025 x 0.025 x 0.005	**wR_2 (obs)**	0.079
		Goof	0.842

Table 3.10 - Key bond lengths in compound IV

Bond	Bond length (Å)	Bond	Bond length (Å)
2x Fe1-F2*	1.925 (3)	P2-O1	1.496 (4)
2x Fe1-O1	1.988 (2)	P1-O4	1.507 (3)
2x Fe1-O4	2.000 (2)	P1-O2*	1.512 (3)
		P1-F1*	1.558 (5)

*Terminal bonds

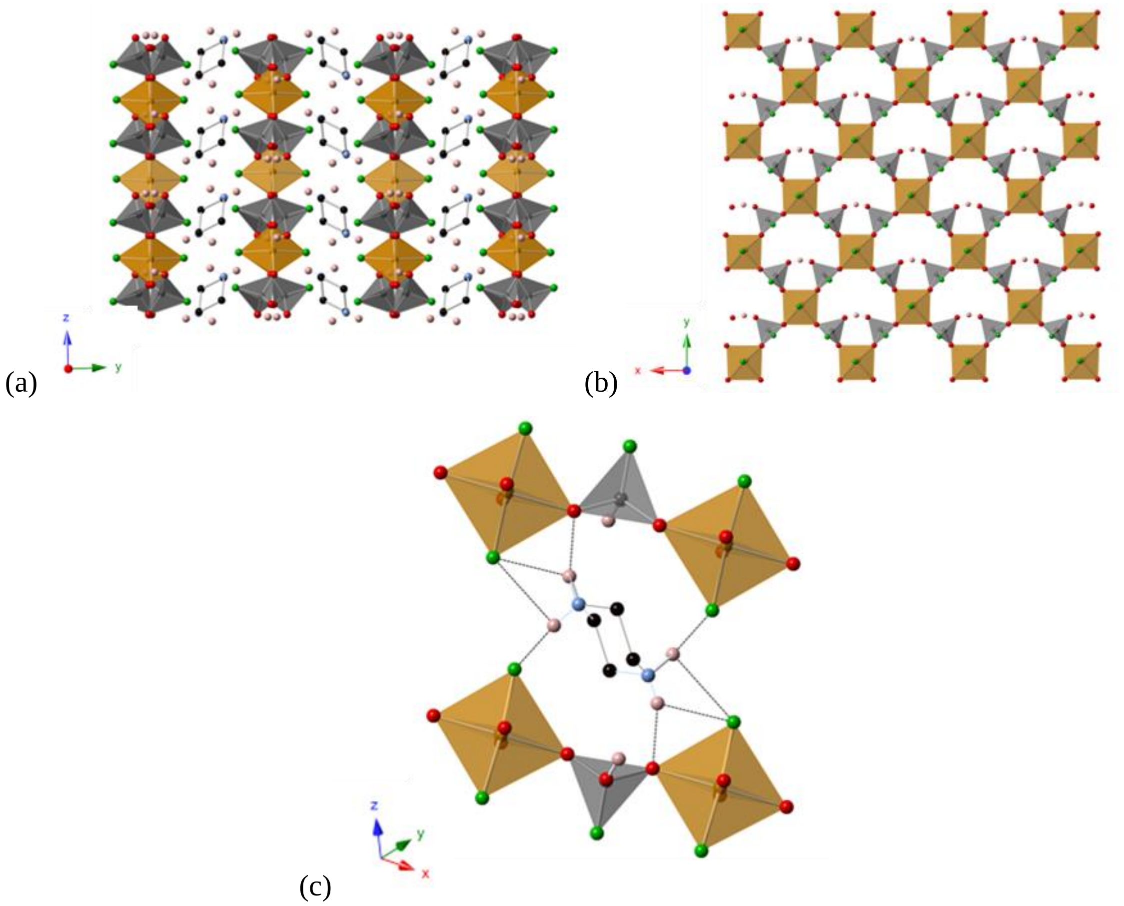

Figure 3-5 – Structure of compound IV viewed along the (a) a-axis and (b) c-axis. (c) H-bonding interactions between amine and framework. H-bonds are shown as dashed black lines. Fe polyhedra in orange, P tetrahedra in grey, O atoms are red spheres, F atoms are green spheres, N atoms are light blue spheres and H atoms are light pink spheres

3.5 Compound V- $(H_2\text{-EDA})Fe^{II}Fe^{III}(HPO_4)(PO_4)F_2(H_2O)$

Compound **V** crystallised in a triclinic unit cell with space group $P\bar{1}$, forming colourless plates of size typically 0.025 x 0.025 x 0.005 mm^3 -the crystallographic information can be found in Table 3.11, with key bond lengths provided in Table 3.12. The structure of compound **V** consists of alternating chains of mixed valence iron-centred octahedra, $Fe^{III}O_4F_2$ and $Fe^{II}O_2F_2(OH_2)$, which are *trans*-linked by μ^2-bridging fluoride in the (110) direction (Figure 3-6). These chains are connected via HPO_4 along the *a*-axis, with the OH orientated to create a hydrogen-bonded pore with an O-O distance of 2.4 Å, Figure 3-6. The hydrogen atom (H10) which creates this H-bonded pore is located at the edge of the unit cell, is split between the O1 sites and has occupancy of 50 %. The O1-H10 distance is 0.7 Å whereas it is probably at a distance of 1.2 Å in the centre of the O-O gap. The assignment of the terminal phosphate vertex as hydroxide led to a lower residual refinement factor and coherent ADP values with other anions. The trend of terminal phosphate vertices being elongated (1.566 Å) compared to bridging sites (1.529 Å) can again be seen in Table 3.12.

Diprotonated ethylenediamine occupies the space in-between the layers, located within the H-bonded pore, and forms H-bonding interactions with the framework and range from 1.622-2.965 Å (Figure 3-6). In order for compound **V** to charge balance it is necessary for the iron centres to be mixed valence: this can be seen from the bond lengths (Table 3.12) and from the BV calculations performed (Table 3.13). Fe3 also shows a minor Jahn-Teller distortion which is to be expected for high-spin d^6 Fe^{II} octahedra.

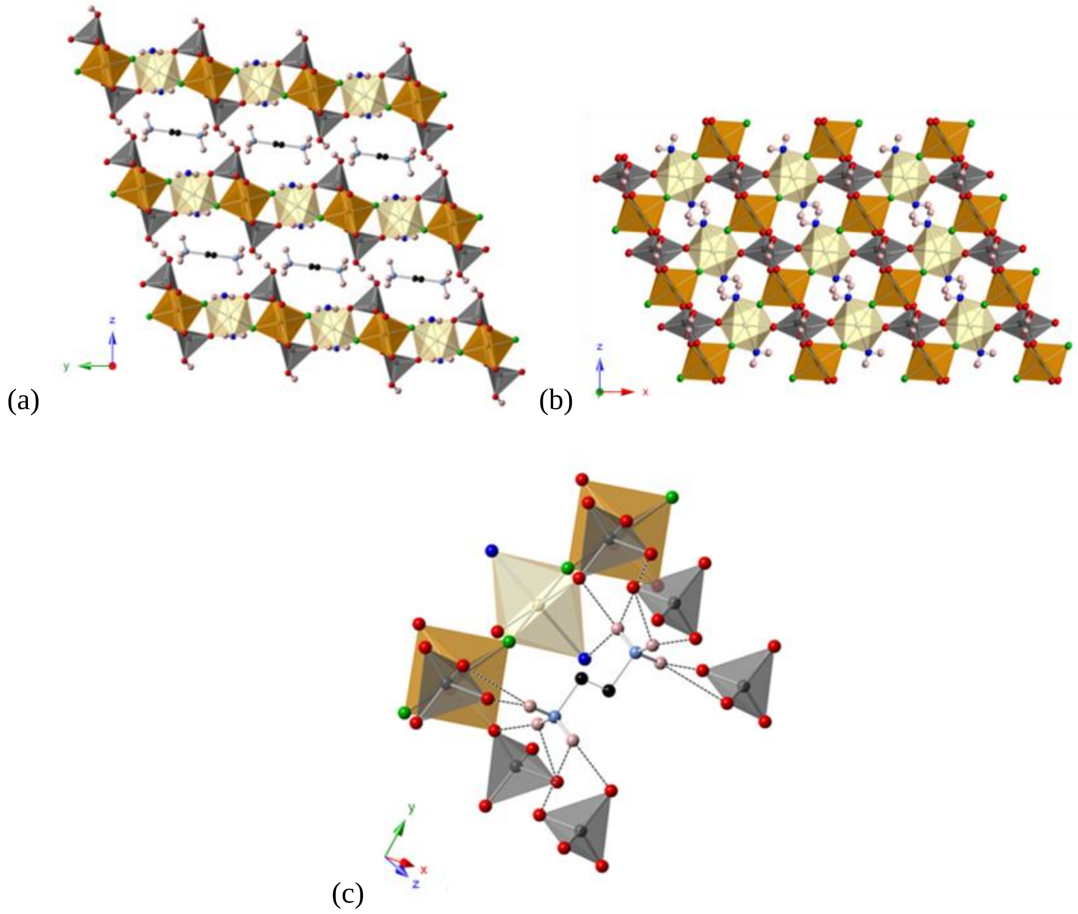

(a)

(b)

(c)

Figure 3-6 - The structure of compound V viewed along the (a) a-axis and (b) the c-axis; (c) showing the H-bonding interaction between the amine and framework. Fe polyhedra in orange, P tetrahedra in grey, O atoms are red spheres, F atoms are green spheres, N atoms are light blue sphere, water ligands are dark blue spheres and H atoms are light pink spheres

Table 3.11-Crystallographic data for Compound V

Cell axes *a,b,c* (Å)	5.163 (10)	7.506 (18)	8.726 (17)
Cell angles *α,β,γ* (deg)	108.58 (7)	97.36 (6)	109.89 (5)
Empirical formula	$C_2H_{15}F_2Fe_2N_2O_{10}P_2$	**Z**	1
Formula weight (gmol^{-1})	438.80	**Cell volume (Å^3)**	290.54(11)
Temperature	100 K	**Density (gcm^{-3})**	2.508
Crystal system	Triclinic	**R_1 (all)**	0.023
Space group	$P\bar{1}$	**wR_2 (all)**	0.053
Crystal appearance	Colourless Plate	**R_1 (obs)**	0.021
Crystal size (mm)	0.025 x 0.025 x 0.005	**wR_2 (obs)**	0.052
		Goof	0.770

Table 3.12 - Key bond lengths in Compound V

Bond	Bond length (Å)	Bond	Bond length (Å)
2x Fe1-F1	1.940 (9)	P1-O5	1.523 (5)
2x Fe1-O2	1.998 (7)	P1-O6	1.531 (4)
2x Fe1-O5	2.001 (6)	P1-O2	1.534 (3)
2x Fe3-O6	2.042 (9)	P1-O1*	1.566 (8)
2x Fe3-F1	2.094 (7)		
2x Fe3-Ow1*	2.206 (8)		

*Terminal bonds

Table 3.13 - Bond valence calculations for iron centres in compound V

Bond	BV	Bond	BV
2x Fe1-O5	0.50	2x Fe3-O6	0.50
2x Fe1-F1	0.48	2x Fe3-Ow1	0.31
2x Fe1-O2	0.50	2x Fe3-F1	0.33
Sum	**2.96**	**Sum**	**2.28**

3.6 Compound VI- $(H_2\text{-Piperazine})_4Fe_4(PO_3F,OH)_6(PO_2(F,OH)_2)_8$

A minor phase of yellow plate crystals were produced, one of which was selected for SXD, and the summary of the crystallographic information can be found in Table 3.14. This compound consists of FeO_6 octahedra, linked together by $PO_3(F,OH)$ tetrahedra to form 8-membered rings creating pores occupied by diprotonated piperazine along the *a*-axes (Figure 3-7). The phosphate tetrahedra that make up these rings (P1A/B, P2A/B, P5, P7, P10 and P11) contain two terminal vertices, one of which has a 1^- charge, and the other a 2^- charge. This has been determined by charge-balancing considerations and taking into account bond lengths. It has been shown in compounds **I** and **II** that the bond lengths for terminal vertices on phosphate tetrahedra with a 1^- charge are elongated compared to bridging or terminal sites with a 2^- charge. From Table 3.15 it can be seen that P1A/B, P2A/B, P5, P7, P10 and P11 contain two terminal vertices, one of which is elongated (1.556 Å) compared to the other (1.500 Å). Other 8-membered rings are formed along the *b*-axes and consist of FeO_6 octahedra, linked together by $PO_2(F,OH)_2$ (P6,P8, P9 and P13) and PO_3F,OH (P1A/B and P2A/B) tetrahedra (Figure 3-7). The charge of the terminal species was again determined by using charge balancing and bond lengths. The bond lengths for terminal vertices on P6, P8, P9 and P13 are elongated (1.541 Å) compared to bridging vertices (1.494 Å). These two different 8-membered building units create infinite sheets along the *a* and *b*-lattice directions. However in the *c*-lattice direction only one of these building units is present, only to be terminated with a $PO_2(OH,F)_2$ (P3, P4, P12 and P14) tetrahedra to create layers containing diprotonated piperazine (Figure 3-7). There is disorder within the compound **VI** (Figure 3-7): two of the phosphate tetrahedra (P1A/B and P2A/B) that are part of the 8-membered rings along the *a*- and *b*-axes can be orientated with P up or down (Figure 3-7). The dominant configuration is P down (A) along the *b*-axes, with P up (B) present approximately 5- 10 % of the time - this phenomenon is associated with partial absence of the amine within the pore along the *a*-axes. With no amine present the terminal $2-$ charge is no longer stabilised by H-bonding. Further disorder is located on the phosphate tetrahedra that contain three terminal vertices (P3, P4, P12 and P14); these terminal vertices can freely rotate and have led to difficulties when trying to solve this structure (Figure 3-7). The nature of these terminal vertices has been assigned by taking into account charge-balancing considerations and bond lengths. In order for Compound **VI** to charge balance it is apparent that two of the terminal vertices should contain a 1^- charge, with the third a 2^- charge. From Table 3.15, it can be seen that there are two terminal vertices that are elongated (1.545 Å) compared to the other (1.472 Å). Previous examples of terminal bonding lengths, within compound **I, II** and **VI**, have shown that vertices with a 1^- charge are elongated compared to terminal vertices with a 2^- charge. Although it is difficult to determine the nature of the 1^- charge as either fluoride or hydroxide, the potential formation of N-H------F bonds would indicate that the terminal species are more likely to be fluoride.

Table 3.14-Crystallographic data for Compound VI

Cell axes *a,b,c* (Å)	12.904 (5)	12.924 (5)	18.281 (13)
Cell angles *α,β,γ* (deg)	72.25 (5)	88.66 (6)	87.96 (6)

Empirical formula	$C_{16}H_{48}F_{17.33}Fe_4N_8O_{38.10}P_{14}$	**Z**	1
Formula weight (gmol^{-1})	1948.45	**Cell volume (Å^3)**	2901.4 (3)
Temperature	100 K	**Density (gcm^{-3})**	2.250
Crystal system	Triclinic	**R_1 (all)**	0.0828
Space group	$P\bar{1}$	**wR_2 (all)**	0.1723
Crystal appearance	Yellow plate	**R_1 (obs)**	0.0539
Crystal size (mm)	0.10 x 0.05 x 0.03	**wR_2**	0.1539
		Goof	1.031

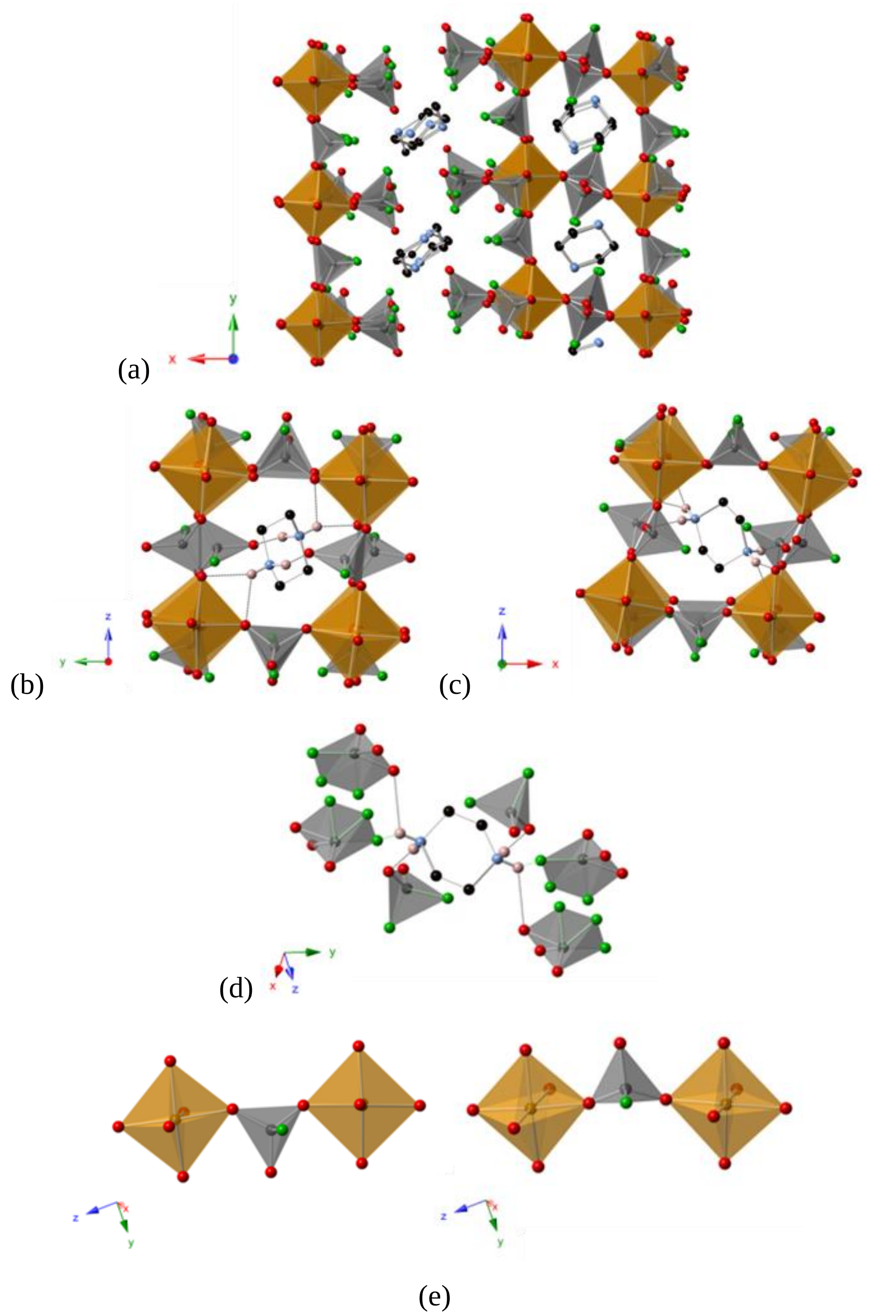

Figure 3-7 - (a) The structure of compound VI viewed along the c-axes. Showing the 8-membered ring along the (b) a-axis (c) and the b-axis. (d) H-bonding of piperazine in channels. (e) The two possible orientations for the disordered phosphate tetrahedron, A (left) and B (right): elongated phosphate vertices are depicted as fluoride. Fe polyhedra in orange, P tetrahedra in grey, O atoms are red spheres, F atoms are green spheres, N atoms are light blue sphere, and H atoms are light pink spheres

Table 3.15 - Key bond lengths in compound VI

Bond	Bond length (Å)	Bond	Bond length (Å)	Bond	Bond length (Å)
Fe1-O160	1.967 (5)	P7-O301*	1.512 (5)	P13-F17*	1.541 (5)
Fe1-O132	1.977 (3)	P7-F101*	1.565 (3)	P13-F8*	1.549 (5)
Fe1-O130	1.980 (3)	P8-O1	1.480 (5)	†P14-O2*	1.432 (8)
Fe1-O161	1.995 (3)	P8-O110	1.492 (6)	P14-O136	1.477 (5)
Fe1-O126	2.012 (5)	P8-F178*	1.548 (5)	†P14-F21*	1.550 (7)
Fe1-O131	2.013 (3)	P8-F11*	1.546 (4)	†P14-F1*	1.551 (5)
†P3-O160*	1.488 (4)	P9-O167	1.493 (6)	†P1A-O5A*	1.497 (4)
P3-O19	1.496 (6)	P9-O161	1.502 (6)	†P1A-O100	1.505 (4)
†P3-F177*	1.534 (6)	P9-F13*	1.538 (5)	†P1A-O101	1.517 (7)
†P3-F18*	1.548 (7)	P9-F12*	1.544 (5)	†P1A-F17A*	1.570 (5)
†P4-O3*	1.433 (8)	P10-O135	1.498 (5)	†P1B-O100	1.397 (12)
P4-O112	1.479 (5)	P10-O120	1.510 (5)	†P1B-O101	1.428 (14)
†P4-F15*	1.546 (8)	P10-O180*	1.514 (6)	†P1B-O5B*	1.486 (43)
†P4-F16*	1.555 (5)	P10-F30*	1.548 (6)	†P1B-F17B*	1.629 (30)
P5-O113	1.500 (5)	P11-O141	1.499 (5)	†P2A-O11A*	1.492 (4)
P5-O132	1.505 (5)	P11-O137	1.501 (5)	†P2A-O125	1.502 (6)
P5-O300*	1.516 (6)	P11-O302*	1.509 (4)	†P2A-O126	1.513 (5)
P5-F100*	1.552 (6)	P11-F102*	1.571 (3)	†P2A-F7A*	1.581 (5)
P6-O111	1.495 (5)	P12-O157	1.488 (4)	†P2B-O125	1.348 (14)
P6-O121	1.502 (6)	†P12-O200*	1.495 (6)	†P2B-O11B*	1.489 (29)
P6-F151*	1.539 (5)	†P12-F181*	1.538 (6)	†P2B-O126	1.502 (13)
P6-F9*	1.544 (5)	†P12-F20*	1.547 (7)	†P2B-F7B*	1.534 (40)
P7-O150	1.499 (5)	P13-O130	1.481 (5)		
P7-O131	1.501 (5)	P13-O147	1.490 (6)		

*Terminal bonds, †- disordered sites

3.7 Compound VII- $NaFeP_2O_7$

Despite not containing any F-atoms, the presence of fluoride was required for the formation of this material, suggesting fluoride acts as a catalyst or as a pH control. Compound **VII** is a polymorph of another monoclinic structure that has been previously described in literature.[156] The previously described polymorph crystallises in the $P2_1/c$ space group and was synthesised by solid-state methods. The studies performed on this polymorph concluded that $NaFeP_2O_7$ is a 3D antiferromagnetic material with a Néel temperature of 29 K.

Compound **VII** crystallised as pink needles with dimensions of 0.05 x 0.03 x 0.015 mm^3, in the monoclinic space group *C*2/*c:* one of these crystals was selected for SXD, and the summary of the crystallographic information can be found in Table 3.16. This compound is made up of FeO_6 octahedra, which are linked by diphosphate units ($P_2O_7^{2-}$), to form infinite chains, Figure 3-8. Key bond lengths are given in Table 3.17. These chains contain 6-membered rings comprised of two iron polyhedra and two diphosphate units; this creates a pore that is occupied by sodium ions, along the (121) lattice plane, Figure 3-8. These chains are linked together in the (-11-1) lattice plane by the apical oxygen's on diphosphate units: the oxygen's are corner-sharing *cis*, *trans*-to the iron polyhedra (Figure 3-8). The diphosphate units contain a P-O-P angle of 130 °, with an elongated bond connecting the ditetrahedra (1.61 Å). The phosphate tetrahedra are staggered by approximately 10 °. These same structural building units are also found in the previous polymorph; however the SBUs are arranged in a more ordered way, forming a more porous structure. The structural similarities between compound **VII** and the previous polymorph would indicate that the magnetic properties of these polymorphs should be comparable.

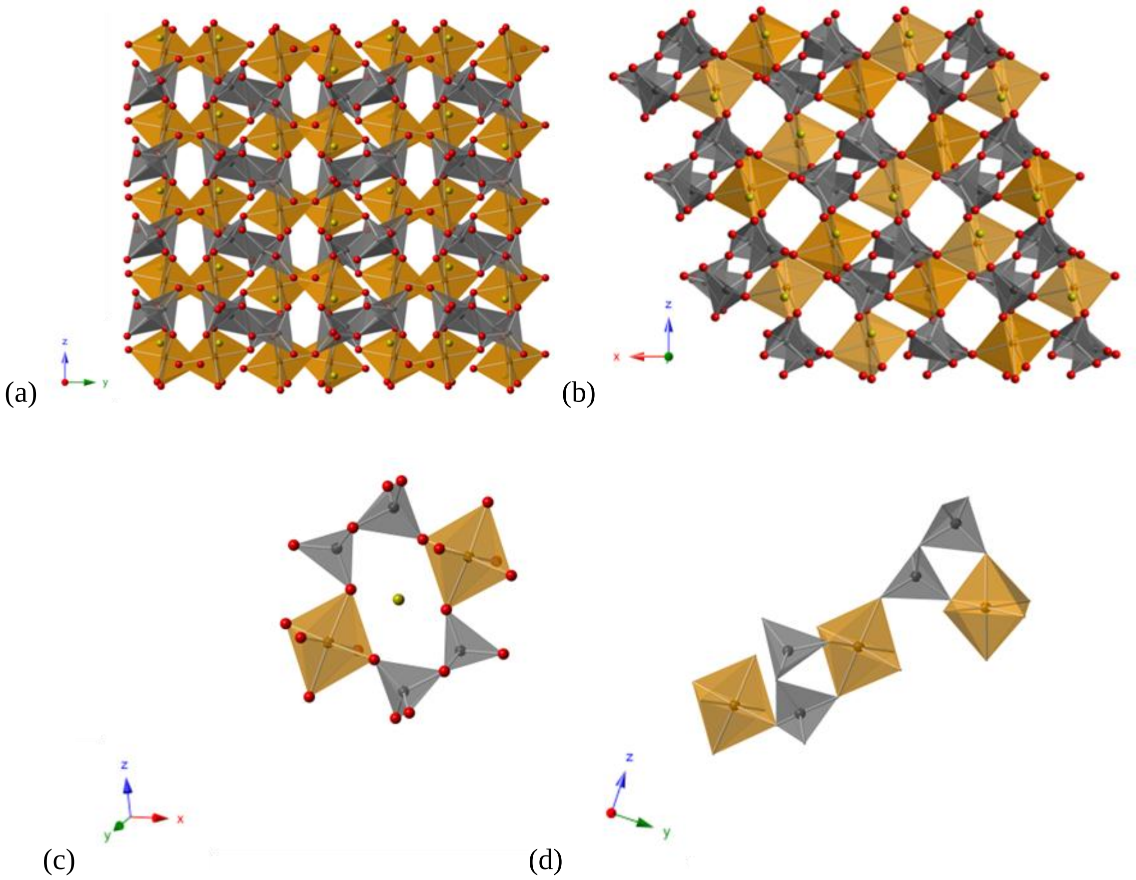

Figure 3-8 - The structure of compound VII viewed along the (a) a-axis and the (b) b-axes. (c) The 6-membered building unit that forms pores for sodium cations. (d) The structural building unit-connecting layers, oxygen has been removed for clarity. Fe polyhedra in orange, P tetrahedra in grey, O atoms are red spheres, Na atoms are yellow spheres.

Table 3.16-Crystallographic data for Compound VII

Cell axes *a,b,c* (Å)	9.674 (6)	8.215 (5)	13.157 (7)
Cell angles *α,β,γ* (deg)	90	109.47 (4)	90
Empirical formula	$FeNaO_7P_2$	**Z**	8
Formula weight (gmol^{-1})	252.78	**Cell volume (Å^3)**	985.83 (10)
Temperature	120 K	**Density (gcm^{-3})**	3.406
Crystal system	Monoclinic	**R_1 (all)**	0.0655
Space group	*C*2/*c*	***w*R_2 (all)**	0.1659
Crystal appearance	Pink needles	**R_1 (obs)**	0.0537
Crystal size (mm)	0.05x 0.03 x 0.015	***w*R_2 (obs)**	0.1521
		Goof	1.146

Table 3.17 - Key bond lengths in compound VII

Bond	Bond length (Å)	Bond	Bond length (Å)
Fe1-O2	1.985 (5)	P2-O5	1.524 (5)
Fe1-O8	1.988 (4)	P2-O2	1.524 (5)
Fe1-O7	1.995 (5)	P2-O3	1.524 (6)
Fe1-O6	2.009 (5)	P2-O4*	1.601 (6)
Fe1-O5	2.031 (5)	P3-O6	1.520 (6)
Fe1-O3	2.032 (5)	P3-O7	1.522 (5)
		P3-O8	1.536 (5)
		P3-O4*	1.628 (5)

*bridging diphosphate

3.8 Compound VIII - $NaFe(HPO_4)_2$

Compound VIII was also found not to contain any fluoride in the final product; however, as this phase has not been previously synthesised using conventional hydrothermal methods, the presence of fluoride has had some structural directing role in its formation. A pink plate crystal of size 0.03 x 0.03 x 0.01 mm3 was selected for SXD: the summary of the crystallographic information can be found Table 3.18 Compound **VIII** crystallised in the triclinic space group $P\bar{1}$, and the key bond lengths can be found in Table 3.19. Compound **VIII** is made up of FeO_6 octahedra, which are linked together by corner-sharing $P(O_3OH)$ tetrahedra to form a three-dimensional network, defining channels that are occupied by sodium cations (Figure 3-9). Compound **VIII** can be envisaged as a sheet structure that contains 4 and 8 membered rings. These sheets run along the a- and b-crystallographic lattice planes, and are connected together by the third P-O bond to Fe octahedra in the c-direction. The remaining vertex on the phosphate tetrahedral is terminal and orientated toward inter-channel space. The assignment of the terminal vertex as oxide led to better refinement and similar ADP values for all the anions. The quality of the SXD data allowed for the presence of hydrogen atoms to be detected and assigned to the terminal oxide vertex. Examination of the bond lengths around the phosphate tetrahedra (Table 3.19) shows that there is elongation of terminal vertices (1.586 Å) compared to bridging vertices (1.522 Å).

The 4-membered ring, Figure 3-9, contains two FeO_6 octahedra and two PO_3OH tetrahedra, where the hydrogen atoms are pointing in opposite directions. The 8-membered ring consists of 4 Fe octahedra and 4 P tetrahedral; these rings propagate along the (011) lattice plane and contain Na cations above and below rings (Figure 3-9).

Table 3.18 - Crystallographic data for Compound VIII

Cell axes *a,b,c* (Å)	6.389 (2)	6.458 (2)	22.206 (8)
Cell angles *α,β,γ* (deg)	83.40 (2)	84.72 (2)	83.20 (2)
Empirical formula	$Fe_3H_6Na_3O_{24}P_6$	**Z**	2
Formula weight (gmol^{-1})	812.39	**Cell volume (Å^3)**	900.92 (5)
Temperature	120 K	**Density (gcm^{-3})**	2.995
Crystal system	Triclinic	**R_1 (all)**	0.0647
Space group	$P\bar{1}$	**wR_2 (all)**	0.1030
Crystal appearance	Pink plate	**R_1 (obs)**	0.0492
Crystal size (mm)	0.03 x 0.03 x 0.01	**wR_2 (obs)**	0.0945
		Goof	1.098

Table 3.19 - Key bond lengths in compound VIII

Bond	Bond length (Å)	Bond	Bond length (Å)	Bond	Bond length (Å)
Fe1-O23	1.955 (9)	Fe3-O6	1.980 (4)	P6-O30	1.543 (2)
Fe1-O16	1.979 (9)	Fe3-O10	1.988 (9)	P6-O15*	1.576 (1)
Fe1-O17	1.991 (6)	Fe3-O7	2.023 (6)	P7-O4	1.517 (2)
Fe1-O19	2.019 (5)	Fe3-O12	2.072 (7)	P7-O8	1.518 (2)
Fe1-O20	2.035 (1)	P4-O9	1.508 (1)	P7-O18	1.525 (1)
Fe1-O30	2.069 (7)	P4-O12	1.531 (2)	P7-O24*	1.588 (1)
Fe2-O5	1.958 (7)	P4-O16	1.536 (2)	P8-O22	1.508 (2)
Fe2-O18	1.986 (4)	P4-O27*	1.584 (1)	P8-O7	1.517 (2)
Fe2-O14	1.996 (8)	P5-O10	1.489 (1)	P8-O6	1.526 (1)
Fe2-O8	2.008 (4)	P5-O19	1.537 (2)	P8-O28*	1.600 (1)
Fe2-O4	2.011 (6)	P5-O17	1.539 (2)	P9-O5	1.507 (1)
Fe2-O29	2.049 (7)	P5-O26*	1.578 (6)	P9-O29	1.525 (2)
Fe3-O22	1.961 (4)	P6-O23	1.515 (1)	P9-O20	1.530 (2)
Fe3-O9	1.971 (5)	P6-O14	1.522 (1)	P9-O21*	1.591 (2)

*Terminal bonds

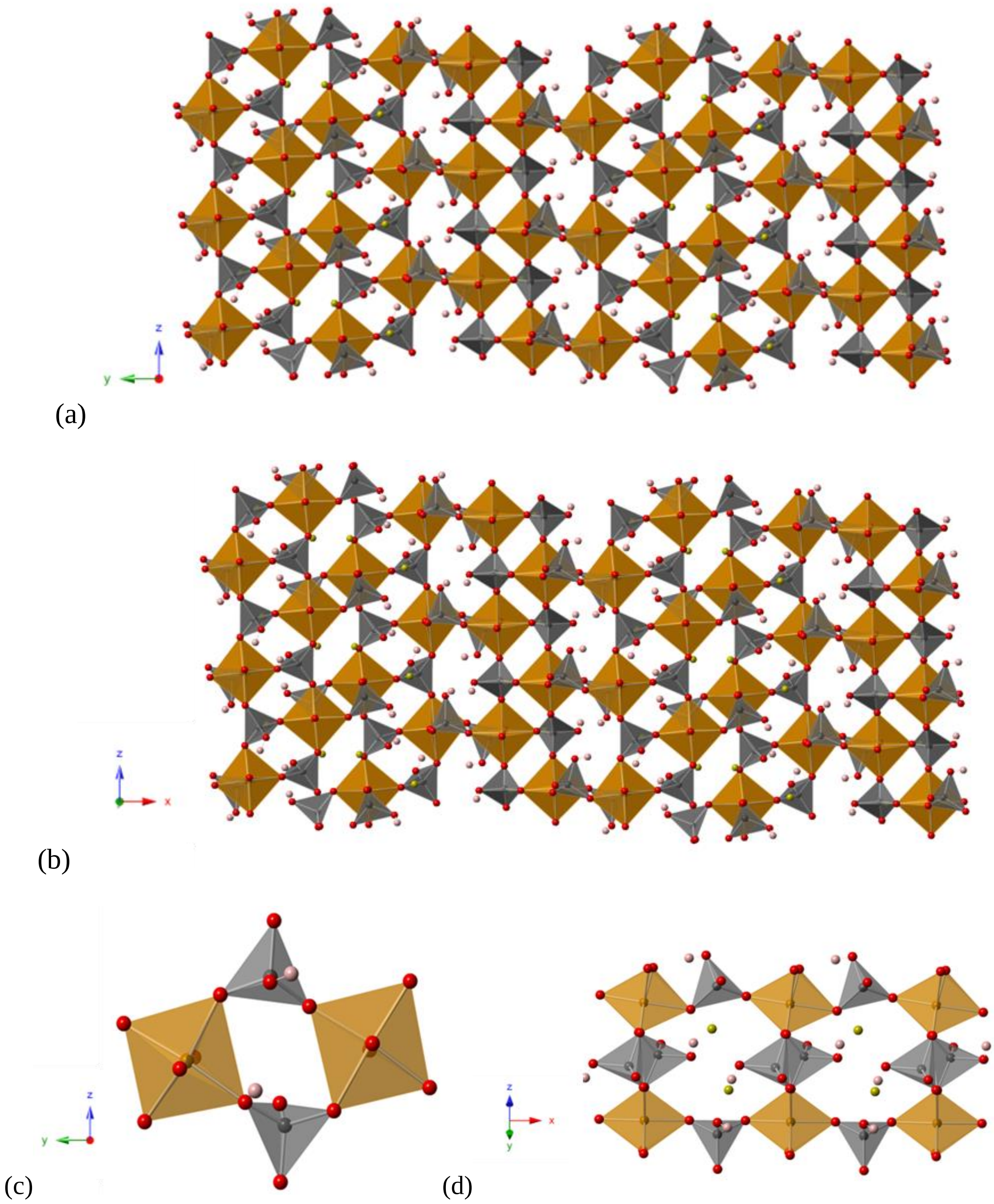

Figure 3-9 - Structure of compound VIII viewed along the (a) a-axis and (b) the b-axis.(c) Showing 4-membered ring SBU and (d) the 8-membered ring SBU. Fe polyhedra in orange, P tetrahedra in grey, O atoms are red spheres, Na atoms are yellow spheres and H atoms are light pink spheres.

.

3.9 Compound IX- $Fe_2(PO_3F)_3$

$Fe_2(PO_3F)_3$ (**IX**) crystallised as colourless block of sizes 0.08 x 0.05 x 0.03 mm^3, and has a hexagonal unit cell with space group $P6_3/m$. The crystallographic information can be found in Table 3.20, with key bond lengths provided in Table 3.21. The structure of **IX** consists of pairs of face-sharing FeO_6 octahedra, which are linked together by PO_3F tetrahedra. These pairs of Fe-octahedra are linked in the *c*-direction to from 4-membered rings, which run along the (110) plane (Figure 3-10). These 4-membered rings are connected to each other through the remaining bridging vertex. PO_3F tetrahedra are bonded such that two O atoms bond to one Fe centre, with the other O atom μ^3-bridging two Fe centres; F/OH-atoms are orientated into channels. In order to assign the terminal vertex, a combination of BV calculations and ADP values will be used. The ADP values of these terminal sites did not change significantly when compared to known oxide/fluoride sites. However, examination of the BV calculations, as shown in

Table 3.22, show a lack of bond valency when refined as oxide anions, in contrast to values approaching the correct bond valency when refined as fluoride anions.

The bond lengths around the phosphate tetrahedra vary depending on the nature of the bonding. The shortest bonds arise from μ^2-bridging O (1.50 Å), followed by μ^3-bridging O (1.53 Å), and the longest bonds are associated with terminal vertices (1.56 Å).

Figure 3-10 illustrates compound **IX** forms two types of F-atom lined channels with an approximate diameter of 5 Å. Attempts have been made by *chemie-douche* methods to insert Li into the F-lined channels with the prospect of investigating potential electrochemical properties; however these soft methods proved unsuccessful.

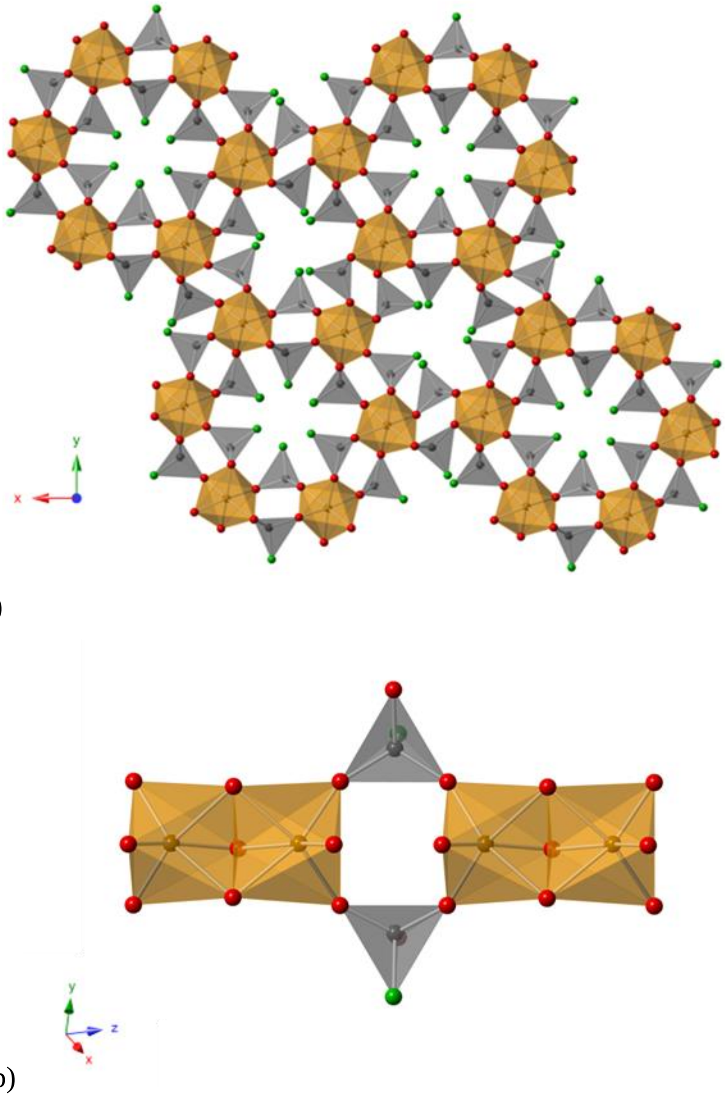

(a)

(b)

Figure 3-10 – Structure of Compound IX viewed along the (a) c-axis and (b) a 4-membered ring SBU. Fe polyhedra in orange, P tetrahedra in grey, O atoms are red spheres and F atoms are green spheres.

Table 3.20 - Crystallographic data for Compound IX

Cell axes *a,b,c* (Å)	14.484 (4)	14.484 (4)	7.332 (2)
Cell angles *α,β,γ* (deg)	90	90	120

Empirical formula	$F_3Fe_2O_9P_3$	**Z**	6
Formula weight (gmol^{-1})	405.61	**Cell volume (Å^3)**	1332.19 (6)
Temperature	120 K	**Density (gcm^{-3})**	3.033
Crystal system	Hexagonal	**R_1 (all)**	0.098
Space group	$P6_3/m$	**wR_2 (all)**	0.090
Crystal appearance	Colourless blocks	**R_1 (obs)**	0.045
Crystal size (mm)	0.08 x 0.05 x 0.03	**wR_2 (obs)**	0.081
		Goof	1.058

Table 3.21 - Key bond lengths in compound IX

Bond	Bond length (Å)	Bond	Bond length (Å)	Bond	Bond length (Å)
Fe1-O4	1.906 (4)	2x P2-O5	1.513 (4)	2x P4-O4	1.500 (4)
Fe1-O6	1.907 (4)	P2-O3	1.544 (5)	P4-O2	1.531 (5)
Fe1-O5	1.914 (5)	P2-F1*	1.554 (7)	P4-F2*	1.548 (8)
Fe1-O2	2.091 (3)	2x P3-O6	1.500 (4)		
Fe1-O8	2.103 (5)	P3-O8	1.529 (5)		
Fe1-O3	2.112 (4)	P3-F3*	1.567 (8)		

*Terminal bonds

Table 3.22 - Bond valence calculations for terminal phosphate vertices in Compound IX

Atom label	Bond valence (O^{2-})	Bond valence (F^{-})	Assignment
F1	1.16	0.90	P-F
F2	1.22	0.90	P-F
F3	1.21	0.90	P-F

3.10 Compound X- $KFe_2(PO_3F)_2(PO_2F_2)F_2$

Compound **X** crystallised in a triclinic unit cell with space group $P\bar{1}$, forming pink plates of sizes 0.005 x 0.005 x 0.0025 mm^3: a summary of the crystallographic information is provided in Table 3.23. The structure of **X** contains chains of octahedral iron centres, FeO_4F_2, that are linked via μ^2-bridging F-atoms and PO_2F_2 tetrahedra. These chains are linked to each other by PO_3F tetrahedra to form a 3D framework, with 2D channels containing K ions along the *b* and (101) directions (Figure 3-11), with key bond lengths summarised in Table 3.24. The chains (Figure 3-11) are formed by staggered *trans* μ^2-bridging F-atoms, where the Fe-F-Fe angle is approximately 140°. These chains run along the (-11-1) lattice direction and creates S-shaped channels along the *b*-axis, which are lined by terminal F atoms from the PO_2F_2 tetrahedra and occupied by K cations (Figure 3-11).

Table 3.23 - Crystallographic data for Compound X

Cell axes *a,b,c* (Å)	7.228 (2)	7.581 (3)	10.347 (3)
Cell angles *α,β,γ* (deg)	101.062 (2)	110.337 (2)	90.521 (2)

Empirical formula	$F_6Fe_2KO_8P_3$	**Z**	2
Formula weight ($gmol^{-1}$)	485.71	**Cell volume (Å^3)**	520.06 (3)
Temperature	120 K	**Density (gcm^{-3})**	3.102
Crystal system	Triclinic	**R_1 (all)**	0.098
Space group	$P\bar{1}$	***w*R_2 (all)**	0.276
Crystal appearance	Pink plate	**R_1 (obs)**	0.088
Crystal size (mm)	0.005 x 0.005 x 0.0025	***w*R_2 (obs)**	0.1801
		Goof	1.153

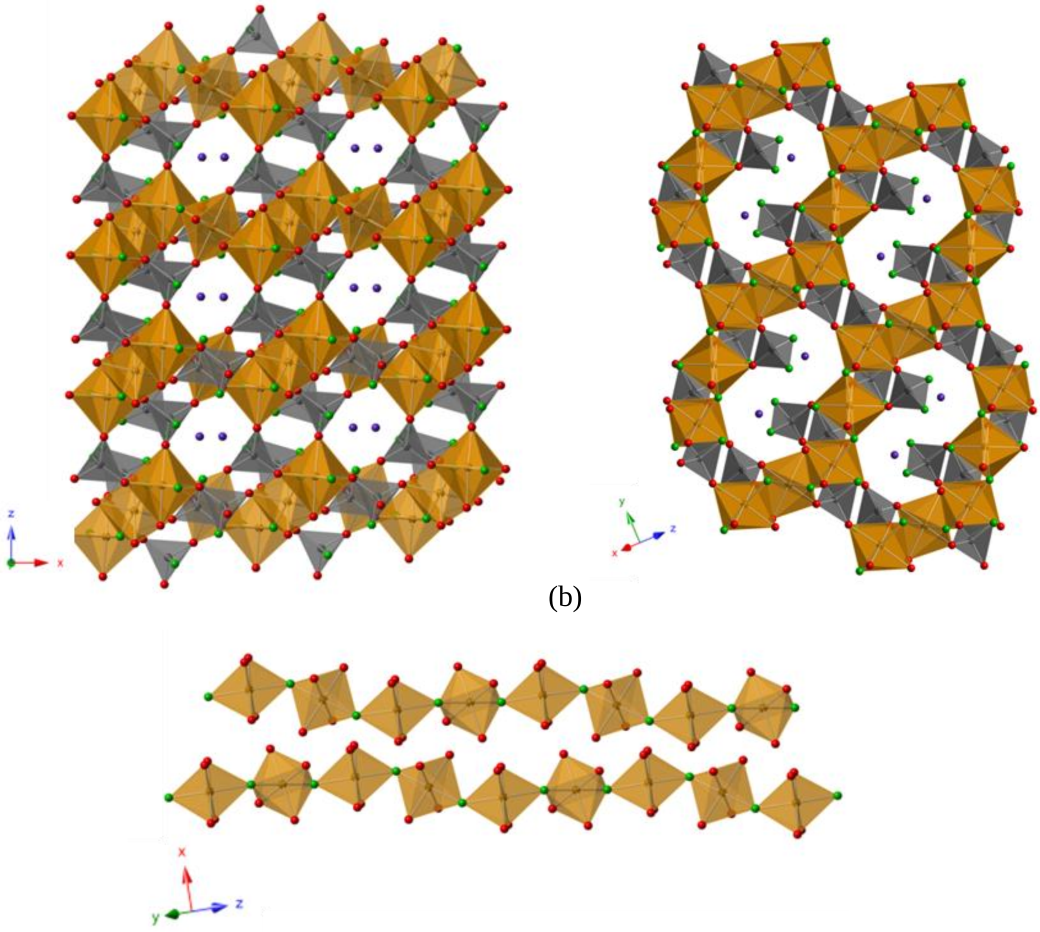

(a) (b)

(c)

Figure 3-11 – Structure of Compound X viewed along (a) the b-axis and (b) the (101) plane. (c) Structure of Fe-F-Fe…chains. Fe polyhedra in orange, P tetrahedra in grey, O atoms are red spheres, K cations are purple spheres and F atoms are green spheres.

Assignment of the fluoride site (F1 and F2) as oxygen yielded non-positive or very small ADP values; reassignment of the site as fluoride produced similar ADP values for all anion sites, as well as a reduction in data fitting residual values. The phosphate tetrahedra contain a mixture of mono- and di-fluorinated species in order for the compound to charge balance. Two phosphate tetrahedra (P1 and P5) have one vertex that does not bridge to iron octahedral units; the other phosphate tetrahedra (P6) contains two vertices, and all terminal vertices are orientated to the inter-channel space. For charge-balancing purposes, these terminal vertices must have a 1^{-} charge, either as hydroxide or fluoride anions. These sites can be assigned with examination of the anisotropic ADP and BV calculations. The ADP values of these terminal sites did not change significantly when compared to known oxide/fluoride sites. However, examination of the BV calculations for the terminated phosphate vertices, as shown in Table 3.25, show a lack of bond valency when refined as oxide anions, in contrast to values approaching the correct bond valency when refined as fluoride anions. The phosphate tetrahedra show similar behaviour with respect to bond lengths. The average P-O bond length, where O is μ^2- bridging to iron, is 1.508 Å, whereas terminal P-F bond lengths are significantly longer 1.570 Å.

Table 3.24 - Key bond lengths in compound X

Bond	Bond length (Å)	Bond	Bond length (Å)	Bond	Bond length (Å)
Fe1-O3	1.946 (7)	Fe2-F1	1.975 (6)	P5-O9	1.512 (7)
Fe1-O17	1.948 (7)	Fe3-O8	1.957 (7)	P5-O11	1.517 (6)
Fe1-O15	1.968 (8)	Fe3-O11	1.984 (6)	P5-F5*	1.572 (8)
Fe1-F1	1.985 (6)	Fe3-F2	1.998 (5)	P6-O15	1.505 (8)
Fe1-O9	1.992 (6)	P1-O3	1.505 (7)	P6-O16	1.513 (6)
Fe1-F2	1.995 (6)	P1-O17	1.506 (8)	P6-F3*	1.565 (7)
Fe2-O10	1.969 (7)	P1-F6*	1.567 (6)	P6-F4*	1.573 (7)
Fe2-O16	1.973 (6)	P5-O10	1.501 (7)		

*Terminal bonds

Table 3.25 - Bond valence calculations for terminal phosphate vertices in compound X

Atom	Bond valence (O^{2-})	Bond valence (F^{-})	Assignment
F3	1.35	0.95	P-F
F4	1.28	0.98	P-F
F5	1.34	1.01	P-F
F6	1.31	1.01	P-F

3.11 Compound XI- $NaFe(PO_3F)_2$

The structure of **XI** is comprised of four membered rings consisting of two FeO_6 octahedra and two PO_3F tetrahedra, running along the crystallographic *a*-lattice direction (Figure 3-12). The sodium cations are in the centre of an 8 membered ring consisting of four FeO_6 octahedra and four PO_3F tetrahedra, with the fluorine atoms pointing into channels running along the (310) lattice direction. Compound **XI** crystallised in a monoclinic unit cell with space group $P2_1/c$, forming a colourless plate crystal of size 0.04 x 0.04 x 0.025 mm^3: the crystallographic summary can be found in Table 3.26.

Assignment of the terminal vertices, within the phosphate tetrahedra (F1 and F2) as oxygen yielded non-positive or very small ADP values; reassignment of this scattering power as fluoride produced similar ADP values for all anion sites, as well as a reduction in data fitting residual values. This was confirmed through examination of the BV calculations, where incorrect assignment of an oxide ion to the F1 and F2 ion sites (during structure refinement) produced very low values for the site valency, Table 3.28.

The phosphate tetrahedra show similar behaviour with respect to bond lengths, Table 3.27. The average P-O bond length, where O is μ^2- bridging to iron, is 1.509 Å, whereas terminal P-F bond lengths are significantly longer 1.571 Å

Table 3.26 - Crystallographic data for Compound XI

Cell axes *a,b,c* (Å)	6.489(7)	14.201(5)	6.464(3)
Cell angles *α,β,γ* (deg)	90	96.26(5)	90

Empirical formula	$F_2Fe_2NaO_6P_2$	**Z**	4
Formula weight ($gmol^{-1}$)	274.78	**Cell volume ($Å^3$)**	592.1(7)
Temperature	100 K	**Density (gcm^{-3})**	3.083
Crystal system	Monoclinic	**R_1 (all)**	0.050
Space group	$P2_1/c$	***w*R_2 (all)**	0.126
Crystal appearance	Pink plates	**R_1 (obs)**	0.044
Crystal size (mm)	0.04 x 0.04 x 0.025	***w*R_2**	0.121
		Goof	0.791

Table 3.27 - Key bond lengths in compound XI

Bond	Bond length (Å)	Bond	Bond length (Å)
Fe1-O8	1.962 (3)	P1-O8	1.494 (3)
Fe1-O4	1.964 (6)	P1-O4	1.499 (8)
Fe1-O3	1.996 (4)	P1-O9	1.525 (2)
Fe1-O2	2.001 (3)	P1-F2*	1.578 (2)
Fe1-O5	2.025 (9)	P2-O3	1.507 (3)
Fe1-O9	2.077 (10)	P2-O2	1.516 (4)
		P2-O5	1.518 (3)
		P2-F1*	1.564 (7)

*Terminal bonds

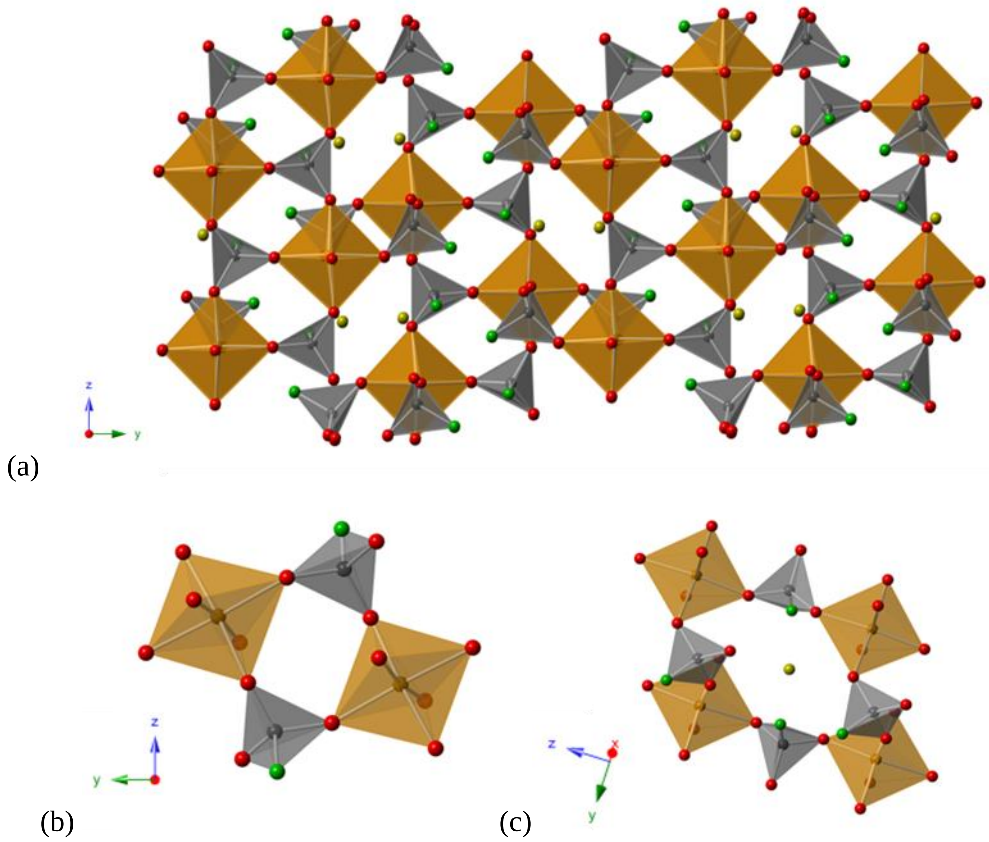

Figure 3-12 - (a) The structure of XI viewed along the a-axis (b) The 4-membered building unit. (c) The 8-membered building unit that forms pores, which are occupied by sodium ions. Fe polyhedra in orange, P tetrahedra in grey, O atoms are red spheres, Na cations are yellow spheres and F atoms are green spheres.

Table 3.28 - Bond valence calculations for terminal phosphate vertices in compound XI

Atom	Bond valence (O^{2-})	Bond valence (F^{-})	Assignment
F1	1.27	0.94	P-F
F2	1.39	1.05	P-F

3.12 -Compound XII- $RbFe^{(II)}_3(PO_3F)(PO_2(OH)_2)F_2$

$RbFe_3(PO_3F)_2(PO_2(OH)_2)F_2$ (**XII**) crystallised as almost colourless needles of sizes 0.15 x 0.025 x 0.025 mm^3, and has a monoclinic unit cell with space group *C*2/*c*; the resulting crystallographic information is summarised in Table 3.29. The structure consists of $Fe^{II}O_4F_2$ octahedra, in addition to phosphate tetrahedra PO_3F and $PO_2(OH)_2$: key bond lengths are summarised in Table 3.30. Examination of the bond lengths around the iron octahedra show that these are associated with iron in the +2 oxidation state - this was confirmed by BV calculations in Table 3.31 FeO_4F_2 octahedra are face-sharing through μ^3-bridging oxygen, which bridges two Fe octahedra and one P tetrahedron; and fluorine atoms, which bridge three Fe octahedra (Figure 3-13). This structural feature propagates in the *b* and *c* -crystallographic directions, with iron octahedra further linked by PO_3F tetrahedra to form 2D-layers. Examination of the scattering power for F1 (μ^3-bridging site) and F2 (terminal phosphate site) confirmed these sites to be fluoride groups when compared to bridging oxygen. The PO_3F tetrahedra are orientated such that the fluorides are terminal and line the inter-layer space. Finally, the layers are cross-linked along the crystallographic *a*-lattice direction by $PO_2(OH)_2$ tetrahedra to form a 3D framework, with OH pointing into channels that contain rubidium ions (Figure 3-13). The hydrogen atoms were identified directly from the SXD data and are consistent with previous work on a copper analogue of this compound reported by Williams *et al* [157], where neutron diffraction data collected from this compound confirmed the presence of $PO_2(OH)_2$ tetrahedra.

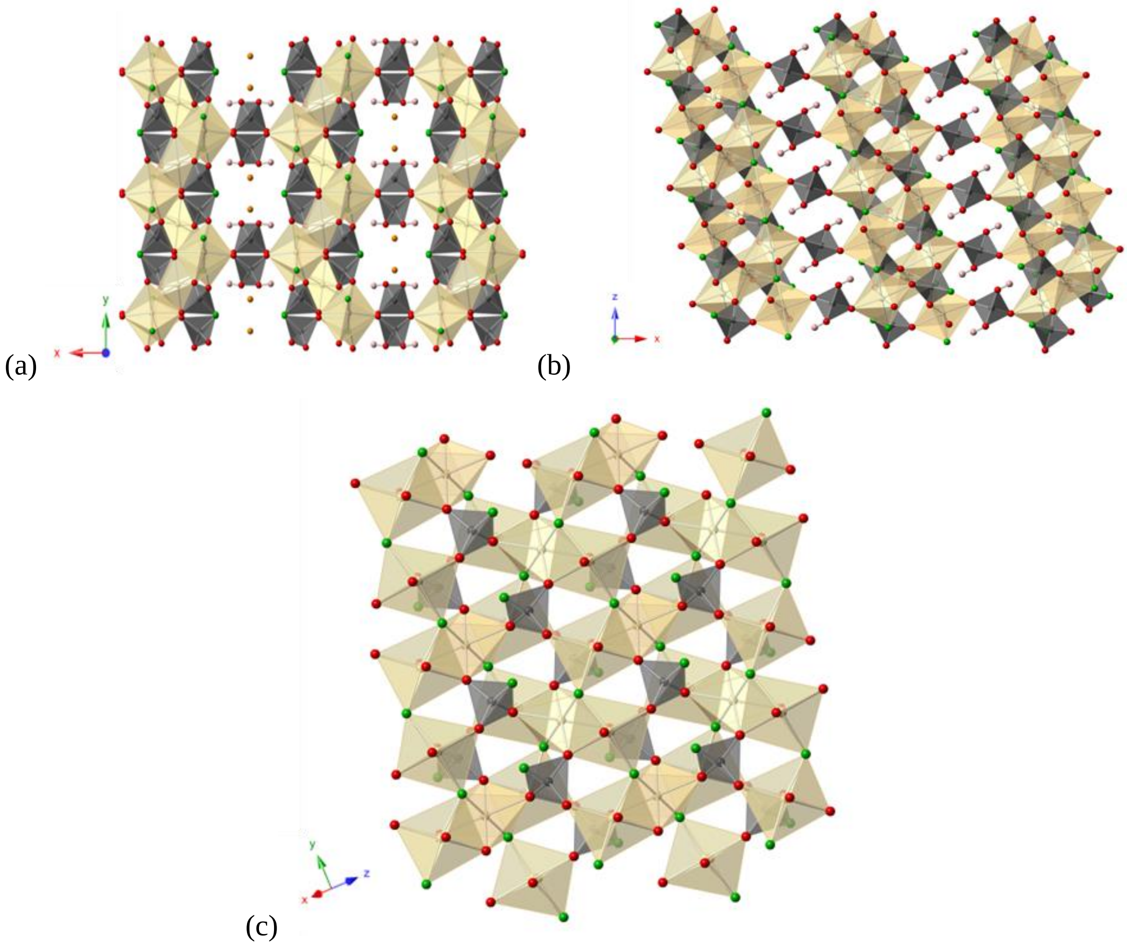

Figure 3-13 - View of compound XII along (a) the c-axis, (b) the b-axis and (c) along the (101) lattice direction Fe^{+2} *polyhedra in cream, P tetrahedra in grey, O atoms are red spheres, Rb cations are orange spheres and F atoms are green spheres*

Table 3.29 - Crystallographic data for Compound XII

Cell axes *a,b,c* (Å)	20.147 (11)	7.451 (4)	7.502 (4)
Cell angles *α,β,γ* (deg)	90	102.72 (1)	90

Empirical formula	$H_2F_6Fe_3O_8P_3Rb$	**Z**	4
Formula weight ($gmol^{-1}$)	587.93	**Cell volume ($Å^3$)**	1098.57 (10)
Temperature	120 K	**Density (gcm^{-3})**	3.555
Crystal system	Monoclinic	**R_1 (all)**	0.058
Space group	*C*2/*c*	**wR_2 (all)**	0.114
Crystal appearance	Colourless Needles	**R_1 (obs)**	0.047
Crystal size (mm)	0.15 x 0.05 x 0.025	**wR_2 (obs)**	0.107
		Goof	1.107

Table 3.30 - Key bond lengths in compound XII

Bond	Bond length (Å)	Bond	Bond length (Å)
2x Fe1-O8	2.052 (5)	Fe2-F1	2.165 (4)
2x Fe1-O5	2.106 (5)	P1-O2	1.514 (5)
2xFe1-F1	2.102 (4)	P1-O5	1.522 (5)
Fe2-O4	2.029 (5)	P1-O8	1.522 (5)
Fe2-O2	2.061 (5)	P1-F2*	1.580 (5)
Fe2-O5	2.107 (5)	2x P5-O4	1.494 (5)
Fe2-O8	2.116 (5)	2x P5-O200*	1.583 (5)
Fe2-F1	2.087 (4)		

*Terminal bonds

Table 3.31 - Bond valence calculations for iron centres in Compound XII

Bond	BV	Bond	BV
Fe1-O8	0.42	Fe2-O4	0.45
Fe1-O8	0.42	Fe2-O2	0.41
Fe1-O5	0.37	Fe2-O5	0.36
Fe1-O5	0.37	Fe2-O8	0.36
Fe1-F1	0.29	Fe2-F1	0.31
Fe1-F1	0.29	Fe2-F1	0.25
Sum	**2.17**	**Sum**	**2.14**

Comparisons of bond lengths around the phosphate tetrahedra indicate varying degrees of elongation when compared to μ^2-bridging oxygens. The average μ^2-bridging oxygen distance is 1.501 Å, there is a slight elongation for μ^3-bridging oxygens, 1.522 Å, with terminal phosphate vertices being the most elongated, 1.582 Å.

3.13 Compound XIII-$(NH_4)_2Fe^{II}Fe^{III}(PO_3F)_2FCl_2$

$(NH_4)_2Fe^{(II)}Fe^{(III)}(PO_3F)_2FCl_2$ **(XIII)** crystallised as near-racemic (refined Flack parameter 0.64(2)) black needles of sizes 0.025 x 0.025 x 0.175 mm^3, and has a orthorhombic unit cell with space group *Pca*2$_1$ (Table 3.32). The structure contains sheets of $Fe^{II}O_2Cl_4$ octahedra linked together by edge-sharing chloride running along the *ab*-lattice plane, and chains of $Fe^{III}O_4F_2$ octahedra *trans* linked by μ^2-bridging fluoride along the crystallographic *a*-lattice direction (Figure 3-14). For charge balancing the compound must contain mixed valance iron octahedral and this was confirmed by BV calculations (Table 3.34). The Fe^{II} sheets are linked to the Fe^{III} chains via edge-sharing PO_3F tetrahedra with fluoride pointing into interlayer space. Assignment of the fluoride site, on the phosphate tetrahedra (F2 and F3) as oxygen yielded non-positive or very small ADP values; reassignment of this scattering power as fluoride produced similar ADP values for all anion sites, as well as a reduction in data fitting residual values. This was confirmed through examination of the BV calculations, where incorrect assignment of an oxide ion to the F2 ion site (during structure refinement) produced very low values for the site valence: BV = 1.26, indicative of a fluoride ion at this position (BV = 0.89). Similar results were obtained for the BV calculations on F3. Pores are formed from 5-membered rings consisting of one Fe^{III} octahedra, two PO_3F tetrahedra and two Fe^{II} octahedra, these pores run in the (110) and *c*- crystallographic directions and are occupied by ammonium ions, which form hydrogen bonding interactions to the framework that range from 1.893-2.821 Å (Figure 3-14).

Once again there is notable elongation of terminal phosphate vertices (1.559 Å) compared to μ^2-bridging oxygen (1.503 Å), Table 3.33. To the author's knowledge, this is the first synthetic iron framework to contain both Cl and F ligand

Table 3.32 - Crystallographic data for XIII

Cell axes *a,b,c* (Å)	7.1380(6)	7.3128(7)	21.337(2)
Cell angles *α,β,γ* (deg)	90	90	90

Empirical formula	$Cl_2F_3Fe_2N_2O_6P_2$	**Z**	4
Formula weight (gmol^{-1})	425.56	**Cell volume (Å^3)**	1113.75(15)
Temperature	100 K	**Density (gcm^{-3})**	2.538
Crystal system	Orthorhombic	**R_1 (all)**	0.043
Space group	$Pca2_1$	**wR_2 (all)**	0.088
Crystal appearance	Black Needles	**R_1 (obs)**	0.036
Crystal size (mm)	0.175 x 0.05 x 0.025	**wR_2 (obs)**	0.086
		Goof	1.252

Table 3.33 - Key bond lengths in Compound XIII

Bond	Bond length (Å)	Bond	Bond length (Å)	Bond	Bond length (Å)
Fe1-O2	1.992 (4)	Fe2-F1	1.955 (3)	P1-O2	1.488 (4)
Fe1-O6	2.000 (4)	Fe2-F1	1.959 (3)	P1-O8	1.505 (4)
Fe1-Cl4	2.520 (1)	Fe2-O4	1.968 (4)	P1-O7	1.510 (4)
Fe1-Cl4	2.566 (1)	Fe2-O8	1.974 (4)	P1-F3*	1.558 (3)
Fe1-Cl1	2.576 (1)	Fe2-O7	1.980 (4)	P2-O6	1.494 (4)
Fe1-Cl1	2.640 (1)	Fe2-O5	1.980 (4)	P2-O4	1.507 (4)
				P2-O5	1.511 (4)
				P2-F2*	1.560 (3)

*Terminal bonds

Table 3.34 - Bond valence calculations for iron centres in Compound XIII

Bond	BV	Bond	BV
Fe1-O6	0.50	Fe2-O5	0.53
Fe1-Cl4	0.29	Fe2-O4	0.55
Fe1-Cl4	0.32	Fe2-O7	0.54
Fe1-Cl1	0.25	Fe2-O8	0.54
Fe1-Cl1	0.28	Fe2-F1	0.47
Fe-O2	0.51	Fe2-F1	0.47
Sum	**2.15**	**Sum**	**3.09**

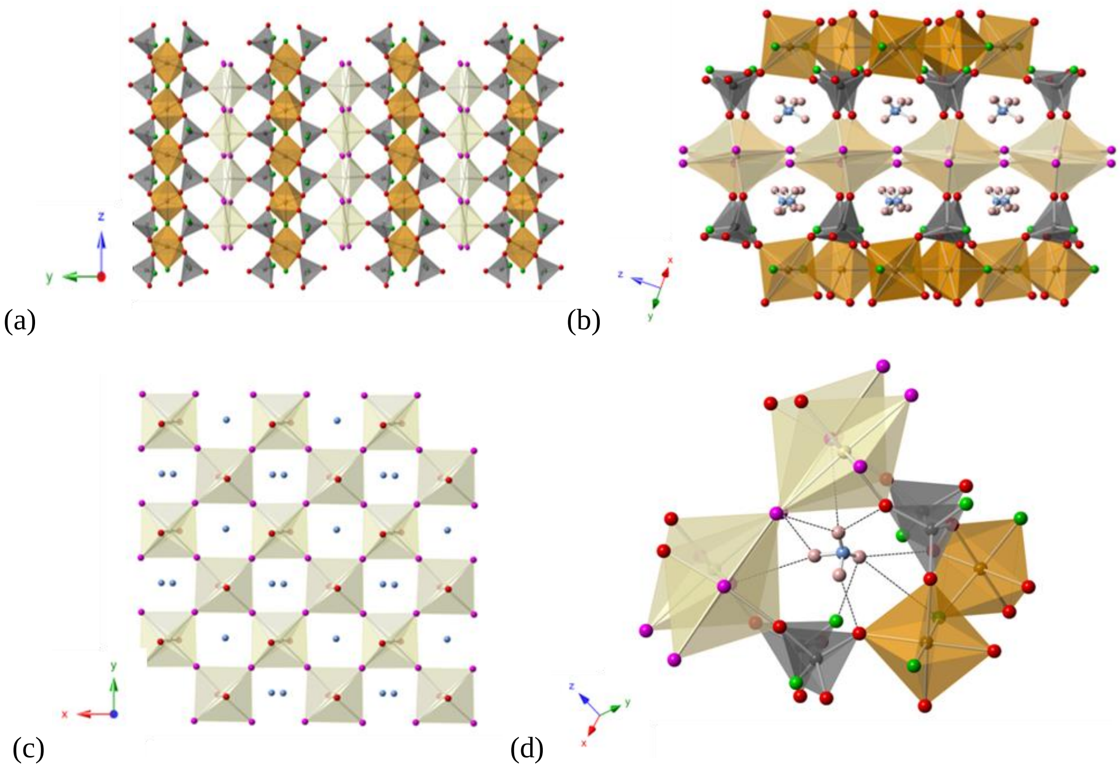

Figure 3-14 - The structure of Compound XIII viewed along the (a) a-axis and (b) the (110) direction. (c) $Fe^{II}O_2Cl_4$ sheets, where Fe^{III} and phosphate polyhedra have been removed for clarity. (d) 5-membered ring containing ammonium cation where H-bonding is represented as black dashed lines. Fe^{+3} polyhedra in orange, Fe^{+2} polyhedra in cream, P tetrahedra in grey, O atoms are red spheres, N atoms are light blue spheres, H atoms are light pink spheres, Cl atoms are magenta spheres and F atoms are green spheres

3.14 Structural summary

The synthesis of iron phosphate materials in fluoride-rich media leads to a wealth of new compounds formed from linked polyhedra. The incorporation of fluorine into these materials leads to a number of noteworthy features.

All of the compounds reported herein contain iron, mainly as Fe (III), in octahedral geometry. This is in contrast to previously-described iron phosphate and fluorophosphate frameworks that contain iron located in clusters of trigonal bipyramids.[73, 88] The compounds exhibit a variety of different structural topologies, though there is no observed correlation between their fluorine contents and the dimensionality of the linked polyhedra in the final products. This behaviour is similar to that found for manganese and cobalt fluorophosphates [104, 105] whereas copper fluorophosphates indicate a relationship between fluorine content and dimensionality.[103] Previous work [102] has suggested that in metal fluorophosphates with Mn, Co and Cu the fluoride anion frequently occurs as a terminal species on both metal and phosphorus polyhedra. This reduces the number of bridging anions present in the system, leaving mainly oxygen to bridge between iron and phosphorus-centred polyhedra. This breaks up the connectivity and produces structures with lower dimensionality. However, in the materials reported in this work, fluoride anions show a tendency to bridge iron centres and increase connectivity, typically as μ^2-F (e.g. **III, V, X, XII** and **XIII**) and in one case μ^3–F (**XII**). Indeed, there is a preference for Fe-coordinated fluoride to occupy bridging sites, with fluoride twice as likely to occupy such a site on iron as compared to a terminal site. This behaviour commonly presents itself in the occurrence of infinite Fe-F-Fe-F-Fe.... chains, a feature present in five of the structures (e.g. **III, V, X, XII** and **XIII**), and previously observed in the ULM-series.[88] Out of these five structures, four exhibit 3D networks, suggesting that the infinite chains can act as a secondary building unit which are linked by fluorophosphate groups into complex 3D networks. Due to these chains, the materials in this work should exhibit similar antiferromagnetic properties to the compounds described in the ULM-series. The terminal fluoride ions are typically orientated into inter-framework, -layer or –chain space and form weak ionic interactions with charge-balancing cations. Comparison of the Fe-O and Fe-F bond distances shows that the average Fe-F bond (1.965 Å) is slightly shorter than the average Fe-O bond (1.992 Å) reflecting a slightly smaller ionic radius of F^-, compared to O^{2-}. A comparison of fluoride bond distances with other transition metals (e.g. Co, Mn, Cu) containing frameworks suggests this behaviour is typical.[102, 157-159]

Another feature of interest is the formation of fluorophosphates groups: PO_3F and more rarely $PO_2(OH,F)_2$. Such groups are known in framework materials but only in a few cases.[160-162] In contrast, eight framework materials reported contain such groups, with PO_3F particularly prevalent. These groups form part of the linked polyhedral structural unit, with oxygen typically bridging to iron sites and fluorine orientated externally, for example into inter-layer space. Examination of the $PO_2(F,OH)_2$ and PO_3F,OH tetrahedra showed a noticeable elongation of bond distances for terminal vertices with a 1− charge, compared to bridging oxygen distances and terminal vertices with a 2− charge. The average terminal P-X distance increases from 1.495 Å (X = O) to 1.564 Å (X = F, OH). The P-O bridging distances also vary, dependent on the number of iron sites bridged by the oxygen atom, increasing from 1.503 Å (μ^2) to 1.526 Å for μ^3-bridging O. This elongation is necessary to overcome the steric constraints from bridging two iron octahedra and one phosphate tetrahedron.

The highly acidic conditions used during synthesis result in any amine template used during synthesis becoming protonated in the product, and therefore these act as both structure-directing agents and counter-ions for a negatively-charged framework. The amine templates arrange themselves in such a way that the amine groups are orientated towards the framework of the structure, creating chain (**III**) or layered structures (**IV, V, VI**,). These amine groups form hydrogen bonds to framework oxygen or fluorine, with particular preference for stabilised terminal 2− charge charges (**I, III, VI**), similar to the 2D iron phosphate structures described by Lii *et al.* [73] Compounds **IV** and **VI** are different from previously-described iron phosphate frameworks, as the amine templates form strong H-bonds to the terminal P-F bonds. This resulted in a larger number of organically-templated 2D layered structures compared to the 3D frameworks produced in the ULM-n series.[88] Attempts to remove the amine templates from the structures through thermolysis, and so create a porous material, typically resulted in structural collapse. This was confirmed by TGA analysis and post-reaction PXD patterns and is consistent with other templated iron phosphates.[73, 88]

3.15 Conclusions

A range of alkali cations and protonated amines have been used as templating agents to synthesise new iron fluorophosphates. These new materials have been synthesised utilising the hydrofluorothermal method which aims to increase the F:O ratio through minimising water content. This has led to 13 new iron fluorophosphates being formed, with 11 containing fluoride either bridging Fe centres or as terminal vertices on phosphate and iron polyhedra. Initial work on incorporating other potential mineralising agents into iron phosphate frameworks led to the formation of the first chlorofluorophosphate material.

Chapter 4 NIR absorption library

In order for an iron or copper framework to be active in the NIR, the difference in the HOMO and LUMO energy levels needs to be separated by approximately 0.5-1.5 eV (780-2500 nm). The earlier absorbance spectra (Figure 1-10) of the hexa-aqua complexes indicated that both iron (II) and copper (II) materials should exhibit an absorbance peak close to the NIR region. The earlier literature research of iron and copper framework materials provided an insight into the structural diversity of these compounds. Apart from the copper silicate, Egyptian blue ($CaCuSi_4O_{10}$), there is little information from the literature review regarding the optical properties of these framework materials. Most of the materials described in the literature contained copper and iron in four-, five- and six-coordinate ligand environments. Each of these different types of coordination environments will give rise to unique absorption properties due to the energy level diagrams for each material. The energy difference between the energy levels – ΔE - can be affected by a wide range of factors: geometry of ligands around the metal, bond distances and the nature of the ligand. The nature of the ligand and the bond length are strongly related to the bonding properties between the metal and ligand, therefore these two factors cannot be separated. The geometry is linked to the coordination environment, which is dependent on the crystal structure.

Due to the lack of information regarding the optical properties of copper and iron framework materials in the literature, a library of compounds have been synthesised and the absorbance spectra recorded. This chapter describes the synthesis and optical properties of a selection of copper (II) and iron (II) frameworks with different four-, five- and six-coordination environments; with the aim to determine possible structural-properties relationships. These possible relationships can enable the tailored synthesis of materials that will have a strong absorbance in the NIR region.

4.1 Four-coordinate structures

The most common types of geometry associated with four-coordinate structures are tetrahedral and square planar.

Square planar geometries are energetically favoured with d^8 configurations when the crystal field is strong enough to favour the low-spin arrangement. This is commonly seen in the $4d^8$ and $5d^8$ complexes Rh(I), Ir(I), Pt(II), Pd (II) and Au (III), in which there is a large ligand-field splitting associated with the 4d and 5d metal series.[130] Square planar geometries are also found in copper complexes with strong π-donor ligands, such as $Cs_2Cu_3P_4O_{14}$ [123] and layered copper silicates such as cuprorivaite ($CaCuSi_4O_{10}$) and effenbergerite ($BaCuSi_4O_{10}$).[115, 116] A rare example of iron (II) in square planar geometry is isostructural to effenbergerite; the iron containing mineral gillipsite ($BaFeSi_4O_{10}$).

Four-coordinate iron (II) compounds are rare due to greater gain in ligand field stabilisation energy when located in octahedral geometries compared to tetrahedral. Only very few examples of complex phosphate frameworks containing iron (II) or copper (II) in exclusively tetrahedral or near-tetrahedral geometry have been described previously, namely $NaFe_2(HPO_4)(PO_4)$[76] , $KFePO_4$ [163] (two iron coordinations to oxygen, fivefold with four short, and one long distance and distorted tetrahedral), and $RbCuPO_4$.[114]

In this section, the synthesis and characterisation - using PXD and UV/Vis/NIR spectroscopy - of several four-coordinate copper and iron frameworks has been described, with an attempt to discover candidate materials with promising near-infrared absorption properties for further studies.

Compound 1 - $Li_2CuP_2O_7$

A polycrystalline sample of compound 1 was synthesised by combining a mixture of copper (II) oxide, ammonium phosphate monobasic, $(NH_4)H_2PO_4$ and lithium carbonate in a molar ratio of 1:2:1. The desired mixture was heated, ground in a pestle and mortar, and transferred to a box furnace and heated at 400 °C for 30 hours, with a heating rate of 2 °C/min. Several intermediate grinding stages, as well as pelletisation, were required to obtain a pure phase.

The experimental pattern matched with the monoclinic *C*2/*c* phase in the ICSD database, therefore, the trial model used for the Rietveld refinement was from Gopalakrishna *et al.*[164] The resulting atomic coordinates, temperature factors and refinement parameters are shown in Table 4.1.

The Rietveld refinement fit profile is provided in Figure 4-1. The reliability values of this refinement are slightly high due to the preferred orientation along the (001) plane in the sample. The preferred orientation was modelled using the March-Dollase method with a ratio of 1.06 for the (001) plane.

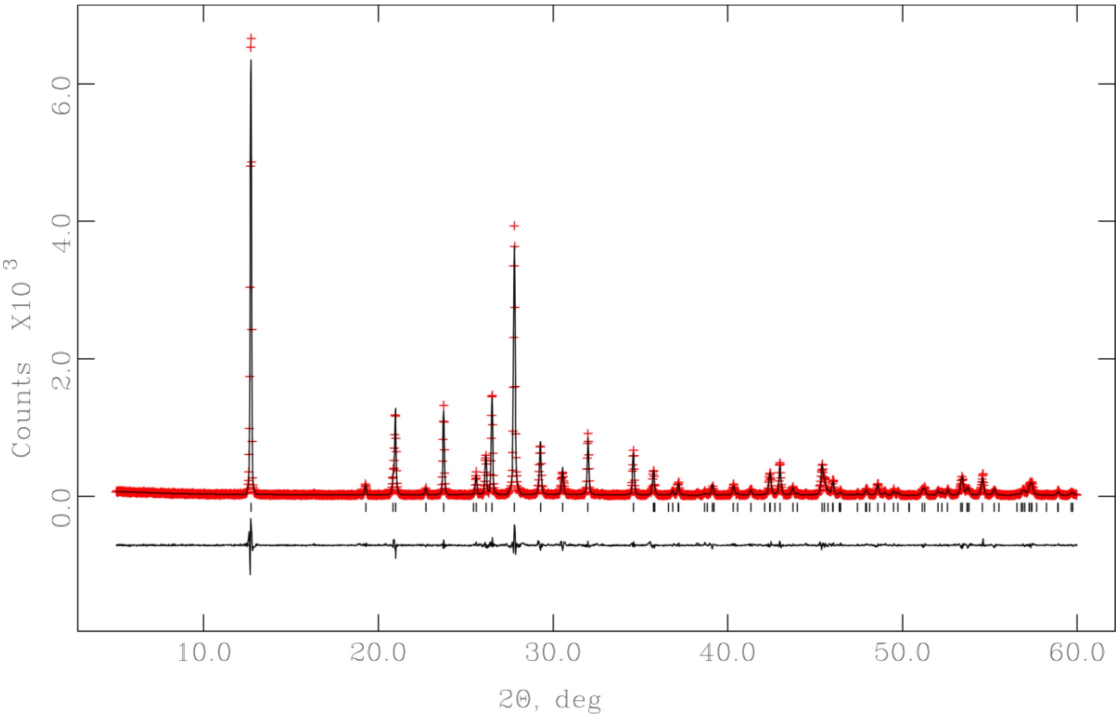

Figure 4-1 - Rietveld refinement fit profile of compound 1. Observed data points are shown as red crosses and the calculated pattern as a solid black line. The difference between the calculated and observed pattern is shown underneath. The position of the peaks are indicated by rows of vertical lines.

Table 4.1 - Atomic coordinates and temperature factors for Compound 1 generated from Rietveld analysis

Space group: *C*2/*c*

Lattice parameters: a = 15.331 (5) Å, b = 4.877 (2) Å, c = 8.622 (3) Å, α = γ = 90°, β = 114.85 (2)

Atom site	*x*	*y*	*z*	U_{iso} x 10^2 ($Å^2$)
Cu1	0.000	0.000	0.000	3.5 (1)
Li1	0.331 (2)	0.355 (6)	0.471 (5)	6.6 (13)
O1	0.898 (6)	0.238 (2)	0.848 (1)	1.7 (4)
O2	0.101 (5)	0.150 (2)	0.940 (1)	1.8 (4)
O3	0.175 (5)	0.424 (2)	0.393 (1)	1.9 (3)
O4	0.000	0.470 (3)	0.250	2.0 (4)
P1	0.102 (3)	0.634 (1)	0.310 (9)	2.2 (2)

Final fit parameters: R (F^2)= 0.0649 R_{wp} =0.1644, R_p = 0.1161

The structure generated from the Rietveld analysis, Figure 4-2, contains layers of diphosphate tetrahedra and copper square planar centres with Li cations occupying the space between the layers. These layers run along the *b*- and *c*-axis, which are separated by approximately 3 Å. The work performed in Chapter 3 on the iron fluorophosphates suggests the average terminal P-X distance is 1.495 Å (X = O) to 1.564 Å (X = F, OH). The terminal P-O bonds in Compound 1 are 1.45 Å, indicating a 2^- charge; this terminal site is stabilised by bonding with two Li cations.

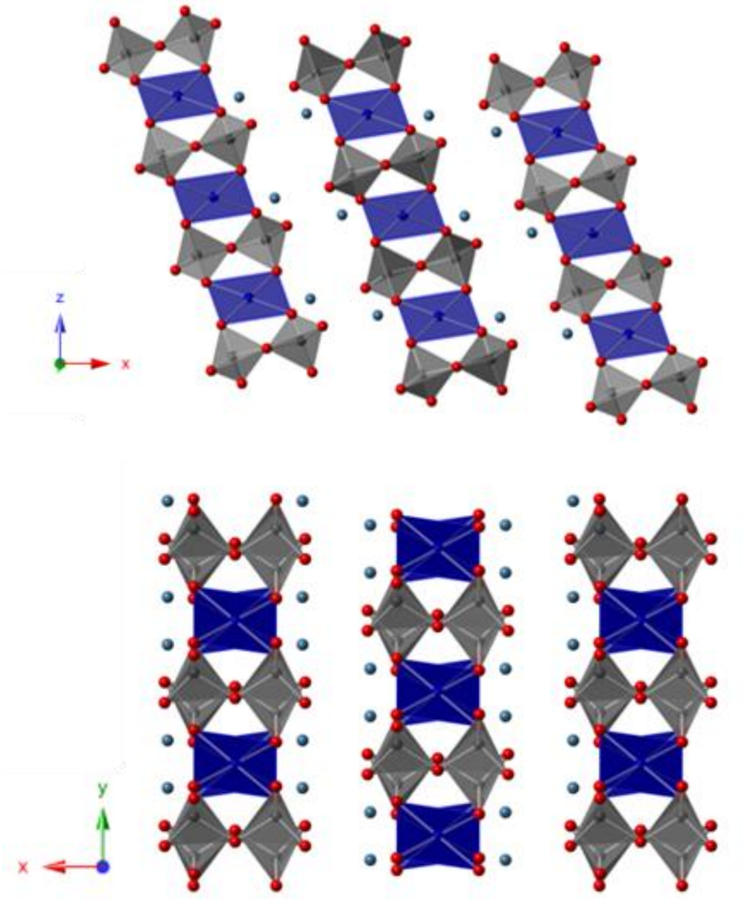

(a)

(b)

Figure 4-2 - View of compound 1 along the: (a) b-axis and the (b) c-axis. Cu polyhedra are dark blue, P tetrahedra are grey, O atoms are red spheres and Li cations are turquoise spheres

Table 4.2 - Bond lengths and angles around copper centres in Compound 1 generated from the Rietveld analysis

Bond	Bond length (Å)	Bond angle	Angle (°)
2x Cu1-O1	1.948 (5)	O1-Cu1-O1	180
2x Cu1-O2	1.967 (5)	O1-Cu1-O2	95.67 (2)
		O1-Cu1-O2	84.33 (2)
		O2-Cu1-O2	180

The copper centre in compound 1 is situated in an almost perfect square planar geometry (Table 4.2). The absorbance spectrum of compound 1 (Figure 4-3) produces a broad asymmetric peak from 500-1500 nm, with a weak maximum centred on 720 nm. The $e_g \rightarrow b_{1g}$ and $a_{1g} \rightarrow b_{1g}$ transitions will have the highest energy; so therefore will be related to the strong absorbance within the visible region. The minor distortion around the equatorial plane of the copper centre will slightly stabilise the $d_{x^2-y^2}$ and destabilise the d_{xy}, making the energy between these levels very small: therefore, the b_{2g} and b_{1g} energy levels could be considered degenerate (Figure 4-4). Further splitting of these levels may occur, often too subtle to be described, and account for the broadening of the band. The presence of a centre of symmetry within the copper coordination indicates the *d-d* transitions are inhibited by the Laporte selection rule. This will significantly reduce the intensity of the bands produced compared to other copper geometries. However due to the distortion of the square planar geometry in compound **I** the Laporte selection rule will be minimised.

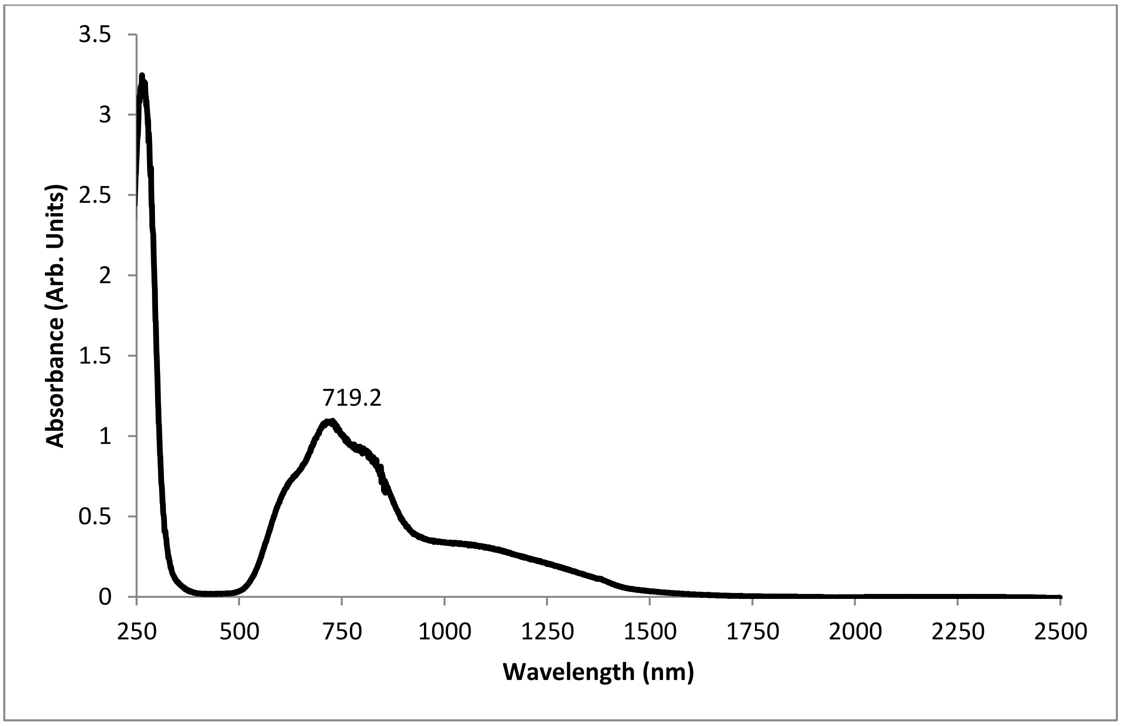

Figure 4-3 - UV/Vis/NIR absorbance spectrum for compound 1

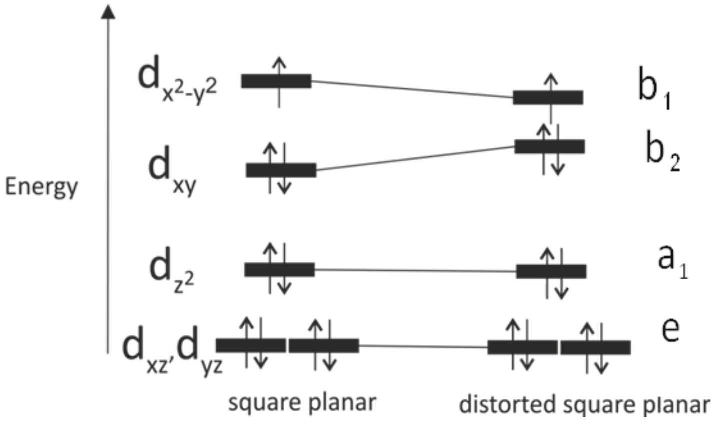

Figure 4-4 - Energy level diagram for copper centre in compound 1

Compound 2 - $CuAl_2O_4$

A powder sample of compound 2 was synthesised by adding stoichiometric amounts of CuO and Al_2O_3 starting materials, which were ground in a pestle and mortar and sealed in a glass tube under vacuum.[165] The sealed glass tube was heated to 850 °C for five days, and this heating procedure in the sealed tube was repeated several times to try to form a pure phase.

Copper (II) in tetrahedral coordination within spinel structures can lead to a reduction of symmetry from $Fd\bar{3}m$ to a tetragonal derivative of the spinel structure ($I4_1/amd$), in which there is a considerable flattening of the copper tetrahedra along the *c*-axis.[166] However, a comparison of the powder-XRD pattern of compound 2 to the ICSD database indicated the cubic spinel was formed, which contains copper located in a perfect tetrahedral site.[167] The resulting atomic coordinates, temperature factors and refinement parameters are shown in Table 4.3, and the Rietveld refinement fit profile is provided in Figure 4-5. The preferred orientation was modelled using the March-Dollase method with a ratio of 0.696 for the (002) plane and 2.108 for the (113) plane. Rietveld parameters with no associated error were fixed to stabilise the refinement.

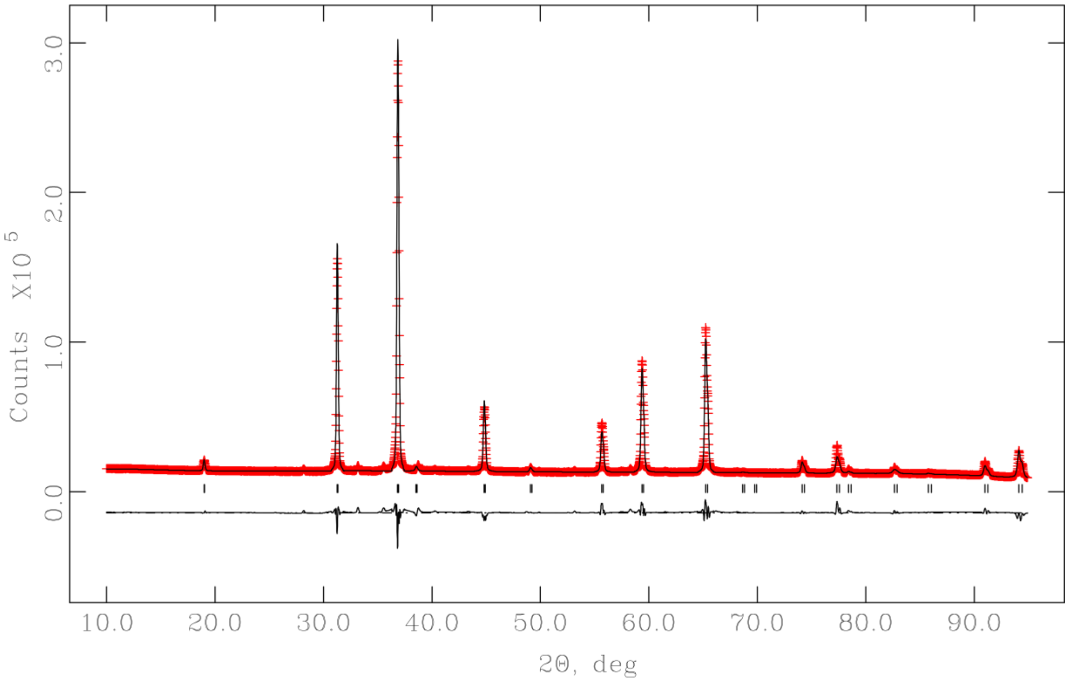

Figure 4-5 - Rietveld refinement fit profile of compound 2. Observed data points are shown as red crosses and the calculated pattern as a solid black line. The difference between the calculated and observed pattern is shown underneath. The position of the peaks are indicated by rows of vertical lines

Table 4.3 - Atomic coordinates and temperature factors for Compound 2 generated from Rietveld analysis

Space group: $Fd\bar{3}m$

Lattice parameters a = b = c = 8.081 (1) Å, α = β = γ = 90°

Atom site	*x*	*y*	*z*	U_{iso} x 10^2 ($Å^2$)	Site occupancy
Al2	0.500	0.500	0.500	5.6 (5)	0.688 (1)
Cu2	0.500	0.500	0.500	5.6 (5)	0.019 (1)
Cu1	0.125	0.125	0.125	3.6 (4)	0.620 (1)
Al1	0.125	0.125	0.125	3.6 (4)	0.204 (1)
O1	0.257	0.257	0.257	2.3 (5)	0.895 (4)

Final fit parameters: R (F^2) = 0.0744 R_{wp} = 0.0456, R_p = 0.0289

It is well-known that the AB_2O_4 spinel structure can be viewed as a cubic close-packed array of anions, in which one-eighth of the tetrahedral and one-half of the octahedral sites are occupied by the cations (Figure 4-6). In this structure, a wide range of cation distributions among the available sites is possible, ranging from the so-called *normal* spinel, in which the A cations occupy the tetrahedral sites and the B cations the octahedral sites; to the ***inverse*** spinel, in which one-half of the B cations are in the tetrahedral sites, while the other half and the A cations share the octahedral sites. The refinement of compound 2 indicates that copper is located on both octahedral and tetrahedral sites (Table 4.3) and can therefore be described as having an inverse spinel structure. Both of these geometries are rare for copper compounds because there is no sign of JT distortion around the metal centre (Table 4.4).

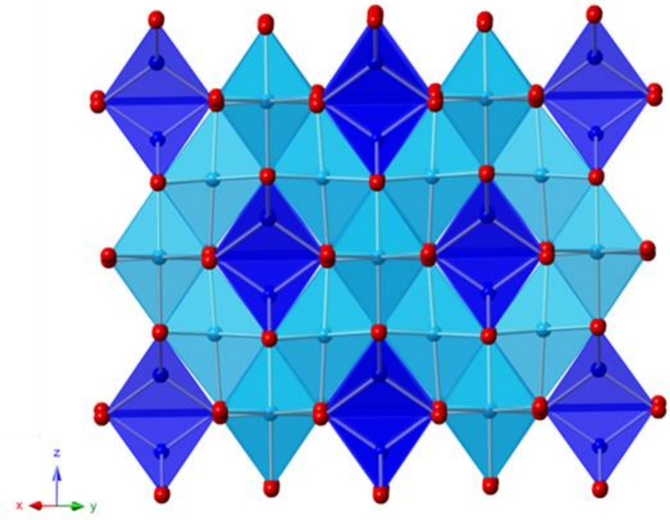

Figure 4-6 - Structure of Compound 2 viewed along the (-1-10) plane. Cu tetrahedra in dark blue, Al octahedra in light blue and O atoms are red spheres

Table 4.4 - Bond lengths and angles around copper centres in Compound 2 generated from the Rietveld analysis

Bond	Bond length (Å)	Bond angle	Angle (°)
6x Cu2-O1	1.944 (1)	2x O1-Cu2-O1	85.1 (0)
		4x O1-Cu2-O1	94.9 (0)
		2x O1-Cu2-O1	180.0
4x Cu1-O1	1.891 (9)	4x O1-Cu1-O1	109.4 (2)

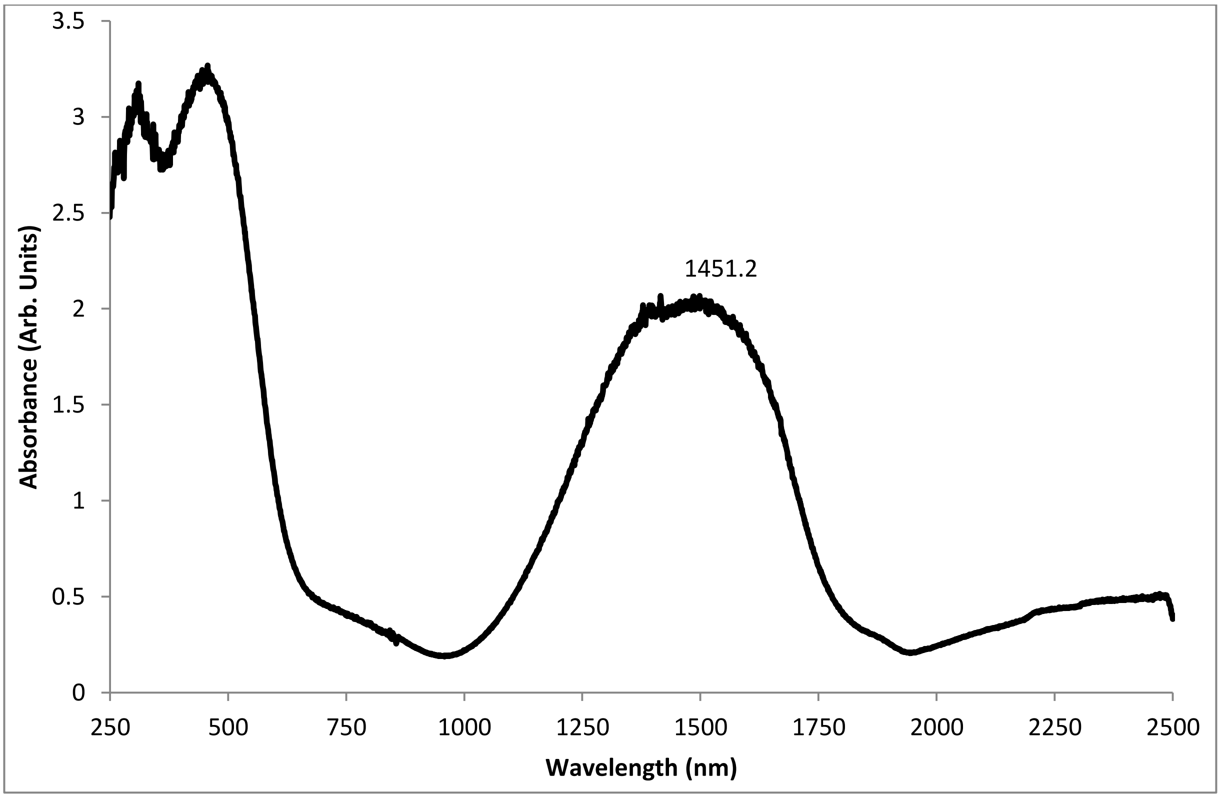

Figure 4-7 - UV/Vis/NIR spectrum for Compound 2

Compound 2 is an intense red-coloured compound due to the charge transfer band from LMCT and IVCT band at 500 nm; the broad band centred on 1451 nm is due to the $t_2 \rightarrow e$ transition from the copper located on the tetrahedral site (Figure 4-7). The refinement would suggest that there is a mixture of copper on both octahedral and tetrahedral sites. The transition around 650 nm arises from the $e_g \rightarrow t_{2g}$ transition from the octahedral site. This transition at 650 nm has been overlapped by the LMCT band.

Compound 3 and compound 4 - $K_2MP_2O_7$ (M=Cu and Fe)

Single crystals of $K_2FeP_2O_7$ (compound 3) were grown by heating a molar ratio 1:2:1 mixture of iron (II) oxalate dihydrate, diammonium hydrogenphosphate, $(NH_4)_2HPO_4$ and potassium carbonate. After grinding the reactants together, the mixture was heated in a tube furnace under a reductive atmosphere (5 % H_2 in N_2) to, initially, 300 °C for 12 hours. The sample was reground and then heated further under these conditions to a final temperature of 600 °C for 24 hours, and the molten solid was slowly cooled to room temperature. The product consisted of many, almost colourless, needle-shaped crystals. Semi-quantitative Energy-Dispersive X-ray Spectrometry (EDX), using a JEOL JSM 5910 SEM fitted with an Oxford Instruments Inca Energy 300 EDX analysis system, showed the presence of Fe, P and K in the crystals, with the atomic ratios of 1:2:2 (all ±0.1) in good agreement with the compound stoichiometry $K_2FeP_2O_7$. $K_2CuP_2O_7$ (compound 4) was synthesised using a solid state method by combining stoichiometric amounts of copper (II) oxide, diammonium hydrogenphosphate, $(NH_4)_2HPO_4$ and potassium carbonate. The finely-ground powder was placed into a box furnace and heated to 350 °C for 15 hours, reground and then heated to 650 °C for 60 hours, in air. Upon cooling, numerous tiny blue ellipse-shaped crystals were obtained; EDX analysis again confirmed the compound stoichiometry $K_2CuP_2O_7$. Polycrystalline bulk material of both $K_2CuP_2O_7$ and $K_2FeP_2O_7$ was obtained using the same procedure described above, but with faster cooling rates (2 °C/min). Phase purity was confirmed from powder X-ray diffraction data, with a minor $(KPO_3)_n$ impurity phase present in both $K_2MP_2O_7$ (M=Fe and Cu) phases. The impurity peaks in the $K_2MP_2O_7$ samples led to difficulties during the refinement (Figure 4-8 and Table 4.6).
The trial structural used in the refinement was grown from melts and solved in this PhD producing large needle and blue ellipsoid crystals for iron and copper respectively; the crystallographic data is shown in Table 4.5.

Table 4.5 - Single crystal structure refinements data for $K_2MP_2O_7$, M=Fe, Cu)

Empirical formula	$K_2FeP_2O_7$	$K_2CuP_2O_7$
Formula weight / gmol^{-1}	307.99	315.69
Temperature / K	100(2)	100(2)
Wavelength / Å	0.71073	0.71073
Crystal system	Tetragonal	Tetragonal
Space group	$P\text{-}42_1m$	$P\text{-}42_1m$
Unit cell dimensions /Å	$a = b$ = 8.092(2) c = 5.496 (2)	$a = b$ = 8.056(2) c = 5.460 (11)
Unit cell volume / Å^3 , Z	359.9(3), 2	354.35 (15), 2
Density (calculated) / gcm^{-3}	2.842	2.959
Absorption coefficient / mm^{-1}	3.689	4.7
F(000)	300	284
Crystal size / mm	0.2 x 0.1 x 0.04	0.02 x 0.01 x 0.01
Goodness-of-fit on F^2	0.956	0.919
Final R indices [(I>2σ(I)]	R1=0.0293, wR2=0.0697	R1=0.0267, wR2=0.0603
R indices (all data)	R1=0.0339, wR2=0.0712	R1=0.0345, wR2=0.0629

Table 4.6 - Atomic coordinates for $K_2MP_2O_7$, M = Fe, Cu produced from the Rietveld analysis.

Atom	x	y	z	10^2x U_{eq}/Å^2
$K_2FeP_2O_7$				
K	0.329 (7)	0.171 (7)	-0.490 (2)	3.3 (4)
Fe	0.0	0.0	0.0	1.2 (3)
P	0.131 (2)	0.639 (2)	-0.069 (4)	5.4 (11)
O1	0.5	0.0	-1.142 (6)	1.8 (12)
O2	0.082 (2)	0.208 (2)	-0.180 (2)	3.3 (6)
O3	0.129 (3)	0.371 (3)	-0.868 (5)	2.5
$K_2CuP_2O_7$				
K	0.334 (8)	0.165 (8)	0.491(3)	7.3 (5)
Cu	0.0	0.0	0.0	6.4 (5)
P	0.633(11)	0.133(11)	0.978(3)	5.9 (8)
O1	0.5	0.0	0.873(11)	6.5 (5)
O2	0.204(4)	0.922(3)	0.856(5)	6.7 (6)
O3	0.635(3)	0.135(3)	0.251(7)	9.9(9)

Final fit parameters: (M = Fe) : R(F^2)= 0.0947, R_{wp} = 0.1743, R_p = 0.1252 and (M = Cu) : R(F2) = 0.1663, R_{wp} = 0.2902, R_p = 0.2109

The poor refinement reliability values have led to using the collected single crystal data for the metal center geometry and further analysis. The Rietveld analysis does confirm that the bulk phase produced is similar to the single crystals grown for compound 3 and compound 4.

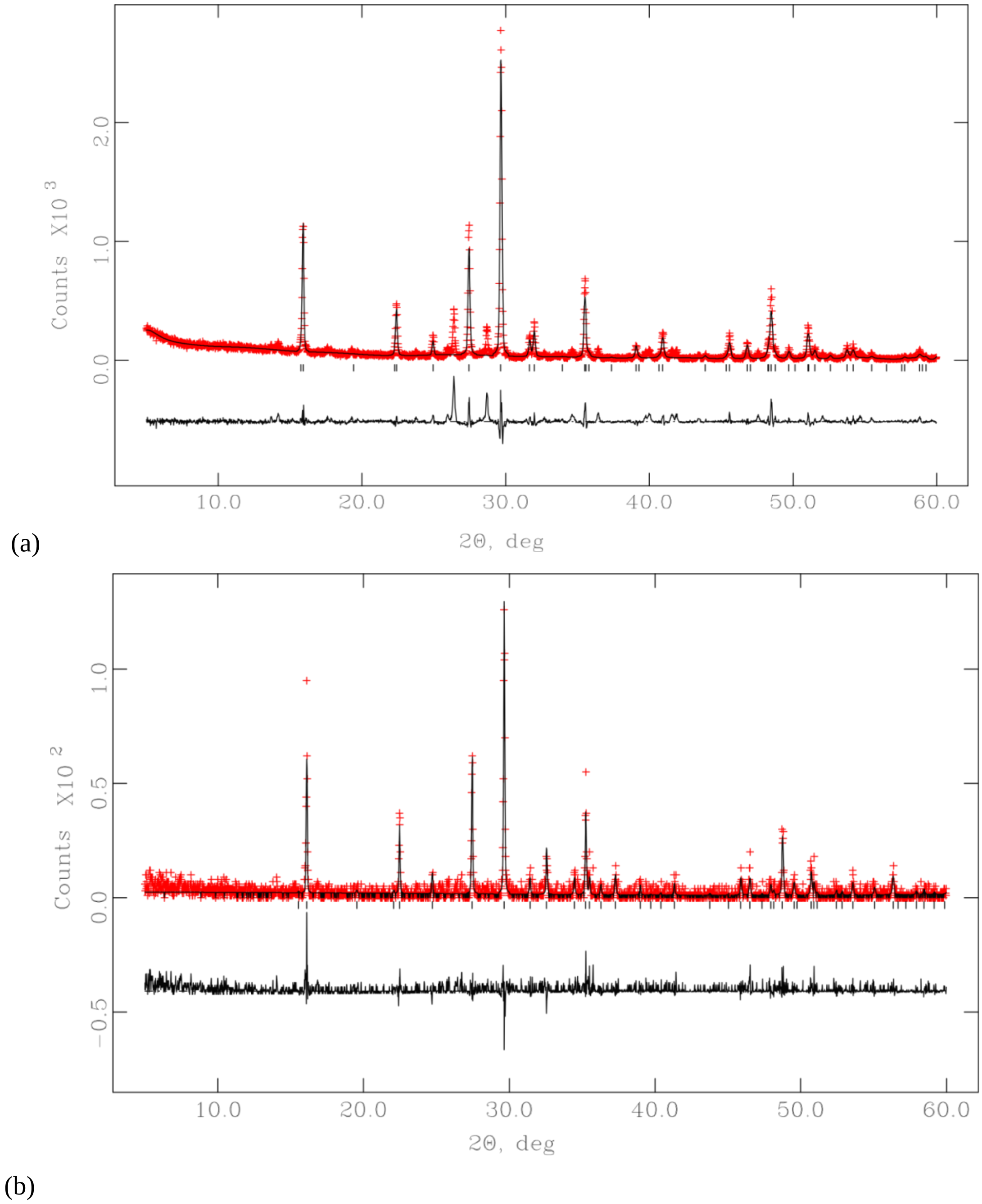

Figure 4-8 - Rietveld refinement of (a) $K_2FeP_2O_7$ and (b) $K_2CuP_2O_7$. Observed data points shown as red crosses, and the calculated pattern is shown as a solid black line. The difference between the observed and calculated pattern is shown underneath. The positions of the peaks are marked by the row of vertical lines.

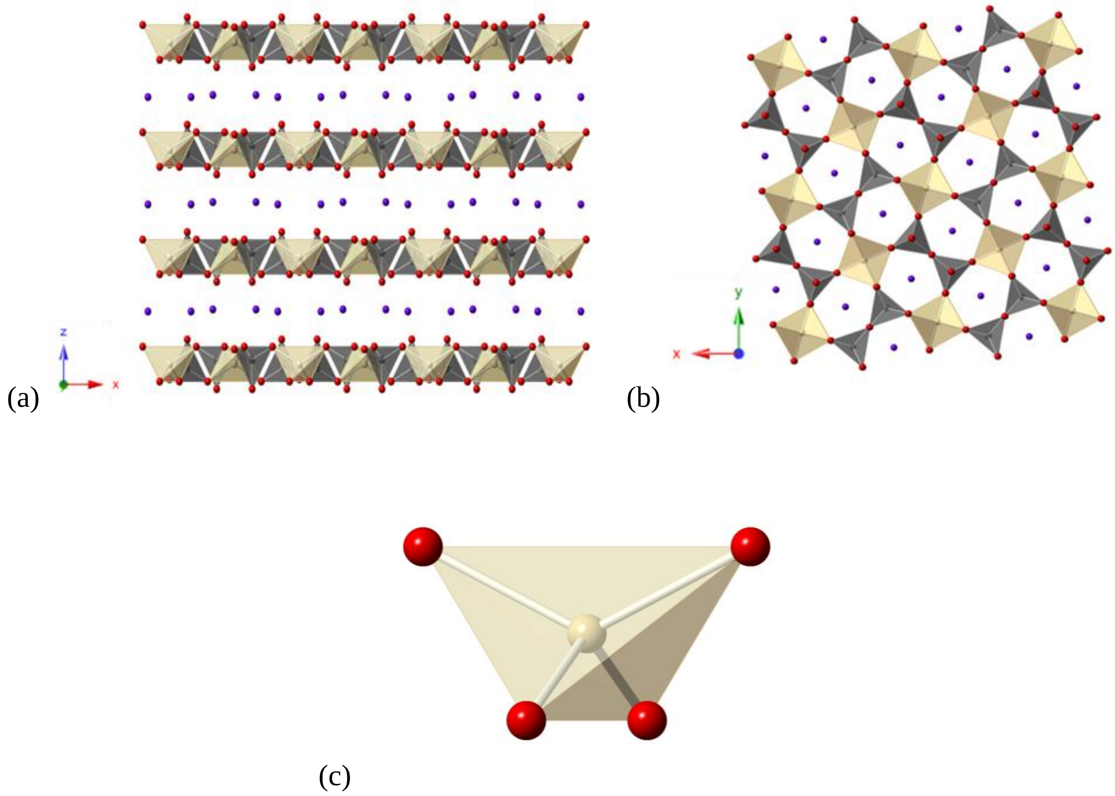

Figure 4-9 - Structure of compound 3 viewed along the (a) b-axis and the (b) c-axis. (c) Iron and copper geometries in compound 3 and 4. M polyhedra in cream, P tetrahedra in grey, O atoms are red spheres and K cations are purple spheres.

Figure 4-9 shows the structure when viewed perpendicular to the *c*-axis, showing the layer-like nature of the structure adopted; each layer consists of flattened MO_4 tetrahedra linked by interconnecting diphosphate groups, $P_2O_7^{4-}$, which form an infinite sheet of connected five-membered rings in the *ab*-plane (Figure 4-9). Potassium ions are located above and below the sheets in a narrow channel, of diameter ~ 4 Å, created by alignment of the five-membered rings in adjacent sheets.

Table 4.7 - Selected bond lengths (Å) and angles (°) for $K_2MP_2O_7$, M = Fe, Cu generated from the single crystal data.

Bond / Angle	*M = Fe*	*M = Cu*
4 x M-O	1.993(2)	1.930(3)
2x O-M-O	101.62(6)	99.47(6)
2x O-M-O	126.66(15)	132.14(17)

The metal centre (Figure 4-9 and Table 4.7) can be described as an intermediate geometry between tetrahedral and square planar, and having D_{2d} symmetry. The crystal field-splitting diagram for this distorted D_{2d} symmetry is given in Figure 4.11.

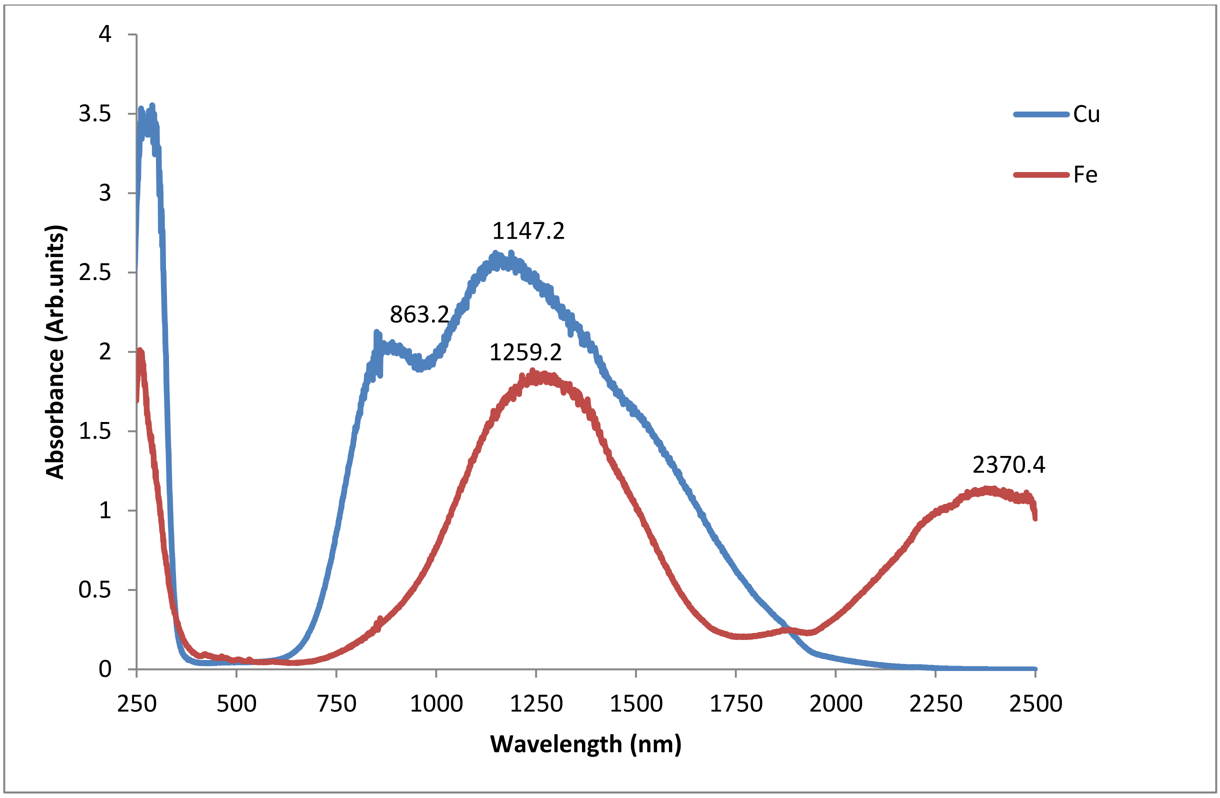

Figure 4-10- Absorbance spectrum for $K_2MP_2O_7$- (M=Fe and Cu)

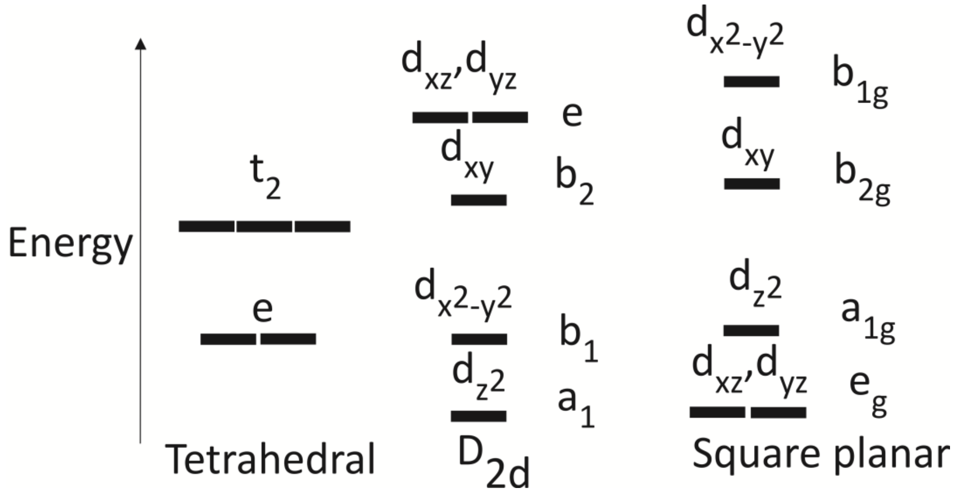

Figure 4-11 - Energy level diagram for D_{2d} symmetry

The absorbance spectra of compound 3 and compound 4 are provided in Figure 4-100. The spectrum of $K_2CuP_2O_7$, (blue plot), has three broad overlapping absorbance bands located at 863, 1147 and 1475 nm, which can be assigned to the three possible $a_1 \rightarrow e$, $b_1 \rightarrow e$, $b_2 \rightarrow e$ spin-allowed, electronic transitions respectively. The two absorbance peaks in the iron compound spectrum, (red plot), located at 1260 nm and weak associated shoulder at near 1450 nm, and 2370 nm, are likely to arise from $a_1 \rightarrow e$, b_2 and $a_1 \rightarrow b_1$ electronic transitions, respectively. The start of the absorbance peak for $K_2CuP_2O_7$ is slightly in the visible region, and is responsible for the pale blue colour of this compound, whereas the iron compound is completely colourless depending on the levels of KPO_3 impurity.

Structural summary

The optical spectra of Egyptian Blue, ($CaCuSi_4O_{12}$)[168], which has a strictly square-coplanar stereochemistry, contains a large maximum at 633 nm with a small shoulders at 532 and780 nm; this is blue-shifted by approximately 100 nm compared to the transitions observed in Compound 1. A similar absorbance to Compound 1 spectrum is reported for $Cs_2Cu_3P_4O_{14}$.[123] The differences between the charge, ionic radii and bonding strength of the silicate and phosphate donor ligands cause a change in the Cu-O bond lengths, which have a significant effect on the position of ΔE (Equation 1.2). The Cu-O bonds for Egyptian Blue are shorter (1.910 Å) compared to Compound 1 (1.956 Å) and $Cs_2Cu_3P_4O_{14}$ (1.946 Å).This decrease in Cu-O bond length will cause the absorbance maxima to shift to shorter/higher energy wavelengths. The absorbance spectrum of the square planar iron silicate mineral gillispite contains a strong, sharp maximum at 500 nm.[169]

Examples of non-distorted copper tetrahedral compounds are rare but occur more commonly in compressed tetrahedral (D_{2d}) geometries as seen in Compound 4. The cubic spinel structures, as reported in Compound 2, have undergone a tetragonal distortion with higher doping levels of copper in $CuAl_2O_4$, $CuCr_2O_4$ and $CuRh_2O_4$ spinel.[170] It was found from these studies that the required level doping on the tetrahedral site to cause this distortion was 0.667, in $CuAl_2O_4$. The doping level of Cu on the tetrahedral site in compound 2 is 0.597, which is below the required amount to induce tetragonal distortions. Previous work performed on copper-doped ZnO systems showed that copper adopts a perfect tetrahedral geometry.[171] The absorbance maximum at 1500 nm for this series of compounds was found to increase with higher copper doping levels. The position of this absorbance maximum is in good agreement with the observed data collected for compound 2 (1451 nm).The absorption spectrum has been reported for a range of spinel materials ($Fe,MgAl_2O_4$) that contain varying levels of Fe (II) on the tetrahedral site.[169] The absorbance spectra of these materials contain maxima at 2100 and 2720 nm, where the intensity of these peaks is linearly related to the amount of Fe content. The M-O bond lengths are slightly longer (1.917 Å) than observed for the copper spinel structure (1.891 Å), which can explain the red shift of the iron spinel compared to the copper.

$K_2MP_2O_7$ (M= Fe, Cu) provided an example of metal centres coordinated in compressed tetrahedral geometries - these materials are structurally related to $Na_2CoP_2O_7$ [172]; divalent high spin cobalt 2+ ion (d^7) would not be expected to demonstrate a Jahn-Teller (JT) effect, and the degree of distortion observed in $Na_2CoP_2O_7$ is correspondingly small. For Fe (II) the high spin d^6 ($e^3t_2^3$) electronic configuration would be expected to undergo a strong JT distortion, splitting the e levels and stabilizing the structure. For Cu (II), d^9 high spin and no distortion of the tetrahedron would be expected on purely first-order JT considerations with its $e^4t_2^5$ configuration. However, this coordination geometry for Cu^{2+} is known to distort strongly to a flattened tetrahedron due to the involvement of the 4s and 4p orbitals in the HOMO of the molecular orbital diagram, though this flattening will be further reinforced by second order JT effects[114]. The coordination around $K_2FeP_2O_7$ has tetrahedral angles ranging between 101 and 126°, and the copper environment in $K_2CuP_2O_7$ is very strongly distorted (O-M-O angles ranging from 99 to 132°) and even more distorted in $RbCuPO_4$ (95 to132°). Indeed the geometry around copper is almost midway between tetrahedral and the more commonly found square planar coordination found for this d^9 species. The distortion of the metal tetrahedron can be quantified by calculating the root mean square deviation:

$$\sqrt{\frac{1}{n}\sum_{i=0}^{n}(\theta_i-\theta_o)^2}$$

where θ_i is the measured bond angle and θ_o is 109.4°, the bond angle in a perfect tetrahedron. These values are respectively 11.8°, 15.4° and 18.5° for the iron, copper and $RbCuPO_4$ compounds. These distortions are much higher than the one calculated for the $NaCoP_2O_7$ structure (3.8°), which is not surprising when considering the JT distortion effects described above.

The optical properties of these materials are radically different; the absorbance spectrum in $RbCuPO_4$ contains a maximum at 610 nm and gives rise to the observed sky blue colour[114] - this maximum is more consistent with the values previously seen in the square planar compounds, whereas the absorbance spectrum for $K_2CuP_2O_7$ has broad absorbance maximum centred on 1147 nm. The degree of distortion away from tetrahedral in $RbCuPO_4$ is not significant enough to completely change the energy level diagram of this material. However, exanimation of the bond lengths around the metal give a clearer explanation to the significant shift in absorbance maximum. In $RbCuPO_4$ the bond lengths around the metal centre range from 1.89-1.95 Å, compared to 1.941 Å in $K_2CuP_2O_7$. The shortest bond length in $RbCuPO_4$ is similar to the bond lengths seen previously in Egyptian Blue (1.91 Å). Therefore bond lengths play an important role in the position of absorbance maxima.

Iron silicate minerals staurolite ($Fe_4Al_{18}Si_8O_{46}(OH)_2$)[173] and pellyite ($Ba_2Ca(Fe,Mg)_2Si_6O_{17}$)[174] both contain Fe (II) in distorted iron tetrahedral geometries. The absorbance spectrum of staurolite contains absorbance maxima at 1821 and 2564 nm, and the observed spectrum for pellyite contains maxima at 1353 and 1718 nm.[169] These values are significantly different compared to the UV/Vis/NIR spectrum of $K_2FeP_2O_7$ (1259 and 2370 nm). A comparison between the bond lengths and angles around the metal centre does not provide an indication to the large discrepancies observed in the position of the absorbance maxima. In pellyite the Fe (II) tetrahedron is highly flattened (O-M-O angles from 90-134 °) and contains bond lengths ranging from 1.94-2.07 Å; this would suggest pellyite should be blue-shifted compared to $K_2FeP_2O_7$. Staurolite contains the least-distorted tetrahedra (O-M-O angles from 104-113 °) with bond lengths ranging from 1.97-2.05 Å.

4.2 Five-coordinate structures

There are two main geometries that allow for five-coordinate environments, trigonal bipyramidal and square pyramidal. The energy difference between these two geometries can be very small and lead to complexes that can switch between the two geometries. A classic example of this phenomenon was first recorded in 1960, and has been dubbed a Berry twist mechanism.[175] This Berry twist mechanism has been observed in five-coordinate copper complexes and normally results in geometries that are intermediate between square pyramidal and trigonal bipyramidal.[176]

Trigonal bipyramidal geometries are frequently found in iron phosphates.[73, 88] Most of these materials contain mixed-valence iron centres that are linked to form clusters. $(C_4H_{11}N_2)_{0.5}$-$[Fe_3(HPO_4)_2(PO_4)(H_2O)]$ has a layered structure with monoprotonated piperazinium cations in the interlayer space.[177] The basic building unit of each layer is a hexamer, which is composed of two FeO_6 octahedra and four FeO_5 trigonal bipyramids. Mossbauer and bond valance calculations indicate that Fe (II) is located on the trigonal bipyramidal sites. The iron phosphate mineral, Graftonite $[(Fe,Mn, Ca, Mg)_3 (PO_4)_2]$, contains one six and two distorted five-coordinate trigonal bipyramidal sites.[178] It has been reported in the literature that it is possible to substitute other transition metals on the five-coordinate site such as Ni[179], Co[180] and Zn.[181]

Copper chemistry is dominated by five-coordinate structures, particularly square pyramidal geometries[103], with fewer examples of copper coordinated in trigonal bipyramidal geometries.

A range of five-coordinate copper materials have been synthesised by Boukhari *et al* [182]: this work involved the synthesis of $BCu_2P_2O_7$ (B = Mg, Ca, Sr and Ba) compounds. The Ca, Sr and Ba materials contain distorted CuO_5 square pyramidal environments connected by diphosphate units (P_2O_7). The variation in the size of the B cation influences the structural type; the larger Ba cation causes the structure to become 2D layered, whereas the smaller Ca and Sr cations are located in pores created by five-membered rings within a 3D framework. $SrFeP_2O_7$ is isostructural with the Ca and Sr copper diphosphates, and contains FeO_5 square pyramids.[183]

A series of copper sulphate and phosphate frameworks have been synthesised, and the UV/Vis/NIR spectra of the materials have been obtained. Unfortunately the only five-coordinate structure synthesised containing iron was the pure iron end member of graftonite, $Fe_3(PO_4)_2$. The material produced was poorly crystalline, and the Rietveld refinement of this material could not be obtained.

Compound 5 - $NaCuPO_4$

$NaCuPO_4$ (compound 5) was synthesised by grinding stoichiometric amounts of Na_3PO_4 and $Cu_3(PO_4)_2$ in a pestle and mortar before transferring to a box furnace, and heating the mixture at 750 °C for 48 hours with a heating rate of 2 °C /min. Several cycles were necessary to obtain a pure powder. $Cu_3(PO_4)_2$ was synthesised by grinding together CuO and $(NH_4)_2HPO_4$ and heating the mixture slowly (a rate of 0.5 °C/min) to 450 °C. The mixture was reground and heated up to 900 °C for 48 hours. The resulting powder was allowed to cool in air and then homogenised with a pestle and mortar.

$NaCuPO_4$ can crystallise into two different polymorphs: the low-pressure α-polymorph and the high pressure β-polymorph. The high pressure β-polymorph was synthesised by Kawahara *et al* in 1993.[184] This structure crystallises in the monoclinic space group of $P2_1/n$ and contains two copper geometries - CuO_6 Jahn-Teller distorted octahedra and CuO_4 square planar. The low temperature α- polymorph was described by Quarton *et al* in 1983 and crystallises in the orthorhombic space group, $P2_12_12_1$.[185]

The resulting powder X-ray diffraction pattern was compared to the ICSD powder database, which indicated the low-pressure α-polymorph was formed. Therefore the initial model used during the Rietveld refinement was the orthorhombic model from Quarton *et al.*[185] The resulting atomic coordinates, temperature factors and refinement parameters are shown in Table 4.8.

The Rietveld refinement fit profile is provided in Figure 4-12, where the 2-10 2Θ values have been excluded from the analysis due to a large noise edge caused by the attached air-scattering screen. Refinement parameters which have no associated error have been fixed due to poor stability during the refinement.

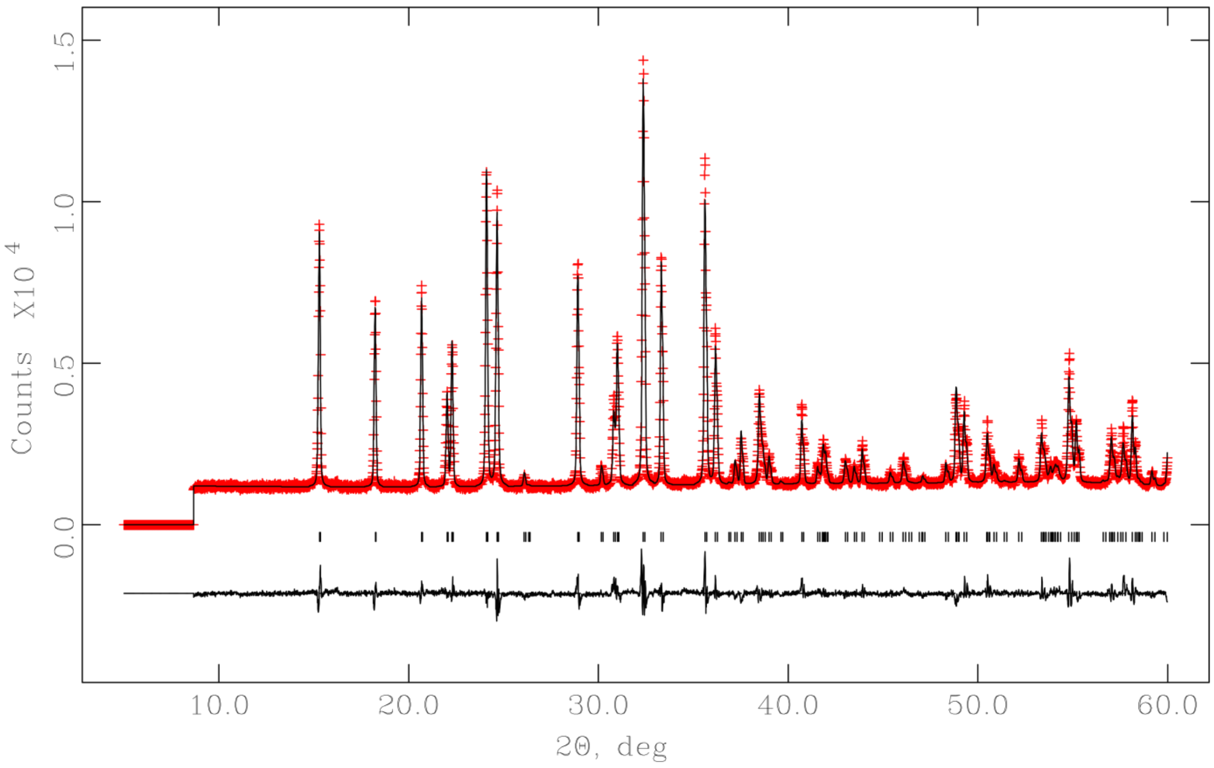

Figure 4-12 - Rietveld refinement fit profile of compound 5. Observed data points are shown as red crosses and the calculated pattern as a solid black line. The difference between the calculated and observed pattern is shown underneath. The position of the peaks are indicated by rows of vertical lines.

Table 4.8 - Atomic coordinates and temperature factors for Compound 5 generated from Rietveld analysis

Space group: $P2_12_12_1$

Lattice parameters a = 9.762 (2) Å, b = 4.799 (1) Å, c = 7.238 (2) Å, α = β = γ = 90°

Atom site	*X*	*y*	*Z*	U_{iso} x 10^2 (Å^2)
Cu1	0.540 (2)	0.496 (4)	0.934 (2)	3.5 (9)
Na1	0.686 (4)	0.035 (13)	0.230 (5)	0.8 (2)
O1	0.779 (8)	0.657 (10)	0.486 (13)	2.50
O2	0.540 (8)	0.693 (17)	0.389 (7)	3.0 (3)
O3	0.612 (6)	0.723 (13)	0.730 (13)	2.5 (4)
O4	0.622 (7)	0.252 (12)	0.532 (14)	0.9 (3)
P1	0.637 (4)	0.571 (8)	0.529 (7)	2.0 (2)

Final fit parameters: R(F^2) = 0.084, R_{wp} = 0.0517, R_p = 0.0385

The structure generated from the Rietveld analysis, Figure 4-13, consists of CuO_5 square pyramids and PO_4 tetrahedra, which are linked through edge and face-sharing vertices to form a 3D framework. This framework creates pores along the *b* and *c*-axes that are occupied by sodium cations, situated in a seven-coordinate pentagonal bipyramidal geometry. The copper centres are linked through axial μ^3-bridging oxygen atoms, forming zig-zag chains along the *b*-axis.

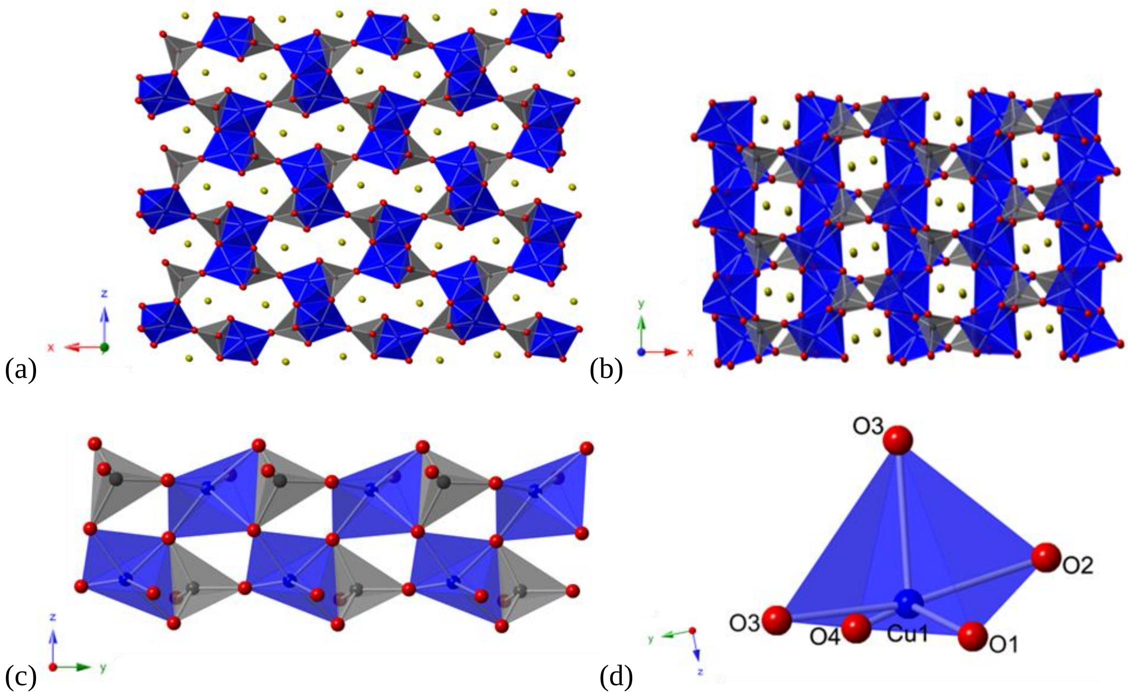

Figure 4-13 - Structure of compound 5 viewed along the (a) b-axis and (b) the c-axis. (c) Showing copper zig-zag chains and (d) highlighting the copper geometry in Compound 5. Cu polyhedra in dark blue, P tetrahedra in grey, Na cations are yellow spheres.

The UV/Vis/NIR spectrum of compound 5 is provided in Figure 4-14. The green colour of this compound gives rise to a broad absorbance across the visible region which extends into the NIR. To understand the transitions involved to create this absorbance spectrum further, a closer examination of the copper centre is required. The geometry of the copper centre can be seen in Figure 4-13, with Table 4.9 providing the bond lengths and angles.

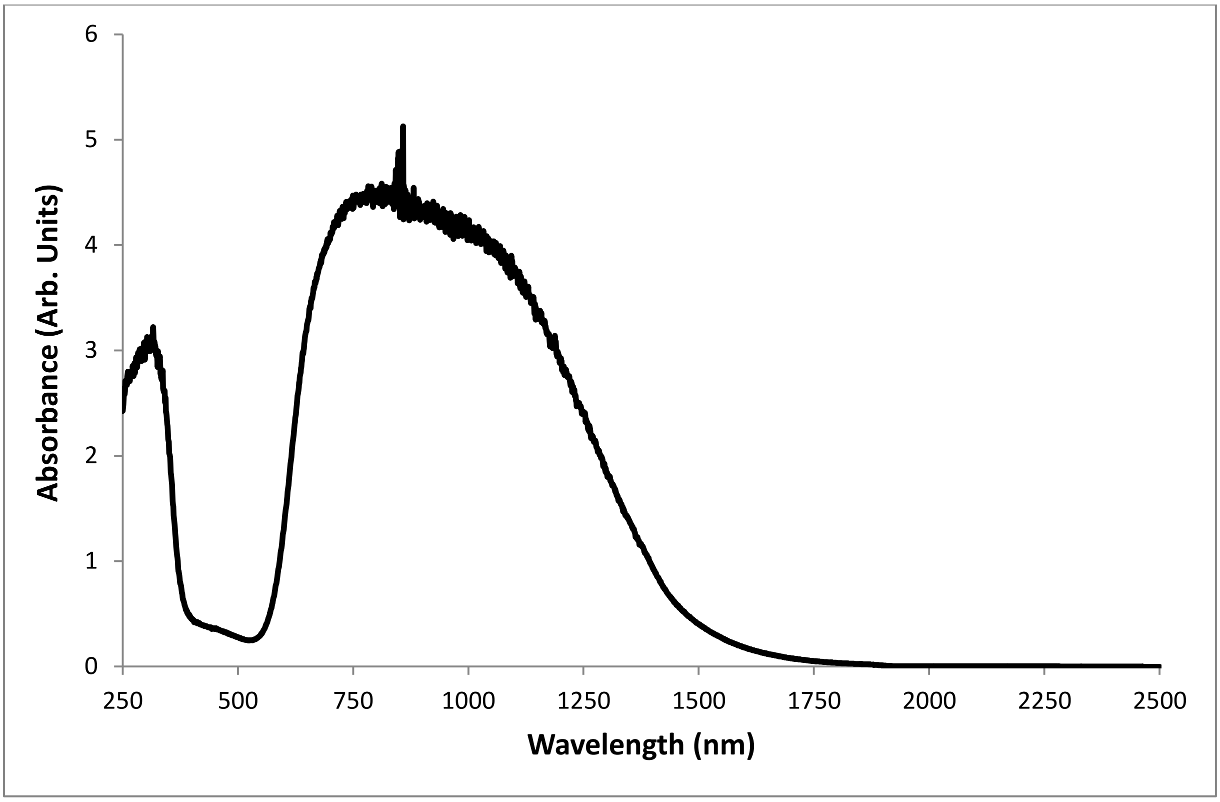

Figure 4-14 - UV/Vis/NIR spectrum of compound 5

Table 4.9 - Bond lengths and angles around copper centres in Compound 5generated from the Rietveld analysis.

Bond	Bond length (Å)	Bond angle	Angle (°)
Cu1-O1	1.950 (8)	O1-Cu1-O2	87.65 (28)
Cu1-O2	2.089 (7)	O1-Cu1-$O3_{eq}$	91.84 (25)
Cu1-O3 $_{equatorial}$	1.962 (8)	O1-Cu1-O4	156.50 (29)
Cu1-O3 $_{axial}$	2.310 (7)	O2-Cu1-$O3_{eq}$	168.38 (29)
Cu1-O4	2.024 (6)	O2-Cu1-O4	93.24 (27)
		$O3_{ax}$-Cu1-O4	91.85 (23)

From Figure 4-13 and Table 4.9 it is clear that there is a slight deviation away from ideal square pyramidal geometry. Due to the distortion around the axial and equatorial plane, this will cause stabilisation of the d_{z^2} and $d_{x^2-y^2}$ orbitals due to less ligand repulsion. These distortions will give rise to a new energy level diagram compared to an ideal square planar geometry (Figure 4-15). The larger broad absorbance is due to the overlapping electronic transitions that occur within the slightly-distorted square pyramidal geometry. The $e \rightarrow b_1$ transition will have the highest energy, and therefore will be related to the strong absorbance within the visible region. The $b_2 \rightarrow b_1$ and $a_1 \rightarrow b_1$ transitions are lower in energy and correspond to the absorbance observed in the NIR region. Further splitting of these levels may occur, often too subtle to be described, and account for the broadening of the band.

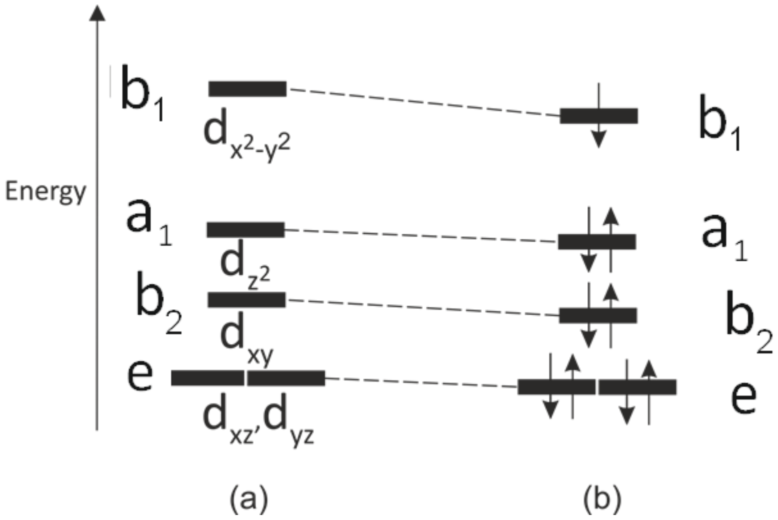

Figure 4-15 - Energy level diagram for (a) ideal square pyramid and (b) distorted square pyramidal in compound 5

Compound 6 - $Cu_2(SO_4)O$

Compound 6 was synthesised by dehydration and dimerization of $CuSO_4 \cdot 5H_2O$, which was performed by annealing at 750 °C for six hours in air with a heating and cooling rate of 2 °C/min. This unfortunately produced CuO as a minor impurity phases. This compound has been previously described by Effenberger[186] in the monoclinic *C*2/*m* space group, and the p-XRD pattern from the ICSD database matches the experimental pattern for this form, and therefore this monoclinic model was used during the Rietveld refinement. The resulting atomic coordinates, temperature factors and refinement parameters are shown in Table 4.10.

The Rietveld refinement fit profile is provided in Figure 4-16, where the 2-10 2Θ values have been excluded from the analysis due to a large background drift. Poor refinement values are due to an CuO and an unknown impurity phase.

Table 4.10 - Atomic coordinates and temperature factors for Compound 6 generated from Rietveld analysis

Space group: *C*2/*m*

Lattice parameters a = 9.347 (5) Å, b = 6.322 (3) Å, c = 7.642 (5) Å, α = γ = 90°, β = 122.34 (2)

Atom site	*x*	*Y*	*z*	U_{iso} x 10^2 (Å ^{2})
Cu1	0.250	0.250	0.000	4.6 (3)
Cu2	0.073 (8)	0.000	0.215 (1)	5.84 (3)
O1	0.210 (3)	0.500	0.224 (4)	7.9 (10)
O2	0.294 (3)	0.000	0.466 (3)	1.2 (9)
O3	0.160 (3)	0.000	0.021 (3)	2.6 (9)
O4	0.500 (1)	0.196 (2)	0.251 (2)	1.5 (5)
S1	0.100 (2)	0.500	0.316 (2)	2.3 (5)

Final fit parameters: $R(F^2)$=0.1466, R_{wp} =0.0743, R_p = 0.0459

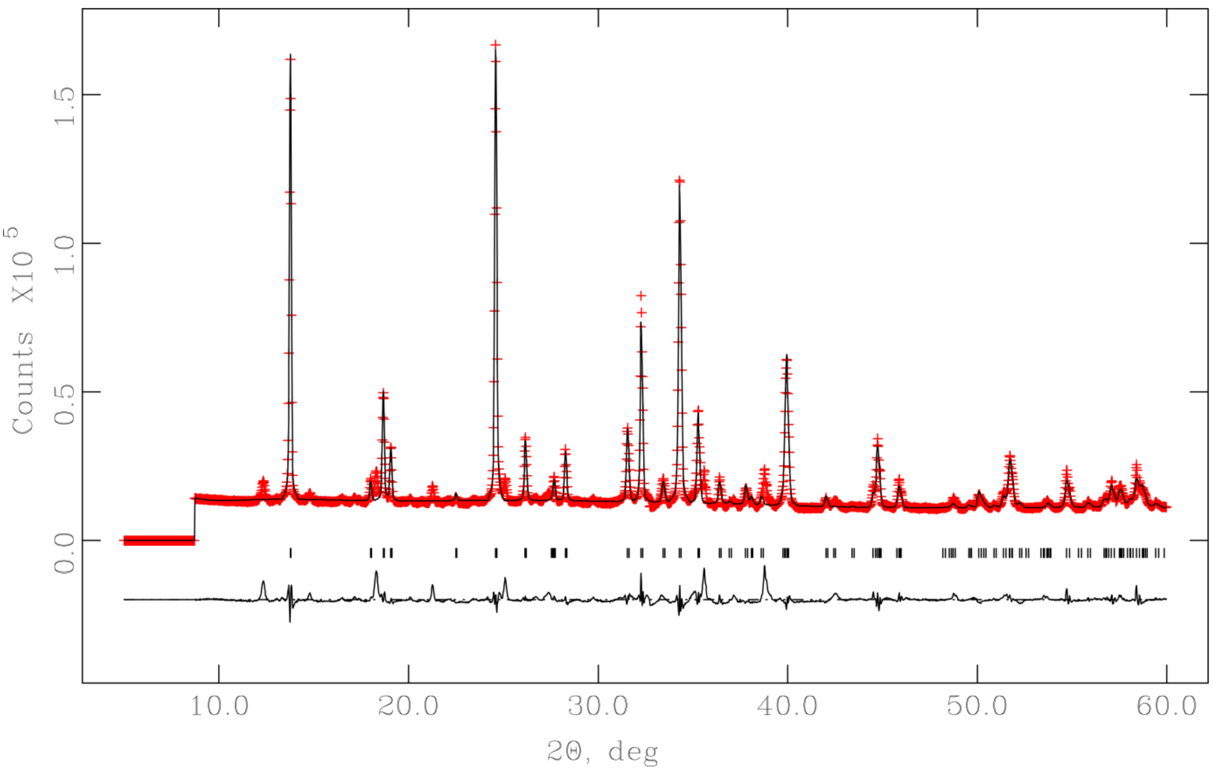

Figure 4-16 - Rietveld refinement fit profile of compound 6. Observed data points are shown as red crosses and the calculated pattern as a solid black line. The difference between the calculated and observed pattern is shown underneath. The position of the peaks are indicated by rows of vertical lines.

The structure of compound 6 generated from the Rietveld analysis contains layers of edge-sharing CuO_6 JT distorted octahedra and CuO_5 square pyramids, which are linked by SO_4 tetrahedra to form a dense 3D network (Figure 4-17).

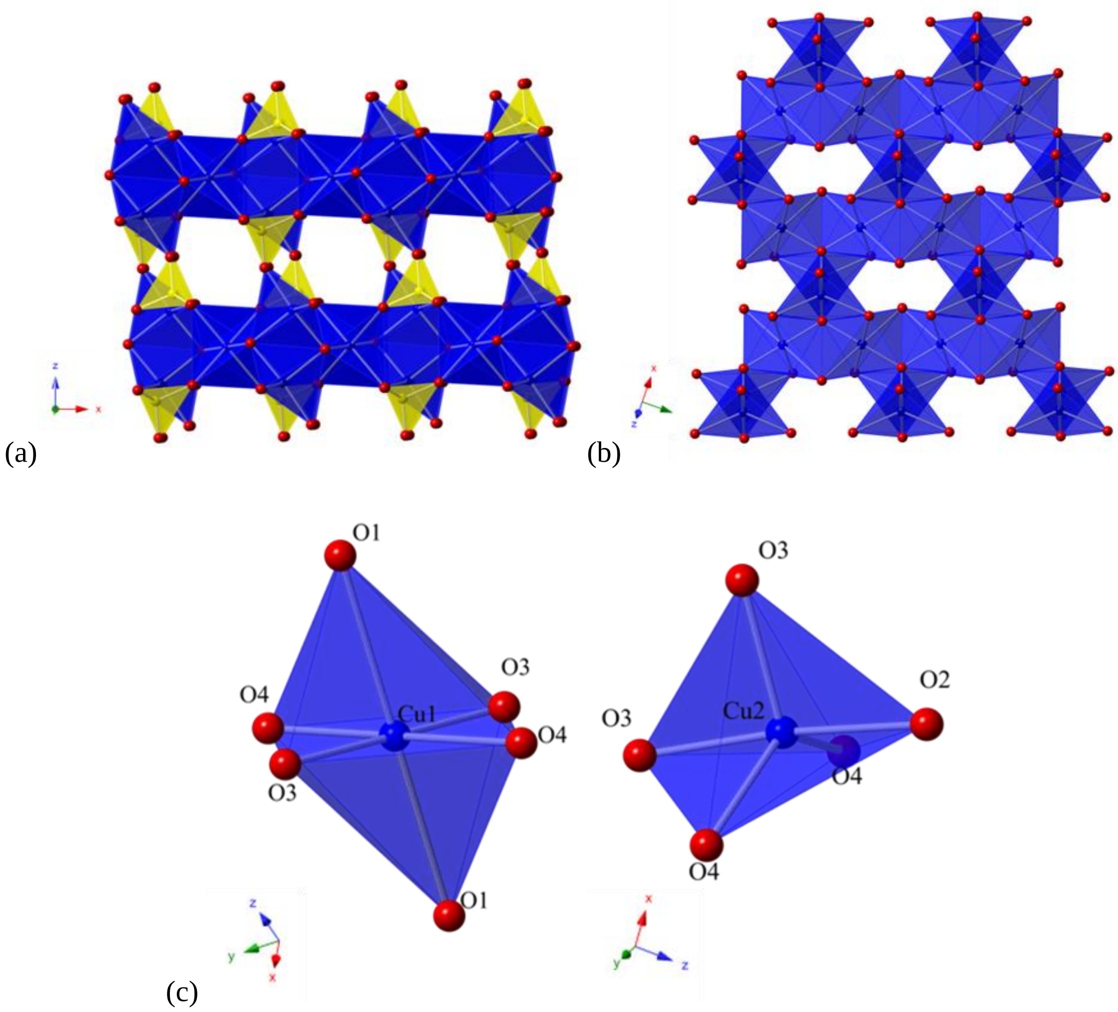

Figure 4-17 - Structure of Compound 6 viewed along (a) the b-axis (b) and the (102) plane. (c) Highlighting the copper centres. Cu polyhedra are dark blue, S tetrahedra in yellow and O atoms are red spheres.

The UV/Vis/NIR spectrum of compound 6 is provided in Figure 4-18. The mustard colour of this compound gives rise to a broad absorbance across the visible region, which extends into the NIR. To understand the transitions involved to create this absorbance spectrum further, a closer examination of the copper centre is required. The geometry of the copper centres can be seen in Figure 4-17, with Table 4.11 providing bond lengths and angles.

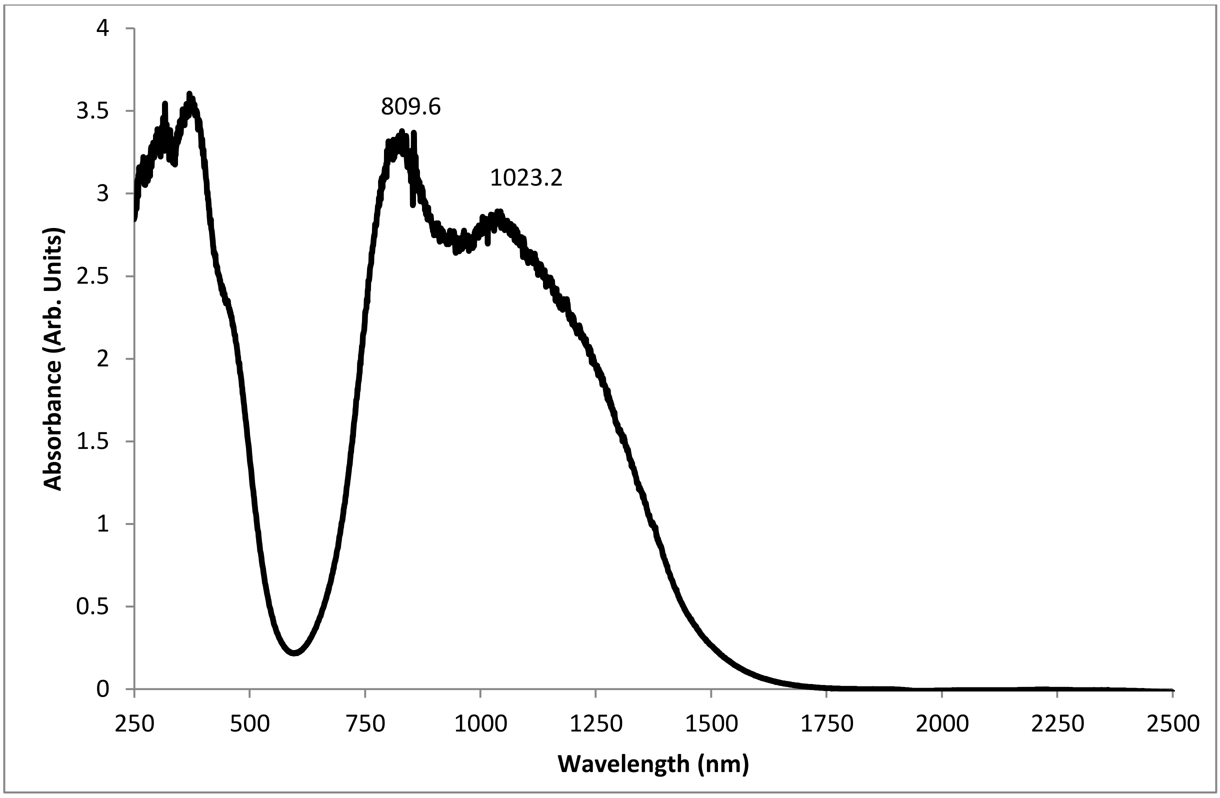

Figure 4-18 - 2UV/Vis/NIR absorbance spectrum for compound 6

Table 4.11 - Bond lengths and angles around copper centres in compound 6generated from the Rietveld analysis.

Bond	Bond length (Å)	Bond angle	Angle (°)
2x Cu1-O1	2.502 (19)	O3-Cu1-O3	180
2x Cu1-O3	1.838(10)	O4-Cu1-O4	180
2x Cu1-O4	2.118(11)	2x O3-Cu1-O4	96.9 (7)
		2x O3-Cu1-O4	83.1
		O1-Cu1-O4	83.1
Cu2-O2	1.928 (20)	O2-Cu2-O3	95.0 (10)
Cu2-O3	2.045 (16)	O2-Cu2-O3	174.3 (12)
Cu2-O3	1.950 (18)	2x O2-Cu2-O4	97.0 (5)
2xCu2-O4	2.108 (13)	O3-Cu2-O3	90.7 (10)
		2x O3-Cu2-O4	112.1 (4)
		2x O3-Cu2-O4	80.8 (4)
		O4-Cu2-O4	131.9 (8)

There are two different copper centres present in compound 6, which both give rise to absorbance peaks, as can be seen in Figure 4-18. Cu1 is situated in a severely JT distorted octahedral site, with the bonding to the Cu1-O1 bond elongated to 2.5 Å, which will weaken this bond and stabilise the d_{z^2} orbital (Figure 4-19). The distortion around the equatorial plane causes stabilisation of the $d_{x^2-y^2}$orbital due to the ligands no longer pointing directly along the axis; this will also destabilise the d_{xy}, d_{xz} and d_{yz}orbitals. Therefore, the energy difference from the $e_g \rightarrow b_{1g}$ electronic transition, arising from the d_{4h} symmetry of the copper centre, will be reduced, and gives rise to the peak centred at 1023 nm. The fivefold site (Cu2) is located in a similar distorted square pyramidal site as compound 5, and will therefore have a similar energy level diagram (Figure 4-15). The $e \rightarrow b_1$ transition will have the highest energy, and therefore will be related to the strong absorbance within the visible region. The $b_2 \rightarrow b_1$ and $a_1 \rightarrow b_1$ transitions are lower in energy and correspond to the absorbance observed in the NIR region. Further splitting of these levels may occur, often too subtle to be described, and account for the broadening of the band.

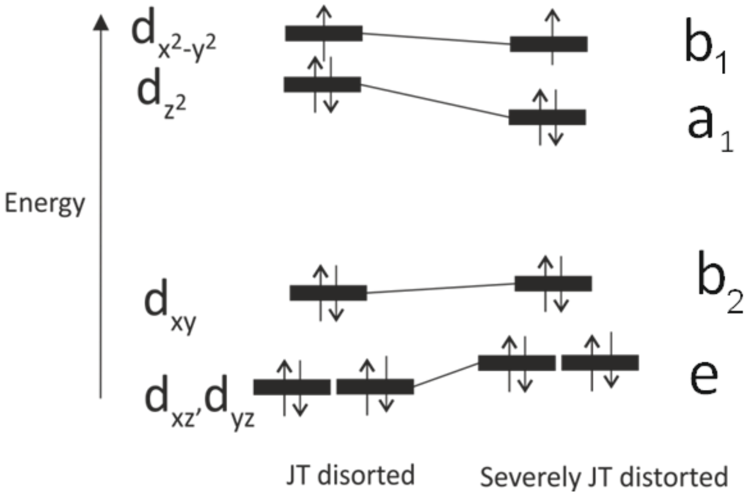

Figure 4-19 - Energy level diagram for Cu1 in compound 6

Compound 7 - $Cu_4(PO_4)_2O$

Compound 7 was synthesised by dehydration and dimerization of $Cu_2(PO_4)OH$, which was performed by annealing at 800 °C for 12 hours in air, with a heating and cooling rate of 2 °C/min. This heating cycle was repeated three times to ensure a pure phase of compound 7. The XRD pattern of this synthesised material matches the previously described triclinic ($P\overline{1}$) phase by Anderson *et al* in 1978.[187] Therefore Anderson's model was selected as the trial structure during the Rietveld refinement.

The resulting atomic coordinates, temperature factors and refinement parameters are shown in Table 4.12.

The Rietveld refinement fit profile is provided in Figure 4-20, where the 2-10 2Θ values have been excluded from the analysis due to a large noise edge from the scattering screen. The presence of a large broad peak under the pattern would indicate the existence of an amorphous phase. Annealing this compound at different temperatures did not result in a more crystalline product and the presence of this broad peak could arise from significant peak overlap. This peak overlap has caused difficulties in the refinement of Compound 7. Refinement parameters with no associated error were fixed to stabilise the refinement.

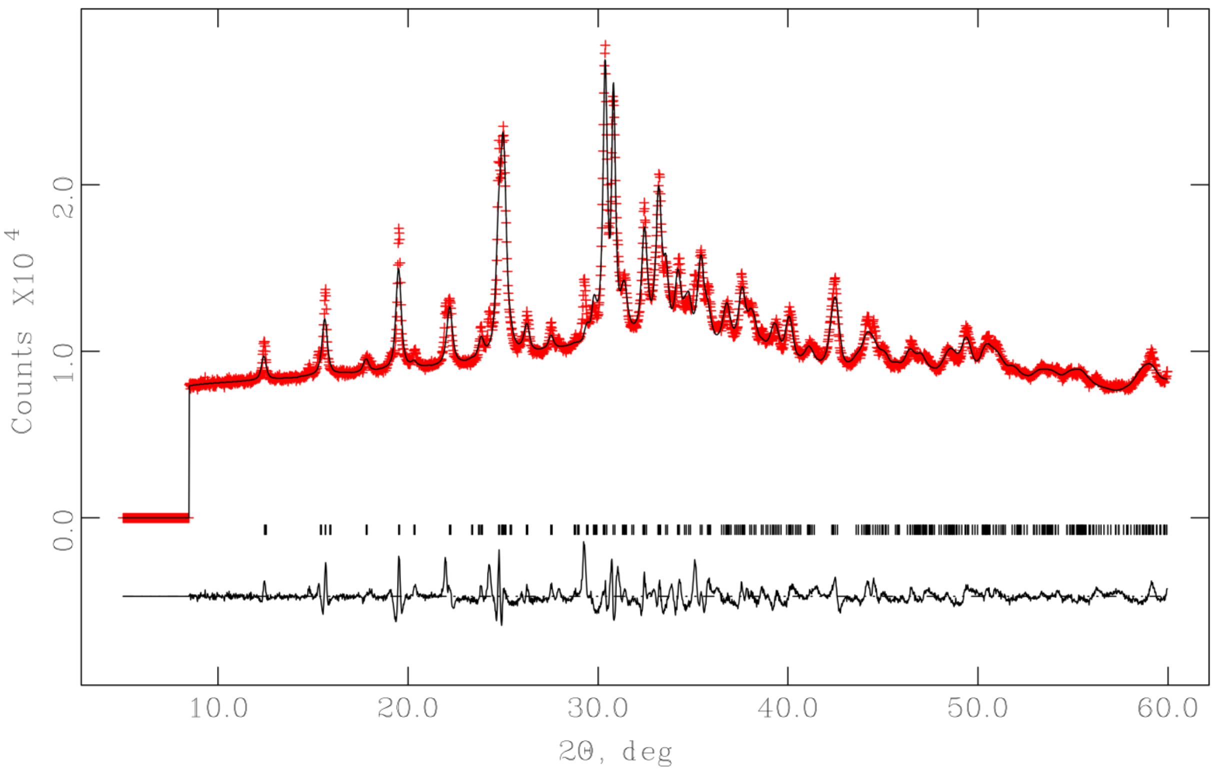

Figure 4-20 - Rietveld refinement fit profile of compound 7. Observed data points are shown as red crosses and the calculated pattern as a solid black line. The difference between the calculated and observed pattern is shown underneath. The position of the peaks are indicated by rows of vertical lines.

Compound 7 contains copper situated in variety of distorted four-, five- and six- coordinate geometries, as shown in Figure 4-21 and Table 4.13. These copper polyhedra are edge-sharing and form tetramers which are connected via μ^4- bridging O (O9) (Figure 4-21). Compound 7 consists of edge-sharing dimers of Cu1 polyhedra and alternating edge/corner-sharing chains of Cu3 and Cu4 polyhedra: these dimers and chains are linked via Cu2 polyhedra to form layers. The copper polyhedra layers are connected via PO_4 tetrahedra to from dense 3D framework (Figure 4-21).

Table 4.12 - Atomic coordinates and temperature factors for compound 7 generated from Rietveld analysis

Space group: $P\overline{1}$

Lattice parameters: a = 7.542(2) Å, b = 8.095(2) Å, c = 6.288(1) Å, α = 113.601(13), β = 98.313(12), γ = 74.336(7)°

Atom site	*x*	*y*	*Z*	U_{iso} x 10^2 ($Å^2$)
Cu1	0.617 (3)	0.574 (4)	0.924 (5)	4.8 (5)
Cu2	0.335 (2)	0.934 (3)	0.778 (4)	3.3 (5)
Cu3	0.903 (4)	0.763 (3)	0.892 (4)	5.7 (6)
Cu4	0.872 (3)	0.768 (3)	0.339 (3)	2.5
O1	0.886 (10)	0.149 (12)	0.800 (14)	2.5
O2	0.760 (10)	0.013 (10)	0.888 (13)	2.1 (15)
O3	0.579 (9)	0.340 (11)	0.804(15)	1.9 (14)
O4	0.269 (8)	0.982 (11)	0.538 (18)	2.5
O5	0.773 (10)	0.545 (9)	0.713 (17)	2.5
O6	0.630 (12)	0.586 (11)	0.619 (18)	2.5
O7	0.767 (12)	0.493 (11)	0.210 (11)	1.3 (16)
O8	0.978 (10)	0.214 (9)	0.367 (12)	2.5
O9	0.229 (13)	0.137 (15)	0.960 (28)	2.5
P1	0.722 (6)	0.157 (7)	0.775 (8)	4.7 (9)
P2	0.804 (6)	0.459 (5)	0.452 (6)	2.6 (8)

Final fit parameters: RF(2) = 0.065, R_{wp} = 0.0392, R_p = 0.0280

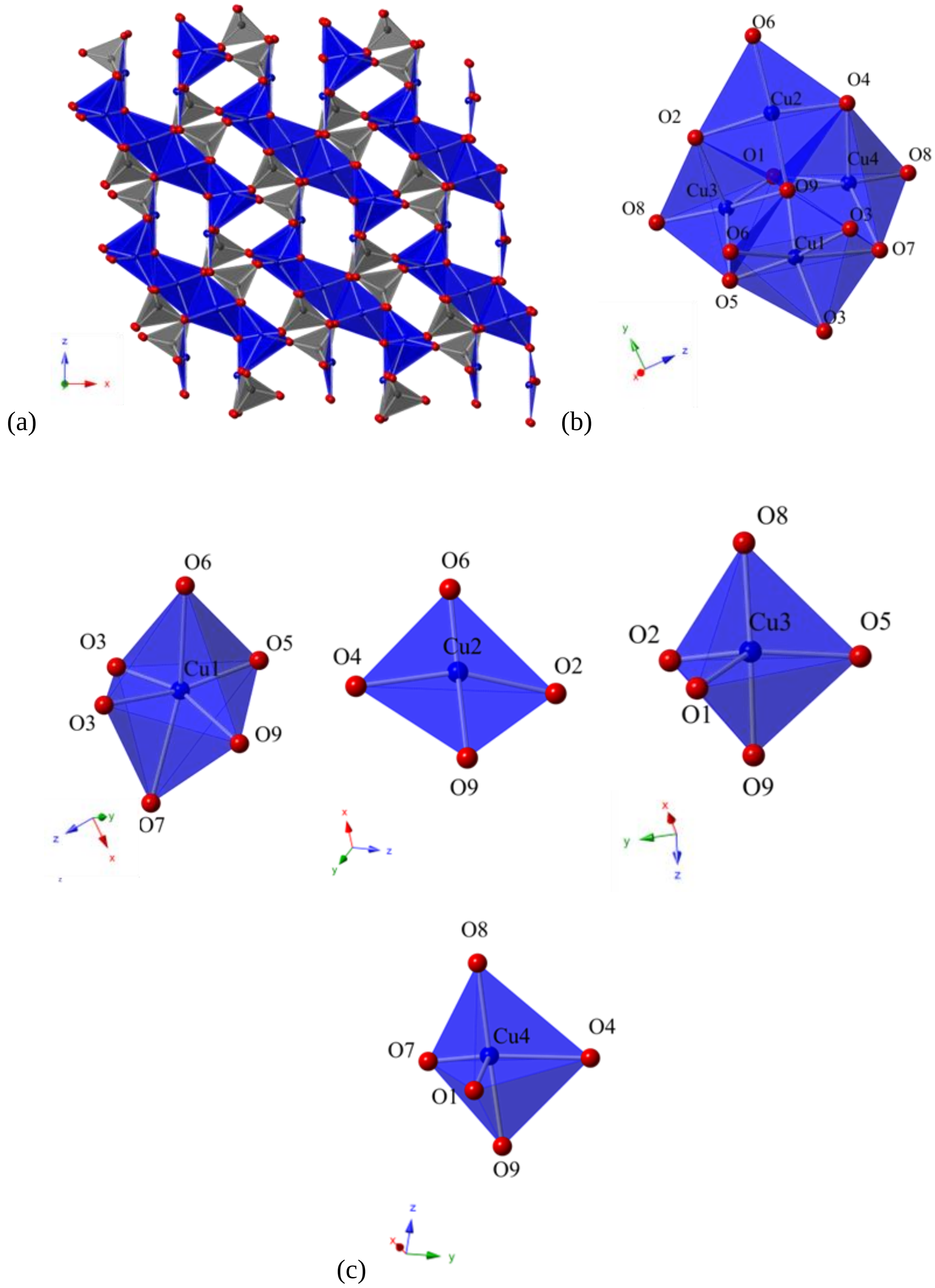

Figure 4-21 - Structure of compound 7 (a) viewed along the b-axis, (b) showing the tetramer building unit and (c) showing the different copper geometries. Cu polyhedra are dark blue, P tetrahedra are grey, and O atoms are red spheres.

Table 4.13 - Bond lengths and angles around copper centres in Compound 7 generated from the Rietveld analysis.

Bond	Bond length (Å)	Bond angle	Angle (°)
Cu1-O3	2.019 (4)	O3-Cu1-O3	87.3 (1)
Cu1-O3	2.060 (5)	O3-Cu1-O5	101.5 (1)
Cu1-O5	1.874 (4)	O3-Cu1-O9	161.0 (4)
Cu1-O6	2.528 (5)	O3-Cu1-O5	169.5 (3)
Cu1-O7	2.398 (5)	O3-Cu1-O9	92.6 (2)
Cu1-O9	2.145 (4)	O5-Cu1-O9	81.5 (2)
Cu2-O2	2.130 (5)	O2-Cu2-O4	170.6 (9)
Cu2-O4	1.927 (4)	O2-Cu2-O9	86.6 (2)
Cu2-O6	2.318 (6)	O4-Cu2-O9	85.9 (2)
Cu2-O9	1.905 (5)		
Cu3-O1-	2.152 (5)	O1-Cu3-O2	105.1 (2)
Cu3-O2	2.057 (7)	O1-Cu3-O8	93.1 (2)
Cu3-O5	2.057 (4)	O1-Cu3-O9	90.1 (2)
Cu3-O8	2.122 (4)	O2-Cu3-O8	82.2 (2)
Cu3-O9	1.909 (4)	O2-Cu3-O9	82.9 (2)
		O8-Cu3-O9	165.1 (4)
Cu4-O1	2.562 (5)	O4-Cu4-O7	120.7 (2)
Cu4-O4	1.934 (4)	O4-Cu4-O8	93.5 (2)

Cu4-O7	2.064 (4)	O4-Cu4-O9	81.6 (1)
Cu4-O8	2.000 (4)	O7-Cu4-O8	107.3 (1)
Cu4-O9	1.875 (4)	O7-Cu4-O9	87.6 (1)
		O8-Cu4-O9	164.6 (4)

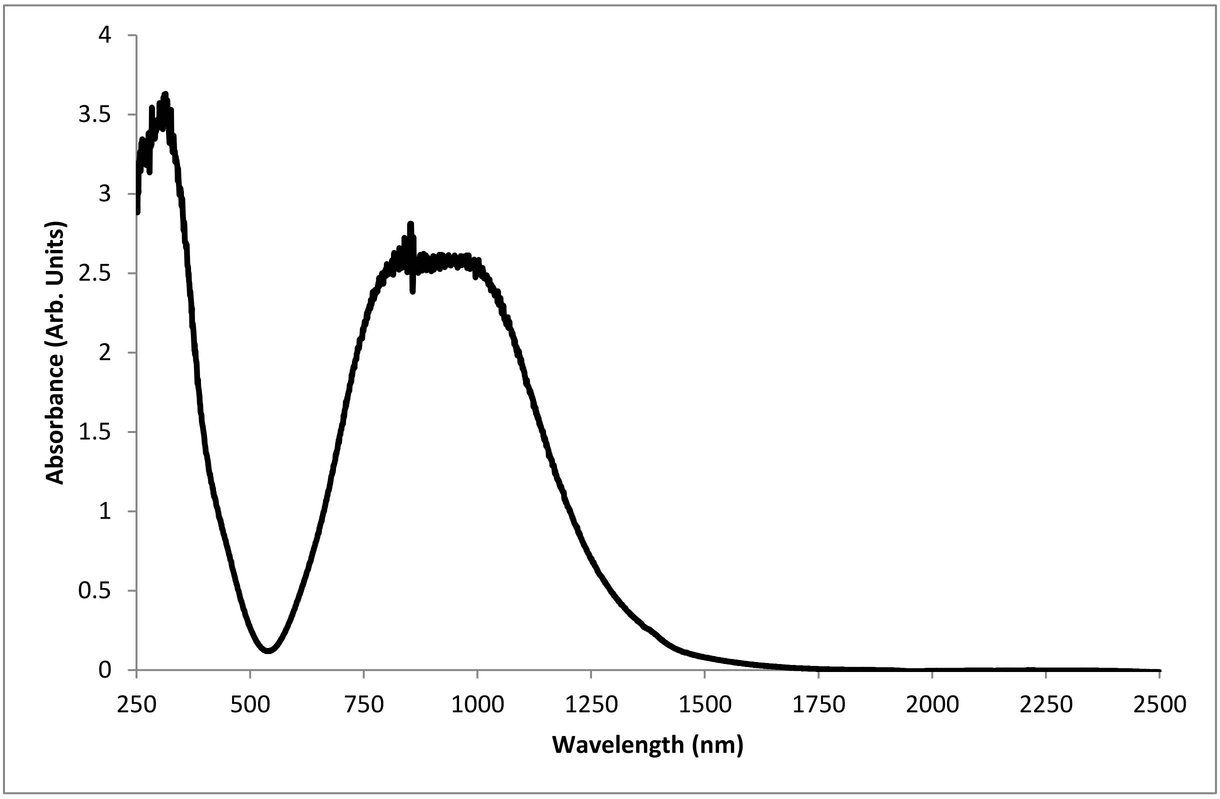

Figure 4-22 - UV/Vis/NIR absorbance spectrum for compound 7

The overlapping transitions from these different copper polyhedra give rise to the strong broad absorbance seen in

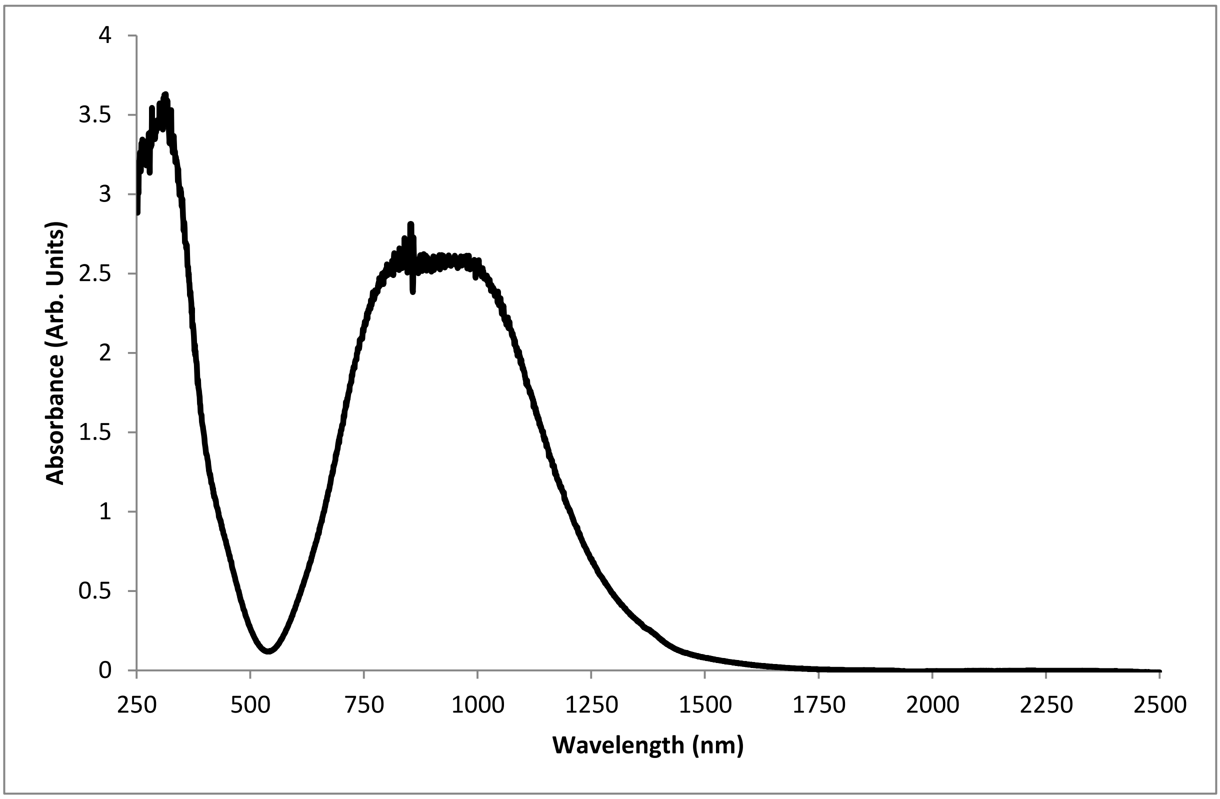

Figure 4-22. The intense green colour of this compound is due to the broad absorbance across the visible region, and these high energy electronic transitions are likely to arise from the square planar Cu2 site. The trigonal bipyramidal sites (Cu3 and Cu4) have a similar energy level diagram to compound 5 ($NaCuPO_4$) (Figure 4-15). Therefore the $e \rightarrow b_1$ transition will have the highest energy, and will be related to the strong absorbance within the visible region. The $b_2 \rightarrow b_1$ and $a_1 \rightarrow b_1$ transitions are lower in energy, and correspond to the absorbance observed in the NIR region. The strongly JT distorted Cu1 octahedra will have a similar energy level diagram to that of Compound 6 (Cu_2SO_4O), Figure 4-19.

Compound 8 - Cu_2PO_4OH

Compound 8 was synthesised hydrothermally by heating CuF_2, H_3PO_4, KOH and water in a 1:1:1:4 ratio at 175 °C for four days, which yielded a pure crystalline product. Compound 8 has been previously described in the literature as a mineral material, and undergoes a phase transition from orthorhombic to monoclinic at low temperatures.[188] Therefore care was taken to ensure the correct phase was chosen as the trial structure. A comparison of the p-XRD pattern of the material produced to the ICSD database indicated that the *Pnnm* orthorhombic phase was formed during hydrothermal synthesis. The resulting atomic coordinates, temperature factors and refinement parameters are shown in Table 4.14.

The Rietveld refinement fit profile is provided in Figure 4-23, where the 2-10 2Θ values have been excluded from the analysis due to a large background drift. Poor refinement values are due to preferred orientation along the (110) and (220) lattice plane, which d lead to some parameters being fixed (i.e.no errors quoted). The preferred orientation was modelled using the March-Dollase method with a ratio of 0.379 and 1.171for the (100) and (220) lattice planes, respectively.

Table 4.14 - Atomic coordinates and temperature factors for compound 8 generated from Rietveld analysis

Space group- *Pnnm*

Lattice parameters a = 8.061 (3) Å, b = 8.398 (3) Å, c = 5.891 (2) Å, α = β = γ = 90°,

Atom site	*x*	*y*	*Z*	U_{iso} x 10^2 ($Å^2$)
Cu1	0.000	0.500	0.271 (1)	3.9 (3)
Cu2	0.642 (8)	0.375 (9)	0.500	6.2 (3)
H1	0.905	0.289	0.500	2.0
O1	0.857 (3)	0.433 (3)	0.000	2.9 (11)
O2	0.921 (3)	0.118 (3)	0.000	2.5
O3	0.679 (3)	0.247 (9)	0.184 (2)	1.6 (8)
O4	0.854 (3)	0.398 (2)	0.500	2.5
P1	0.783 (2)	0.243 (2)	0.000	8.4 (8)

Final fit parameters: R(F2) = 0.118, R_{wp} = 0.0934, R_p = 0.0659

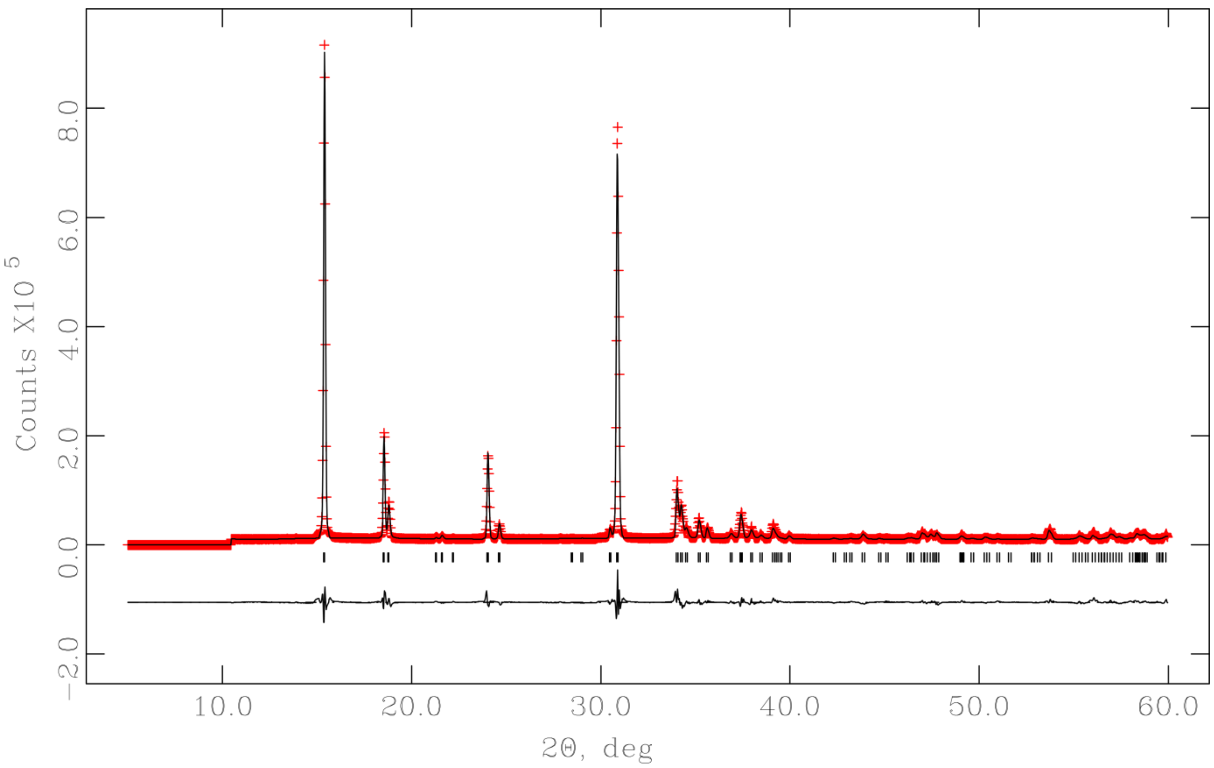

Figure 4-23 - Rietveld refinement of compound 8. Observed data points shown as red crosses, and the calculated pattern is shown as a solid black line. The difference between the observed and calculated pattern is shown underneath. The positions of the peaks are marked by black lines.

The structure of compound 8 (libethenite) is shown in Figure 4-24, and consists of linked $CuO_4(OH)$ and $CuO_4(OH)_2$ copper polyhedra to form a dense 3D network. These copper polyhedra are linked along the c-axis to form infinite chains of edge-sharing $CuO_4(OH)_2$ octahedra: the octahedra are edge sharing through alternating O and OH bridges (Figure 4-24). These chains are connected to each other through PO_4 tetrahedra and dimers of edge-sharing $CuO_4(OH)$ trigonal bipyramidal copper centres, through the μ^3-bridging OH**.**

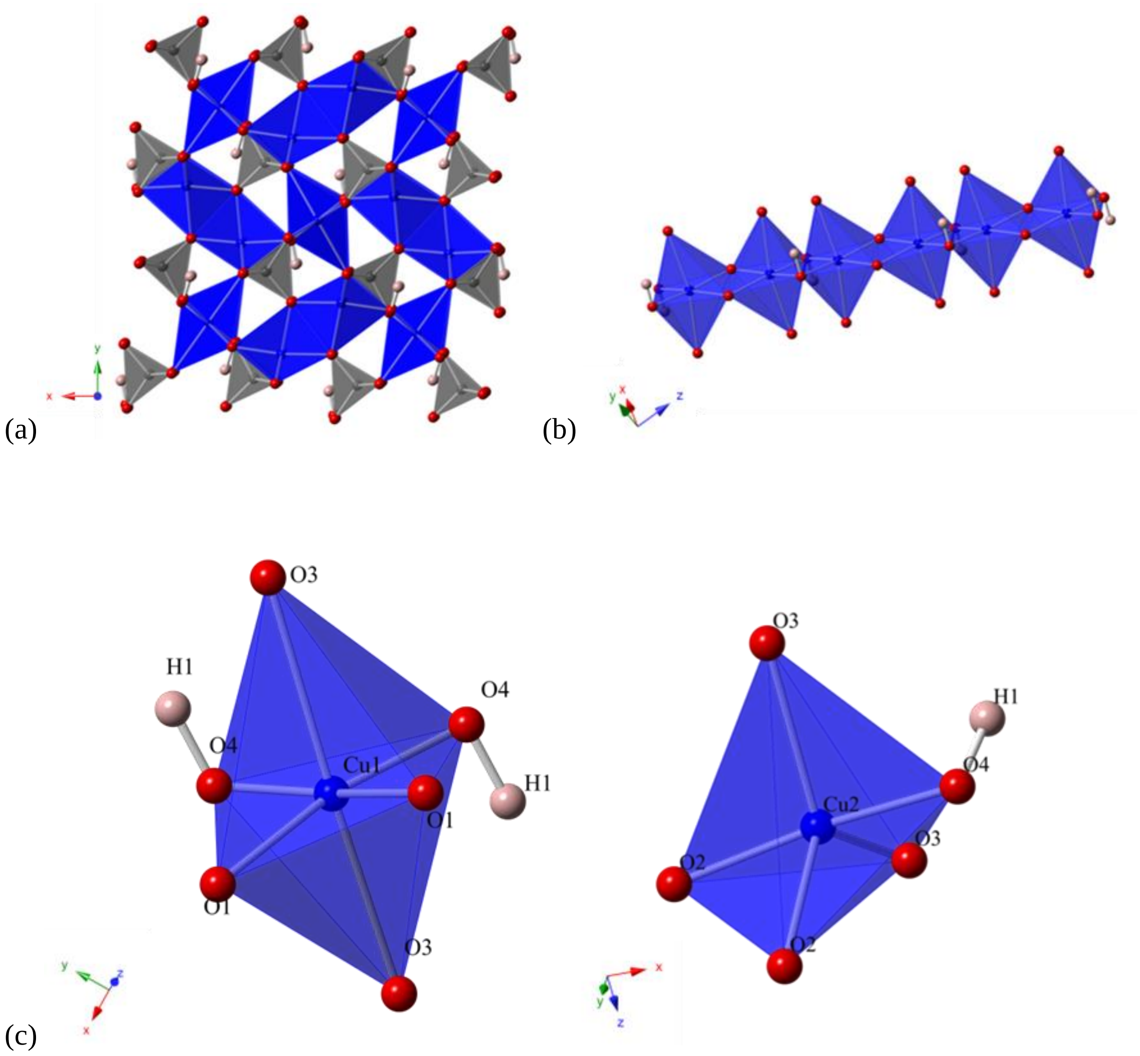

Figure 4-24 - (a) Structure of compound 8 when viewed along the c-axis; (b) edge-sharing chains of $CuO_4(OH)_2$ octahedra; and (c) copper coordination geometries in compound 8.

Table 4.15 - Bond lengths and angles around copper centres in Compound 8 generated from the Rietveld analysis.

Bond	Bond length (Å)	Bond angle	Angle (°)
2x Cu1-O1	2.040 (15)	O1-Cu1-O1	86.8 (12)
2x Cu1-O3	2.545 (9)	2x O1-Cu1-O4	168.5 (10)
2x Cu1-O4	2.015 (16)	2x O1-Cu1-O4	93.9 (6)
		O3-Cu1-O1	95.5 (6)
		O3-Cu1-O4	91.2 (5)
Cu2-$O2_{equatorial}$	2.117 (20)	$O2_{eq}$-Cu2-$O2_{ax}$	85.4 (14)
Cu2-$O2_{axial}$	1.941 (0)	$O2_{eq}$-Cu2-O4	97.4 (12)
2x Cu2-O3	2.183 (16)	$O2_{ax}$-Cu2-O4	172.8 (14)
Cu2-O4	2.014 (0)	2x $O2_{eq}$-Cu2-O3	120.9 (7)

The bond lengths and angles around the Cu1 octahedral site indicate that there is a high degree of symmetry, although there is a deviation away from perfect octahedral geometry (Table 4.15). The presence of OH on the O4 site further reduces this symmetry due to the presence of non-equivalent sites - this would imply that the Cu1 site is of D_{2d} symmetry compared to the D_{4h} expected for a JT distorted copper octahedra. The energy level diagrams for the Cu1 and Cu2 sites are provided in Figure 4-26

.

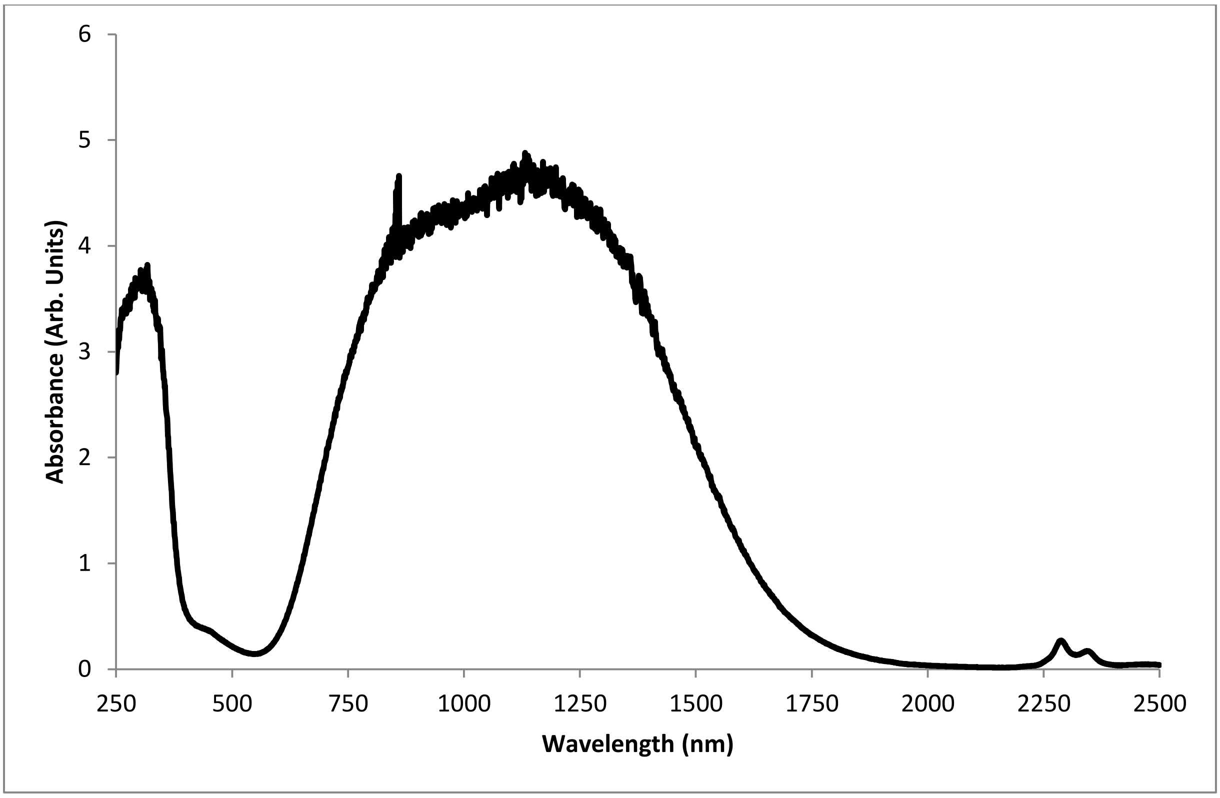

Figure 4-25 - 2UV/Vis/NIR absorbance spectrum for compound 8

The absorbance spectrum (Figure 4-25) consists of a strong broad absorbance ranging from 700-1800 nm, due to the e→ a_1, e→ b_1 and e→ b_2 electronic transitions from the $CuO_4(OH)_2$ octahedra in D_{2d} symmetry, and the e→a_1 electronic transition from the $CuO_4(OH)$ trigonal bipyramidal in C_{3v} symmetry. The absorbance peak located at 2300 nm is due to an OH overtone stretching mode. The larger broad absorbance is due to the overlapping electronic transitions that occur within the slightly-distorted copper polyhedra. Further splitting of these levels may occur, often too subtle to be described, and account for the significant broadening of the band.

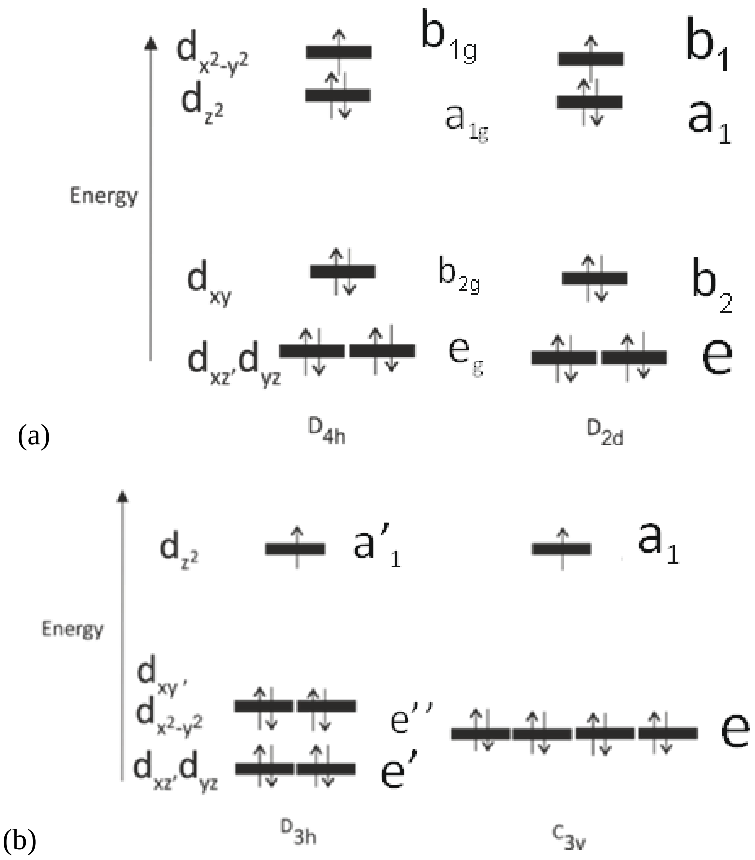

Figure 4-26 - Energy level diagram for distorted copper geometries in Compound 8 (a) Cu1 and (b) Cu2

Structural summary

The structural trends observed in the square pyramidal geometries in compounds 5,6 and 7 are consistent with previous observations. The fifth (apical) ligand is bonded at a distance of 0.2-0.6 Å greater than the basal in-plane ligands[168], and, in most cases, the copper (II) ion is not strictly coplanar with the equatorial ligands, but is shifted ca. 0.2 Å towards the apical ligand.[168] In 1984, Addison, Reedijk and co-workers introduced the parameter τ, which provides a measure to the degree of square-based pyramidal *versus* trigonal bipyramidal geometries in five-coordinate copper (II) centres.[189] This parameter provides a convenient tool for comparing structures of similar five-coordinate copper (II) centres. The parameter τ is defined as $(\beta - \alpha)/60$, where β and α are the largest coordination angles, and its value varies from 0 (in regular square based pyramid) to 1 (in regular trigonal bipyramidal). The τ values obtained for the compounds described in this section are present in Table 4.16. The results indicate that compounds 5 and 6 are more square-based pyramidal in character than trigonal bipyramidal. Compound 8 Cu_2PO_4OH is the only compound that indicates a high level of trigonal bipyramidal geometry. The five-coordinate copper centres in $Cu_4(PO_4)O$ show a small degree of distortion between the two geometries, but are more square-based pyramidal in character.

Table 4.16 - Degree of square-based pyramidal versus trigonal bipyramidal geometries

Compound	τ
Compound 5 - $NaCuPO_4$	0.02
Compound 6 - Cu_2SO_4O	0.03
Compound 8 - $Cu_2(PO_4)OH$	0.87
Compound 7 - $Cu_4(PO_4)O$-Cu3	0.20
Compound 7 - $Cu_4(PO_4)O$-Cu4	0.23

The absorbance spectrum of the distorted square pyramidal structures described above are comparable to previous spectra collected on $Cu_2P_2O_7$ and $BCu_2P_2O_7$ (B= Ca, Ba).[171] All of these diphosphate materials contain the same slightly distorted five-coordinate environments, and have a strong broad absorbance ranging from 500-1800 nm.

Compound 7 contains all of the different coordination environments commonly found in copper framework materials. The mixture of four-, five- and six-coordinate geometries give rise to a broad absorption spectrum arising from the overlapping maxima from each copper centre. It is possible to interpret this complex absorption spectrum by analysing the individual copper centres. Compound 3 contains square planar copper environments, and can be used to distinguish the square planar transitions from the five- and six-coordinate transitions. The presence of the square planar site shifts the absorbance spectrum further into the visible region (maxima starting at 500 nm) compared to the other five-coordinate compounds (600 nm). This shift gives rise to the intense green colour of compound 7 compared to the light green/turquoise colour of other five-coordinate structures presented in this work and previously.

Work performed in this project and previously looked at the optical properties of iron containing graftonite.[171] The absorbance spectra obtained in both of these studies indicate that this material contains two absorbance maxima at 1000 and 1890 nm. In the previous work, iron was doped into a pure Zn containing graftonite material, and it was shown that the Fe (II) showed preference for the octahedral site.[88] This is not surprising considering the CFSE of Fe (II) in octahedral geometry compared to trigonal bipyramidal. The work performed in this project looked at the pure iron graftonite material, as the previous work showed that the intensity of the absorbance spectrum was related to the amount of Fe in the framework.

The optical spectrums of graftonite materials are similar to a previously-described iron silicate mineral joaquinite[169] ($Ba_4Fe_2RE_4Ti_4O_4[Si_4O_{12}](OH)_2$ (RE-rare earth)). Joaquinite contains Fe (II) in almost perfect trigonal bipyramidal geometry, and has absorbance maxima at 1050 and 2000 nm arising from the $e'' \rightarrow a_1$ and $e'' \rightarrow e'$ electronic transitions respectively. This is considerably different from the absorbance spectrum of compound 8, which contains copper located in similar octahedral and trigonal bipyramidal geometries. The strong broad absorbance of compound 8 compared to the two absorbance maxima observed for $Fe_3(PO_4)_2$ highlights the differences in absorbance spectra between copper and iron materials. These differences arise from the larger magnitudes of the splitting of the electronic energy levels in copper complexes compared to other first-row transition metals, due to the large bond-length distortions present.[168]

Evidence of this can be seen in the copper bond lengths in Cu_2PO_4OH, which range from 1.94-2.5 Å compared to the much narrower bond length range observed in $Fe_3(PO_4)_2$ 1.96-2.2 Å.

4.3 Six-coordinate structures

Six-coordinate environments are the most common type of geometries encountered for 3D metal frameworks.[3] The most common geometry for six-coordinate is octahedral, however due to the Jahn-Teller effect (JTE) this can be distorted away from ideal O_h symmetry. The JTE can cause tetragonal distortion, which results from axial elongation and equatorial compression or *vice versa*. The JTE enhances the preference for copper (II) compounds to adopt octahedral geometries.

An octahedral complex has six M-L bonding interactions and, in the absence of significant steric and electronic effects, this arrangement will have a lower energy than five and four geometries. The ligand field stabilisation energy (LFSE) indicates that d^3 and d^8 configurations strongly favour octahedral geometries. For other configurations this preference is less pronounced. Because the LFSE, and hence the size of ΔE, depends on the ligand, it follows that a preference for octahedral coordination will be less pronounced for weak-field ligands.

The effect of the ligand type on ΔE is well understood in the spectrochemical series. However, the magnitude of this effect becomes more complicated when there is more than one ligand donor. A large number of six-coordinate iron (II) and copper (II) frameworks have been synthesised, which contain different ligand types, during the course of this thesis. The absorption spectra of these materials have been recorded and combined with literature values of other frameworks to provide a picture of how the ligand type affects the absorbance maxima, and the results of this study are presented and discussed below.

Copper compounds

A number of copper sulphate, phosphate, silicate, fluoride and hydrate frameworks have been synthesised and analysed using UV/Vis/NIR spectroscopy. The results of this work are summarised in Table 4.17 and Figure 4-27. The purity of these compounds was confirmed by powder XRD (Appendix-C) and can be considered pure phase unless otherwise stated. The UV/Vis/NIR spectra of the compounds in Table 4.17 are presented in Appendix D.

Table 4.17 - Summary of absorbance data for six-coordinate copper compounds

Compound No.	Chemical formula	Synthesis conditions	Absorbance maxima (nm)
9	$CuSO_4 \bullet 5H_2O$	As received from Sigma Aldrich	764
10	$CuSO_4 \bullet 3H_2O$	Heat $CuSO_4 \bullet 5H_2O$ to 70 °C under vacuum	781
11	$CuSO_4 \bullet H_2O$	Heat $CuSO_4 \bullet 5H_2O$ to 110 °C under vacuum	817
12*	$CuSO_4$	Heat $CuSO_4 \bullet 5H_2O$ to 220 °C under vacuum	839
13*	Cu_2SO_4O	Heat $CuSO_4 \bullet 5H_2O$ to 670 °C	809
14	$Rb_2Cu(SO_4)_2 \bullet 6H_2O$	From literature [190]	830 [190]
15	$Na_2Cu(SO_4)_2 \bullet 2H_2O$	Heat an equimolar solution of Na_2SO_4 and $CuSO_4 \bullet 5H_2O$ to approximately 60 °C	834
16*	$KCu_2(SO_4)_2 OH \bullet H_2O$	Pelletising $2CuSO_4$+KF and heating the reaction mixture to 225 °C for 48 h in a hydrothermal bomb	804
17	$NaCu_2(SO_4)_2 OH \bullet H_2O$	Pelletising $2CuSO_4$+NaF into pellets and heating the reaction	764

		mixture to 225 °C for 48 h in a hydrothermal bomb	
18	$K_2Ca_2Cu(SO_4)_4 \cdot 2H_2O$	K_2SO_4, $CuSO_4 \cdot 5H_2O$, $CaCl_2$ and distilled water with the mole ratio of 1:1:1:44, the solution was put in a water bath at 50 ℃ for 48 h	808
19	$Na_2CuSO_4F \cdot 2H_2O$	Heating $CuSO_4 \cdot 5H_2O$, NaF and benzene at 200 °C for 1 min in a hydrothermal bomb [191]	859
20	CuF_2	From literature [192]	926
21	$KCuF_3$	Excess KF in HF solution of $CuCO_3$	800
22	K_2CuF_4	Heating a 1:1 mixture $KCuF_3$ and KF under vacuum to 750 °C for 100 h	800
23	K_3CuF_7	Heating a 2:1 mixture $KCuF_3$ and KF under vacuum to 750 °C for 100 h	800
24	Cu_2PO_4F	Hydrothermally heating CuF_2, H_3PO_4 and KF in a 1:1:1 ratio, at 175 °C for 4 days.	950
25	$Na_2Cu(PO_4)_3$	Na_2CO_3, CuO and $NH_4H_2PO_4$ with ratio of 1:1:4, heated to 350 °C, 15 h then 600 °C 30 h	834
26	$K_2Cu(PO_4)_3$	K_2CO_3, CuO and $NH_4H_2PO_4$ with ratio of 1:1:4, heated to 350 °C, 15 h then 600 °C, 30 h	900
27	$Cu_2(P_4O_{12})$	From literature [171]	800 [171]
28	$Zn_{12}Cu_4P_8O_{36}$	ZnO, CuO and $(NH_4)_2HPO_4$ with ratio of 12:3:8 heated to 500 °C, 15 h then 900 °C, 30 h	845
29	$Cu_4(PO_4)_2O$	Cu_2PO_4OH heated to 800 °C for 12 h	900

30	Cu_2PO_4OH	Heating CuF_2, H_3PO_4 and KOH in a 1:1:1 ratio, at 175 °C for 4 days in a hydrothermal bomb.	880
31	$MgCuSi_2O_6$	From literature [171]	900 [171]
32	$CuSiO_3{\bullet}H_2O$	Mineral [193]	800
33	$Cu_5(OH)_2(SiO_3)_4$	Mineral [194]	750

*Minor impurity phase present

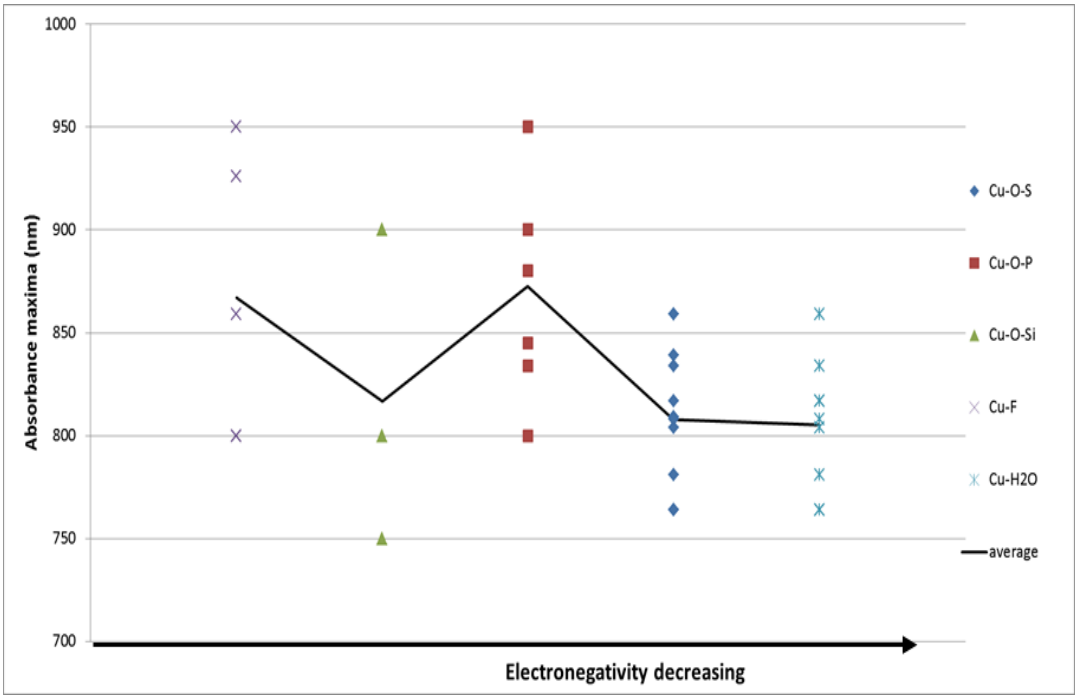

Figure 4-27 - Summary of copper six-coordinate ligand types and absorption maxima

From Figure 4-27 the average Cu-O-P ligand linkage have the lowest ΔE compared to the other ligand types. The inductive effect of the XO_4 (X=S, P and Si) building unit on transition metal centres has been well studied in electrochemical systems.[64, 68, 195-197] This inductive effect is related to the electronegativity of the X atoms. The electronegativity increases across a period and decreases down a group, which is related to the number of charges and distance from the nucleus respectively. With this inductive effect in mind, the Cu-O-Si bonds are the least electronegative, which will reduce ΔE compared to the phosphate and sulphate bonds. The reduction in electronegativity results in a lower ΔE due to stronger π-donor properties of the O ligand: this trend can be observed from the average bond lengths (Table 4.18). The shortest equatorial and axial bonds are observed in sulphate compounds, which explains the blue shift compared to phosphate and silicate. However the average bond lengths in silicate compounds are the longest, and should suggest the lowest ΔE: the reason for this anomaly could be due to the lack of examples found for six-coordinate copper silicate materials.

Table 4.18 - Average bond lengths in the six-coordinate copper compounds

	Average Cu-O-S bond length (Å)	Average Cu-O-P bond length (Å)	Average Cu-O-Si bond length (Å)	Average Cu-F bond length (Å)	Average Cu-H_2O bond length (Å)
All	2.127	2.205	2.223	2.110	2.178
Equatorial	1.850	1.974	1.999	1.970	1.940
Axial	2.404	2.436	2.468	2.250	2.417

Changing the ligand environment around the metal centre, by increasing the π-donor properties, should cause a red shift in the absorbance maxima, according to the spectrochemical series. Evidence of this can be seen in the dehydration of $CuSO_4•5H_2O$ (compound 9) by replacing the weak π-donor properties of water to O^{2-} ligands. The copper centre in compound 9 contains four equatorial water ligands with an average bond length of 1.965 Å. The absorption maximum of compound 9 is centred on 764 nm, which results in the intense blue-coloured material. The dehydration mechanism of $CuSO_4•5H_2O$ is well understood in the literature, and results in the loss of two water molecules at 95 and 120 °C.[198] Upon losing two water molecules from the crystal structure, only one water molecule is lost from the copper coordination environment. This change from four to three water ligands around the copper centre causes the absorption maxima to red shift to 781 nm. Further dehydration to $CuSO_4•H_2O$ results in another water molecule being lost from the copper coordination, and causes a further red-shift of the absorbance maxima to 817 nm. Upon complete dehydration to $CuSO_4$ (compound 12) all the water ligands have been replaced by O^{2-} ligands, resulting in an absorbance maximum at 839 nm, this is a shift of 75 nm which is a decrease in ΔE by 0.145 eV.

The inclusion of fluoride into materials that contain Cu-O/H_2O linkages has shown to dramatically reduce the ΔE compared to equivalent ligand compounds due to the higher electronegativity of the fluoride ligand. In Cu_2PO_4F (compound 24), the copper is coordinated in two octahedral sites (Figure 4-28), with an absorbance maximum at 950 nm. In Cu1 the four equatorial bonds consist of three Cu-O bonds and one Cu-F bond, and these were found to be very similar in length; the average length was calculated to be 1.98 Å. Two axial bonds, Cu-O and Cu-F are clearly elongated; the lengths of the two bonds are 2.293 Å and 2.509 Å respectively. For the Cu2 coordination, the equatorial bonds between the copper and the equatorial oxygen and fluorine ligands range from 1.93-2.04 Å; the average length of the four equatorial bonds is 1.97 Å. Similar to the Cu1 site, the axial Cu-O and Cu-F bonds are noticeably elongated with lengths of 2.335 Å and 2.431 Å respectively. Similarly-distorted copper centres are present in $K_2Cu(PO_4)_3$ (compound 26), which results in absorbance maxima centred on 900 nm. In compound 26, the Cu average equatorial and axial bond lengths are 1.96 and 2.5 Å, respectively (Figure 4-28). The only significant difference between compound 24 and 26 is the presence of the fluoride ligand, which results in a red shift of the absorbance maxima of 50 nm.

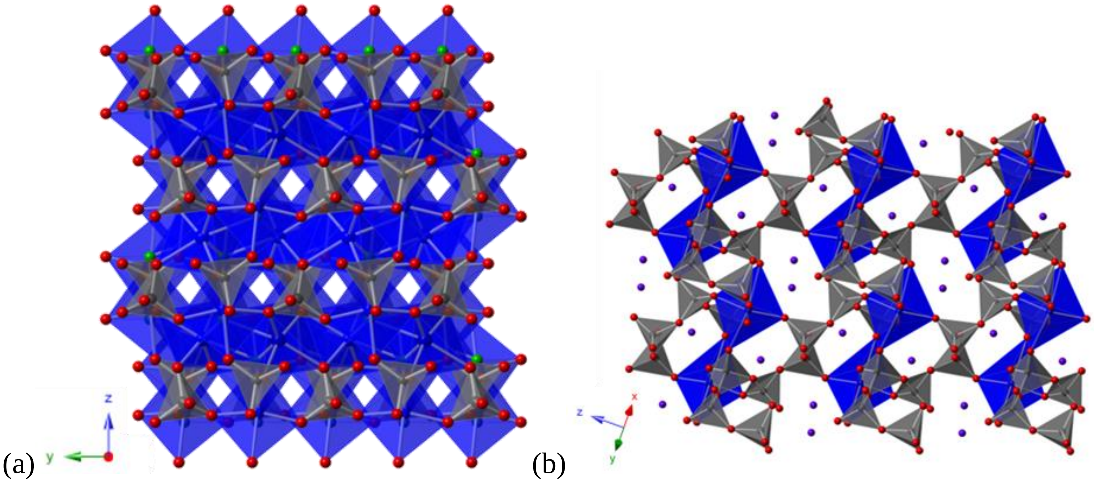

Figure 4-28 - Structure of (a) compound 24 viewed along the a-axis and (b) compound 26 viewed along the (110) direction. Cu polyhedra in dark blue, P tetrahedra in grey, K cations are purple sphere and F atoms are green spheres.

The inclusion of fluoride has a similar effect on the absorption maxima in copper sulphate materials. $NaCuSO_4F•2H_2O$ (compound 19) contains chains of $CuO_2F_2(H_2O)_2$ octahedra linked through bridging fluoride ligands and bridging SO_4 tetrahedra (Figure 4-29), which result in an absorption maxima of 859nm. The water ligands are axial and elongated to 2.42 Å; the Cu-F bonds are equatorial and are shorter (1.89 Å) than the Cu-O-S bonds (2.04 Å). The structure of $Na_2Cu(SO_4)_2•2H_2O$ (compound 15) consists of linked SO_4 tetrahedra and $CuO_4(H_2O)_2$ octahedra to form Kroehnkite-type chains (Figure 4-29). The water ligands are axial and elongated compared to the equatorial ligands, similar to compound 19 (NaCuSO4F). The resulting absorption maxima of $Na_2Cu(SO_4)_2•2H_2O$ is centred around 834 nm, implying that the addition of fluoride to Cu-O-S materials with a similar ligand environment has caused the absorbance maximum to shift by 20 nm. This is small shift compared to the one observed for the copper phosphate example due to the smaller Cu-F bond length. This small bond distance observed in the Cu-F-Cu bond is unexpected due to the fact that fluorides in metal-metal bridging sites are normally longer.[199]

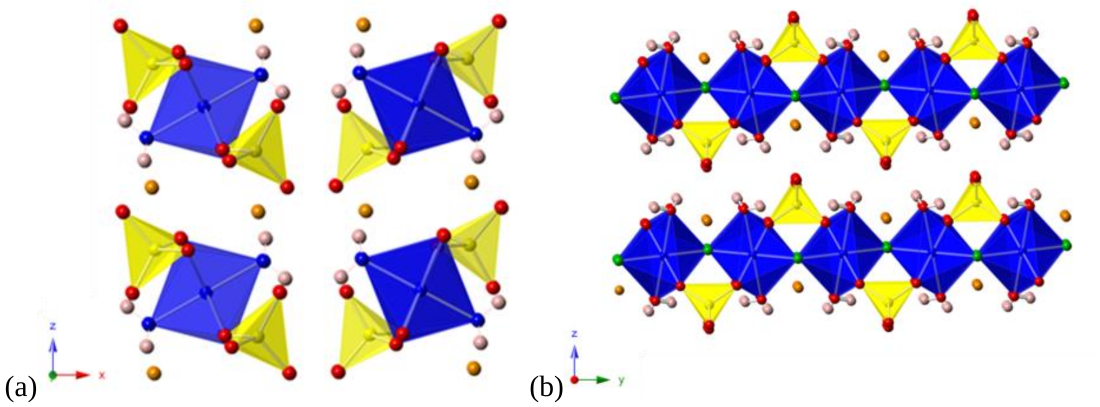

Figure 4-29 - (a) View of $Na_2Cu(SO_4)_2$•$2H_2O$ along the b-axis; (b) $NaCuSO_4F$•$2H_2O$ viewed along the a- axis. Cu polyhedra in dark blue, S tetrahedra in yellow, water ligands are dark blues spheres, Na cations are orange spheres and F atoms are green spheres.

Silicates and phosphates are very similar in terms of their structural and coordination chemistry.[40] However, in contrast to the latter, silicate materials need very demanding synthesis conditions such as high temperature, pressure and time for the reaction to occur. This is the main reason that only a few copper silicates can be found in nature, and even then only as secondary minerals.[194] The few structurally-investigated simple copper silicates found in the literature all exhibit copper situated in a square planar environment.[59, 200] One of these simple copper silicates is the mineral dioptase, $CuSiO_3$•H_2O (compound 32), which has a blue to green colour and is composed of $CuO_4(H_2O)_2$ octahedra (Figure 4-30), resulting in an absorption maxima centred on 800 nm.[193] The equatorial bond lengths around the copper centre in dioptase range from 1.95-1.98 Å, with a severe axial elongation of the water molecules at 2.5 and 2.6 Å. Due to the extreme elongation of the axial ligands in dioptase, the energy level diagram of this material is a hybrid between the energies of square planar and octahedral. The copper silicate material, clinopyroxene $Mg_{(2-x)}Cu_xSi_2O_6$ (Compound 31), contains cations situated in two different octahedral sites (M1 and M2), with copper preferentially situated in the M2 site (Figure 4-30). The M2 site can be considered as a slightly tetragonally-distorted octahedral site with two shortened bond lengths (2.08 Å), compared to the basal plane (2.14 Å). The negligible distortion of this site results in the sharp absorption maxima centred at 800 nm.[171] The peak position of the absorbance maximum is the same for both clinopyroxene and dioptase, which is unanticipated considering the significant differences in the degree of JT distortion. The similarity of the absorbance maxima could be linked to different π-donor properties of the water and O $^{2-}$ ligands, which counteract the JT distortion effects.

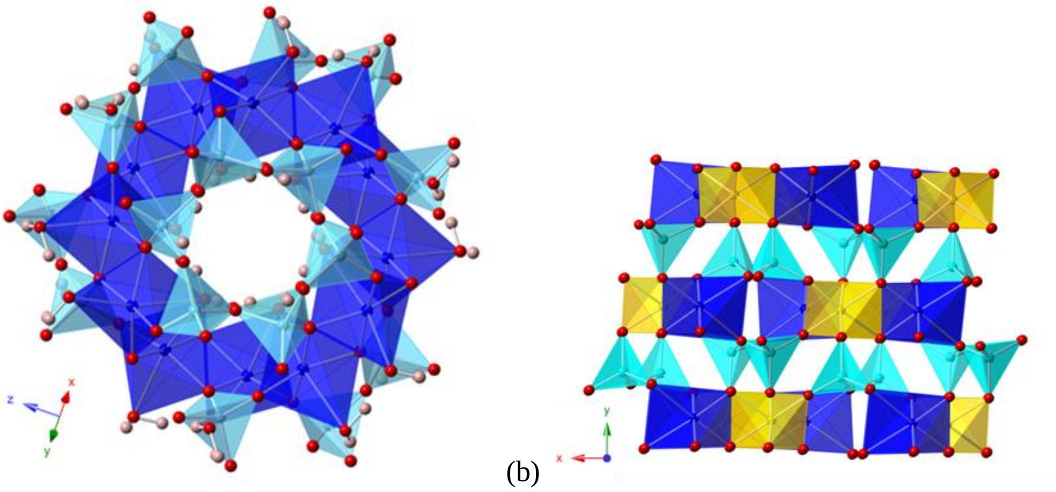
(a) (b)

Figure 4-30 - Structure of (a) Compound 32 viewed in the (110) plane and (b) Compound 31 along the c-axis. Cu polyhedra in dark blue, Si tetrahedra in light blue, Mg polyhedra in yellow, O atoms are red spheres, and H atoms are light pink spheres.

Iron compounds

A number of iron sulphate, phosphate, silicate, fluoride and hydrate frameworks have been synthesised and analysed using UV/Vis/NIR spectroscopy. The results of this work are summarised in Table 4.19 and Figure 4-31. The purity of these compounds was confirmed by powder XRD (Appendix-C) and can be considered pure phase unless otherwise stated. The UV/Vis/NIR spectra of the compounds in Table 4.19 are presented in Appendix D.

Table 4.19 - Summary of absorbance data for six-coordinate iron compounds

Compound No.	Chemical formula	Synthesis conditions	Absorbance maxima (nm)
34	$FeSO_4$•$7H_2O$	As received from Sigma Aldrich	885
35*	$FeSO_4$•$4H_2O$	Heat $FeSO_4$•$7H_2O$ to 110 °C under vacuum	963

36†	$FeSO_4 \bullet H_2O$	Heat $FeSO_4 \bullet 7H_2O$ to 200 °C under vacuum	925
37	$K_2Fe(SO_4)_2 \bullet 2H_2O$	Slow evaporation of equimolar solution of K_2SO_4 and $FeSO_4 \bullet 7H_2O$	1024
38	$K_2Fe(SO_4)_2 \bullet 4H_2O$	Equimolar solution of K_2SO_4 and $FeSO_4 \bullet 7H_2O$ to heated to 50 °C	970
39	$(NH_4)_2Fe(SO_4)_2 \bullet 6H_2O$	As received from Sigma Aldrich	912
40*	$Na_2FeSO_4F \bullet 2H_2O$	Hydrothermally heating $FeSO_4 \bullet 7H_2O$, NaF and benzene at 200 °C for 1 min [191]	931
41†	FeF_2	As received from Sigma Aldrich	950
42	$KFeF_3$	From literature [201]	952 [201]
43†	$Fe_2(P_2O_7)$	Heated 1:1 mixture of $FeC_2O_4 \bullet 2H_2O$ and $(NH_4)_2HPO_4$ to 700 °C for 3 h under H_2/N_2 atmosphere	995
44†	$Fe_2(P_4O_{12})$	Heated 1:2 mixture of $FeC_2O_4 \bullet 2H_2O$ and $(NH_4)_2HPO_4$ to 700 °C for 3 h under H_2/N_2 atmosphere	880
45	$Fe_3(PO_4)_2$	From literature [171]	1000 [171]
46†	$LiFePO_4$	Hydrothermally heating LiH_2PO_4, urea and $FeSO_4 \bullet 7H_2O$ at 180 °C for 1 h	1064
47	$CaFe(Si_2O_6)$	Mineral	1000 [169]
48	Fe_2SiO_4	Mineral	1000 [169]
49	$FeSiO_3$	Mineral	909 [169]

*Minor impurity phase present, †- poor crystallinity.

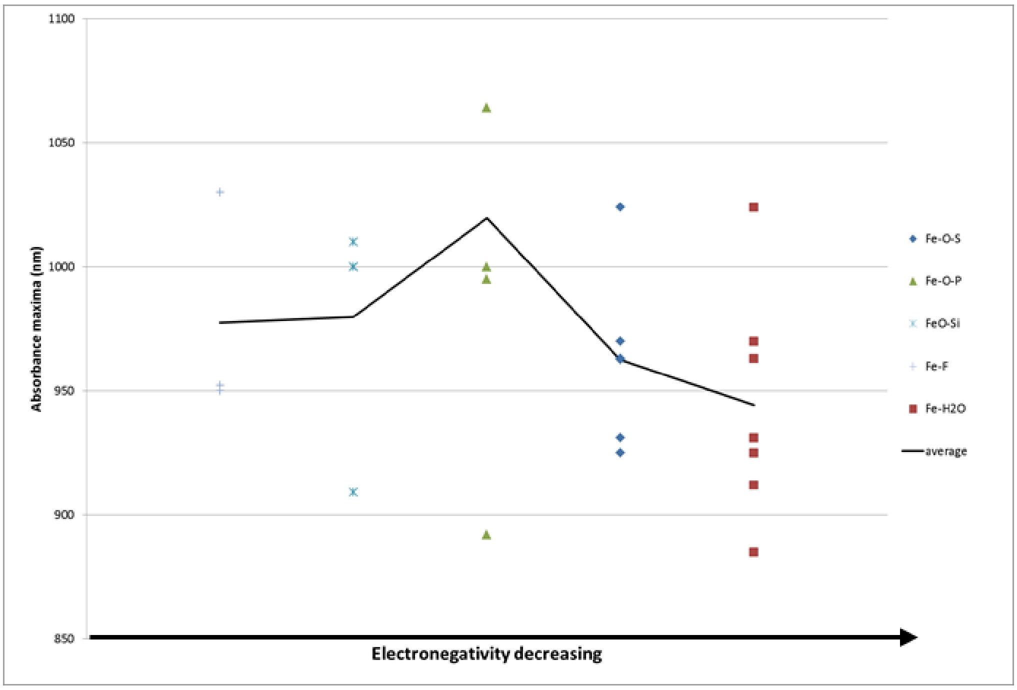

Figure 4-31 - Summary of iron six-coordinate ligand types and absorption maxima

The same inductive effect of the tetrahedral building unit can be seen in iron (II) sulphate and phosphate frameworks as was seen previously for the copper materials. The absorbance maximum for compound 44 ($Fe_2P_4O_{12}$) has been removed from the average analysis due to the possible presence of Fe (III). This inductive effect can be seen in the bond lengths around the iron centre (Table 4.20), where the average bond lengths around the iron centre generally increase from sulphate to silicate materials. The trends are more difficult to observe in the iron six-coordinate compounds due to the low number of compounds synthesised in this work and lack of optical data in the literature. This lack of data arises from the difficulty in forming iron (II) frameworks, due to oxidation to iron (III). The higher charge on iron (III), compared to iron (II), results in iron (III) compounds being more stabilised by negatively-charged ligands such as Cl and NO_3, relative to iron (II) compounds.[202] These negatively-charged ligands are good π-donor ligands, which are required to lower ΔE and enable absorbance in the NIR region.

Table 4.20 - Average bond lengths in the six-coordinate iron compounds

	Average Fe-O-S bond length (Å)	Average Fe-O-P bond length (Å)	Average Fe-O-Si bond length (Å)	Average Fe-F bond length (Å)	Average Fe-H_2O bond length (Å)
All	2.077	2.128	2.159	2.059	2.115
Equatorial	2.065	2.111	2.112	2.068	2.123
Axial	2.088	2.145	2.207	2.035	2.108

The stronger π-donor properties of fluoride ligands compared to water can be seen from Figure 4.31. A comparison between iron compounds that contain $Fe(H_2O)_6$ and FeF_6 coordination environments confirm this trend. The structures of FeF_2 and $KFeF_3$ (compounds 41 and 42) contain FeF_6 octahedra, and have absorbance maxima centred on 950 nm. FeF_2 adopts a Rutile structure; with iron centers linked through edge-sharing fluorine atoms and $KFeF_3$ (Figure 4-32) crystallizes with a perovskite type structure.

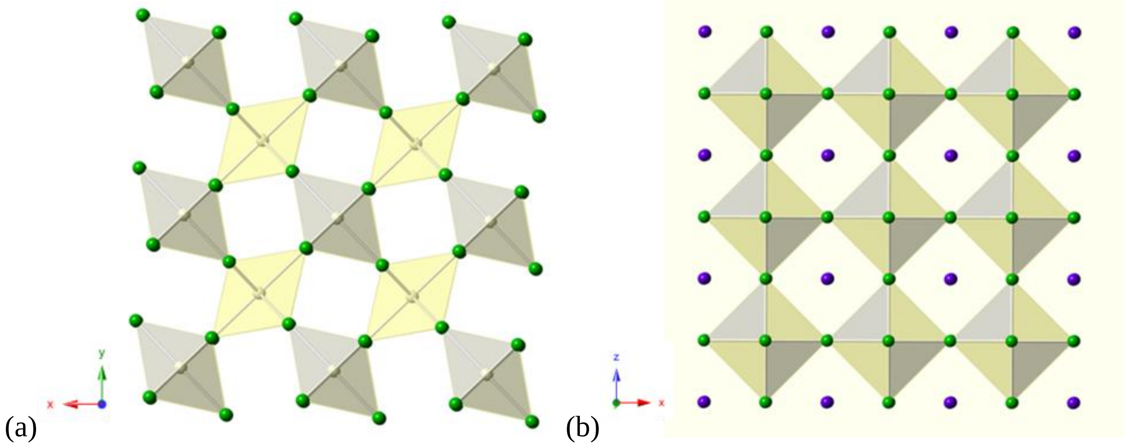

Figure 4-32 - Showing structure of (a) FeF_2 (compound 41) viewed along the c-axis and (b) $KFeF_3$ (compound 42) viewed along the b-axis. Fe^{+2} polyhedra in cream, K cations are purple spheres and F atoms are green spheres

The structures of $FeSO_4•7H_2O$ and $(NH_4)_2Fe(SO_4)_2•6H_2O$ (compounds 34 and 39) contain $Fe(H_2O)_6$ octahedra, where the metal-oxygen distances show the two longer equatorial bonds (2.15 Å) and a slightly shorter axial bond (2.07 Å). This same axial compression is observed in FeF_2 where the equatorial Fe-F bonds are 2.12 Å compared to 1.99 Å for axial ligands. The structures for compound 34 and 39 (Figure 4-33) contain $Fe(H_2O)_6$ octahedra, each bonded by two hydrogen bonds to oxygen atoms of surrounding sulphate ions.

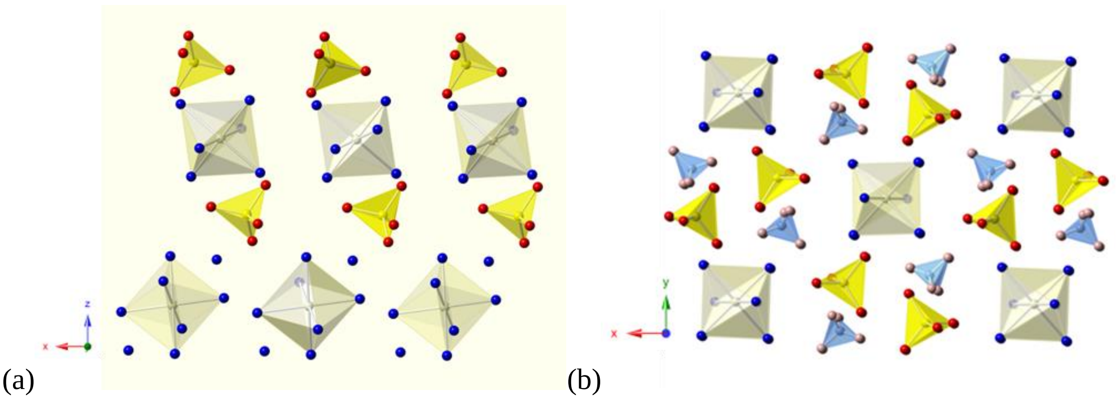

Figure 4-33 - Structure of (a) $FeSO_4 \cdot 7H_2O$ (compound 34) viewed along b-axis, and (b) $(NH_4)_2Fe(SO_4)_2 \cdot 6H_2O$ (compound 39) viewed along the c-axis. Fe $^{+2}$ polyhedra in cream, S tetrahedra in yellow, oxygen for water ligands are dark blue spheres, O atoms are red spheres, N atoms are light blue spheres and H atoms are light pink spheres

The absorption maximum in both of these hexaaqua compounds is centred on 900 nm; compared to the 950 nm observed in the hexafluoride compounds, this red shift of 50 nm is analogous to the trend observed in the six-coordinate copper compounds.

The inclusion of fluoride has a similar effect, as seen in the copper compounds, on the absorption maxima in iron sulphate materials. $NaFeSO_4F \cdot 2H_2O$ (compound 40) is isostructural with the previously-described copper compound 19, however the absorption maxima of the iron-containing material is 931 nm.

The water ligands are axial and elongated to 2.23 Å; the Fe-F bonds are equatorial and are shorter (1.84 Å) than the Fe-O-S bonds (1.98 Å). The structure of $FeSO_4 \cdot H_2O$ (compound 36) consists of chains of Fe octahedra linked through μ^2-bridging H_2O ligands; these chains are connected to each other through sulphate groups to form a 3D network (Figure 4-34). The water ligands are axial and elongated compared to the equatorial ligands, similar to compound 40. The resulting absorption maximum of $FeSO_4 \cdot H_2O$ is centred on 925 nm, implying that the addition of fluoride to Fe-O-S materials, with a similar ligand environment, has caused the absorbance maxima to shift by 6 nm. This shift is not as large as previously seen in the copper example.

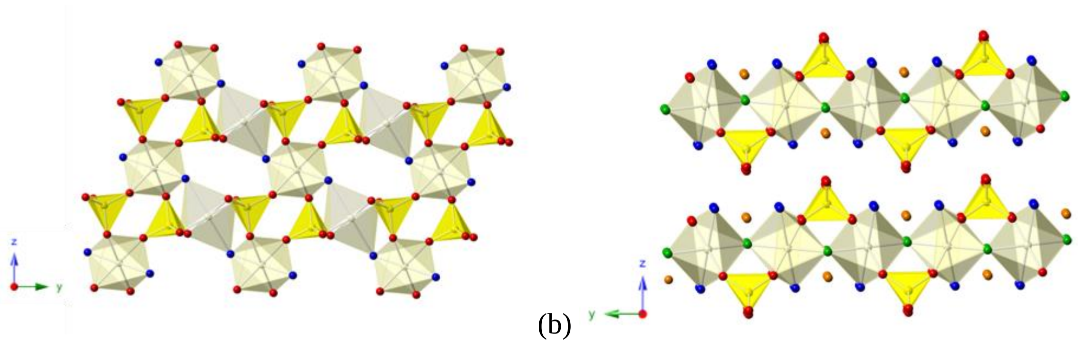

(a) (b)

Figure 4-34 - Structure of (a) Compound 36 viewed along the a-axis and (b) Compound 40 viewed along the a-axis. Fe $^{+2}$ *polyhedra in cream S tetrahedra in yellow, water ligands are dark blue spheres, O atoms are red spheres, Na cations are orange spheres and F atoms are green spheres*

Structural summary

From the bond length values presented in Table 4.18 and Table 4.20, it is clear that copper compounds undergo a stronger JT distortion compared to the iron compounds. This classic JT distortion is also observed in more than fifty Cu-O,OH,H_2O,Cl coordination polyhedra examined in a series of mineral species.[203] The JTE is stronger in the copper compounds compared to iron due to the less pronounced shielding effects in triply degenerate configurations. This reduction in shielding occurs because the orbital lobes of the t_{2g} state are oriented between the ligands, resulting in distortions that are not as severe. This distortion results in a lower symmetry around the copper centres compared to iron, and relaxes the Laporte selection rule, which consequently leads to stronger absorbance maxima in copper compounds. It is difficult to get an accurate evaluation of the intensities of absorbance maxima in the solid state due to particle size effects: however all of these materials were hand ground for p-XRD analysis, and it can be assumed that there are not significant differences in the particle size. The average absorbance maxima of the iron (II) compounds are at a longer wavelength compared to the copper compounds, 820 nm for copper and 963 nm for iron. This significant difference between the ΔE of iron and copper (1.51 eV for Cu and 1.28 eV for Fe) is expected due to the partially-filled t_{2g} orbital of iron d^6 materials, which enables π-donor ligands to decrease ΔE. This implies that for the six-coordinate compounds observed in this study, the effect of π-donor ligands on ΔE is more significant than the JTE. The evidence of this stronger π-bonding can be observed in the bond lengths: the average bond length in the iron compounds was 2.11 Å compared to 2.18 Å for copper. The ionic radius of iron (II) is larger than for copper

(II), so it should be expected that iron (II) materials should contain longer bond lengths compared to copper.

The value of ΔE is altered by the inclusion of fluoride, compared to similar ligand environments, and evidence of a red shift was noted in Cu_2PO_4F and $NaMSO_4F \cdot 2H_2O$ (M=Fe and Cu) compounds. This result is expected due to the stronger π-donor properties of fluoride compared to the other ligands found in this work.

Out of the 40 compounds described in this section, 13 of these compounds contain a mixture of water and M-O-S ligands; this is because transition metal sulphates in solution are equally likely to form with either water or sulphate, due to the bonding valences for the oxygen within H_2O and SO_4 being approximately the same (0.17 v.u), whereas PO_4 species are less soluble in water because of their greater oxygen bond valences (~0.25 v.u).[204]

It was found that the inductive effect of the tetrahedral building units (T = P. S and Si) also influenced the position of ΔE. From this trend it was expected that ΔE would decrease in the following series:

M-O-Si < M-O-P < M-O-S.

From the data collected in this study there is evidence that ΔE is reduced as the tetrahedral building unit is changed from phosphate to sulphate. The lack of data collected on six coordinate copper (II) and iron (II) silicate species reduced the reliability of the ΔE values, which could explain why silicate materials appear not to follow the expected trend.

4.4 Coordination comparison

A comparison between the absorbance maximum observed for the square planar, tetrahedral and compressed tetrahedral geometries would indicate that square planar materials are the least suitable for NIR absorbance. Tetrahedral compounds have strong absorbance in the NIR, but can also have strong absorbance in the visible region due to metal-metal and/or MLCT bands. The most promising candidates from the four-coordinate structures contain D_{2d} symmetry, as these materials have little absorbance over the visible region but very broad absorbance across the NIR region.

The absorbance spectrum of the five-coordinate trigonal bipyramids is shifted compared to the compounds that contain square pyramidal geometries. The same type of optical shift has been observed in structures containing cobalt in octahedral and square-based pyramidal environments, which display pink/purple colouring, in contrast to structures with trigonal bipyramidal Co, which are blue.[105]

The UV/Vis/NIR spectrum between the five-coordinate structures would indicate that there are no significant differences between these materials. All contain a strong absorbance in the visible region giving rise to green-coloured compounds, except for Compound 6 which is mustard coloured, which extends into the NIR region. This similarity in the absorbance spectrum can be related to the Berry twist mechanism, which enables inter-conversion between square-planer and trigonal bipyramidal geometries.[175] All of the geometries described contain distorted square pyramidal geometries, which can be perceived as a hybrid geometry between square pyramidal and trigonal bipyramidal, similar to the compressed tetrahedral geometry observed in the four-coordinate compounds.

The tetrahedral peak position can be approximately predicted using the following relationship: $\Delta_{\text{tet}} = \frac{4}{9}\Delta_{\text{oct}}$ (assuming identical ligand fields). The calculated tetrahedral absorbance maxima for copper and iron compounds should be 1845 nm and 2166 nm respectively (using 820 nm as $\Delta_{\text{oct-Cu}}$ and 963 nm as $\Delta_{\text{oct-Fe}}$). The predicted absorbance maxima of tetrahedral iron (2166 nm) is in relatively good agreement with the optical spectrum for the reported iron spinel, which contains a broad absorbance maximum at 2000 nm[169], compared to the poor agreement between the predicted absorbance maximum of tetrahedral copper (1845 nm) and observed maxima in $CuAlO_4$, 1451 nm (compound 2). The position of the peak positions can similarly be predicted for square planar geometries using the same following relationship: $\Delta_{\text{SP}} = 1.3\Delta_{\text{oct}}$. Using the same Δ_{oct} values as above, the predicted absorbance maxima was calculated to be 631 nm and 740 nm for copper and iron compounds respectively. The predicted absorbance maxima for copper square planar is in good agreement with the optical spectra of Egyptian Blue, ($CaCuSi_4O_{12}$)[168], which has a strictly square-coplanar stereochemistry and a large absorption maximum at 633 nm. The absorbance spectrum of the square planar iron silicate mineral gillispite contains a strong, sharp maximum at 500 nm[169], which is in poor agreement with the predicted value of 740 nm.

Both iron (II) and copper (II) should exhibit some form of JTE. The JTE can induce the Plasticity Effect, [168] which stems from the ability of the metal (particularly copper(II)) to accommodate, within a given set of ligands, a range of different geometries and, within a given geometry, a range of differing degrees of distortion of that geometry. These differences arise, partly, due to the cooperative Jahn-Teller effect (CJTE).[205] The CJTE in the solid-state allows random distortions and could still oscillate between the energetically-degenerate shapes in the crystal, depending on the magnitude of the perturbing forces generated by the environment in the crystal, being sufficiently strong to block the full dynamic expression of the JTE, but not big enough to suppress the distortion in its entirety. [206]

The plasticity effect in these compounds gives rise to an explanation of the broadening of the peaks. The ability of the iron and copper centres to adopt a variety of slightly different geometries within the same framework material leads to a range of energy level diagrams. Each of these geometries will have different bond lengths and angles which will affect the position of the peak. Therefore the peak maximum is the average, most common coordination environment, where the absorbance at longer wavelengths is due to coordination environments with longer bond lengths, and vice versa for absorbance at shorter wavelengths.

The splitting of the electronic energy levels in copper compounds tend to be larger than for other first-row transition metals, due to the large bond-length distortions present.[205] This behaviour has been observed for the selection of copper and iron compounds synthesised in this work. The results of this larger distortion gives rise to absorbance spectra of copper compounds, which are much broader and stronger compared to iron compounds.

4.5 Conclusions

The structural-property relationships of a range of synthesised and literature-based materials have been linked to the UV/Vis/NIR absorbance of these materials. In all of the compounds described, the weak field ligand from the phosphate/sulphate/aluminate/silicate groups result in d-d transitions that lie predominantly in the NIR region of the electromagnetic spectrum.

The assignment of electronic transitions in the absorbance spectrum is complicated by the presence of multiple metal centres with different coordination and ligand environments within the same compound. This was seen in 12 compounds; however, the overlapping absorbance maxima from the different metal sites gives rise to materials that have a strong broad absorbance spectrum.

From the materials produced in this thesis, the following compounds have been selected to be tested for their potential laser marking properties:

$K_2MP_2O_7$ (M = Cu and Fe), Cu_2PO_4OH, $Cu_4(PO_4)_2O$, $Cu_2(SO_4)O$, $NaCuPO_4$ and
$Na_2M(SO_4)_2F \bullet 2H_2O$ (M = Cu and Fe)

The results of these laser-marking trials are provided in Chapter 5: these compounds were selected as they all contain a strong NIR absorbance around 1064 nm, which should enable maximum absorption of Nd:YAG laser energy, producing an effective marking.

Chapter 5 Laser-marking

A selection of compounds which showed strong absorbance in the NIR region have been sent to Merck (Darmstadt) to test the laser-marking potential of these materials. The type of laser that was employed for the laser marking is a beam-steered Nd:YAG laser, which has an output wavelength of 1064 nm. Therefore compounds that have a strong absorbance around this wavelength were of great interest for further testing.

Once the laser type and pigment have been selected, the laser parameters need to be optimised, as these parameters have a strong influence on the laser-marking performance. In general, laser marking is achieved by introducing an amount of energy per pulse per surface area – this is called the energy density, and a higher energy density has a greater impact on the plastic. The main parameters that affect the energy density are the power, frequency, spot size, marking speed and line distance of the laser beam. The power is related to energy per pulse, and a high pulse power is achieved by storing average power over time, which is then released during a very short pulse. If the frequency of these pulses (i.e. the number of pulses per second) is low, the pulse power will increase due to more power storage between pulses. The spot size of the laser beam determines both the line width and the power of the marking process. By increasing the spot size, the line width increases and the energy density decreases. The speed at which the laser beam moves over the plastic - the marking speed - needs to be adjusted to the frequency and the number of dots per inch (dpi) that the laser marks on the plastic. Lines influence one another by transfer of heat depending on the line separation distance and the polymer type.

To evaluate the laser-marking potential of a material, a matrix is created where the laser pulse power and marking speed are varied, Figure 5-1. The marking speed decreases from the bottom to the top, and the power of the laser pulses increases from left to right. That means that the square on the bottom left receives the lowest laser energy density, and the square at the top right the highest energy density. Each test square is produced by marking numerous small dots that join to create a series of individual parallel lines, which can merge to form a solid square. The resolution of the mark is also tested by producing a matrix containing a letter matrix, mda, (Merck Darmstadt), using the same variations of laser parameters.

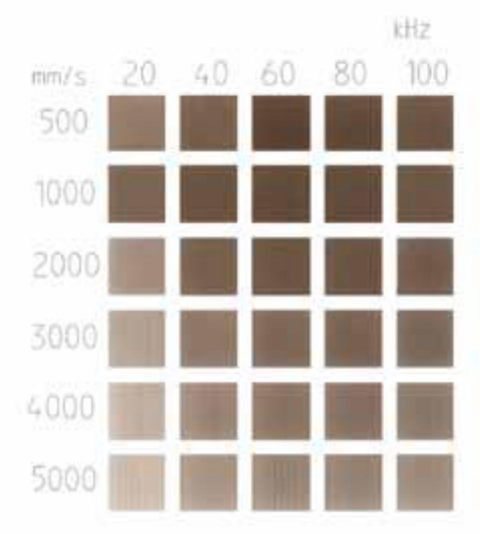

Figure 5-1-Evaluation matrix for judging laser-marking performance [9]

The initial testing of the samples is performed by doping a poly(vinyl alcohol) (PVA) film with the NIR pigment on glass, a substrate. PVA is the polymer of choice because it has very low NIR absorbance, and therefore it is easier to evaluate the performance of the pigment. The PVA film has a typical composition of 9.9 g PVA to 0.1 g sample, and is mixed with the polymer in a molten state. This polymer solution is then deposited onto a glass substrate using an ethanol solvent cast process. If the results from the initial testing are promising, the NIR pigment will be incorporated into a polycarbonate/acrylonitrile butadiene styrene (PC/ABS) polymer wafer. PC/ABS polymer mixtures are commonly used throughout the automotive industry as both interior and exterior parts, making it highly desirable to laser-mark these types of polymers. The pigment is incorporated into the polymer using the same solvent cast method described previously.

A series of eight compounds have been selected for laser-marking testing trials, and the results of these test matrices are presented within.

5.1 Compound 3-$K_2FeP_2O_7$

Compound 3 contains FeO_4 compressed tetrahedra that give rise to a strong broad absorbance centred on 1250 nm. This compound has a weak absorbance in the visible region and is almost colourless. Compound 3 was one of the first samples to be tested on a glass substrate, as can be seen in Figure 5-2. The resulting marking matrix is very rough, with poor mixing of the pigment into the polymer film. This poor mixing has decreased the marking potential of this compound. Therefore more work was needed to optimise the particle size of the pigment. This was done through ball-milling the samples, using a Retsch Mixer mill MM 200, for varying time intervals at 500 Hz. The absorbance spectrum of the different ball-milled samples can be seen in Figure 5-3. The Hand Ground (HG) sample has the broadest and most intense peak at 1250 nm and the sample ball-milled for four hours has a sharper, weaker peak. The trend of decreasing intensity of the band at 1250 nm with decreasing particle size is to be expected, due to the higher number of particles for scattering the incident beam therefore lowering the absorbance measured. The LMCT band at 300 nm shows an increase in intensity and broadness with longer milling times, which causes the milled samples to have a slightly yellow discolouration. This is possibly due to some oxidation of the iron species during the milling process, through a reaction with the stainless steel walls of the milling jar.

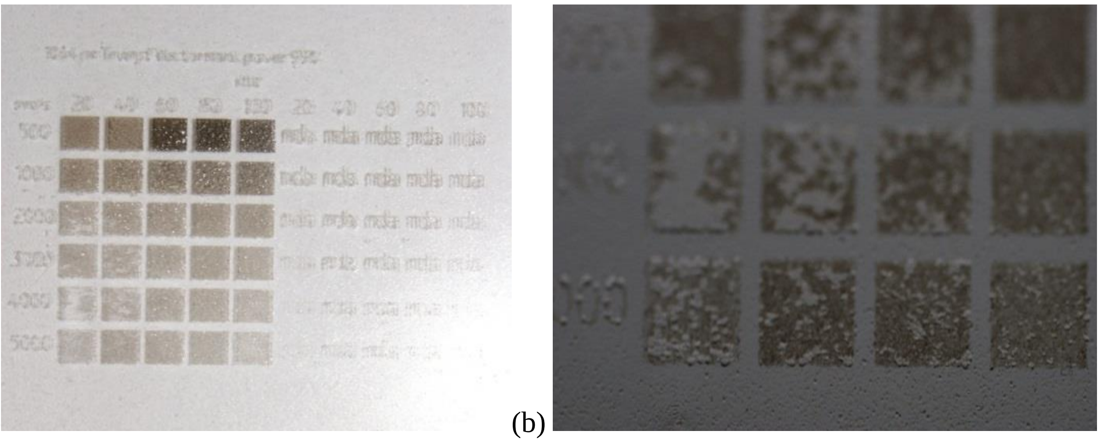

(a) (b)

Figure 5-2- (a) Initial laser-marking test matrix for compound 3 (b) close up of bottom rows of test matrix

It has been shown that particle size has a significant effect on both the intensity and position of the absorbance peak when collected using diffuse scattering. [207] This is not surprising, considering the absorbance is strongly linked to the scattering factor. The scattering of electromagnetic radiation from particles can be explained using Mie's and Rayleigh scattering theories, both of which are strongly dependent on the particle size and shape.

To determine the effect of ball-milling on the particle sizes, a combination of SEM images (Figure 5-4) and the Scherrer equation (Equation 5.1) have been employed to give approximate dimensions. The average crystallite sizes of compound 3 particles were determined from the full-width at half maximum of the $(1\bar{2}1)$ peak using the well-known Scherrer equation :[208]

$$d = \frac{0.89\lambda}{B\cos\theta}$$

Equation 5.1

Where λ is the X-ray wavelength, θ is the angle of Bragg diffraction, and B is the difference between the full width at half maximum and the instrumental broadening. The results are shown in Table 5.1 and can used as a qualitative guide to see if the particle size reduced with increasing milling times.

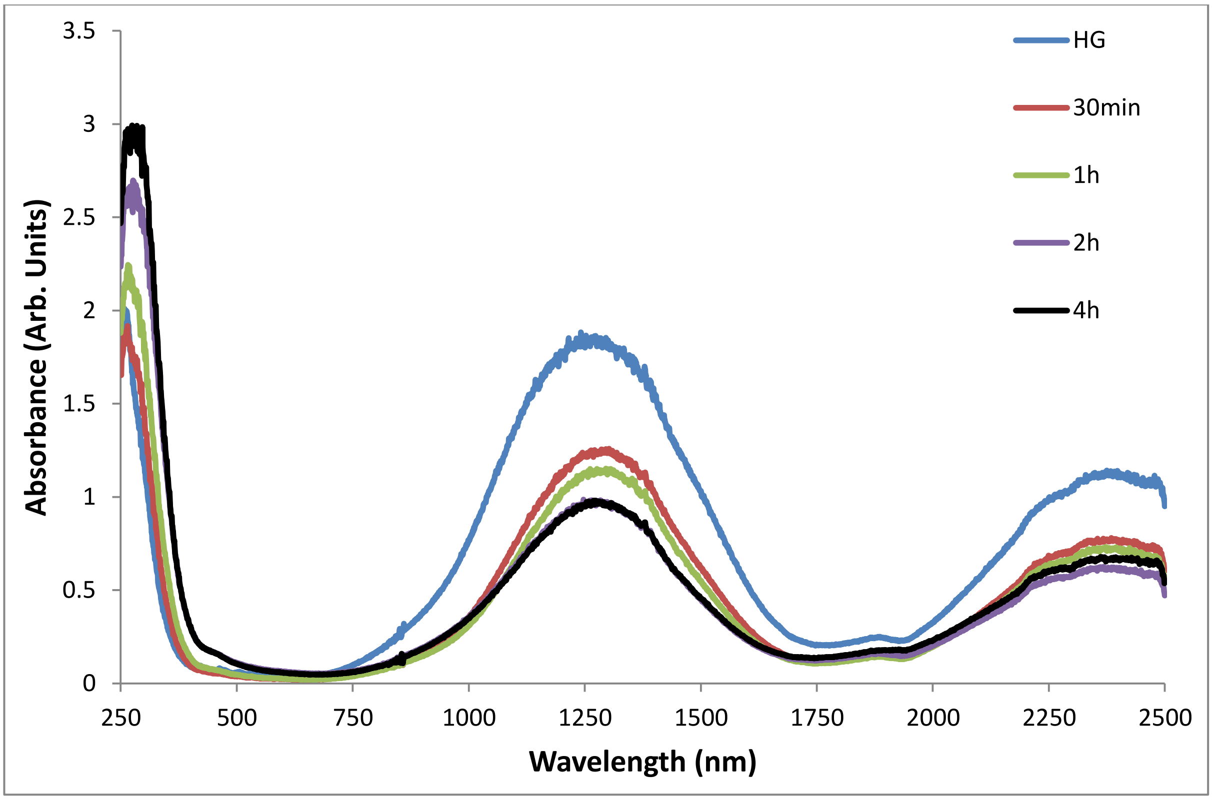

Figure 5-3-Absorbance spectrum of Compound 3 hand ground and ball-milled at different times.

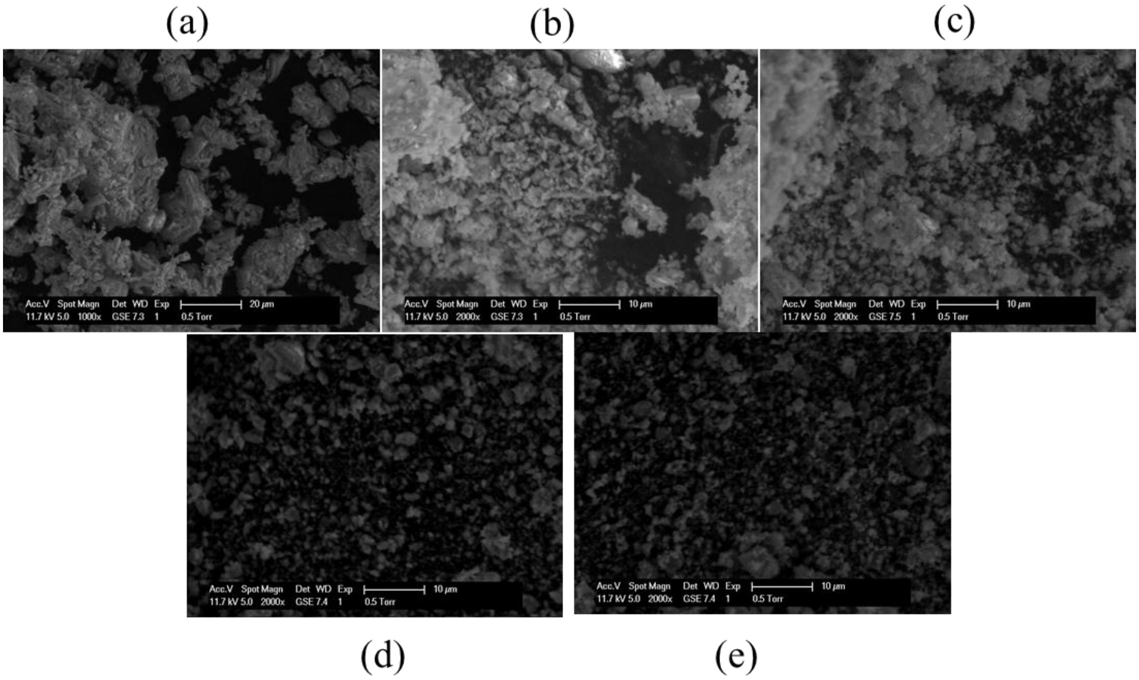

Figure 5-4-SEM images of Compound 3. (a) Hand Ground and ball milled for: (b) 30min (c) 1h (d) 2h (e) 4h

The SEM images show that there is a decrease in particle size when samples have been ball-milled for a longer length of time. The results from the Scherer equation support the trend that a decrease in crystallite size is observed from longer milling times, Table 5.1. The SEM images, Figure 5-4, indicate a tendency for smaller particles to aggregate and that the particle size distribution is non-uniformal.

Table 5.1-Crystallite size of Compound 3, determined using Scherer equation

Sample	Approximate crystallite size (nm)
Hand Ground	722
30 min	662
1 h	567
2 h	496
4 h	467

These samples with varying particle sizes were tested for their laser-marking potential with the results shown in Figure 5-5.

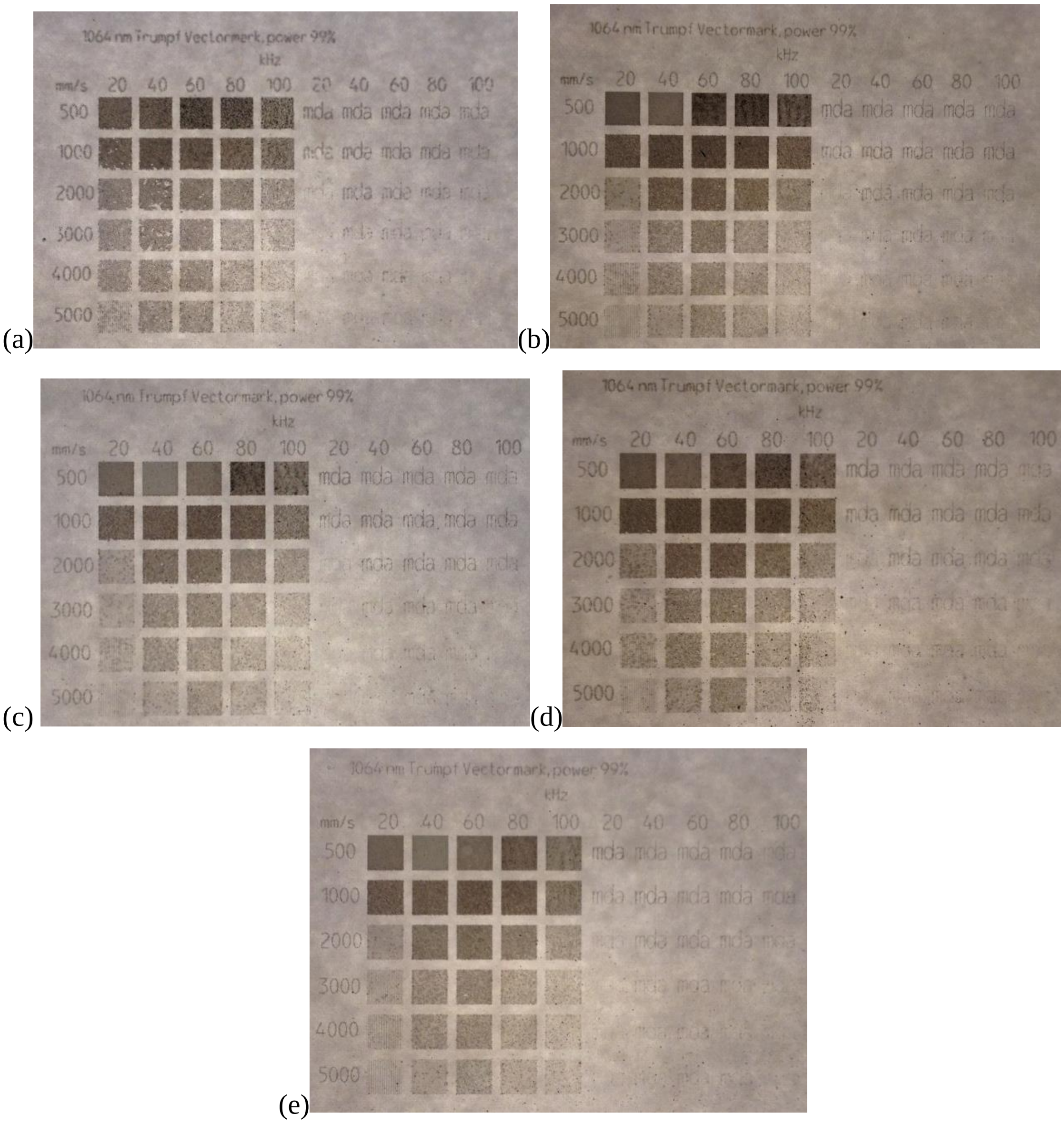

Figure 5-5- Laser-marking results for Compound 3 (a) HG and ball-milled for: (b) 30mins (c) 1h (d) 2h and (e) 4h

All of the test matrices for the ball milled samples show a dark marking, which indicates that there is carbonisation of the surrounding polymer. It has been shown that the carbonisation of the PVA polymer can occur at 200 °C with an inorganic additive. The squares in the top row show the most intense colour change, and this is to be expected as they are exposed to the highest laser energy density. A comparison of the test matrices between the different milling times show there are no significant differences in the laser-marking contrast and resolution. The presence of large pigment particles produced a rough film in all the samples and indicates that the dispersion within the polymer matrix can still be improved. However, it is unclear if these large aggregates are due to the KPO_3 impurity phase or compound 3.

The remaining samples sent for laser-marking testing were ball-milled for 30 minutes under the same conditions previously described.

5.2 Compound 5-$NaCuPO_4$

Compound 5 contains CuO_5 slightly-distorted square pyramids, which gives rise to a strong broad absorbance from 600-1500 nm. Therefore Compound 5 should strongly absorb the Nd:YAG laser radiation. The result of the laser-marking for compound 5 indicates that there is a colour change upon absorption of the laser beam at all intensities and frequency, Figure 5-6. Unfortunately the glass slide was broken during transit, which slightly hinders the examination of the laser-marking results for the text test square. The squares in the top row show the most intense colour change, and this is to be expected as they are exposed to the highest laser energy density. From Figure 5-6 it is clear to see the individual lines that make up the test squares exposed to the lowest laser energy density. Although not visible in Figure 5-6, it is also possible to see the individual laser spots within the mda test matrix, indicating an excellent resolution at low laser energy density. The polymer film produced is very smooth and no solid particles are visible: the small particle size of this compound led to a high resolution at lower laser intensities.

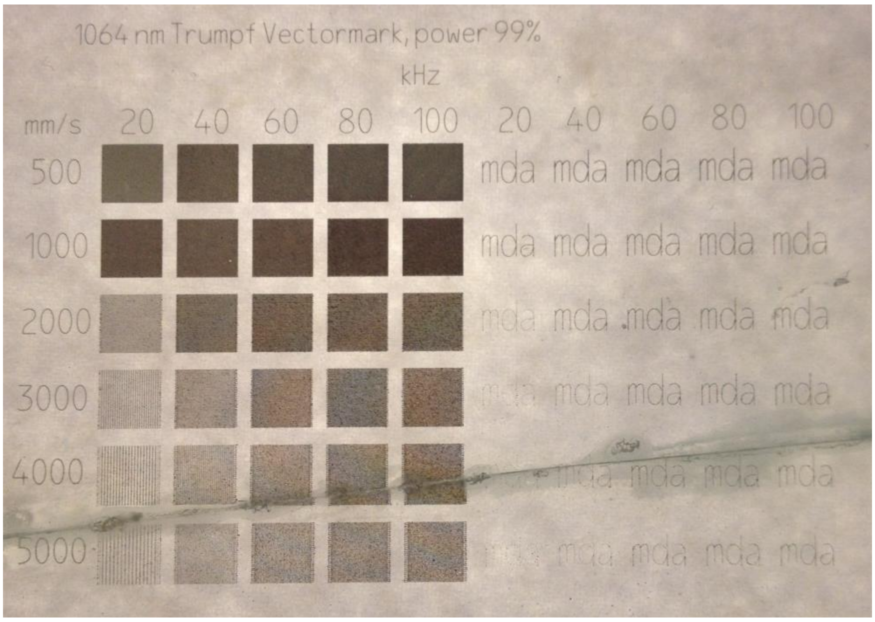

Figure 5-6-Laser-marking test matrix for Compound 5

5.3 Compound 4- $K_2CuP_2O_7$

The structure of Compound 4 contains CuO_4 JT distorted tetrahedra, which gives rise to a hybrid geometry between square planar and tetrahedral. The resulting strong absorbance spectrum of 600-2000 nm gives rise to a very pale blue/colourless compound depending on the amount of KPO_3 impurity, which darkens the colour compound to a grey/blue. A high purity sample of Compound 4 was selected for laser-marking trials, Figure 5-7. The strong NIR absorbance of this compound gives rise to good laser-marking properties at all laser intensities. A charring process gives rise to a dark marking, which is most intense at the highest laser energy densities. The strong NIR absorbance of Compound 4 means that it is possible to distinguish individual laser spots that make up the mda mark for the lowest laser density. Unfortunately, this cannot be seen clearly using the photo in Figure 5-7. However, the dark marking effect is not as pronounced as seen for Compound 5, which is surprising considering the similarity in the absorbance of these materials at 1064 nm. The difference between the marking strength of these compounds could be related to poor thermal transfer between pigment and polymer, which is related to the particle size and dispersion.

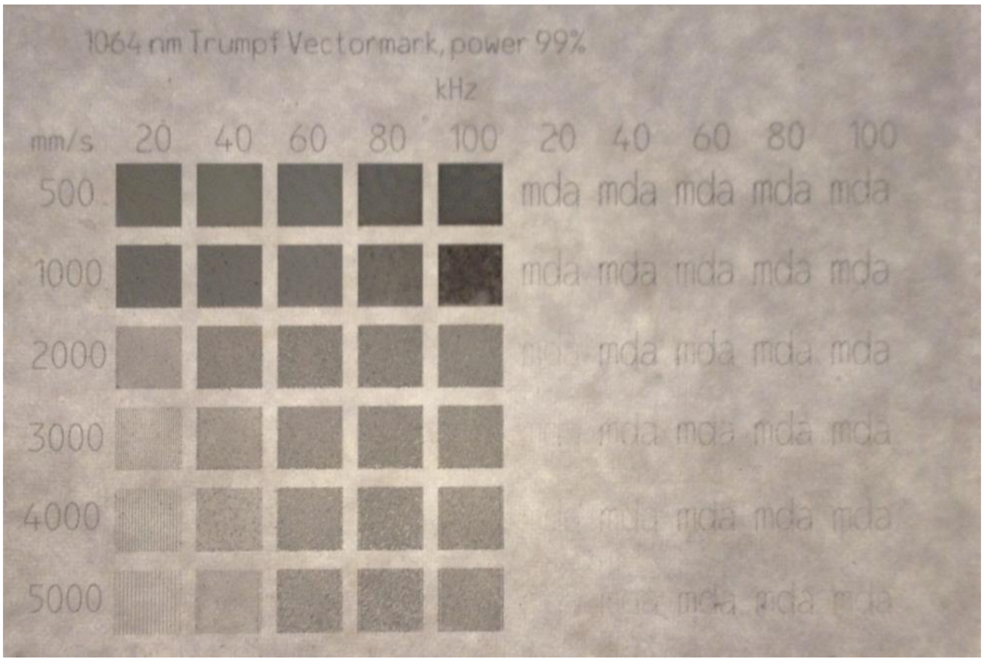

Figure 5-7-Laser-marking test matrix for Compound 4

5.4 Compound 6- Cu_2SO_4O

Compound 6 contains CuO_6 octahedra and CuO_5 square pyramid centres, with an absorbance band from 600 to 1500 nm, which gives rise to a mustard yellow coloured pigment. This mustard colour has stained the PVA polymer film which gives the illusion of a coloured mark, Figure 5-8. The pigment has caused carbonisation of the surrounding polymer thereby inducing a dark marking. The most intense dark marking is observed in the highest laser energy densities, which are consistent with previous compounds, Figure 5-8. The poor laser-marking properties of this material are surprising considering the strong absorbance maxima around 1064 nm. Compound 6 also produces a relatively smooth film, which indicates a smaller particle size that should enable efficient heat transfer to the polymer and provide an intense marking effect.

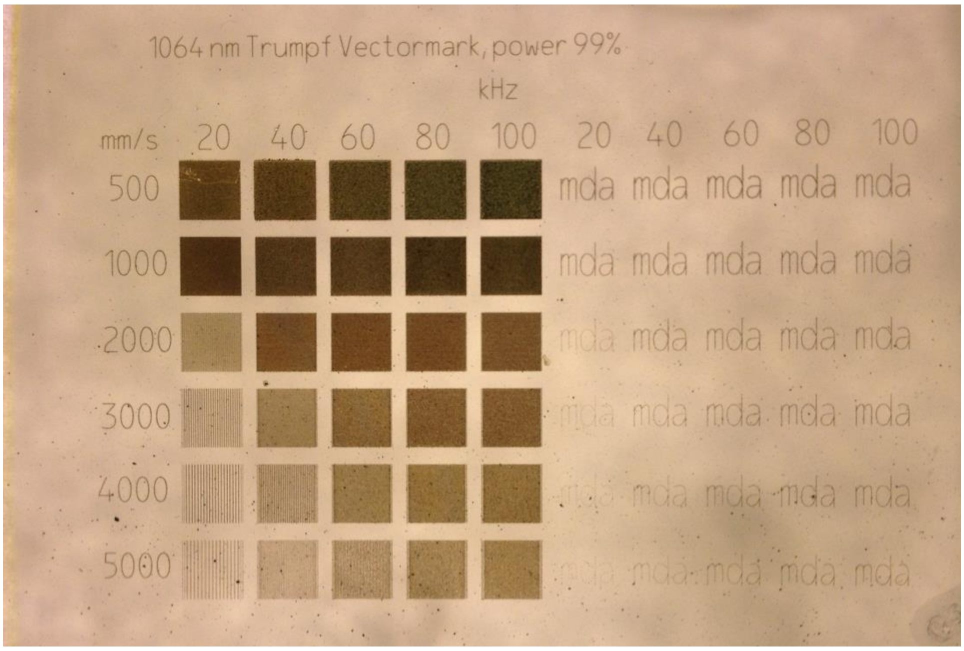

Figure 5-8-Laser-marking test matrix for Compound 6

5.5 Compound 40- $Na_2Fe(SO_4)_2F\bullet2H_2O$

Compound 40 contains $FeO_2F_2(H_2O)_2$ octahedra, with a weak absorbance spectrum centred around 1000 nm due to the almost perfect octahedral coordination around the iron centre. This compound also contains a minor impurity of the dehydrated phase, $Na_2Fe(SO_4)_2F$. This compound changes from a pale cream to yellow in colour when exposed to air, suggesting there is oxidation of the iron centre. This has caused the polymer film to be stained yellow once the pigment has been incorporated into the matrix. It was anticipated that the heating of this compound would lead to a change in the coordination environment due to the removal of water ligands. However, the results (Figure 5-9) show that there is no significant colour change once the pigment has been irradiated under the laser beam. The laser matrix shows the same charring effect as the other pigments, and results in a dark marking. Figure 5-9 shows there is a more pronounced marking effect with higher laser energy density, but it is still very weak: although it’s clear to see that at lower laser energy density the lines that make up the test matrix are visible, indicating a good resolution and small particle size. There is no apparent marking for any of the mda test matrices at low laser energy density, which suggests this material is a weak NIR absorber which is not surprising when considering the high symmetry metal coordination.

The TGA results of this compound suggest that water is lost at 150 °C [204], which induces the structural change in compound 40. This temperature is lower than the melting point and possible carbonisation of PVA film at 200 °C. It may still be possible that a colour change could be induced, but the laser energy density is too high, causing carbonisation rather than the desired colour change.

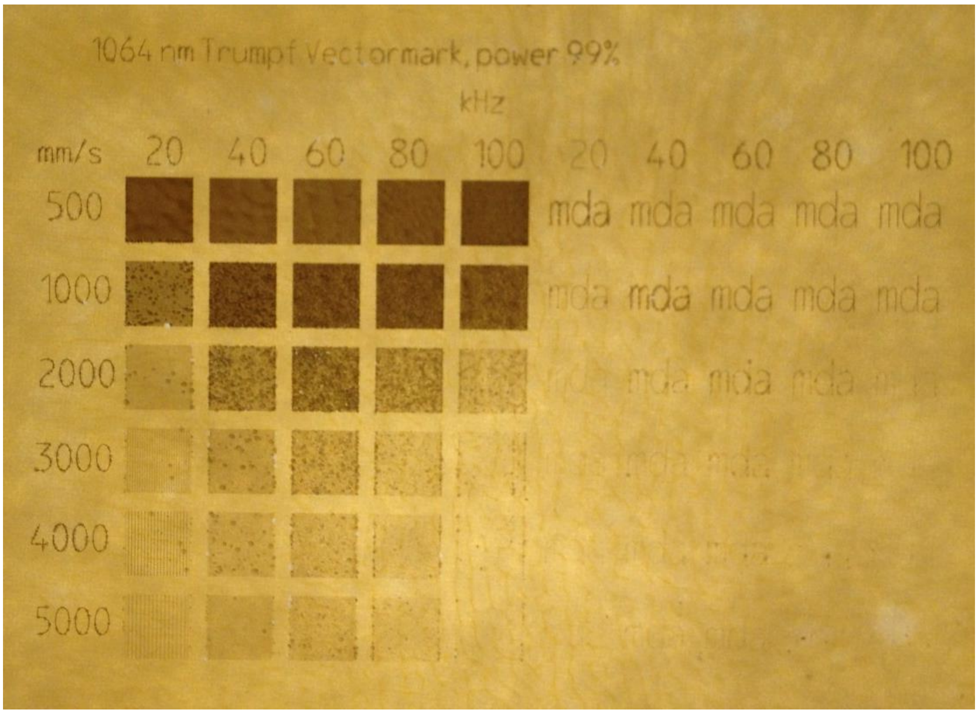

Figure 5-9-Laser-marking test matrix for Compound 40

5.6 Compound 19- $Na_2Cu(SO_4)_2F\bullet 2H_2O$

Compound 19 contains the same coordination environment as compound 40, however the JTE of the copper centre changes the optical properties of this material. The absorbance spectrum of compound 19 has a peak centred on 808 nm- the tail end of this absorbance peak gives rise to a very pale green blue. When this compound was heated to 250 °C there was a clear colour change from blue to green: again it was anticipated that this compound would change colour upon being irradiated under the laser beam. The laser-marking results, Figure 5-10, show that there is a colour change of this material at higher laser energy densities. However, as the polymer film has been dyed blue/green by the pigment, the marking is still due to a charring effect, and forms a dark mark. The resolution of the mark for this compound is very high, which is the same for compound 40, suggesting the solid state hydrothermal technique used to produce these materials gives rise to very small particles. The high symmetry of the copper centre in compound 19, results in a weak absorbance at 1064 nm, which consequently leads to a relatively-weak marking effect.

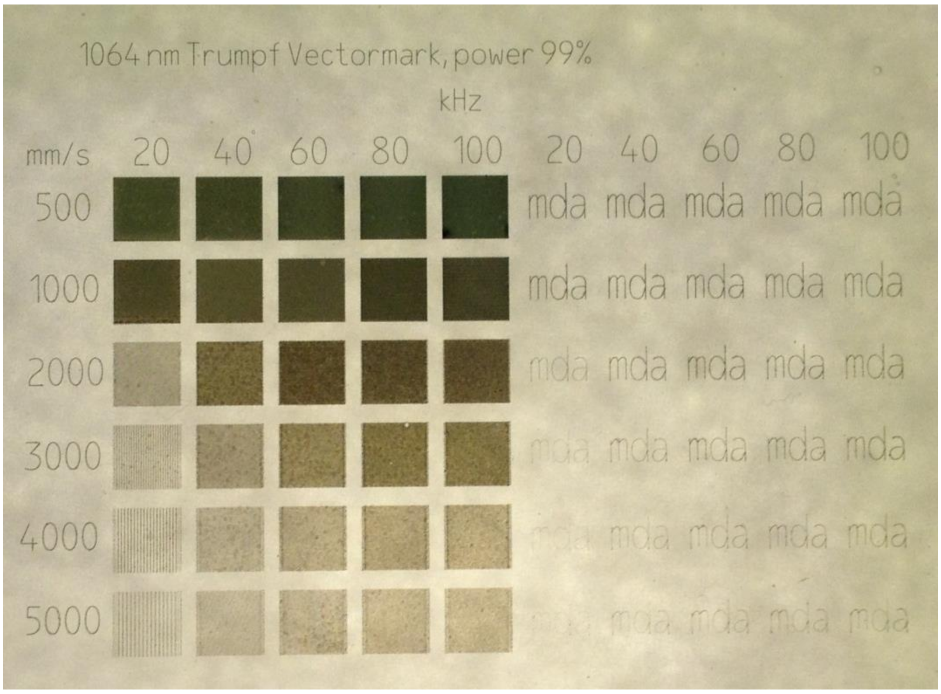

Figure 5-10-Laser-marking test matrix for Compound 19

5.7 Compound 8- Cu_2PO_4OH

Compound 8 produced an opaque film that contains visible particles of the pigment that aggregated during the milling process. The $CuO_4(OH)$ and $CuO_4(OH)_2$ copper polyhedra give rise to a strong broad absorbance from 500 to 1800 nm- this means the compound results in a pale green colour. The film produced is opaque with visible pigment particles that have not been fully dispersed. The laser-marking matrix for compound 8 (Figure 5-11) shows a high degree of charring, which gives rise to a dark marking. This dark marking is present at all laser intensities for both the test squares and letter matrices. The mda test matrix shows that the matrix exposed to the highest laser energy density has the strongest marking. However, for the square matrix this is not the case, and it's at 1000 mm/s that the strongest marking is observed. The test squares exposed to the highest energy density look patchy. This is due to the excess heat causing a foaming effect on the polymer, compared to the charring that is normally seen. Due to the excellent laser-marking produced on the test matrix, it was decided that Compound 8 would be selected for full testing in the PC/ABS polymer system.

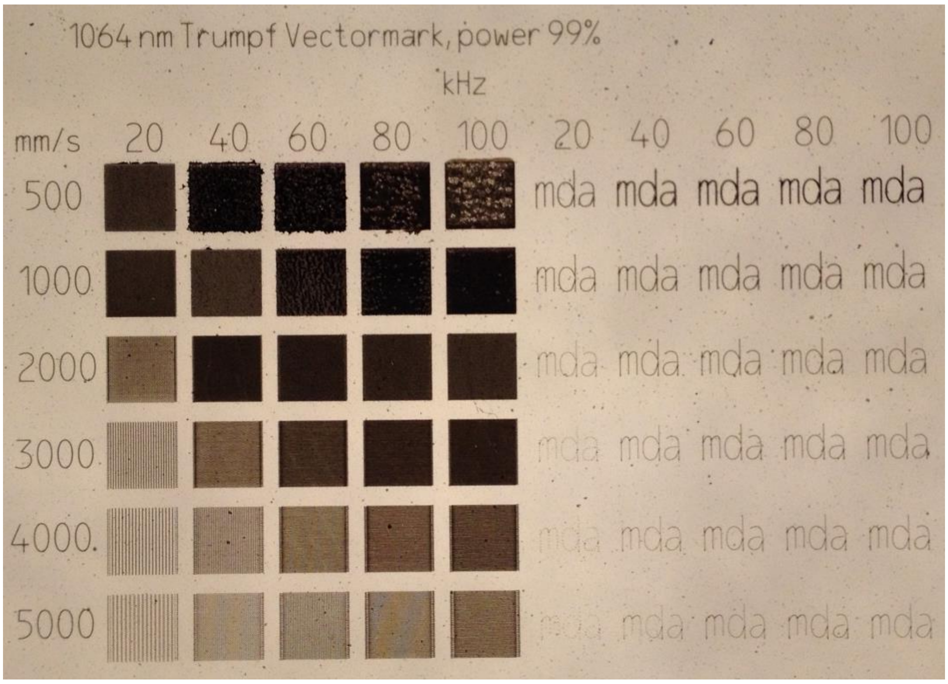

Figure 5-11-Laser-marking test matrix for Compound 8

5.8 Compound 7- $Cu_4(PO_4)_2O$

Compound 7 contains copper situated in variety of distorted four, five and six coordinate geometries, which gives rise to a strong absorbance maxima from 500-1500 nm. The strong absorbance in the visible region gives rise to a green-coloured polymer film. The test matrices of Compound 7 (Figure 5-12) show a similar trend to Compound 8 (Figure 5-11). Both have a very strong charring effect and excellent laser-marking at all laser energy densities for both the square and letter matrices. Compound 7 also shows that the test squares exposed to the highest laser energy density do not provide the strongest marking due to the potential foaming effect. There is a poor dispersion of compound 7 in the polymer matrix, which results in the presence of visible pigment particles and poor resolution of the mark, particularly on the mda test matrix.

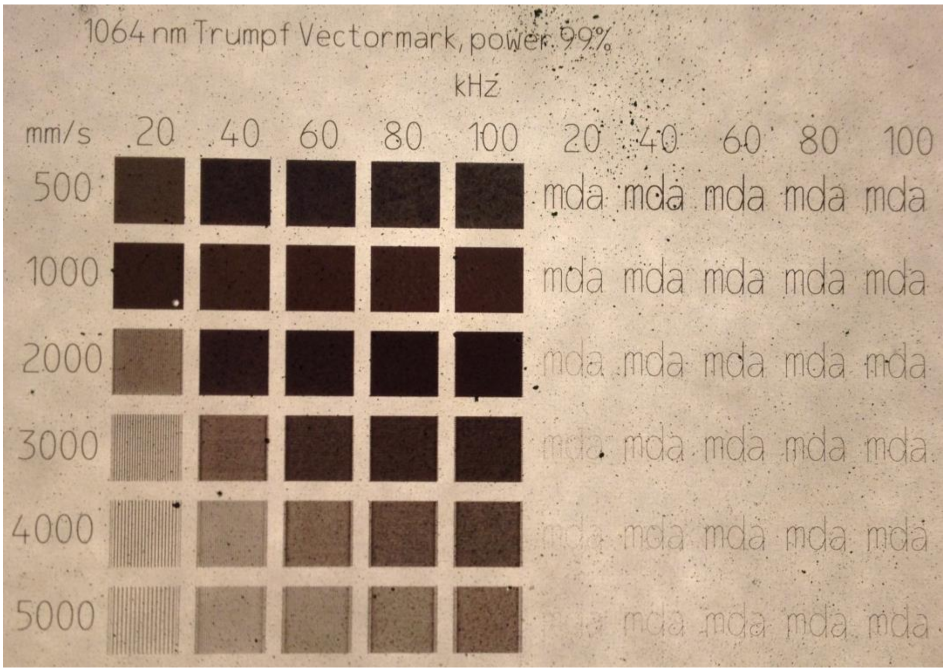

Figure 5-12-Laser-marking test matrix for Compound 7

5.9 PC/ABS polymer wafer test

Compound 7 and 8 were selected for further laser-marking trials and the initial results (Figure 5-13) showed that a significant amount of oxidative degradation of the polymer matrix occurs. The degradation reduces the polymers molecular weight and as a consequence of this change the material becomes more brittle, with a reduction in its tensile, impact and elongation strength. Discoloration and loss of surface smoothness accompany degradation. The degradation of carbonyl groups in the PC/ABS matrix, in the presence of oxygen, leads to the formation hydroperoxide groups, which can further decompose to produce free radicals. [209] The copper center, at the higher loadings in the wafer tests, can act as a catalyst in the propagation step for this degradation by providing electrons.

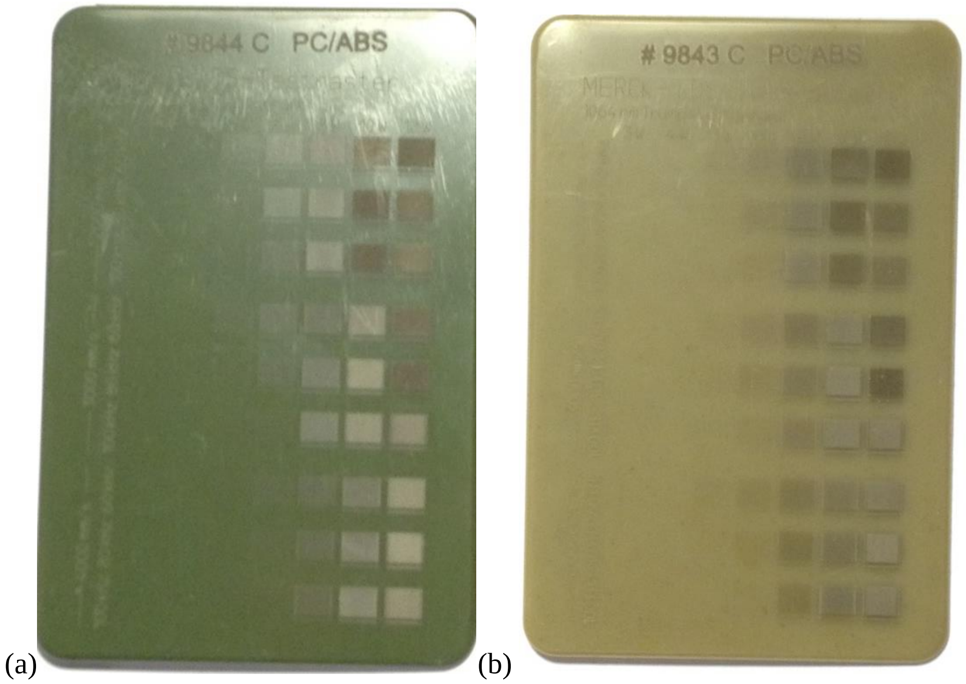

Figure 5-13-Test matrices in PC/ABS wafer without antioxidant agent for (a) compound 7 and (b) compound 8

The experiments were repeated with 1% wt antioxidant agent present to prevent the degradation of the polymer. The antioxidant used during these trials was Irganox® 1010 – a sterically-hindered phenolic antioxidant, which was shown to inhibit degradation from other laser-marking trails. In order to evaluate the suitability of these compounds as potential laser-marking pigments, a test matrix for Iriotec 8840 ®- a commercial Merck laser-marking pigment- has been provided as a standard, Figure 5-14.

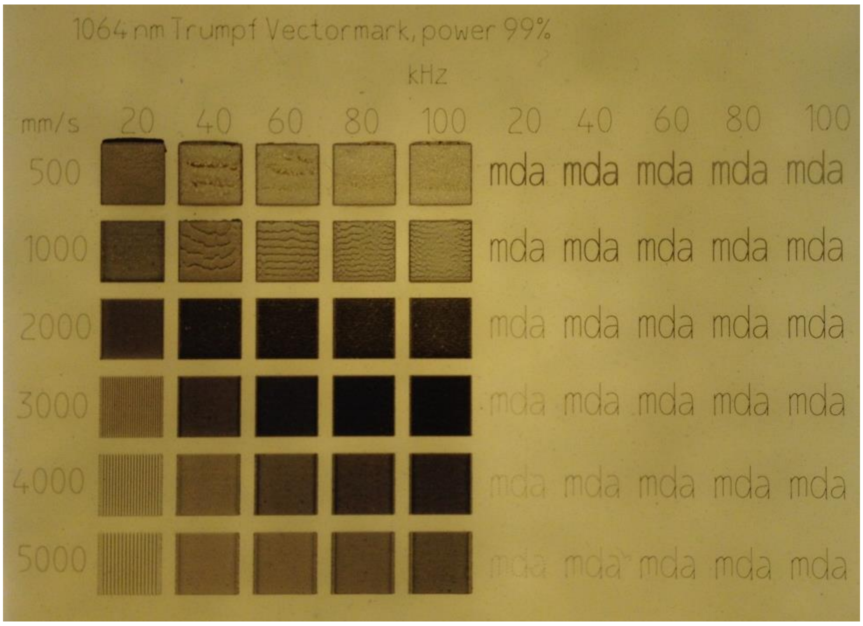

Figure 5-14-Laser-marking test matrix for Iriotec 8840 ® in *PC/ABS polymer wafer*

Compound 8- Cu_2PO_4OH

The green colour of the polymer matrix (Figure 5-15) indicates that there is still some oxidative degradation: however, this degradation is significantly less than seen in Figure 5-13. The marking of the ABS/PC wafer shows a similar trend to the previous PVA test matrix of this compound (Figure 5-11). The most intense marking is not at the highest laser energy densities but along the 2000 mm/s row. The test squares at the highest energy densities are textured, which could arise from the degradation of the polymer.

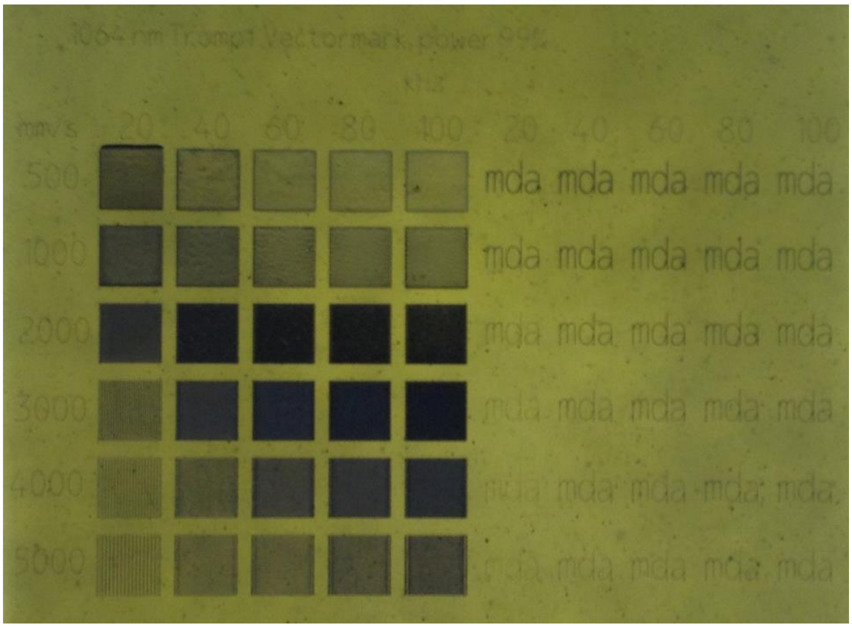

Figure 5-15-Laser-marking test matrix for Compound 8 in *PC/ABS polymer wafer*

Compound 7- $Cu_4(PO_4)_2O$

The results from the PC/ABS polymer matrix (Figure 5-16) are comparable to Iriotec 8840 ® (Figure 5-14). At the highest laser energy densities the marking is weaker, but is textured, which would suggest that there is some foaming of the polymer. This textured marking is also present in Iriotec 8840 ® and Compound 7, indicating this is fairly common in laser-marking pigments. The lower laser energy densities (3000 mm/s) show a particularly strong marking contrast, which suggests that the pigment is effectively carbonising the surrounding polymer matrix. There are still some visible particles of Compound 7 in the PC/ABS polymer matrix, which result in poor resolution of the test matrices at low laser energy densities.

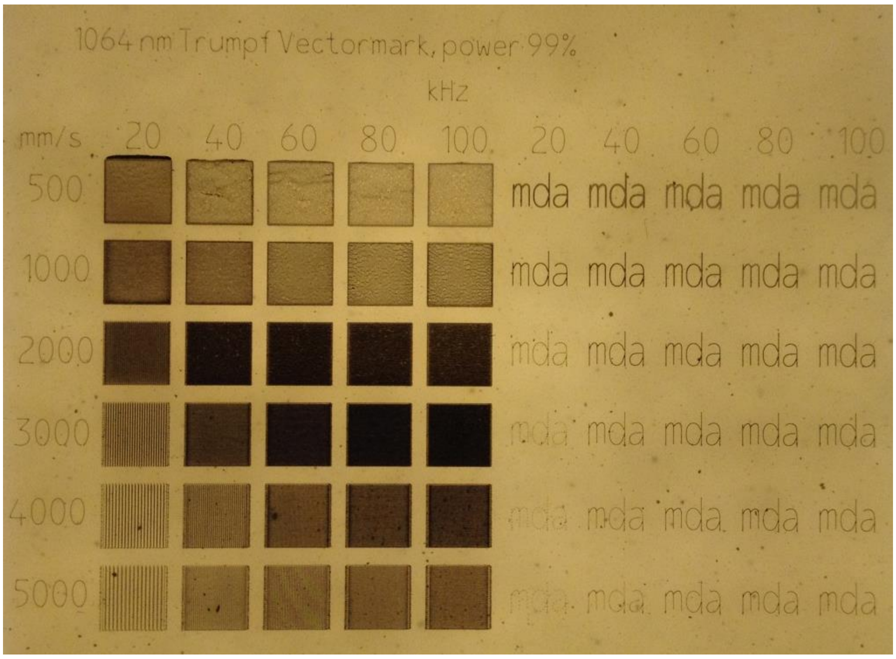

Figure 5-16-Laser-marking test matrix for Compound 7 in *PC/ABS polymer wafer*

5.10 Conclusion

Eight compounds have been sent to Merck Darmstadt and irritated under a Nd:YAG laser to test for new laser-marking pigments. The majority of the compounds were tested using a PVA polymer matrix. All of the compounds showed a charring effect when exposed to the laser beam, which results in a dark marking. This dark marking was generally more pronounced with the test matrices exposed to the highest laser energy density. Compounds 7 and 8 showed a very intense charring effect in the PVA polymer test, and were selected for further testing in a PC/ABS wafer. These compounds needed the addition of an antioxidant to prevent reaction of the copper center with the polymer. Compound 7 showed similar laser-marking effect to a commercial Merck laser-marking pigment (Iriotec 8840 ®)

Chapter 6 Conclusions and further work

The reviews of current iron and copper frameworks provided in Chapter 1 highlight the lack of research into the optical properties of these materials, specifically for NIR absorbance. The aim was to create a library of iron and copper frameworks, and determine their NIR absorbance and the prospect of developing structural-property relationships.

The initial work to build this library focused on using hydrothermal techniques to synthesise new materials, which included fluoride to add further structural diversity. The result of this initial work was provided in Chapter 3, which described the structures of 13 iron fluorophosphate compounds and provides insight into the unique structural features due to fluoride inclusion. Most of these iron fluorophosphate materials contained iron (III) and mixed valence iron centres, even though reactions were performed under an inert atmosphere or reducing conditions. It is possible that the additional electron-withdrawing/sigma donor character of the fluoride ion stabilises higher oxidation states on the iron centre.[102]

These new materials have been synthesised utilising the hydrofluorothermal method, which aims to increase the F:O ratio through minimising water content: this has led to 13 new iron fluorophosphates being formed, with 11 containing fluoride. The incorporation of fluoride into the iron phosphate framework structures effectively replaces oxide with fluoride on the iron or phosphorus site: this changes both the structural and compositional aspects of the chemistry.[102]

Three interesting features involving fluoride were found in this thesis, specifically: (i) the preference for fluoride to adopt bridging sites between iron centres; (ii) the common formation of PO_3F and more rarely PO_2F_2 linking polyhedral units; and (iii) the fluoride ligand always points into a channel or interlayer region. The drawback of this hydrofluorothermal method is the large number of variables that can affect the purity of the final product. If the synthesis conditions were modified to yield pure phases of these materials, it would be possible to investigate possible electrochemical and magnetic properties.

Initial thermal properties showed these compounds to be relatively stable, with the introduction of OH-groups or organic template molecules acting to reduce the thermo-stability. The TGA results of some of these iron fluorophosphate materials are consistent with structural collapse, which is consistent with previously-reported, organically-templated iron frameworks [73]. This structural collapse arises from the strong template-framework interaction, which occurs due to the protonation of the amine template from the acidic conditions. The synthesis was performed under strong acidic conditions to stabilise iron (II) metal centres. Future work could centre on using more neutral or alkaline pH conditions to reduce protonation of amine templates, therefore diminishing template-framework interactions, which could improve the thermal stability of these frameworks.

This thesis briefly investigated the incorporation of chloride and fluoride ligands into iron frameworks, forming the first example of a synthesised iron chlorofluorophosphate material (compound XII). The introduction of halide anions, in particular chloride, has been shown to facilitate the formation of new structural features in copper phosphate frameworks, which include the inclusion of Cl salts in the crystal lattice.[210, 211] These compounds were found to readily undergo ion-exchange , and contain a high thermal stability, as well as interesting catalytic behaviour in the aerobic selective oxidation of benzyl alcohol to benzaldehyde for a partial-thermally decomposed, $[AuCl_4]^-$-containing material.[211] The lack of research into these halide-containing iron frameworks leads to a possibility of synthesising new materials with interesting electrochemical, catalytic and magnetic properties.

A range of iron (II) and copper (II) frameworks have been synthesised using solid state and precipitation methods. The effect of the geometry and ligand environment on the optical properties of these materials was investigated and presented in Chapter 4.This is one of the first examples of investigating the potential of framework materials for their optical properties. It was shown that copper and iron (II) materials in four-, five- and six-coordinate geometries have absorbance in the NIR region.

A selection of four coordinate structures with square planar, tetrahedral and compressed tetrahedral geometries were synthesised, and optical properties reported for the first time. The square planar compound 1 had an absorbance maximum at 720 nm which is similar to the well-known optical properties of Egyptian Blue, a square planar copper silicate framework. A rare example of a tetrahedral copper framework, compound 2, indicated an absorbance maximum of 1451 nm.

The tetrahedral peak position can be approximately predicted using the following relationship: $\Delta_{\mathrm{tet}}= \frac{4}{9}\Delta_{\mathrm{oct}}$,- similarly, the peak positions for square planar geometries can be predicted using the following relationship: $\Delta_{\mathrm{SP}}= 1.3\Delta_{\mathrm{oct}}$. It was found that the predicted values for the square planar and tetrahedral geometries in both iron (II) and copper (II) were in poor agreement with observed absorbance maxima. It has been shown in chapter 5, that particle size has a significant effect on both the intensity and position of the absorbance peak when collected using diffuse scattering. This is not surprising considering that the absorbance is strongly linked to the scattering factor. The scattering of electromagnetic radiation from particles can be explained using Mie’s and Rayleigh’s scattering theories, both of which are strongly dependant on the particle size and shape.

The structures of $K_2MP_2O_7$ (M=Fe and Cu) were solved by SXD, and the bulk material confirmed by Rietveld refinement. The geometry of the metal centres was determined to have D_{2d} symmetry due to the compressed tetrahedral coordination. The degree of this compression varied for the iron and copper analogues, where it was found the copper compound was more square planar in character than iron. This hybrid geometry was reflected in the optical properties of these materials which had a strong broad absorbance maximum at 1147 nm and 1230 nm for iron and copper respectively.

Numerous five-coordinate copper compounds were reported which contained square pyramidal and trigonal bipyramidal geometries. The UV/Vis/NIR spectrum between the five-coordinate structures would indicate that there are no significant differences between these materials. All contain a strong absorbance in the visible region, giving rise to green coloured compounds, except for Compound 6 which is mustard coloured, and which extends into the NIR region. This similarity in the absorbance spectrum can be related to the Berry twist mechanism, which enables inter-conversion between square-planer and trigonal bipyramidal geometries.[175] All of the geometries described contain distorted square pyramidal geometries which can be perceived as hybrid geometry between square pyramidal and trigonal bipyramidal, similar to the compressed tetrahedral geometry observed in the four-coordinate compounds.

A large number of six-coordinate iron and copper frameworks were synthesised allowing the investigation of the effect of ligand environment on the optical properties. A comparison between the ligand environment between hexaaqua and hexafluoride followed the expected trend from the spectrochemical series, where the position of O_2^- oxide and O_2^- water is still uncertain. The optical properties of the six-coordinate frameworks were influenced by the inductive effect of the tetrahedral building units (T= P. S and Si). From this trend in inductive effect, it was expected that ΔE would decrease in the follow series:

$$\text{M-O-Si} < \text{M-O-P} < \text{M-O-S}.$$

From the data collected in this study there is evidence that ΔE is reduced as the tetrahedral building unit is changed from phosphate to sulphate. The lack of data collected on six coordinate copper (II) and iron (II) silicate species reduced the reliability of the ΔE values, which could explain why silicate materials appear not to follow the expected trend. The stronger inductive effect of the tetrahedral unit would result in fewer electrons for π-bonding to the metal centre, producing weaker and longer M-L bonds, triggering a red shifting of the optical properties.

The average absorbance maxima of the iron (II) compounds are at a longer wavelength compared to the copper compounds: 820 nm for Copper and 963 nm for iron. This significant difference between the ΔE (HOMO and LUMO) of iron and copper (1.51 eV for Cu and 1.28 eV for Fe) is expected due to the partially-filled t_{2g} orbital of iron d^6 materials enables π-donor ligands to decrease ΔE. This implies that for the six-coordinate compounds observed in this study, the effect of π-donor ligands on ΔE is more significant than the JTE.

Most of the copper and iron frameworks described in this work and in the literature contain more than one type of coordination environment around the metal centre. This makes accurate interpretation of the absorbance spectrum difficult. To get a better understating of the impact of geometry distortions on the energy levels involved during electronic transitions, it is possible to perform energy level calculations using density functional theory. [212]

The splitting of the electronic energy levels in copper complexes tend to be larger than for other first-row transition metals, due to the large bond-length distortions present. [205] This behaviour has been observed for the selection of copper and iron compounds synthesised in this work. The ability of the iron and copper centres to adopt a variety of slightly different geometries within the same framework material leads to a range of energy level diagrams. Each of these geometries will have different bond lengths and angles, which will affect the position of the peak. Therefore the peak maximum is the average, most common coordination environment, where the absorbance at longer wavelengths is due to coordination environments with longer bong lengths, and vice versa for absorbance at shorter wavelengths.

A selection of eight compounds which showed strong absorbance in the NIR were sent to Merck Darmstadt and irradiated under a Nd:YAG laser to test as a new laser-marking pigment. The majority of the compounds were tested using a PVA polymer matrix. All of the compounds showed a charring effect when exposed to the laser beam, which results in a dark marking. This dark marking was generally more pronounced with the test matrices exposed to the highest laser energy density. Compounds 7 and 8 showed a very intense charring effect at all laser energy densities in the PVA polymer test, and were selected for further testing in a PC/ABS wafer. The initial test of these compounds indicated that there was oxidative degradation of the polymer matrix due to the inclusion of the copper. The addition of the anti-oxidative agent Irganox® 1010 resulted in Compound 7 showing similar laser-marking effect to a commercial Merck laser-marking pigment (Iriotec 8840 ®), whereas compound 8 still showed signs of oxidative degradation. This work has shown that iron (II) and copper (II) framework materials can be used as laser-marking pigments with comparable results to commercial products. However, the next generation of laser-marking pigments need to exhibit intrinsic colour-changing properties to move away from the dark or light marking currently available. In order for a material to have intrinsic colour changing properties, a significant change in the optical properties are required when irradiated under the laser beam.

A strong possibly was to investigate dehydration around the metal centre, which can induce changing in the metal coordination number and environment. The results from Compounds 40 and 19 showed there was no significant change in colour when the sample was irritated under the laser beam, even though these materials should dehydrate around 200 °C. The temperature of the pigment when irradiated under the laser beam needs to be investigated, which would help gain further understanding as to the temperature range possible before inducing a charring or foaming process of the polymer. This change in ligand environment did not produce a large enough colour change: however, materials that could change coordination number upon dehydration have the potential for large difference in ΔE. A cobalt-containing framework has been reported to change from a six-coordinate octahedral to a five-coordinate square pyramid upon dehydration.[213] The solid-state optical properties of this transformation indicate a shift from 634 nm to 504 nm in the octahedral and square pyramidal geometries respectively.

Chapter 7 References

1. D. F. Shriver and P. W. Atkins, *Inorganic Chemistry: third edition*, Oxford University press, Oxford, 1999.
2. O. G. Holmes and D. S. McClure, *The Journal of Chemical Physics*, 1957, **26**, 1686-1694.
3. D. F. Shriver, P. W. Atkins, T. L. Overton, J. P. Rourke, M. T. Weller and F. A. Armstrong, *Inorganic chemistry: fourth edition*, Oxford University press, Oxford, 2006.
4. H. W. Siesler, Y. Ozaki, S. Kawata and H. M. Heise, *Near-Infrared Spectroscopy: Principles, Instruments, Applications*, Wiley, Weinheim, 2002.
5. R. J. C. Brown, A. C. Keates and A. S. Brown, *Anal. Chim. Acta*, 2011, **690**, 47-52.
6. S. R. Sabreen, *Method and system for laser marking*, The Sabreen Group, Inc., WO2010011227 A1, 2010.
7. Y. M. Noor, S. C. Tam, L. E. N. Lim and S. Jana, *J. Mater. Process. Technol.*, 1994, **42**, 95-133.
8. B. H. Klimt, *Laser and optronics*, 1988, **7**, 61-67.
9. Iriotec® 8000 Series – additives for the laser marking of plastics.
10. G. Lecomte, Google Patents,U.S. Pat. No. 4,816,374 1989.
11. G. E. Sakoske and J. E. Sarver, Google Patents,U.S. Pat. No. 6,503,316 2003.
12. M. Mathias and M. Saatze, Google Patents, Patent No. 2010105735 A1 2012.
13. G. Turner, C. Katsileros and V. Cuming, *Global Renewable Energy Market Outlook*, Bloomberg New Energy Finance, 2011.
14. M. S. Hossain, R. Saidur, H. Fayaz, N. A. Rahim, M. R. Islam, J. U. Ahamed and M. M. Rahman, *Renewable and Sustainable Energy Reviews*, 2011, **15**, 3801-3812.
15. S. A. Kalogirou, *Prog. Energy Combust. Sci.*, 2004, **30**, 231-295.
16. O. Bernhard, *Solar Energy Conversion: Solid-State Physics Aspects*, Springer-Verlag, Berlin, 1979.
17. O. P. Agnihotri and B. K. Gupta, *Solar Selective Surfaces*, Wiley-Interscience, New York, 1981.
18. T. J. McMahon and D. L. Stierwalt, Cost-Effective PbS-Al Selective Solar-Absorbing Panel, 1976.
19. Q.-C. Zhang, Y. Yin and D. R. Mills, *Sol. Energy Mater. Sol. Cells*, 1996, **40**, 43-53.
20. S. Süzer, F. Kadirgan, H. M. Söhmen, A. J. Wetherilt and İ. E. Türe, *Sol. Energy Mater. Sol. Cells*, 1998, **52**, 55-60.
21. G. L. Harding and M. R. Lake, *Solar Energy Materials*, 1981, **5**, 445-464.
22. I. Hamberg and C. G. Granqvist, *Appl. Opt.*, 1983, **22**, 609-614.
23. N. Selvakumar and H. C. Barshilia, *Sol. Energy Mater. Sol. Cells*, 2012, **98**, 1-23.

24. C. E. Kennedy, *Review of Mid- to High-Temperature Solar Selective Absorber Materials*, National Renewable Energy Laboratory, 2002.

25. W. B. Stine and M. Geyer, http://www.powerfromthesun.net/book.html, Accessed 06/08/2013.

26. H. Lee, H. C. Leventis, S.-J. Moon, P. Chen, S. Ito, S. A. Haque, T. Torres, F. Nüesch, T. Geiger, S. M. Zakeeruddin, M. Grätzel and M. K. Nazeeruddin, *Adv. Funct. Mater.*, 2009, **19**, 2735-2742.

27. M. Grätzel, *Journal of Photochemistry and Photobiology C: Photochemistry Reviews*, 2003, **4**, 145–153.

28. H. Hoppe; and N. S. Sariciftci, *Journal materials research*, 2004, **19**, 1924-1944.

29. B. Kippelen; and J.-L. Bredas, *Energy & Environmental Science*, 2009, **2**, 241-332.

30. E. Radziemska, *Renewable Energy*, 2003, **28**, 1-12.

31. H. A. Zondag, *Renewable and Sustainable Energy Reviews*, 2008, **12**, 891-959.

32. A. Ibrahim, M. Y. Othman, M. H. Ruslan, S. Mat and K. Sopian, *Renewable and Sustainable Energy Reviews*, 2011, **15**, 352-365.

33. S. Luo, E. Zhang, Y. Su, T. Cheng and C. Shi, *Biomaterials*, 2011, **32**, 7127-7138.

34. X. Michalet, F. F. Pinaud, L. A. Bentolila, J. M. Tsay, S. Doose, J. J. Li, G. Sundaresan, A. M. Wu, S. S. Gambhir and S. Weiss, *Science*, 2005, **307**, 538-544.

35. S. Kim, Y. T. Lim, E. G. Soltesz, A. M. De Grand, J. Lee, A. Nakayama, J. A. Parker, T. Mihaljevic, R. G. Laurence, D. M. Dor, L. H. Cohn, M. G. Bawendi and J. V. Frangioni, *Nat Biotech*, 2004, **22**, 93-97.

36. X. Huang, I. H. El-Sayed, W. Qian and M. A. El-Sayed, *J. Am. Chem. Soc.*, 2006, **128**, 2115-2120.

37. C. H. Baerlocher and L. B. McCusker, Database of Zeolite Structures: http://www.iza-structure.org/databases/.

38. W. Loewenstein, *Am. Mineral.*, 1954, **39**, 92-97.

39. C. C. Freyhardt, M. Tsapatsis, R. F. Lobo, K. J. Balkus and M. E. Davis, *Nature*, 1996, **381**, 295-298.

40. A. K. Cheetham, G. Férey and T. Loiseau, *Angew. Chem. Int. Ed.*, 1999, **38**, 3268-3292.

41. S. T. Wilson, B. M. Lok, C. A. Messina, T. R. Cannan and E. M. Flanigen, *J. Am. Chem. Soc.*, 1982, **104**, 1146-1147.

42. M. E. Davis, C. Saldarriaga, C. Montes, J. Garces and C. Crowder, *Nature*, 1988, **331**, 698-699.

43. J. B. Parise, *J. Chem. Soc., Chem. Commun.*, 1985, 606-607.

44. M. Gabelica-Robert, M. Goreaud, P. Labbe and B. Raveau, *J. Solid State Chem.*, 1982, **45**, 389-395.

45. D. Riou and M. Goreaud, *Acta Crystallogr. Sect. C*, 1990, **46**, 1191-1193.

46. J. L. Guth, H. Kessler and R. Wey, in *Stud. Surf. Sci. Catal.*, eds. A. I. Y. Murakami and J. W. Ward, Elsevier, 1986, vol. Volume 28, pp. 121-128.

47. H. Kessler, J. Patarin and C. Schott-Darie, in *Stud. Surf. Sci. Catal.*, eds. M. S. H. G. K. J.C. Jansen and J. Weitkamp, Elsevier, 1994, vol. Volume 85, pp. 75-113.

48. M. Goepper and J. L. Guth, *Zeolites*, 1991, **11**, 477-482.

49. A. Merrouche, J. Patarin, H. Kessler, M. Soulard, L. Delmotte, J. L. Guth and J. F. Joly, *Zeolites*, 1992, **12**, 226-232.

50. L. Lakiss, A. Simon-Masseron, F. Porcher, S. Rigolet and J. Patarin, *Eur. J. Inorg. Chem.*, 2007, **2007**, 4043-4049.

51. G. Férey, *J. Fluorine Chem.*, 1995, **72**, 187-193.

52. T. Loiseau and G. Férey, *J. Fluorine Chem.*, 2007, **128**, 413-422.

53. B. M. lok, C. A. Messina, L. R. Patton, R. T. Gajek, T. R. Cannan and E. M. Flanigen, *J. Am. Chem. Soc.*, 1984, **106**, 6092-6093.

54. E. M. Flanigen, B. M. Lok, L. R. Patton and S. T. Wilson, *Pure Appl. Chem.*, 1986, **58**, 1351-1358.

55. R. F. Lobo, M. Tsapatsis, C. C. Freyhardt, S. Khodabandeh, P. Wagner, C.-Y. Chen, K. J. Balkus, S. I. Zones and M. E. Davis, *J. Am. Chem. Soc.*, 1997, **119**, 8474-8484.

56. Y. P. Wang, K. H. Lii and S. L. Wang, *Acta Crystallogr. Sect. C*, 1989, **45**, 1417-1418.

57. S. Natarajan and S. Mandal, *ChemInform*, 2008, **39**, 4798 – 4828.

58. J. O. Nriagu and P. B. Moore, *Phosphate minerals*, Spinger, New York, 1984.

59. H. Berke, *Chem. Soc. Rev.*, 2007, **36**, 15-30.

60. A. S. Andersson, B. Kalska, L. Häggström and J. O. Thomas, *Solid State Ionics*, 2000, **130**, 41-52.

61. S. Franger, F. Le Cras, C. Bourbon and H. Rouault, *J. Power Sources*, 2003, **119-121**, 252-257.

62. A. K. Padhi, K. S. Nanjundaswamy and J. B. Goodenough, *J. Electrochem. Soc.*, 1997, **144**, 1188-1194.

63. C. V. Ramana, A. Ait-Salah, S. Utsunomiya, J. F. Morhange, A. Mauger, F. Gendron and C. M. Julien, *The Journal of Physical Chemistry C*, 2006, **111**, 1049-1054.

64. S. Yang, P. Y. Zavalij and M. Stanley Whittingham, *Electrochem. Commun.*, 2001, **3**, 505-508.

65. S. Choi and A. Manthiram, *J. Electrochem. Soc.*, 2002, **149**, A162-A166.

66. C. Masquelier, A. K. Padhi, K. S. Nanjundaswamy and J. B. Goodenough, *J. Solid State Chem.*, 1998, **135**, 228-234.

67. K. S. Nanjundaswamy, A. K. Padhi, J. B. Goodenough, S. Okada, H. Ohtsuka, H. Arai and J. Yamaki, *Solid State Ionics*, 1996, **92**, 1-10.

68. A. Nyten, A. Abouimrane, M. Armand, T. Gustafsson and J. O. Thomas, *Electrochem. Commun.*, 2005, **7**, 156-160.

69. P. Bonnet, J.-M. M. Millet, C. Leclercq and J. C. Vedrine, *J. Catal.*, 1996, **158**, 128-141.

70. J.-M. M. Millet, *Cat. Rev. - Sci. Eng.*, 2006, **40**, 1-38.

71. A. Benarafa, M. Kacimi, S. Gharbage, J.-M. M. Millet and M. Ziyad, *Mater. Res. Bull.*, 2000, **35**, 2047-2055.

72. M. Cavellec, D. Riou and G. Ferey, *Acta Crystallogr. Sect. C*, 1995, **51**, 2242-2244.

73. K.-H. Lii, Y.-F. Huang, V. Zima, C.-Y. Huang, H.-M. Lin, Y.-C. Jiang, F.-L. Liao and S.-L. Wang, *Chem. Mater.*, 1998, **10**, 2599-2609.

74. J. T. Chalker, P. C. W. Holdsworth and E. F. Shender, *Phys. Rev. Lett.*, 1992, **68**, 855-858.

75. T. Inami, M. Nishiyama, S. Maegawa and Y. Oka, *Phys. Rev. B*, 2000, **61**, 12181-12186.

76. Z.-F. Zhao, B.-B. Zhou, Z.-H. Su, X. Zhang and G.-H. Li, *Cryst. Growth Des.*, 2006, **6**, 632-635.

77. M. Grodzicki, G. Redhammer, M. Reissner, W. Steiner and G. Amthauer, *Phys Chem Minerals*, 2010, **37**, 11-23.

78. O. V. Yakubovich, M. A. Simonov, E. N. Matvienko and N. V. Belov, *Dokl. Akad. Nauk. SSSR*, 1978, 576-579

79. R. Yu, D. Wang, T. Takei, H. Koizumi, N. Kumada and N. Kinomura, *Journal of the Society of Inorganic Materials, Japan*, 2002, **9**, 99-104.

80. E. N. Matvienko, O. V. Yakubovich, M. A. Simonov and N. V. Belov, *Dokl. Akad. Nauk. SSSR*, 1979, **246**, 875-878.

81. O. YAKUBOVICH, M. SIMONOV and O. MELNIKOV, *Kristallografiya*, 1984, **29**, 484-488.

82. O. YAKUBOVICH, O. MELNIKOV and V. URUSOV, *Dokl. Akad. Nauk*, 1995, **342**, 615-620.

83. J. M. Le Meins, M. P. Crosnier-Lopez, A. Hemon-Ribaud and G. Courbion, *J. Solid State Chem.*, 1999, **148**, 260-277.

84. O. V. Yakubovich, O. A. Evdokimova and O. K. Mel'nikov, *Dokl. Akad. Nauk. SSSR*, 1985, **282**, 625-630.

85. G. Frenzen, O. V. Yakubovich and O. K. Mel'nikov, *Acta Crystallogr. Sect. C*, 1996, **52**, 749-753.

86. T. Loiseau, Y. Calage, P. Lacorre and G. Férey, *J. Solid State Chem.*, 1994, **111**, 390-396.

87. J. B. Goodenough, *Magnetism and the Chemical Bond*, Interscience, New York, 1963.

88. M. Riou-Cavellec;, D. Riou; and G. Ferey;, *Inorg. Chim. Acta*, 1999, **291**, 317-325.

89. M. Cavellec, D. Riou, J.-. Grenèche and G. Férey, *J. Magn. Magn. Mater.*, 1996, **163**, 173-183.

90. M. Cavellec, C. Egger, J. Linares, M. Nogues, F. Varret and G. Férey, *J. Solid State Chem.*, 1997, **134**, 349-355.

91. M. Cavellec, D. Riou and G. Férey, *J. Solid State Chem.*, 1994, **112**, 441-447.

92. M. Cavellec, D. Riou and G. Ferey, *Eur. J. Solid State Inorg. Chem.*, 1995, **32**, 271-281.

93. M. Cavellec, D. Riou, C. Ninclaus, J.-M. Grenèche and G. Férey, *Zeolites*, 1996, **17**, 250-260.

94. M. Cavellec, D. Riou, J.-M. Grenèche and G. Férey, *Inorg. Chem.*, 1997, **36**, 2187-2190.

95. M. Cavellec, J. M. Grenèche, D. Riou and G. Férey, *Microporous Mater.*, 1997, **8**, 103-112.

96. M. Cavellec, J. M. Grenèche and G. Férey, *Microporous Mesoporous Mater.*, 1998, **20**, 45-52.

97. J. M. Le Meins, A. Hemon-Ribaud and G. Courbion, *Eur. J. Solid State Inorg. Chem.*, 1998, **35**, 117-132.

98. J. M. Le Meins, J. M. Grenèche and G. Courbion, *J. Solid State Chem.*, 1999, **148**, 286-294.

99. B. L. Ellis, W. R. M. Makahnouk, W. N. Rowan-Weetaluktuk, D. H. Ryan and L. F. Nazar, *Chem. Mater.*, 2009, **22**, 1059-1070.

100. T. Berrocal, J. L. Mesa, J. L. Pizarro, L. Lezama, B. Bazán, M. I. Arriortua and T. Rojo, *J. Solid State Chem.*, 2008, **181**, 884-894.

101. J. Rouse and M. T. Weller, *Dalt. Trans.*, 2009, 10330-10337.

102. J. A. Armstrong, E. R. Williams and M. T. Weller, *J. Am. Chem. Soc.*, 2011, **133**, 8252-8263.

103. E. R. Williams, S. A. Morris and M. T. Weller, *Dalt. Trans.*, 2012, **41**, 10845-10853.

104. J. A. Armstrong, E. R. Williams and M. T. Weller, *Dalt. Trans.*, 2013, **42**, 2302-2308.

105. J. A. Armstrong, E. R. Williams and M. T. Weller, *Dalt. Trans.*, 2012, **41**, 14180-14187.

106. A. C. Keates, J. A. Armstrong and M. T. Weller, *Dalt. Trans.*, 2013. **42***(30):* 10715-10724

107. S. Sato, Y. Yoshihiro, H. Yahiro, N. Mizuno and M. Iwamoto, *Applied Catalysis*, 1991, **70**, L1-L5.

108. W. A. Carvalho, M. Wallau and U. Schuchardt, *Journal of Molecular Catalysis a-Chemical*, 1999, **144**, 91-99.

109. X. Wang, L. Liu, L. Wang and A. J. Jacobson, *Solid State Sciences*, 2005, **7**, 1415-1422.

110. X. Wang, L. Liu and A. J. Jacobson, *Angew. Chem. Int. Ed.*, 2003, **42**, 2044-2047.

111. G. L. Shoemaker, E. Kostiner and J. B. Anderson, *Z. Kristallogr.*, 1980, **152**, 317-332.

112. H. Effenberger, *Acta Crystallographica Section A*, 1984, **40**, C230.

113. G. L. Shoemaker, E. Kostiner and J. B. Anderson, *Zeitschrift fur Kristallographie - Crystalline materials*, 1980, **152**, 317-332.

114. P. F. Henry, R. W. Hughes, S. C. Ward and M. T. Weller, *Chem. Commun.*, 2000, **2000**, 1959-1960.

115. G. Giester and B. Rieck, *Mineralogical Magazine*, 1994, **58**, 663-670.

116. H. Jaksch, W. Seipel, K. L. Weiner and A. Elgoresy, *Naturwissenschaften*, 1983, **70**, 525-535.

117. J. G. Bednorz and K. A. Muller, *Zeitschrift Fur Physik B-Condensed Matter*, 1986, **64**, 189-193.

118. A. A. Belik, M. Azuma and M. Takano, *J. Magn. Magn. Mater.*, 2004, **272-276**, 937-938.

119. S. G. Carling, P. Day and D. Vissen, *Inorg. Chem.*, 1995, **34**, 3917-3927.

120. A. M. dos Santos, P. Brandão, A. Fitch, M. S. Reis, V. S. Amaral and J. Rocha, *J. Solid State Chem.*, 2007, **180**, 16-21.

121. K. M. S. Etheredge and S.-J. Hwu, *Inorg. Chem.*, 1995, **34**, 5013-5016.

122. K. M. S. Etheredge and S.-J. Hwu, *Inorg. Chem.*, 1996, **35**, 1474-1477.

123. K. G. Sanjaya Ranmohotti, X. Mo, M. K. Smith and S.-J. Hwu, *Inorg. Chem.*, 2006, **45**, 3665-3670.

124. G. Cheivrier, *Acta Crystallographica*, 1990, **C46**, 175-177.

125. S. Menchetti, L. Bindi, P. Bonazzi and F. Olmi, *Am. Mineral.*, 2002, **87**, 721-725.

126. T. R. Dabinett, v. Humberstone, P. Leverett and P. A. Williams, *Pure Appl. Chem.*, 2008, **80**, 1317-1323.

127. C. Sabelli, *Acta Crystallographica*, 1972, **B28**, 1182-1189.

128. F. C. Hawthorne and R. B. Fergurson, *Acta Crystallographica*, 1975, **B31**, 1753-1755.

129. X.-J. Zhang, Y.-H. Xing, J. Han, M.-F. Ge and S.-Y. Niu, *Z. Anorg. Allg. Chem.*, 2007, **633**, 2692-2694.

130. M. T. Weller, *Inorganic materials chemistry*, Oxford University press, Oxford, 1994.

131. A. Wold; and K. Dwight, *Solid State Chemistry-Synthesis, structure, and properties of selected oxides and sulfides*, Chapman and Hall, New York, 1993.

132. K. Byrappa and M. Yoshimura;, *Handbook of Hydrothermal Technology: A Technology for Crystal Growth and Materials Processing*, Noyes publications, New York, 2001.

133. R. Xu, W. Pang and Q. Huo, *Modern Inorganic Synthetic Chemistry*, Elsevier, Amsterdam, 2011.

134. C. S. Cundy and P. A. Cox, *Microporous Mesoporous Mater.*, 2005, **82**, 1-78.

135. C. Giacovazzo, H. L. Monaco, G. Artioli, D. Viterbo, G. Ferraris, G. Gilli, G. Zanotti and M. Catti, *Fundamentals of Crystallography: second edition*, Oxford University Press, Oxford, 2002.

136. C. Hammond, *The basics of crystallography and diffraction: second edition*, Oxford University Press, Oxford, 2001.

137. W. Friedrich, P. Knipping and M. Laue, *In Sitzungsber. Kgl. Bayer: Akad. Wiss.*, 1912, 303-322.

138. W. L. Bragg, *Proc. Cambrige Philos. Soc.*, 1913, **17**, 43-57.

139. W. Clegg, *Crystal structure determination*, Oxford university press, New York, 1998.

140. J. W. Pflugrath, *Acta Crystallogr. Sect. D. Biol. Crystallogr.*, 1999, **55**, 1718-1725.

141. Rigaku, *CrystalClear-SM Expert 2.0 r5*, 2010.

142. T. Higashi, *FS-Process*, 2001.

143. G. M. Sheldrick, *XPREP. Space Group Determination and Reciprocal Space Plots.*, Madison, Wisconsin, USA, 1991.

144. G. M. Sheldrick, *Acta Crystallogr. Sect. A: Found. Crystallogr.*, 2008, **A64**, 112-122.

145. Bruker, *DIFFRAC^{plus} Evaluation Package,* Sun Mi-crosystems Inc., Regents of the University of California, 2004.

146. A. C. Larson and R. B. V. Dreele, *General Structure Analysis System (GSAS)*, Los Alamos National Laboratory, USA, 2004.

147. B. Toby;, *J. Appl. Crystallogr.*, 2001, **34**, 210.

148. V. Dzimbeg-Malcic, Z. Barbaric-Mikocevic and K. Itric, *Technical Gazette*, 2011, **18**, 117-124.

149. J. Goldstein, D. Newbury, D. Joy, C. Lyman, P. Echlin, E. Lifshin, L. Sawyer and J. Michael, *Scanning electron microscopy and X-ray microanalysis 3rd edition*, Plenum publishers, New York, 2003.

150. N. E. Brese and M. O'Keeffe, *Acta Crystallographica*, 1991, **B47**, 192-197.

151. I. D. Brown and D. Altermatt, *Acta Crystallogr. Sect. B: Struct. Sci.*, 1985, **41**, 224-247.

152. J.-X. Mi, C.-X. Wang, Z.-B. Wei, F.-J. Chen, C.-Y. Xu and S.-Y. Mao, *Acta Crystallogr. Sect. Sect. E: Struct. Rep. Online*, 2005, **61**, i143-i145.

153. M. Jinxiao, H. Borrmann, H. Zhang, Y. X. Huang, ;, W. Schnelle, J.-T. Zhao and R. Kniep, *Z. Anorg. Allg. Chem.*, 2004, **630**, 1632-1636.

154. J. Lesage, L. Adam, A. Guesdon and B. Raveau, *J. Solid State Chem.*, 2007, **180**, 1799-1808.

155. L.-Y. Duan, F.-C. Liu, E.-B. Wang, Y.-G. Li, C.-W. Hu and L. Xu, *Chin. J. Chem* . 2004, **22**, 55-59.

156. R. C. Mercader, L. Terminiello, G. J. Long, D. G. Reichel, K. Dickhaus, R. Zysler, R. Sanchez and M. Tovar, *Phys. Rev. B*, 1990, **42**, 25-32.

157. E. Williams, S. Morris and M. T. Weller, *Dalt. Trans.*, 2012, **41**, 10845-10853.

158. J. A. Armstrong, E. R. Williams and M. T. Weller, *Dalt. Trans.*, 2012, **41**, 14180-14187.

159. J. A. Armstrong, E. R. Williams and M. T. Weller, *Dalt. Trans.*, 2012, **42**, 2302-2308.

160. M. Berraho, C. R'Kha, A. Vegas and M. Rafiq, *Acta Crystallogr. Sect. C*, 1992, **48**, 1350-1352.

161. M. Berraho, A. Vegas, M. Martinez-Ripoll and M. Rafiq, *Acta Crystallogr. Sect. C*, 1994, **50**, 666-668.

162. P. Shiv Halasyamani, M. J. Drewitt and D. O'Hare, *Chem. Commun.*, 1997, **0**, 867-868.

163. O. V. Yakubovich, W. Massa and O. V. Dimitrova, *Z. Anorg. Allg. Chem.*, 2005, **631**, 2445-2449.

164. G. S. Gopalakrishna, M. J. Mahesh, K. G. Ashamanjari and J. S. Prasad, *Mater. Res. Bull.*, 2008, **43**, 1171-1178.

165. J. S. Diez Vinuela, C. O. Arean and F. S. Stone, *Journal of the Chemical Society, Faraday Transactions 1: Physical Chemistry in Condensed Phases*, 1983, **79**, 1191-1198.

166. H. S. C. O'Neill, W. A. Dollase and C. R. Ross, *Phys. Chem. Miner.*, 1995, **18**, 302-319.

167. H. S. C. O'Neill, M. James, W. A. Dollase and S. A. T. Redfurn, *Eur. J. Mineral.*, 2005, **17**, 581-586.

168. B. J. Hathaway and D. E. Billing, *Coord. Chem. Rev.*, 1970, **5**, 143-207.

169. G. R. Rossman and M. N. Taran, *Am. Mineral.*, 2001, **86**, 896–903.

170. W. A. Dollase and H. S. C. O'Neill, *Acta Crystallogr. Sect. C*, 1997, **53**, 657-659.

171. F. Norindr, Doctor of Philosophy, University of Southampton, 2009.

172. F. Sanz, C. Parada, J. M. Rojo, C. Ruiz-Valero and R. Saez-Puche, *J. Solid State Chem.*, 1999, **145**, 604-611.

173. K. Stahl and J. P. Legros, *Acta Crystallogr. Sect. B: Struct. Sci.*, 1990, **46**, 292-301.

174. E. P. Meagher, *Am. Mineral.*, 1976, **61**, 67-73.

175. S. R. Berry, *The Journal of Chemical Physics*, 1960, **32**, 933-938.

176. S. Youngme, P. Phuengphai, C. Pakawatchai, P. Kongsaeree and N. Chaichit, *Acta Crystallographica Section B*, 2008, **64**, 318-329.

177. V. Zima, K.-H. Lii, N. Nguyen and A. Ducouret, *Chem. Mater.*, 1998, **10**, 1914-1920.

178. A. G. Nord, *Mater. Res. Bull.*, 1982, **17**, 1001-1010.

179. J. K. Warner, A. K. Cheetham and D. E. Cox, *J. Appl. Crystallogr.*, 1995, **28**, 494-502.

180. A. G. Nord, G. Aberg, H. Annersten, T. Ericsson and T. Stefanidis, *Chemica Scripta*, 1985, **25**, 189-193.

181. H. Annersten, T. Ericsson and A. G. Nord, *J. Phys. Chem. Solids*, 1980, **41**, 1235-1240.

182. A. Boukhari, A. Moqine and S. Flandrois, *J. Solid State Chem.*, 1990, **87**, 251-256.

183. J.-M. Le Meins and G. Courbion, *Acta Crystallogr. Sect. C*, 1999, **55**, 481-483.

184. A. Kawahara, T. Kageyama, I. Watanabe and J. Yamakawa, *Acta Crystallogr. Sect. C*, 1993, **49**, 1275-1277.

185. M. Quarton and A. W. Kolsi, *Acta Crystallogr. Sect. C*, 1983, **39**, 664-667.

186. H. Effenberger, *Monatsh. Chem.*, 1985, **116**, 927-931.

187. J. B. Anderson, G. L. Shoemaker and E. Kostiner, *J. Solid State Chem.*, 1978, **25**.

188. A. A. Belik, P. Naumov, K. Jungeun and T. Shunsuke, *J. Solid State Chem.*, 2011, **184**, 3128-3133.

189. A. W. Addison, T. N. Rao, J. Reedijk, J. van Rijn and G. C. Verschoor, *J. Chem. Soc., Dalton Trans.*, 1984, 1349-1356.

190. V. Somasekharam and Y. P. Reddy, *J. Phys. B: At., Mol. Opt. Phys.*, 1986, **36**, 1074-1078.

191. Z. Yuan, D. Wei, Y. Wang, Y. Zhu, Y. Qian and K. Tang, *Cryst. Eng.*, 2012, **14**, 4251-4254.

192. J. D. Swalen, B. Johnson and H. M. Gladney, *The Journal of Chemical Physics*, 1970, **52**, 4078-4086.

193. K. M. Reddy, A. S. Jacob and B. J. Reddy, *Ferroelectrics Letters Section*, 1986, **6**, 103-112.

194. H. T. Evans and M. E. Mrose, *Am. Mineral.*, 1977, **62**, 491-502.

195. K. B. N. Sarma, B. J. Reddy and S. V. J. Lakshman, *Phys. Lett. A*, 1982, **92**, 305-308.

196. F. Zhou, K. Kang, T. Maxisch, G. Ceder and D. Morgan, *Solid State Commun.*, 2004, **132**, 181-186.

197. A. S. Andersson, B. Kalska, P. Eyob, D. Aernout, L. Häggström and J. O. Thomas, *Solid State Ionics*, 2001, **140**, 63-70.

198. R. L. White, *Thermochim. Acta*, 2012, **528**, 58-62.

199. A. C. Keates, J. A. Armstrong and M. T. Weller, *Dalt. Trans.*, 2013, **42**, 10715-10724.

200. S. Pagès-Camagna and S. Colinart, *Archaeometry*, 2003, **45**, 637-658.

201. G. D. Jones, *Phys. Rev. A: At. Mol. Opt. Phys.*, 1967, **155**, 259-261.

202. R. Davis, *Coord. Chem. Rev.*, 1982, **41**, 1-77.

203. P. H. Ribbe, G. V. Gibbs and M. M. Hamil, *Am. Mineral.*, 1977, **62**, 807-811.

204. M. Ati, L. Dupont, N. Recham, J. N. Chotard, W. T. Walker, C. Davoisne, P. Barpanda, V. Sarou-Kanian, M. Armand and J. M. Tarascon, *Chem. Mater.*, 2010, **22**, 4062-4068.

205. B. Murphy and B. Hathaway, *Coord. Chem. Rev.*, 2003, **243**, 237-262.

206. L. R. Falvello, *J. Chem. Soc., Dalton Trans.*, 1997, 4463-4476.

207. M. P. Fuller and P. R. Griffiths, *Anal. Chem. (Wash.)*, 1978, **50**, 1906-1910.

208. J. I. Langford and A. J. C. Wilson, *J. Appl. Crystallogr.*, 1978, **11**, 102-113.

209. G. Geuskens and David. C, *Pure Appl. Chem.*, 1979, **51**, 233-240.

210. Q. Huang, M. Ulutagay, P. A. Michener and S.-J. Hwu, *J. Am. Chem. Soc.*, 1999, **121**, 10323-10326.

211. E. R. Williams, R. M. Leithall, R. Raja and M. T. Weller, *Chemical Communications (Cambridge)*, 2013, **49**, 249-251.

212. M. Ramzan, S. Lebegue, P. Larsson and R. Ahuja, *J. Appl. Phys.*, 2009, **106**, 043510.

213. S. J. Fu, C. Y. Cheng and K. J. Lin, *Crystal Growth & Design*, 2007, **7**, 1381-1384.

Appendices

CIFs generated in chapters 3 and 4 are located on accompanying CD.

Appendix C Powder X-ray diffraction patterns of six coordinate compounds

C.1 Copper compounds

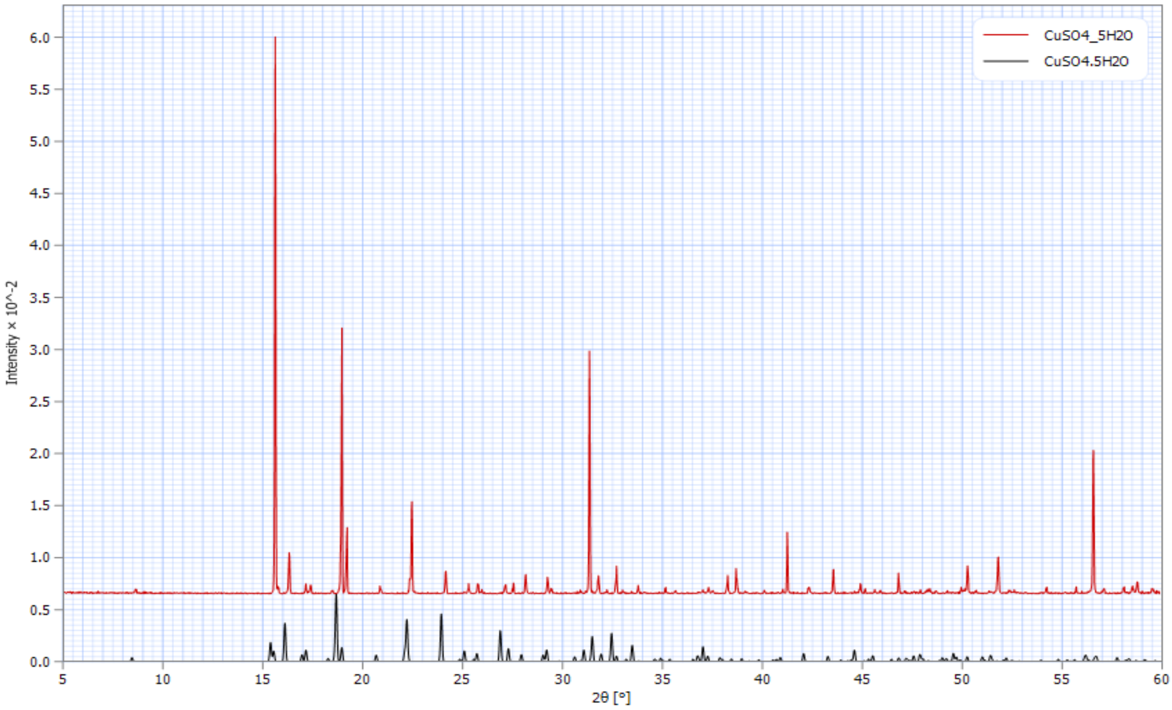

Figure 7-1-Predicted (black) and experimental (red) p-XRD pattern for compound 9. Predicted pattern from ICSD collection code 20657

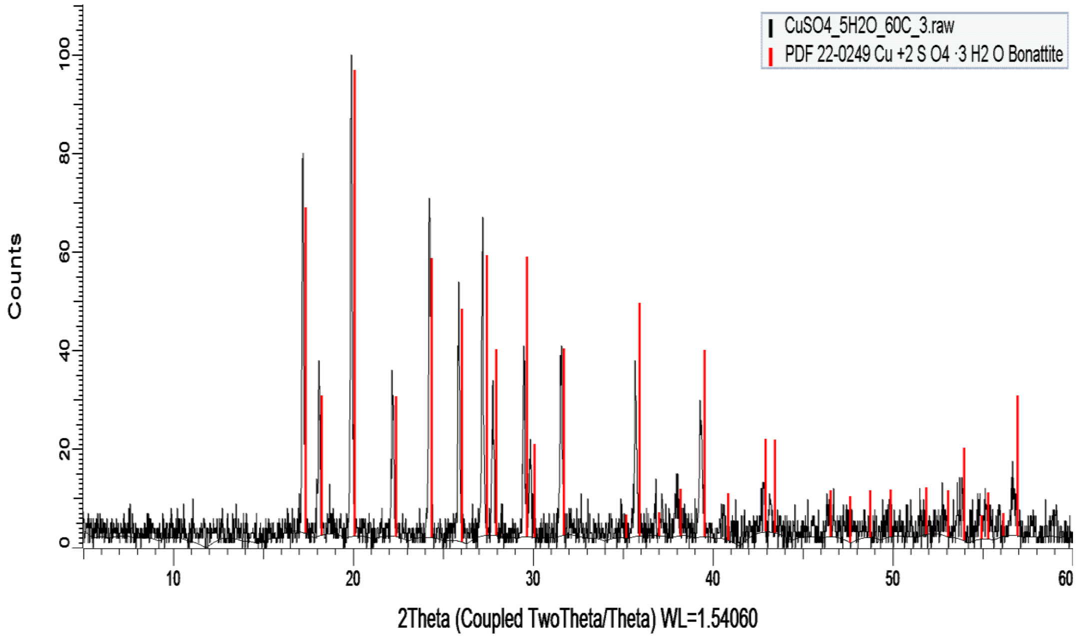

Figure 7-2-p-XRD of compound 10. Red lines indicate peak positions from ICSD database (PDF 22-0249).

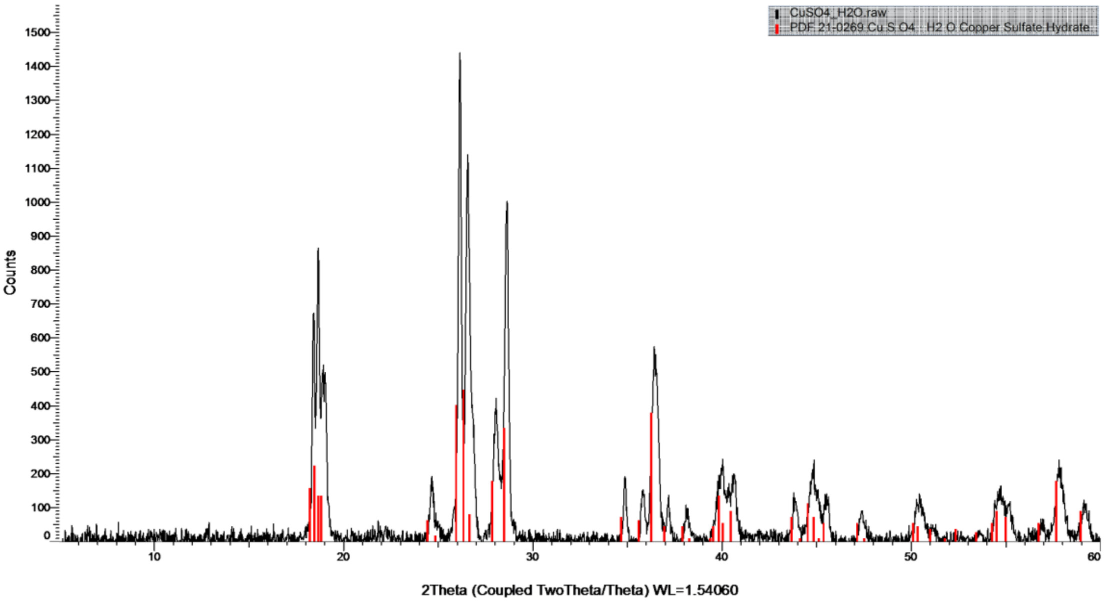

Figure 7-3-p-XRD of compound 11. Red lines indicate peak positions from ICSD database (PDF 21-0269).

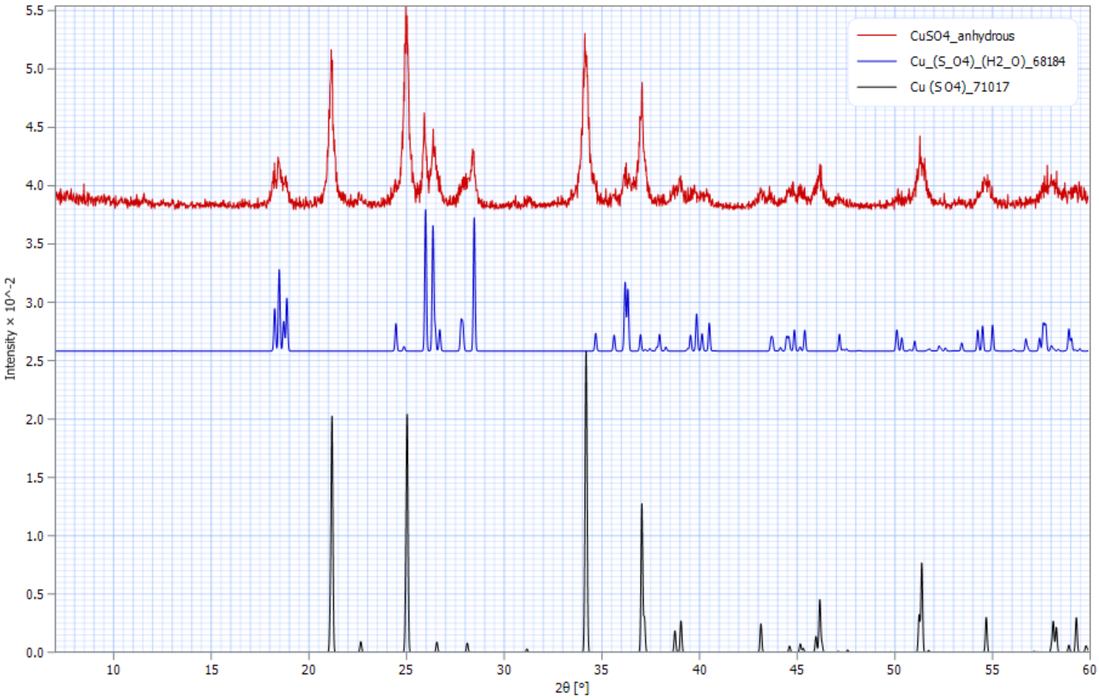

Figure 7-4-Predicted (black) and experimental (red) p-XRD pattern for compound 12. Predicted patter from ICSD from collection code 71017. $CuSO_4$•H_2O impurity phase present indicated by blue pattern (PDF 21-0269).

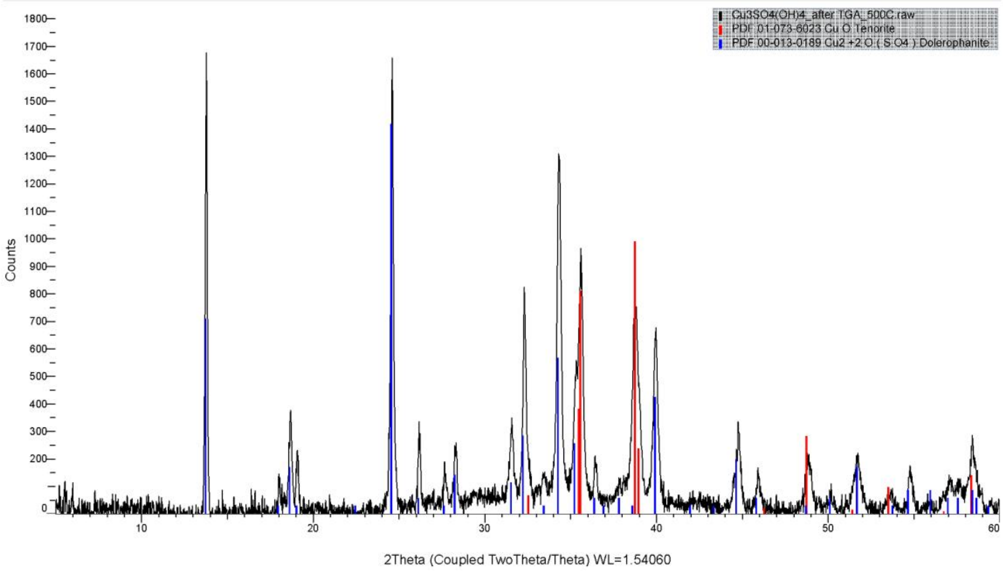

Figure 7-5p-XRD of compound 13. blue lines indicate peak positions from ICSD database (PDF 00-013-0189), red lines indicate CuO impurity peaks (PDF 01-073-6023).

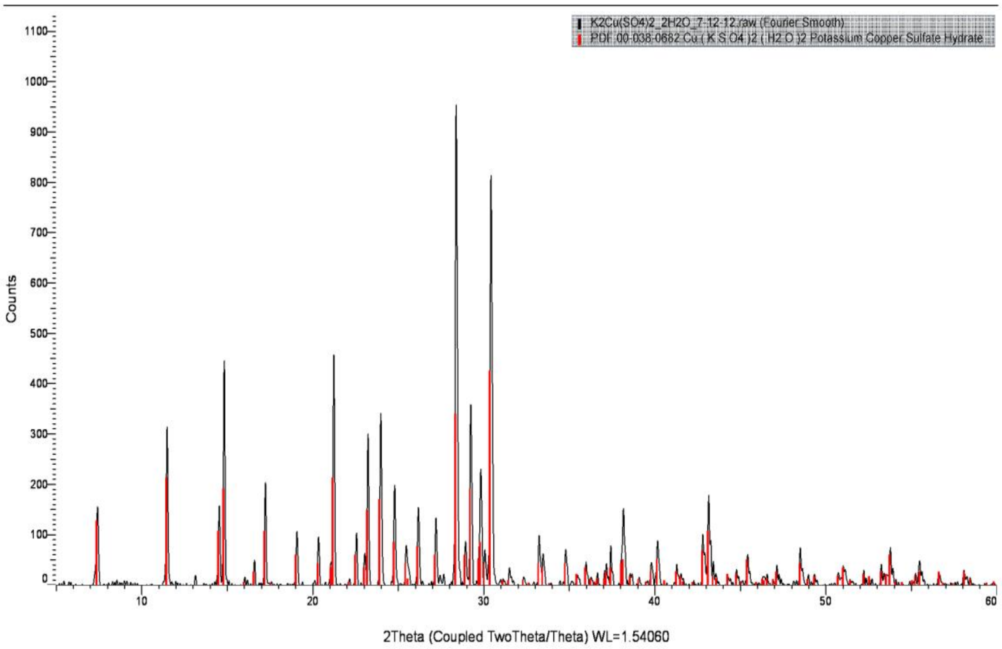

Figure 7-6-p-XRD of compound 15. Red lines indicate peak positions from ICSD database (PDF 00-038-0682).

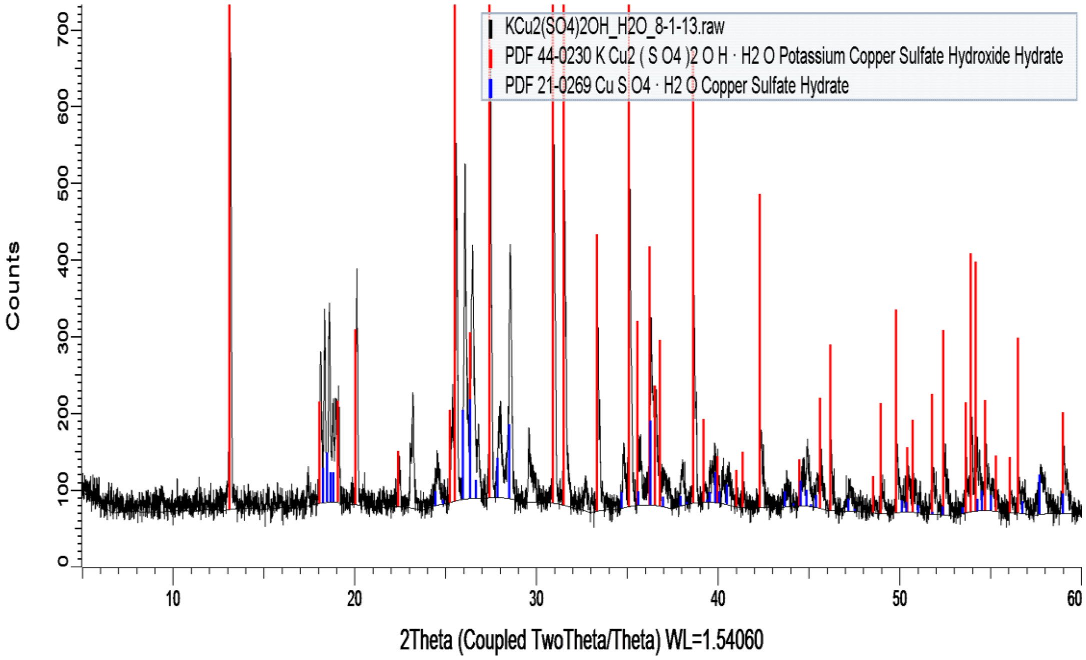

Figure 7-7-p-XRD of compound 16. Red lines indicate peak positions from ICSD database (PDF 44-0230), blue lines indicate $CuSO_4•H_2O$ impurity peaks (PDF 21-0269).

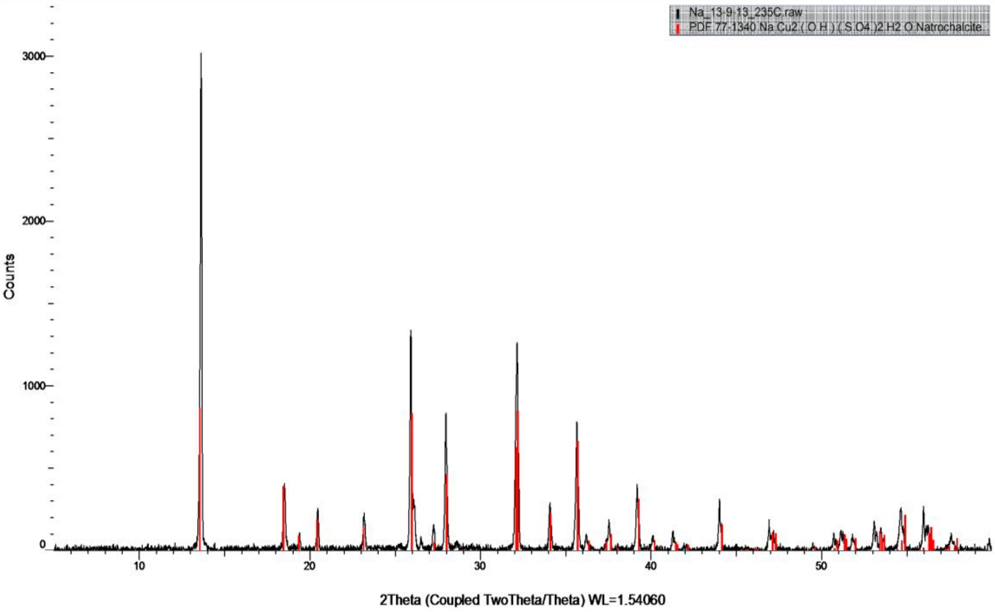

Figure 7-8-p-XRD of compound 17. Red lines indicate peak positions from ICSD database (PDF 77-1340).

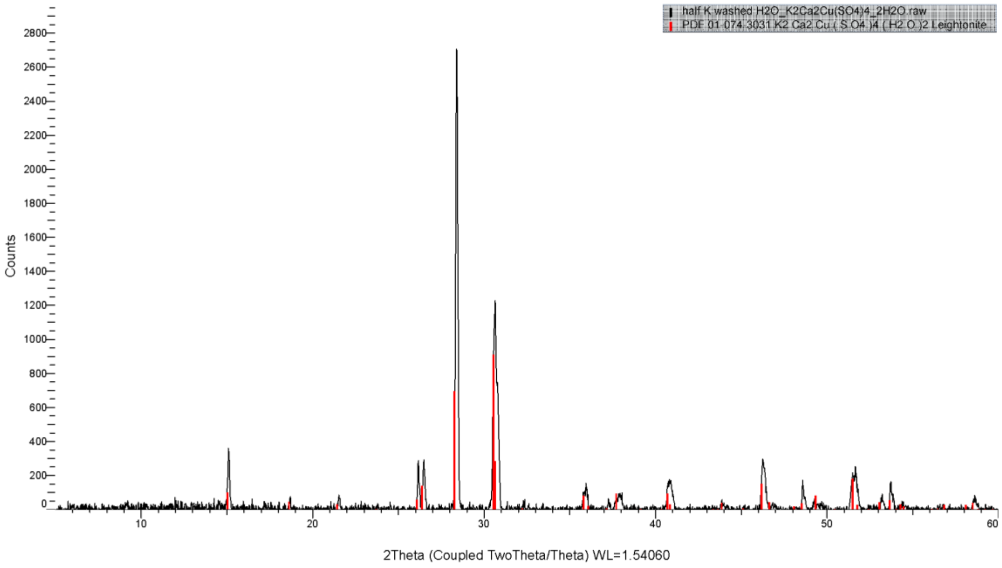

Figure 7-9-p-XRD of compound 18. Red lines indicate peak positions from ICSD database (PDF 01-074-3031).

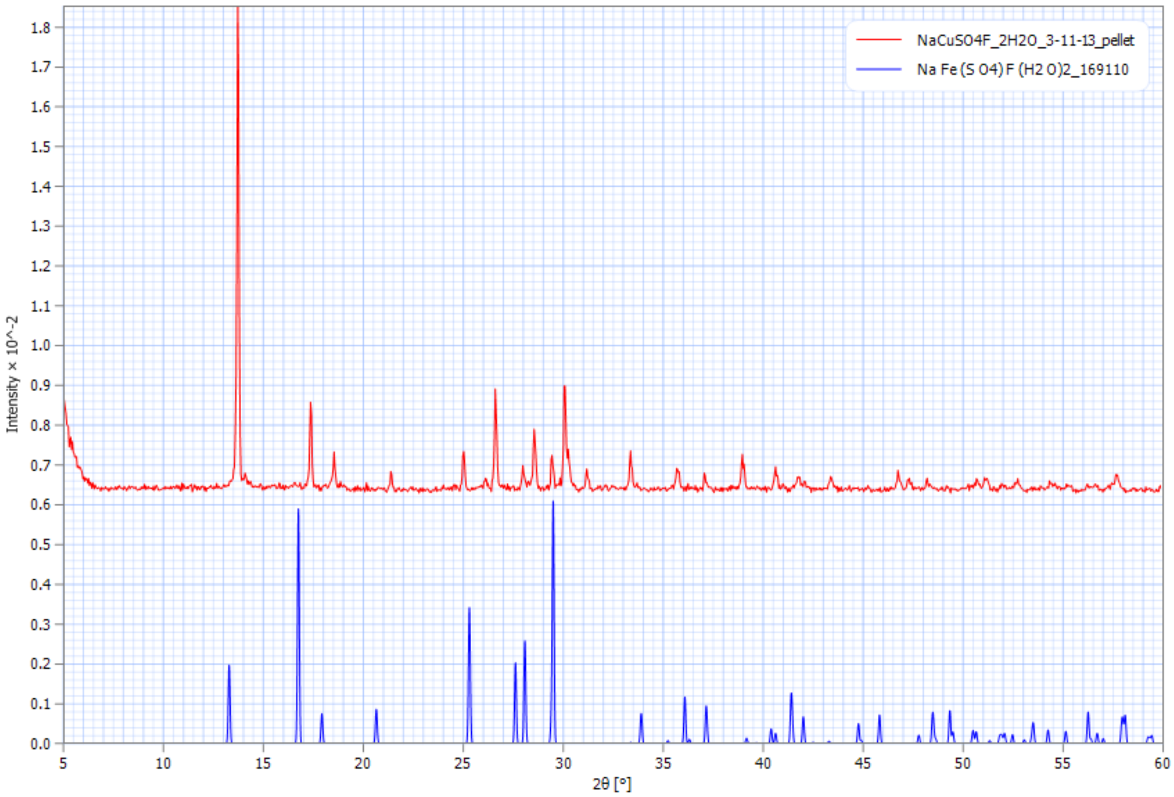

Figure 7-10-Predicted (blue) and experimental (red) p-XRD pattern of compound 19. Predicted pattern from Collection Code 169110

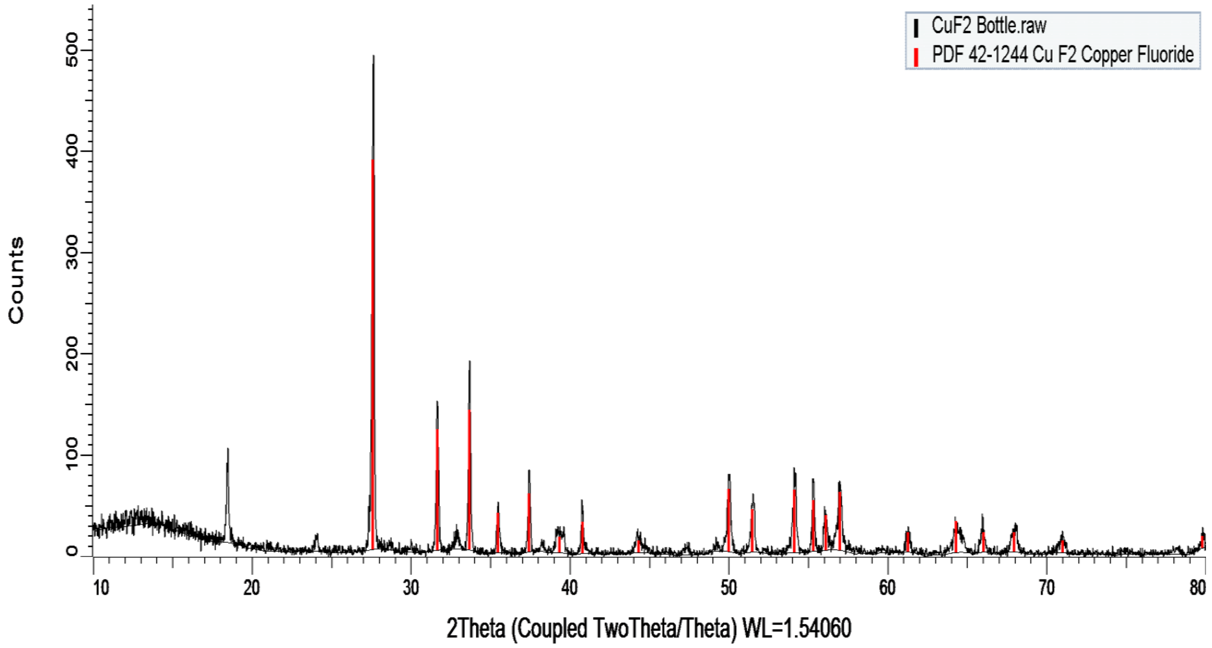

Figure 7-11-p-XRD of compound 20. Red lines indicate peak positions from ICSD database (PDF 42-1244).

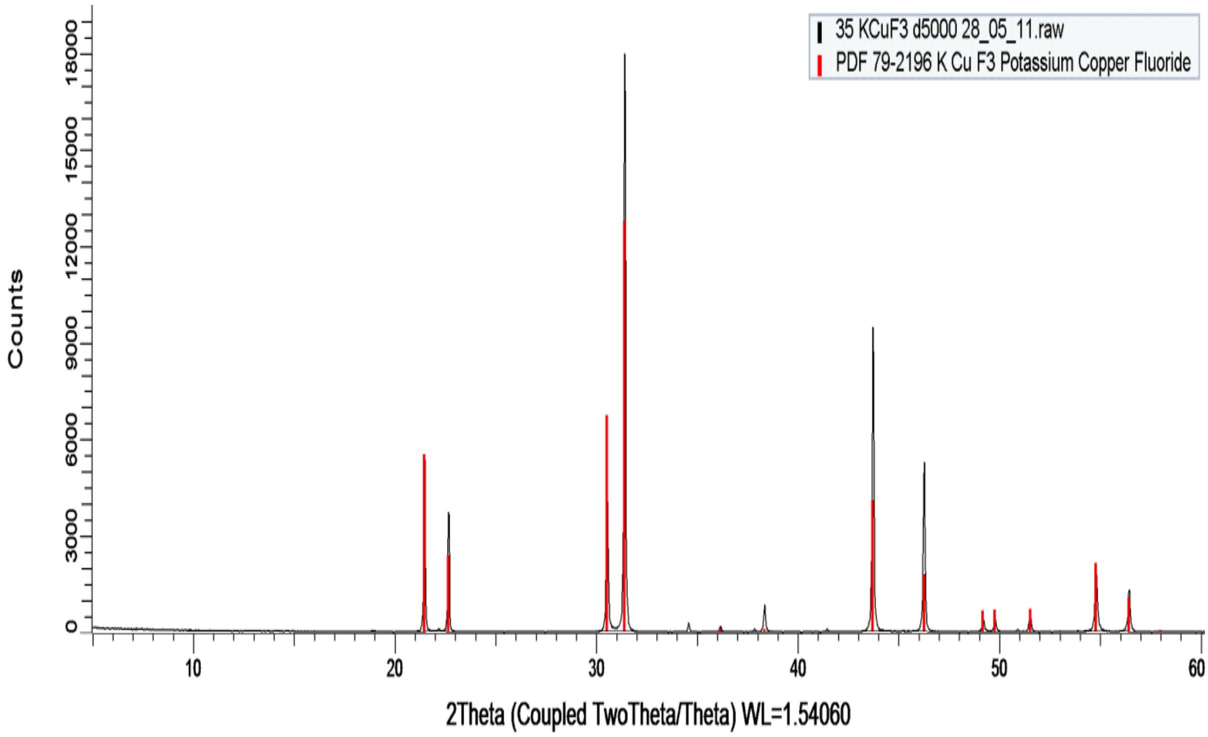

Figure 7-12-p-XRD of compound 21. Red lines indicate peak positions from ICSD database (PDF 79-2196).

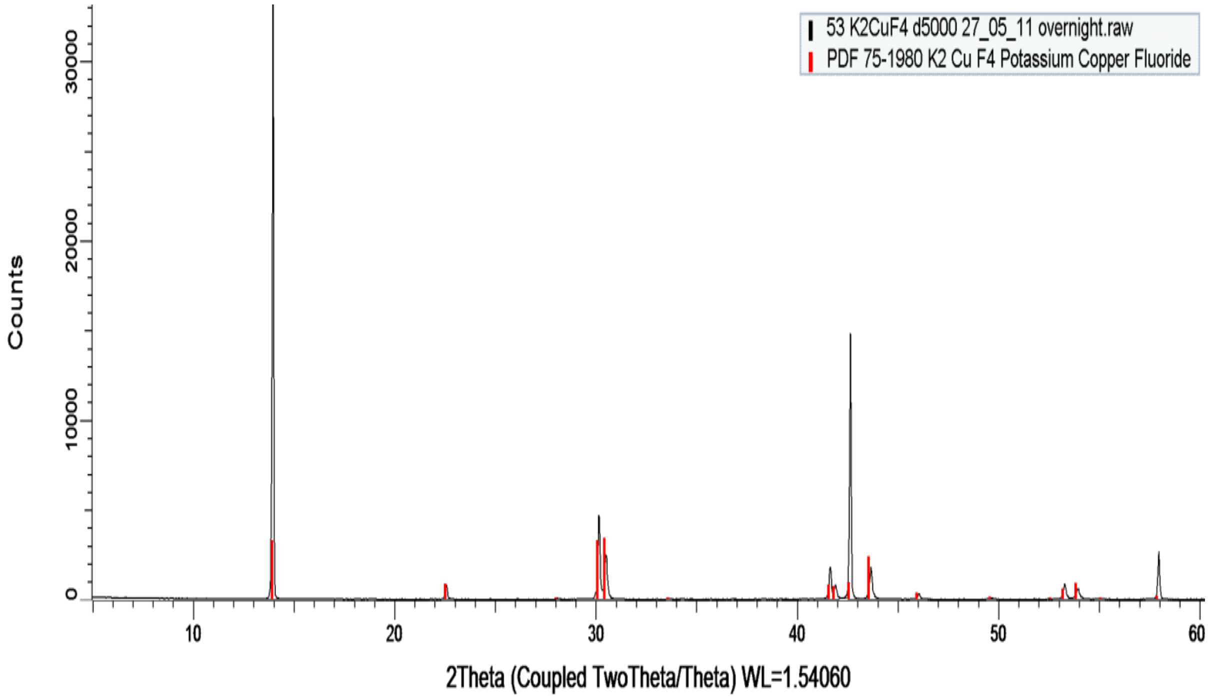

Figure 7-13-p-XRD of compound 22. Red lines indicate peak positions from ICSD database (PDF 75-1980).

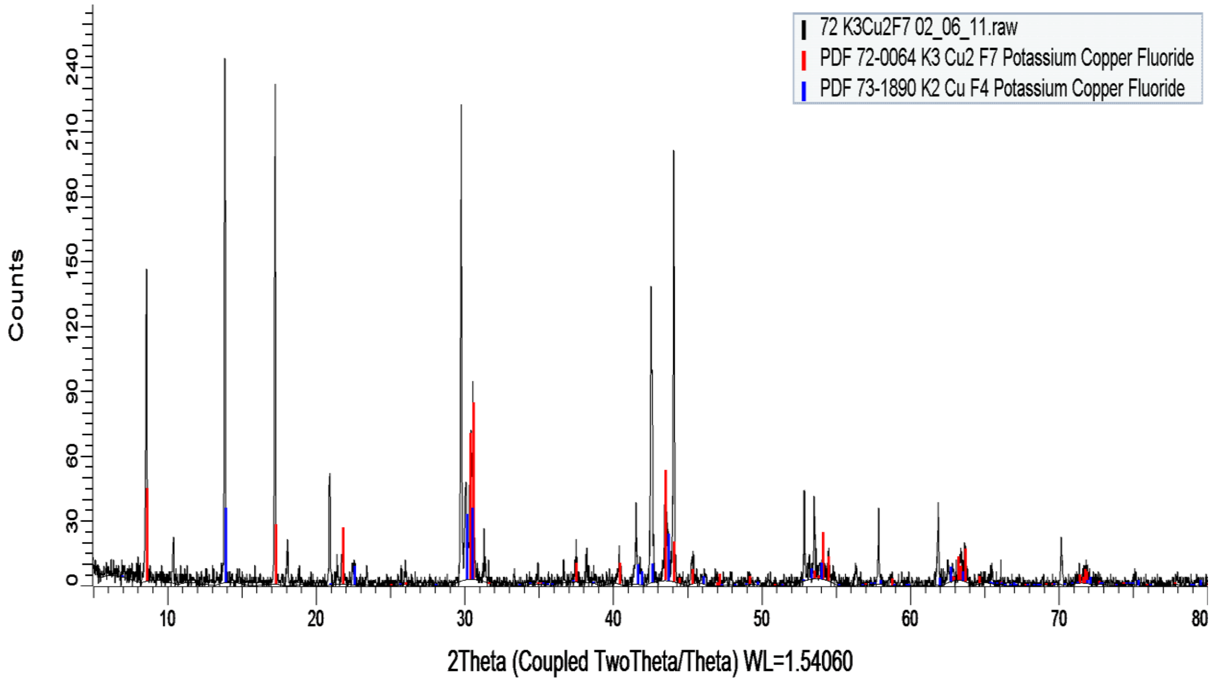

Figure 7-14-p-XRD of compound 23. Red lines indicate peak positions from ICSD database (PDF 72-0064), blues peaks are impurity phase from ISCD database (PDF 75-1980).

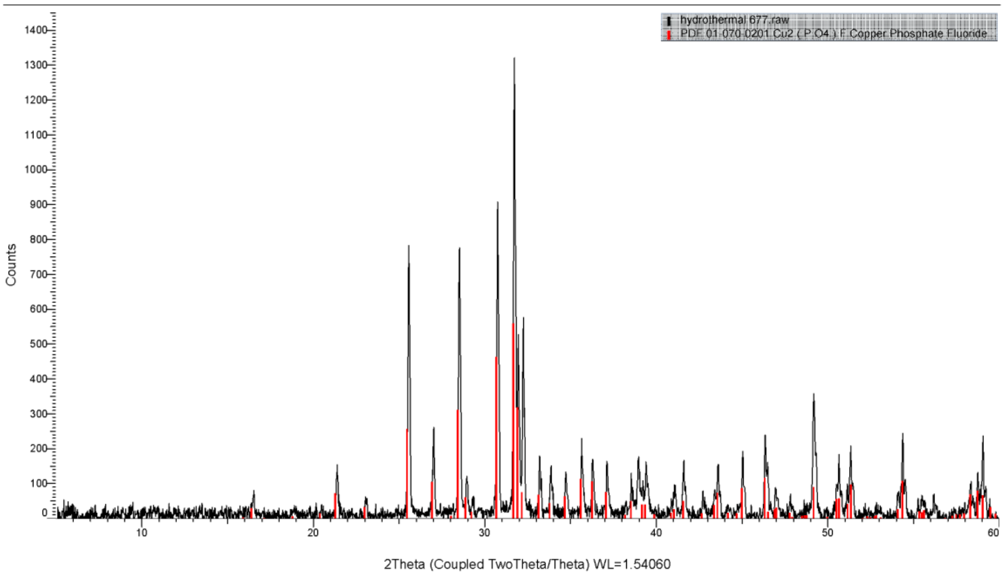

Figure 7-15-p-XRD of compound 24. Red lines indicate peak positions from ICSD database (PDF 01-070-0201).

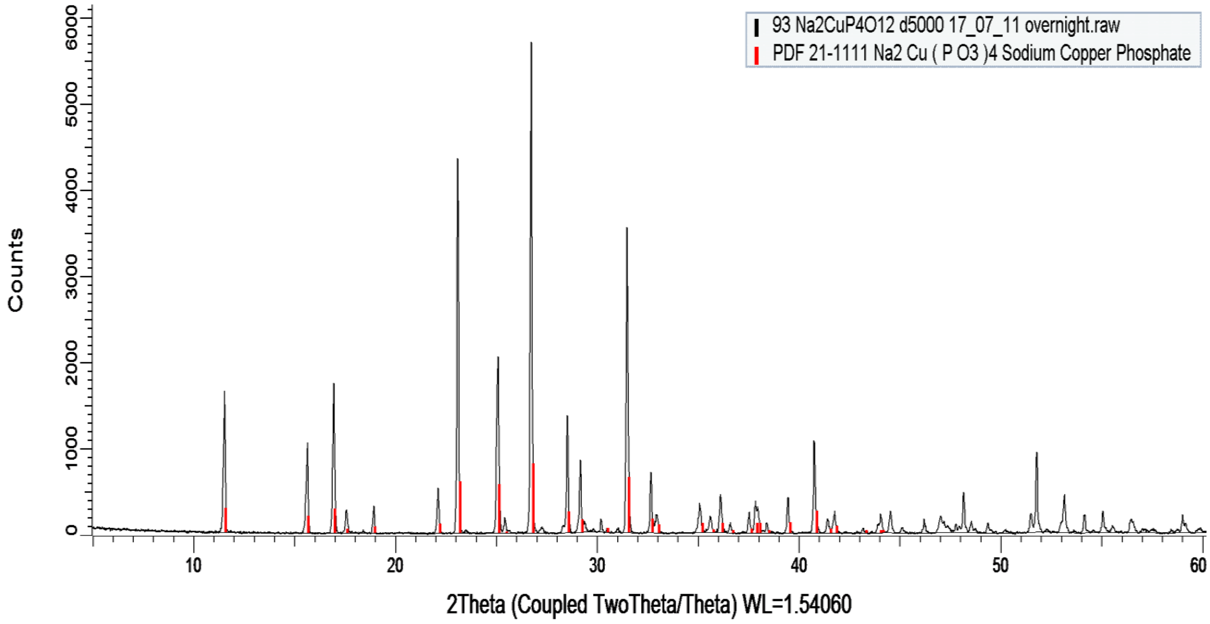

Figure 7-16--p-XRD of compound 25. Red lines indicate peak positions from ICSD database (PDF 21-1111).

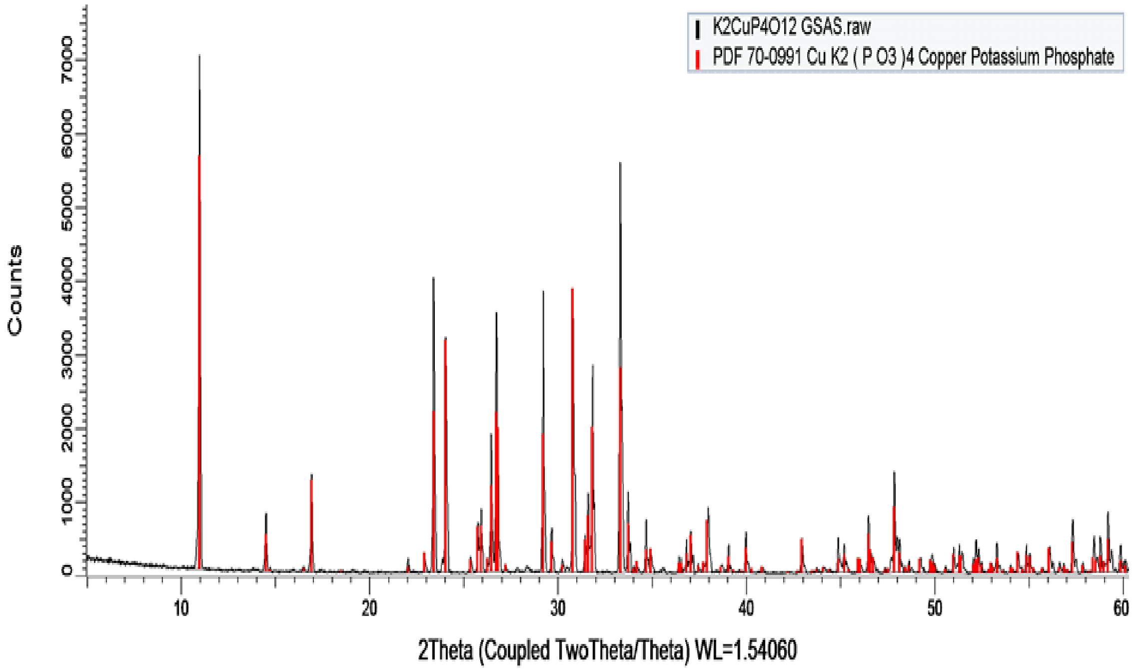

Figure 7-17-p-XRD of compound 26. Red lines indicate peak positions from ICSD database (PDF 70-0991).

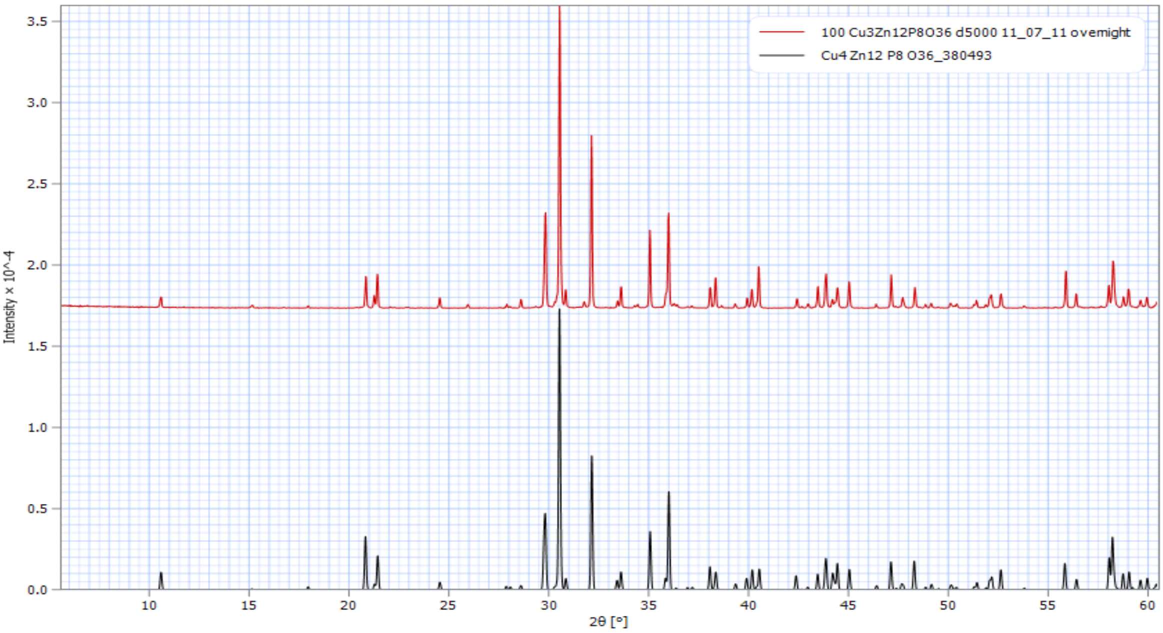

Figure 7-18-p-XRD pattern of predicted (black) and experimental (red) of compound 28. Predicted pattern from Collection Code 380493

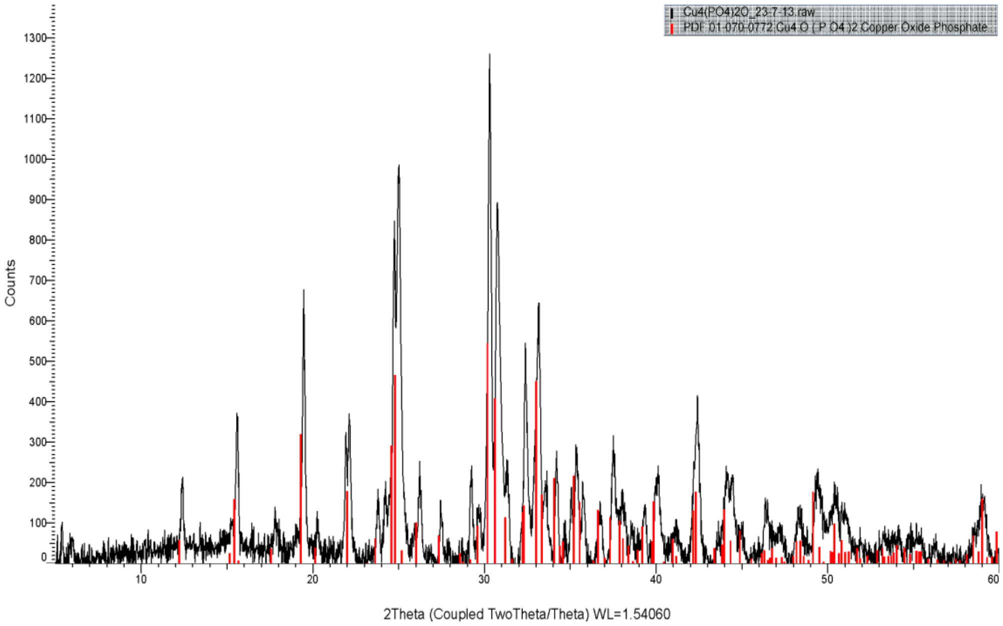

Figure 7-19-p-XRD of compound 29. Red lines indicate peak positions from ICSD database (PDF 01-070-0772).

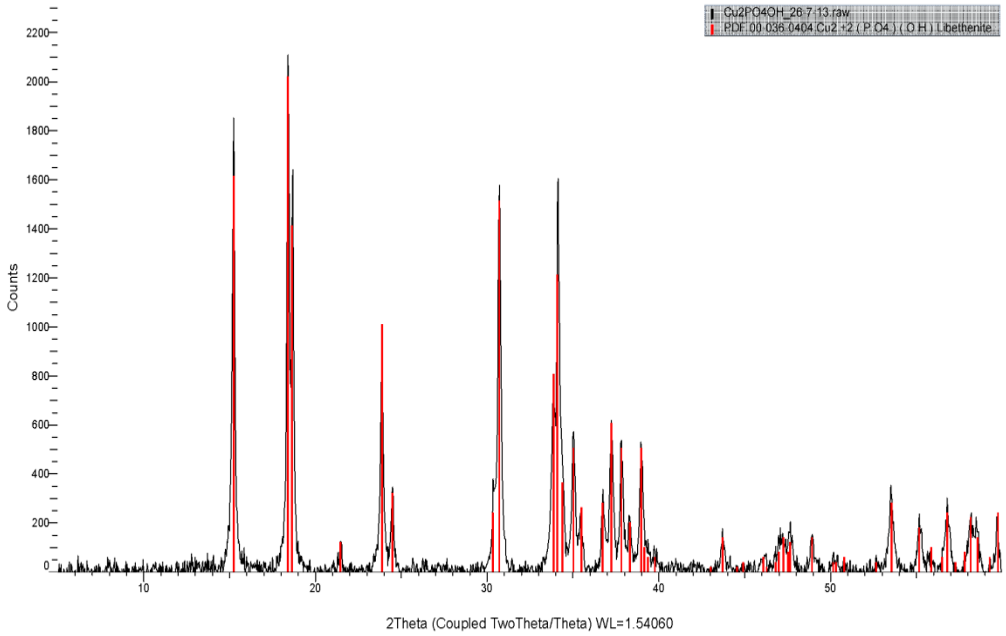

Figure 7-20-p-XRD of compound 30. Red lines indicate peak positions from ICSD database (PDF 00-036-0404).

C.2 Iron compounds

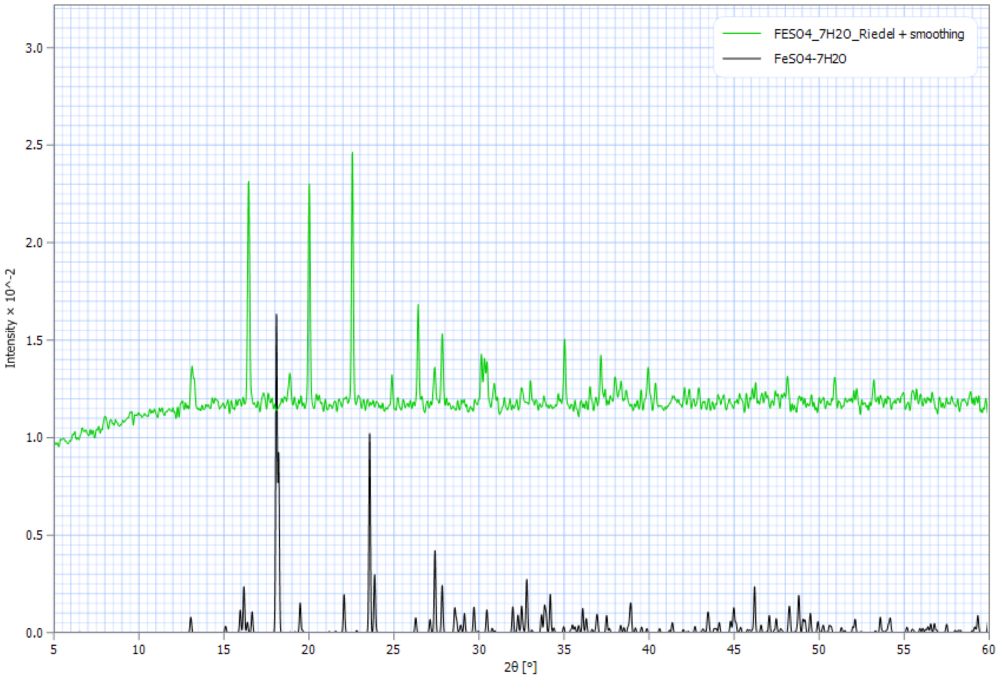

Figure 7-21- Predicted (black) and experimental (green) p-XRD pattern of compound 28. Predicted pattern from Collection Code 16589

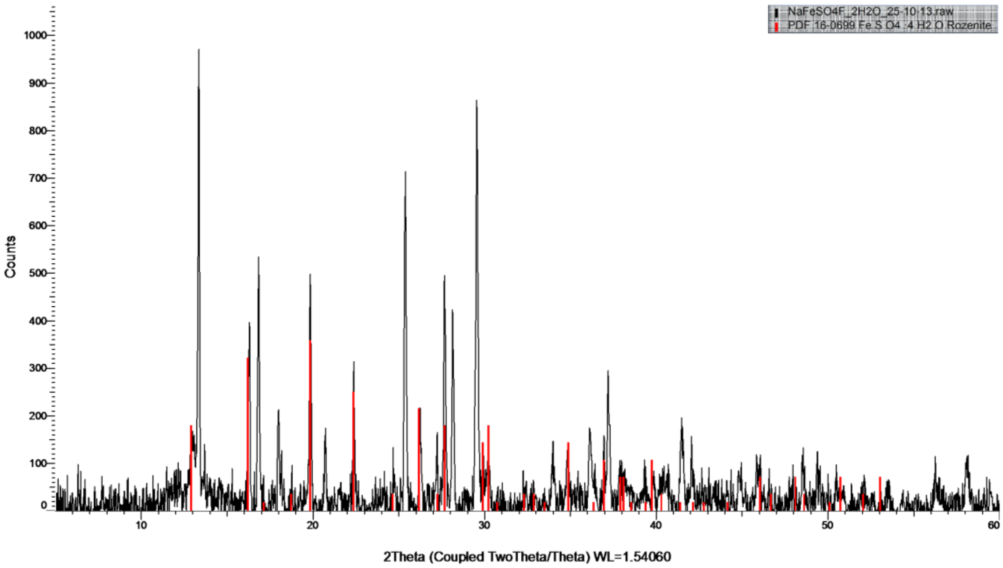

Figure 7-22-p-XRD of compound 35. Red lines indicate peak positions from ICSD database (PDF 16-0699).

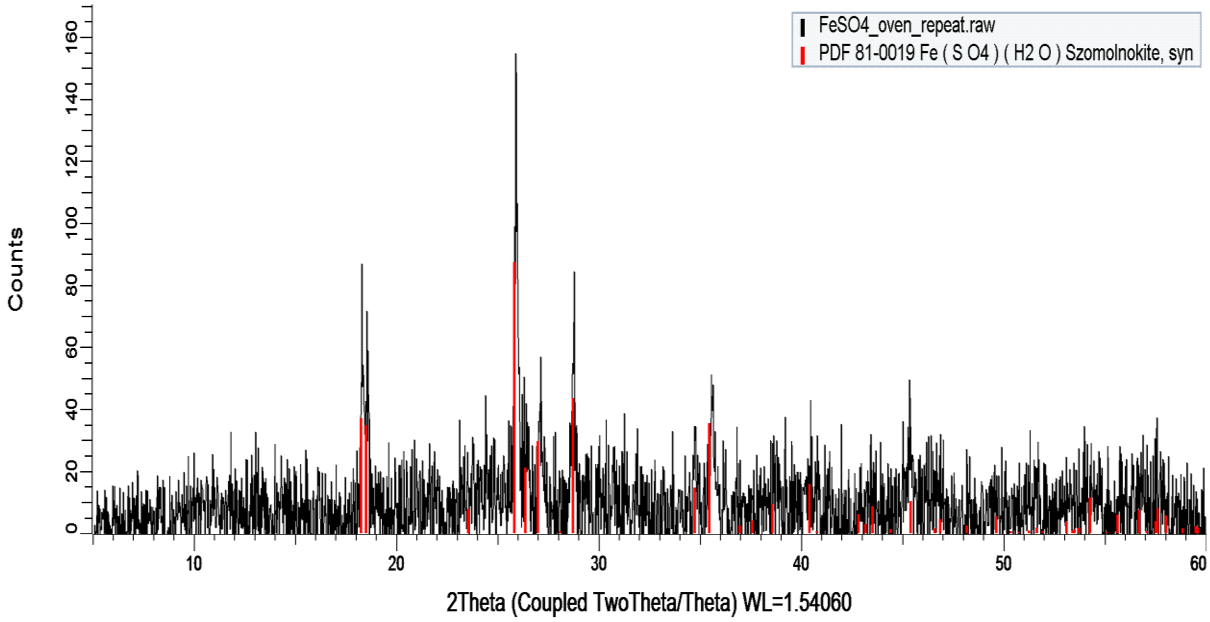

Figure 7-23-p-XRD of compound 36. Red lines indicate peak positions from ICSD database (PDF 81-0019).

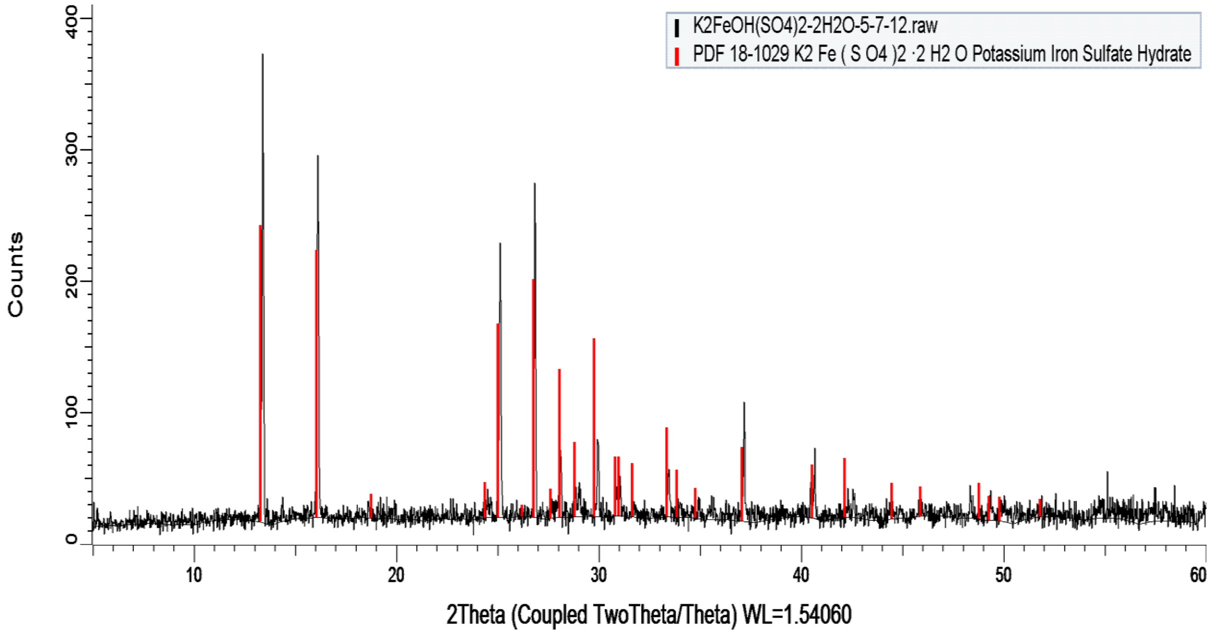

Figure 7-24-p-XRD of compound 37. Red lines indicate peak positions from ICSD database (PDF 18-1029).

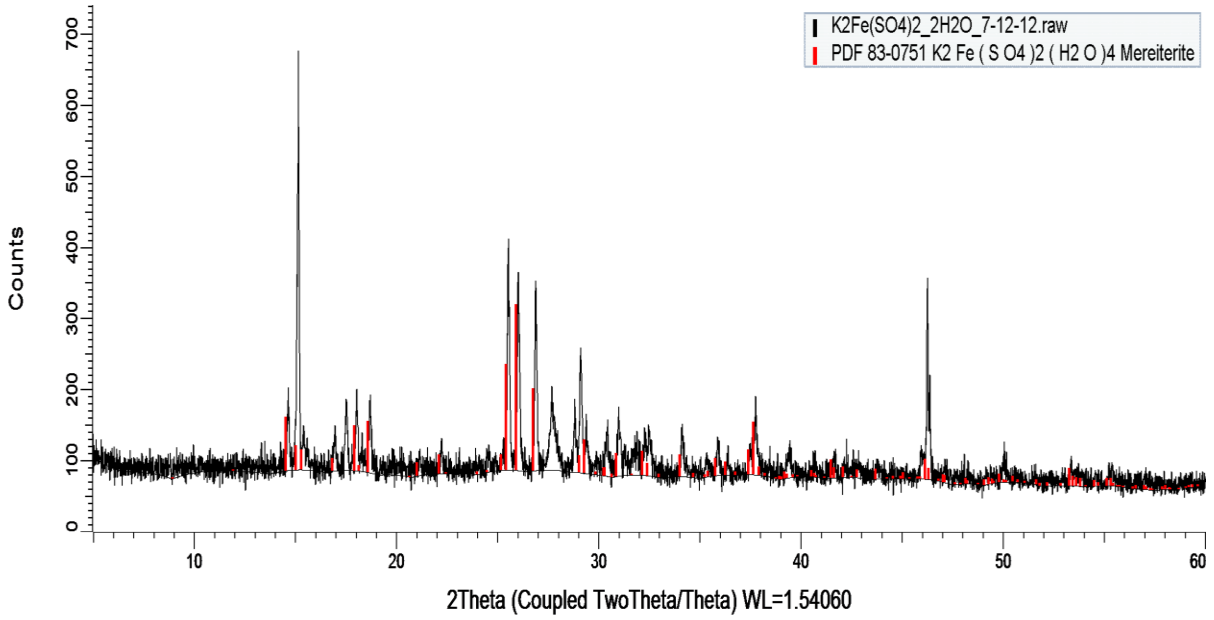

Figure 7-25--p-XRD of compound 38. Red lines indicate peak positions from ICSD database (PDF 83-0751).

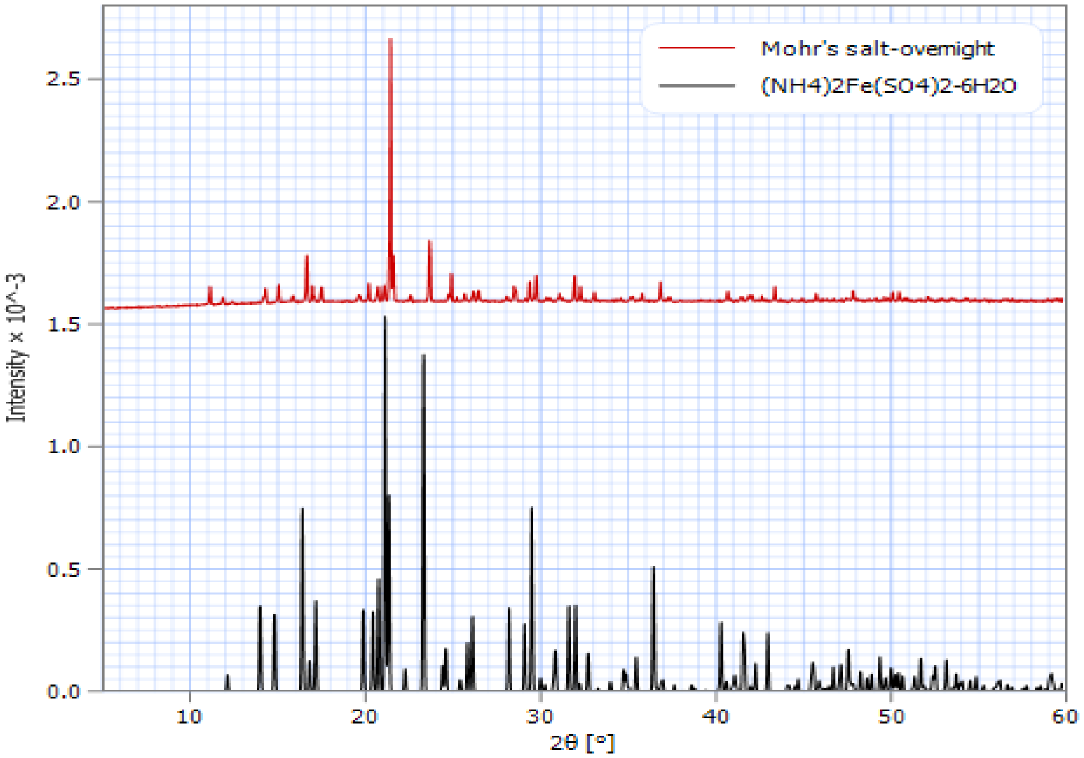

Figure 7-26- Predicted (black) and experimental (red) p-XRD pattern of compound 39. Predicted pattern from Collection Code 14346

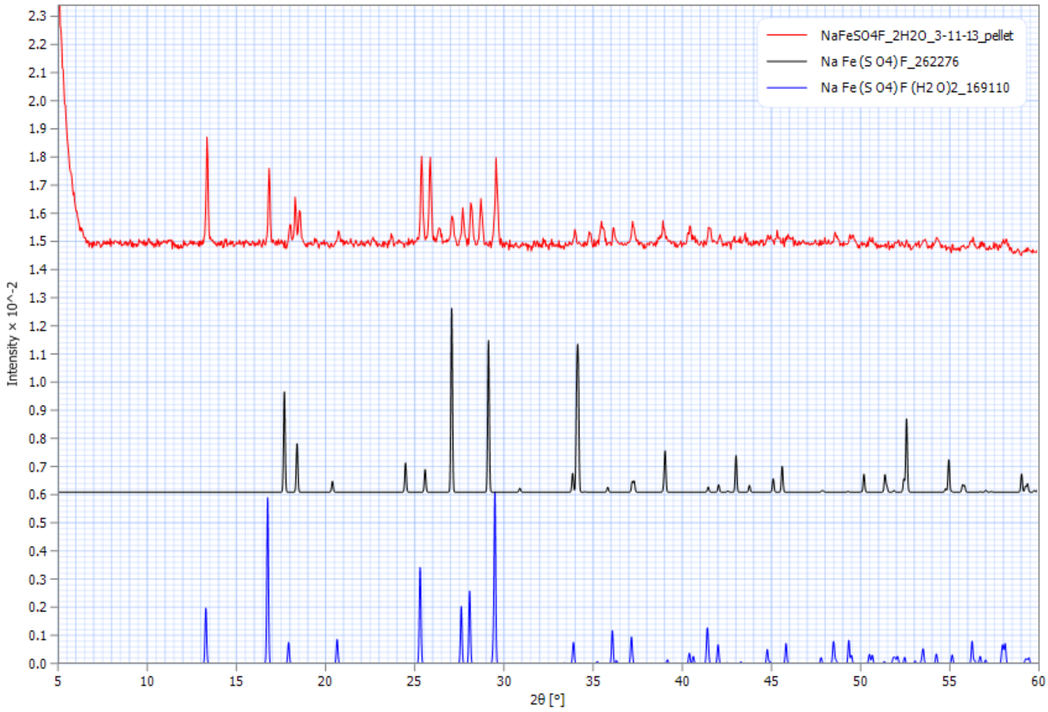

Figure 7-27-Predicted (blue) and experimental (red) p-XRD pattern of compound 40. The black pattern indicates the NaFe(SO$_4$)F impurity phase. Predicted pattern from Collection Code 169110 and 262276 for the impurity phase

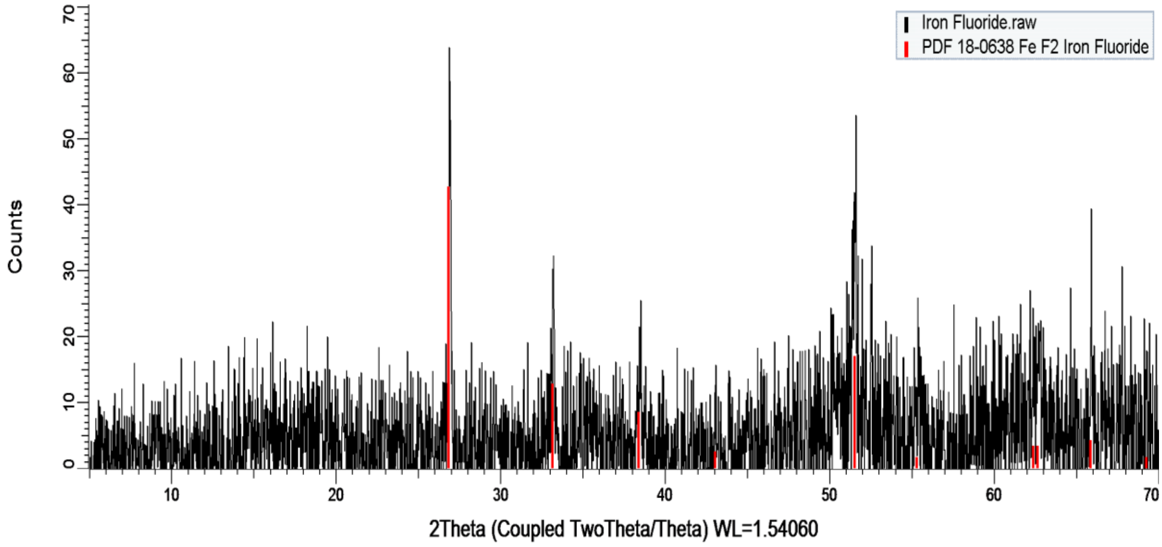

Figure 7-28-p-XRD of compound 41. Red lines indicate peak positions from ICSD database (PDF 18-0638).

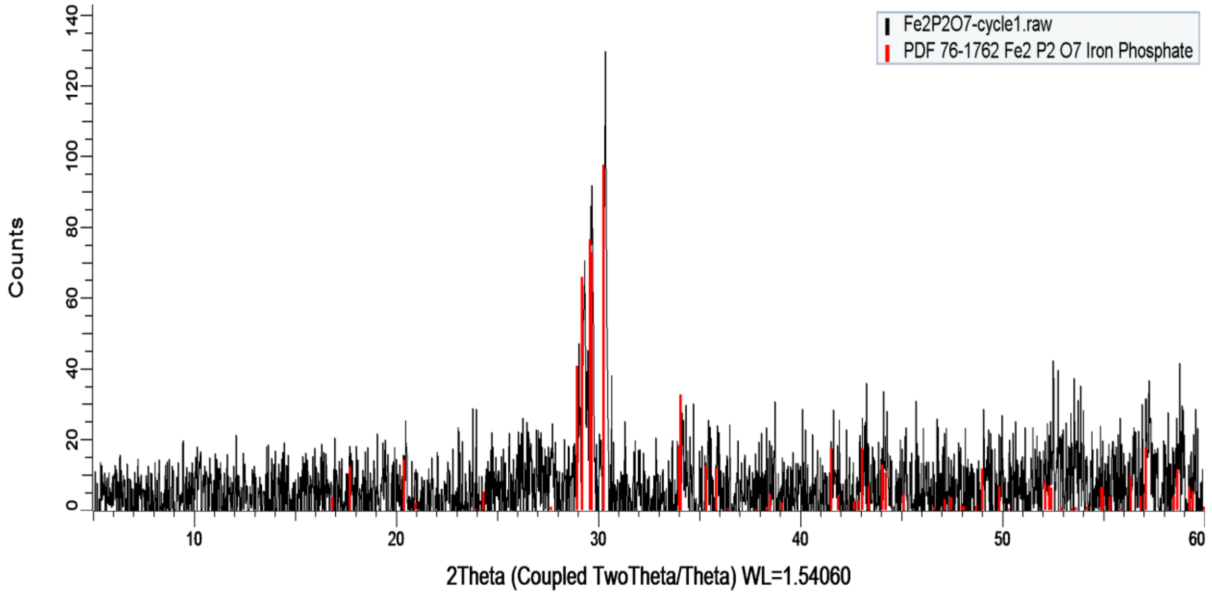

Figure 7-29--p-XRD of compound 43. Red lines indicate peak positions from ICSD database (PDF 76-1762).

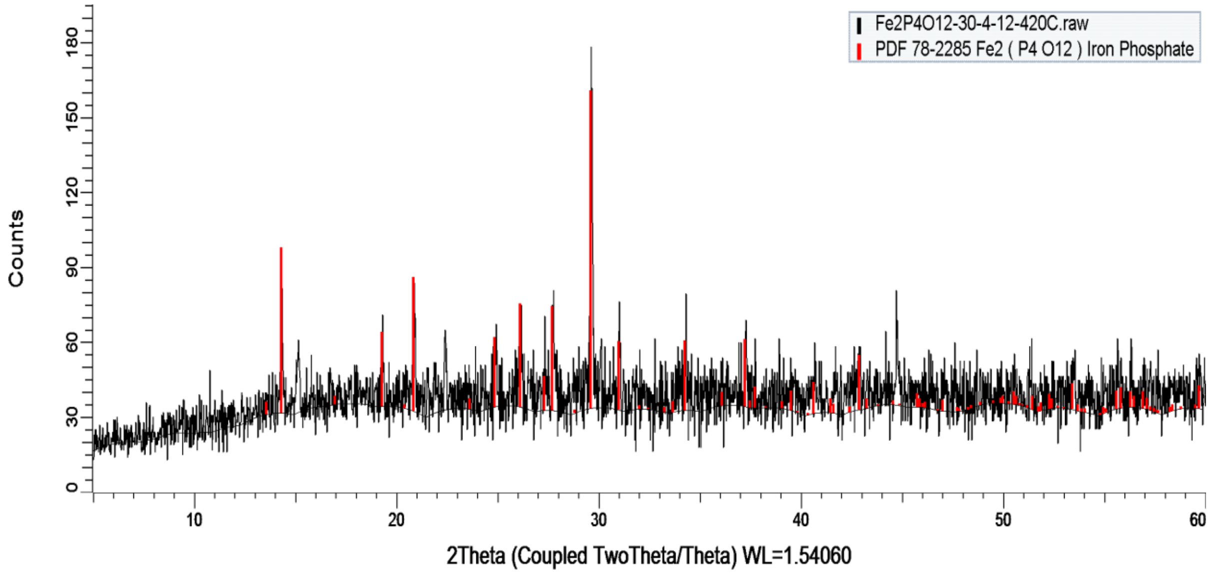

Figure 7-30-p-XRD of compound 44. Red lines indicate peak positions from ICSD database (PDF 78-2285).

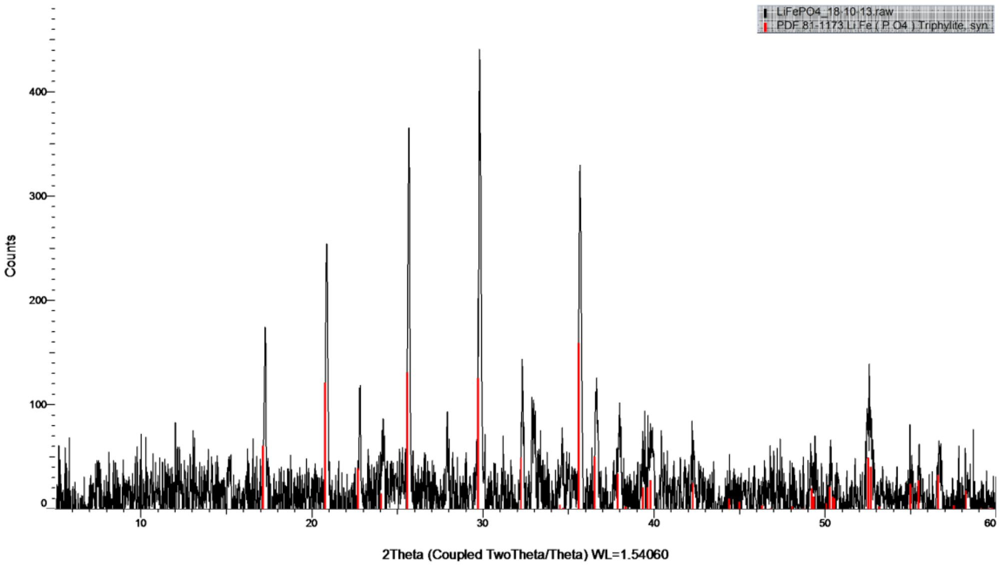

Figure 7-31-p-XRD of compound 46. Red lines indicate peak positions from ICSD database (PDF 81-1173).

Appendix D Six coordinate UV/Vis/NIR spectra

D.1 Copper compounds

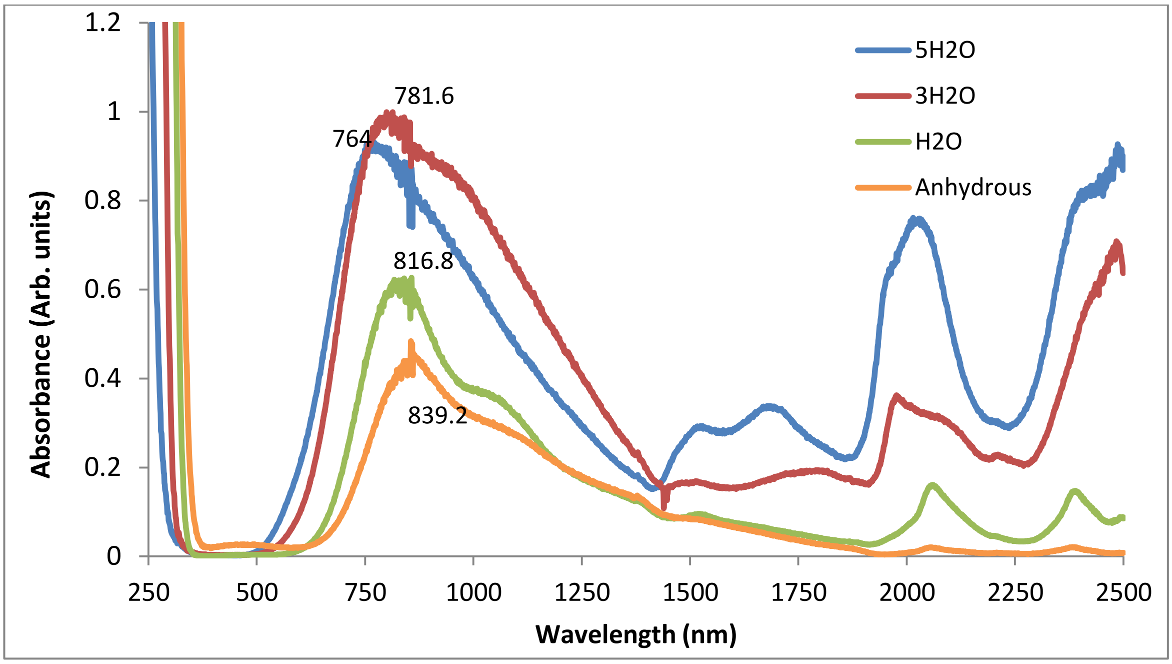

Figure 7-32-UV/Vis/NIR absorbance spectra of Compounds 9-12

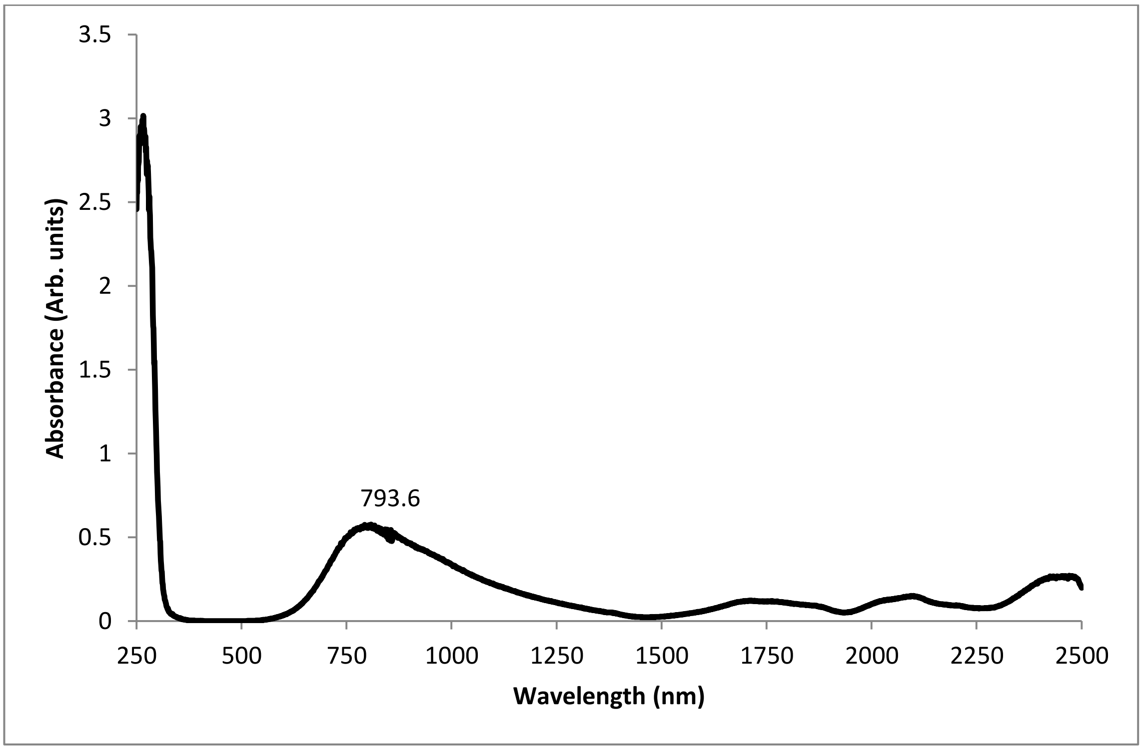

Figure 7-33-UV/Vis/NIR absorbance spectrum of Compound 15

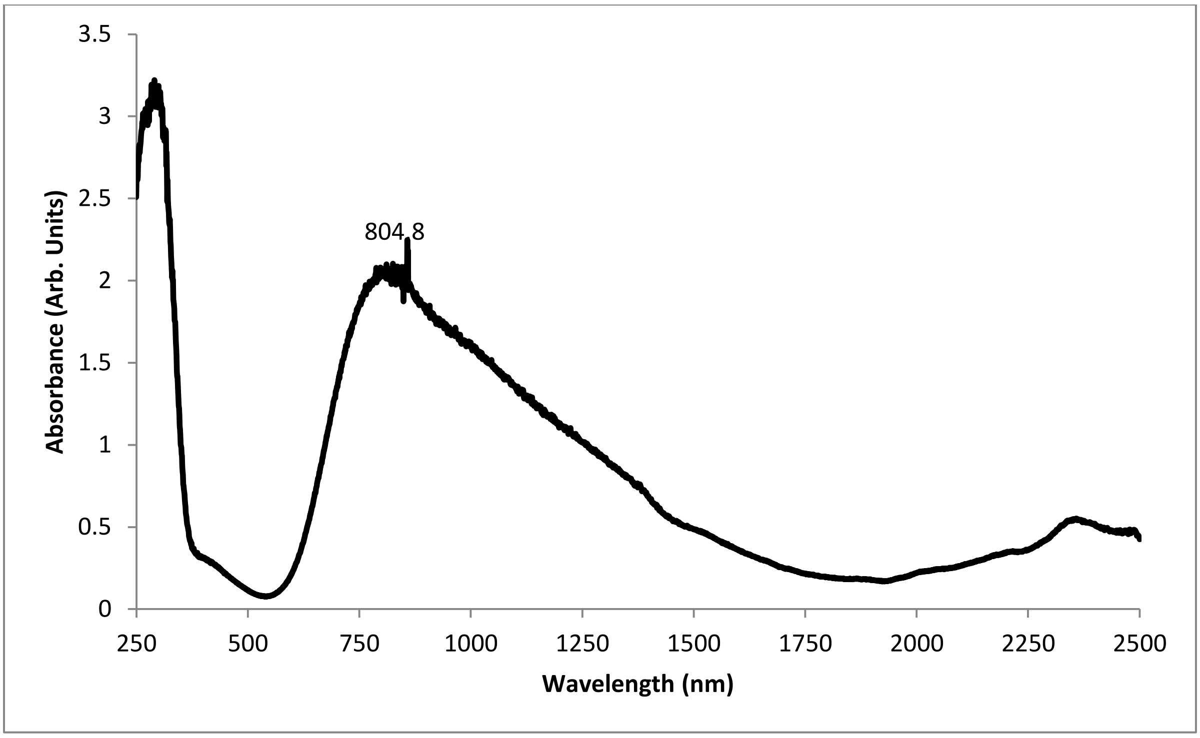

Figure 7-34-UV/Vis/NIR absorbance spectrum of Compound 16

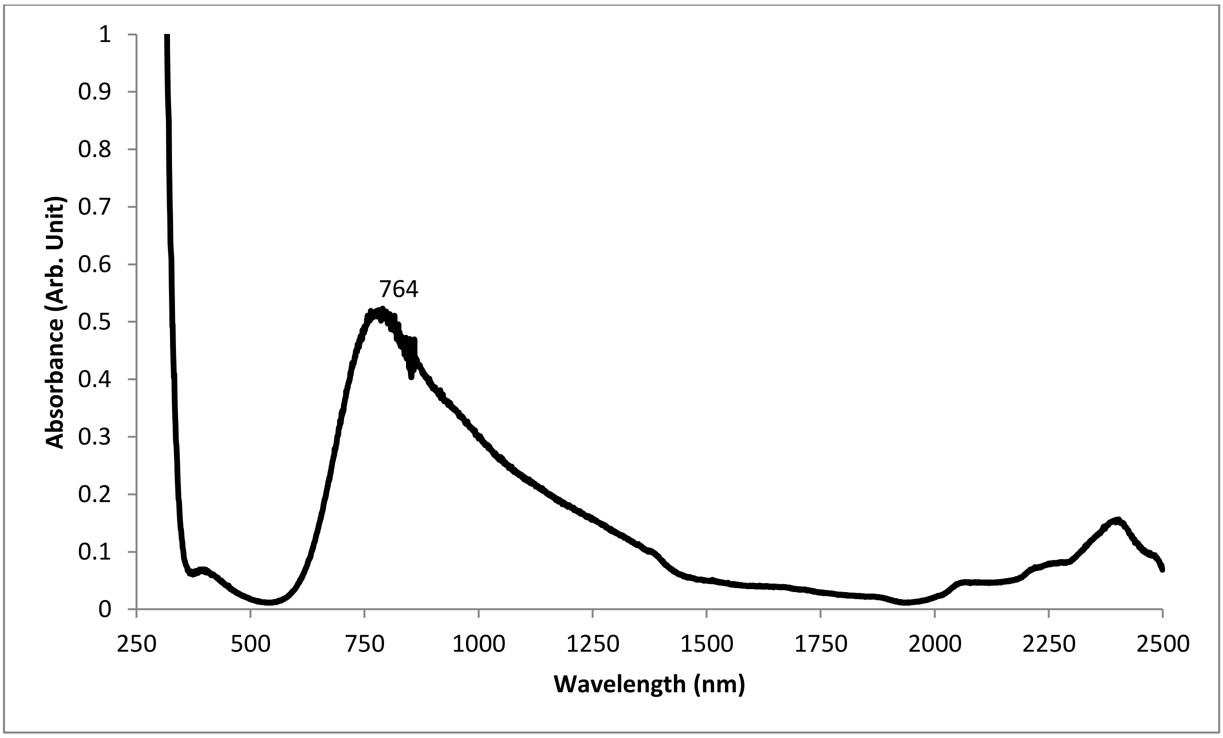

Figure 7-35-UV/Vis/NIR absorbance spectra of Compound 17

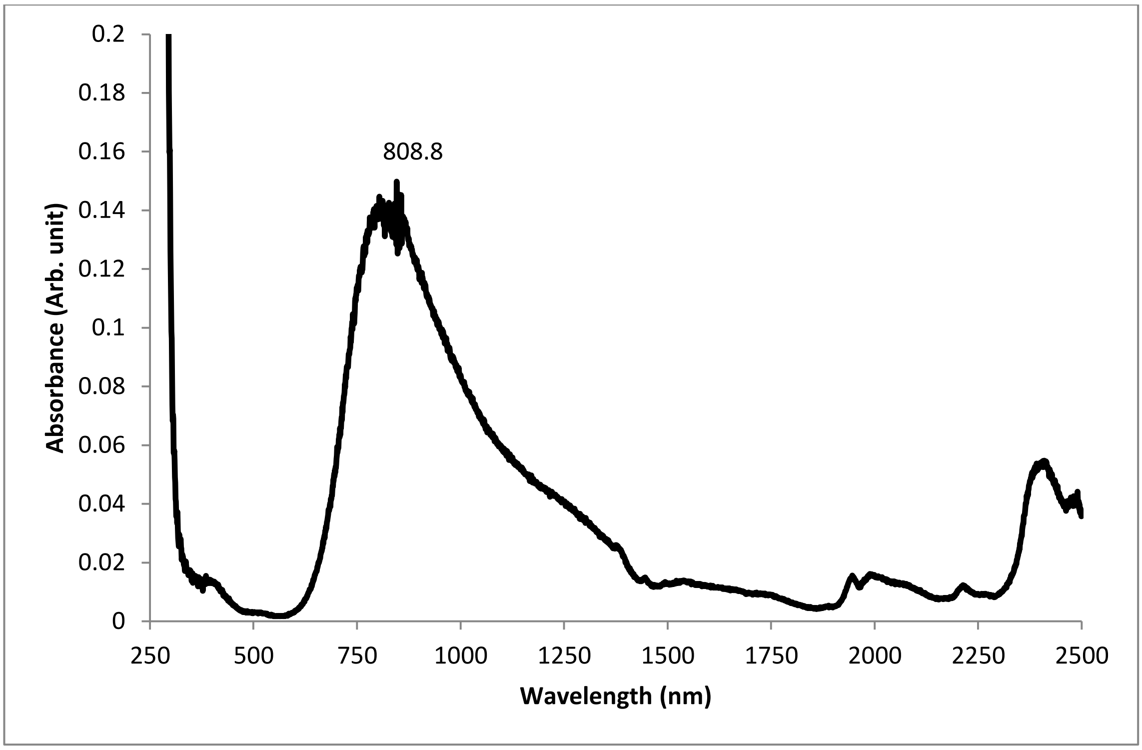

Figure 7-36-UV/Vis/NIR absorbance spectra of Compound 18

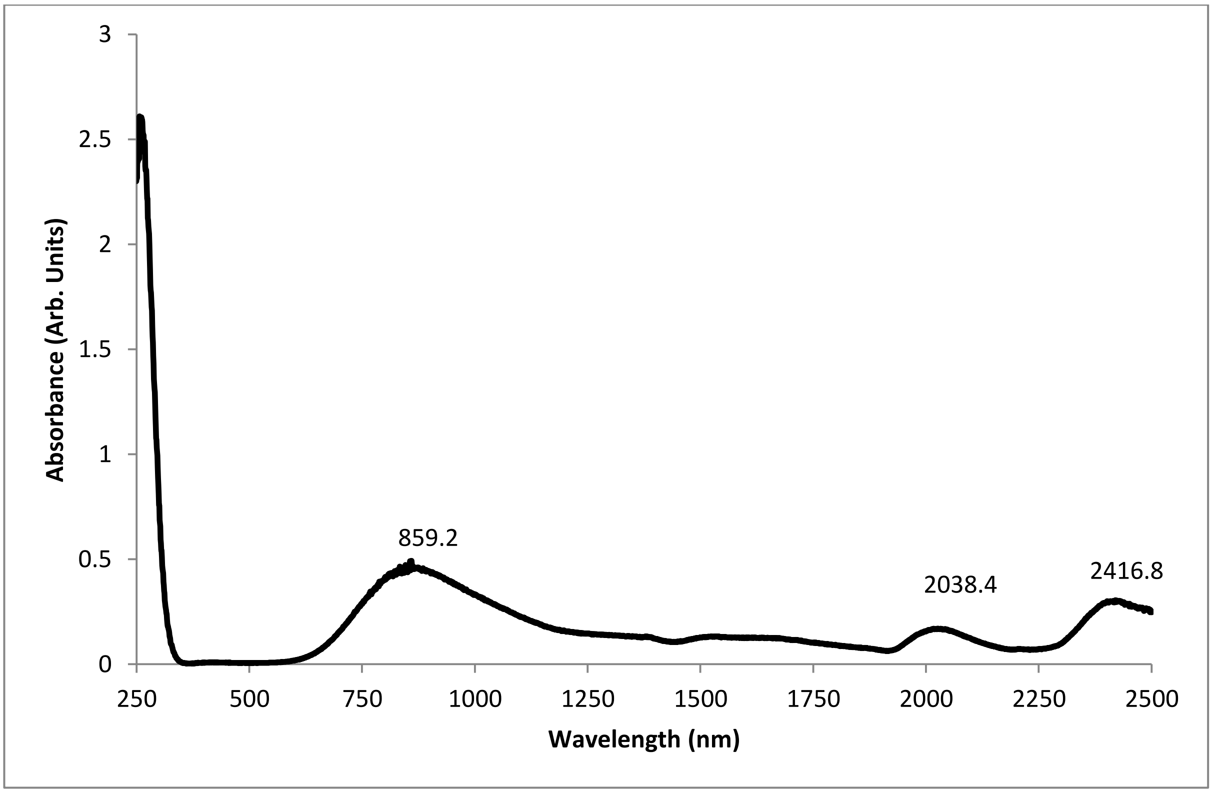

Figure 7-37-UV/Vis/NIR absorbance spectrum for Compound 19

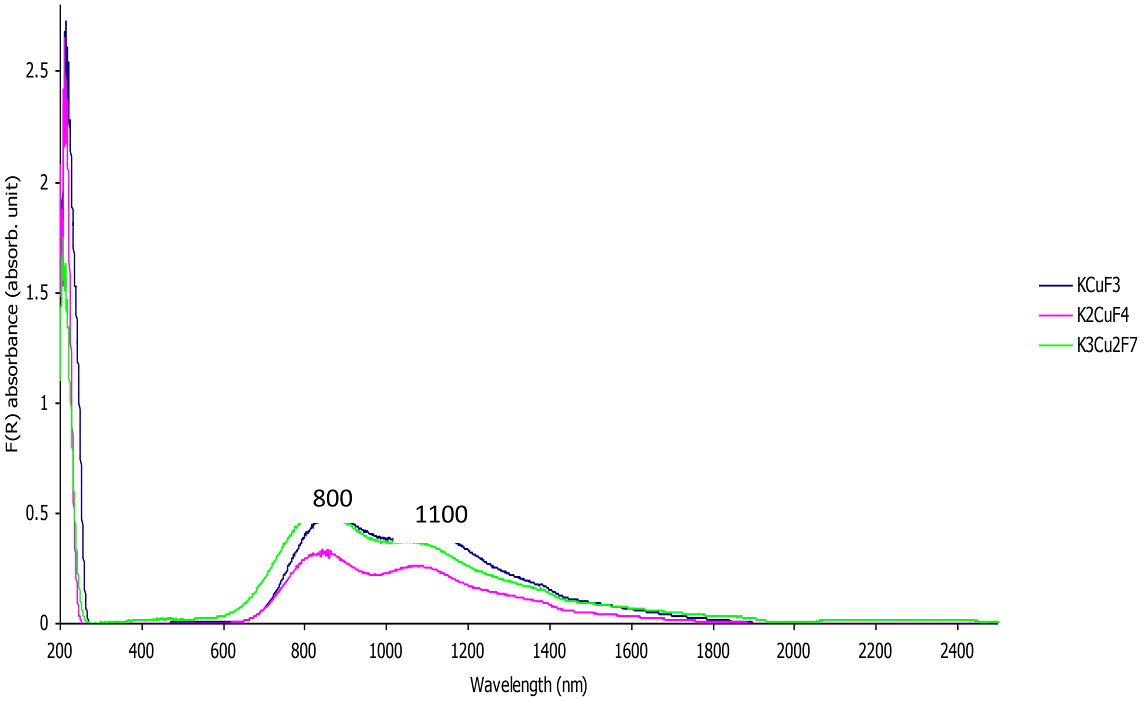

Figure 7-38-UV/Vis/NIR absorbance spectra of Compounds 21-23

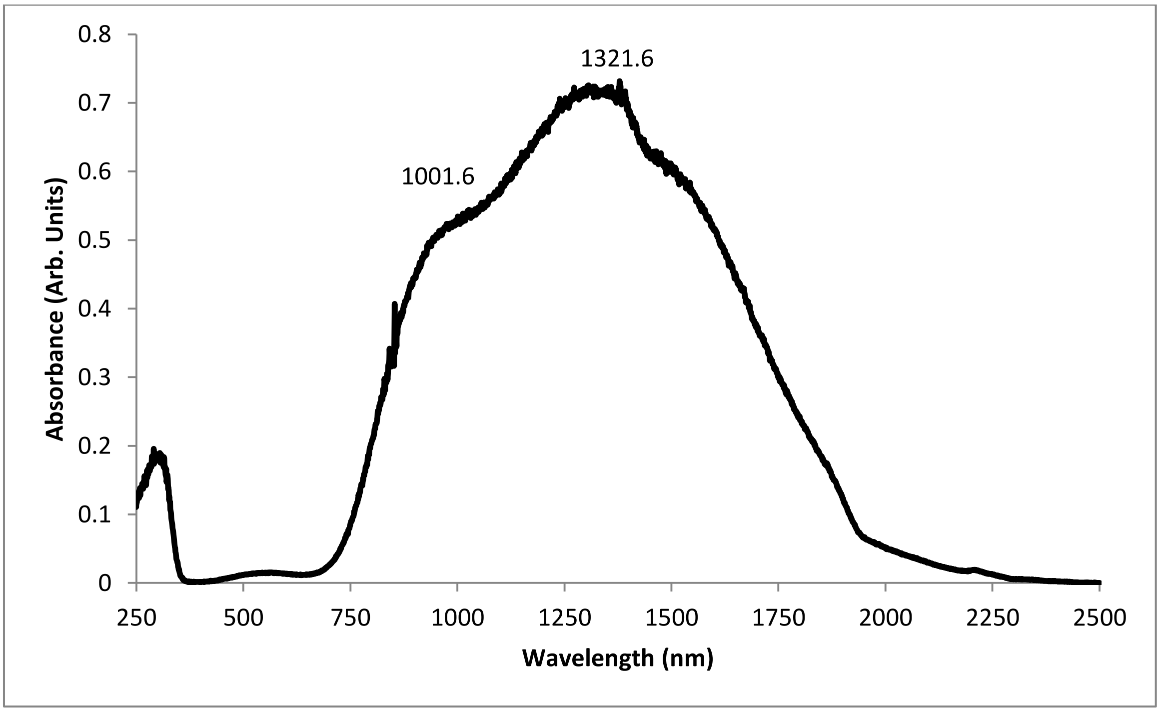

Figure 7-39-UV/Vis/NIR absorbance spectrum for Compound 24

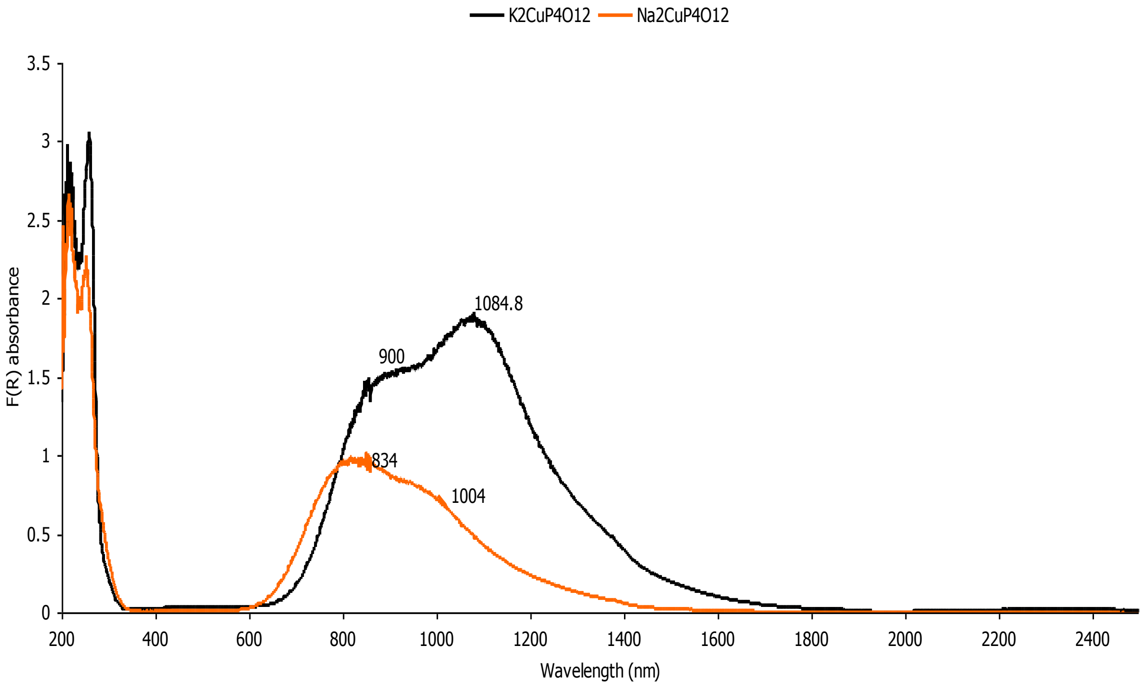

Figure 7-40-UV/Vis/NIR absorbance spectrum for Compounds 26 and 27

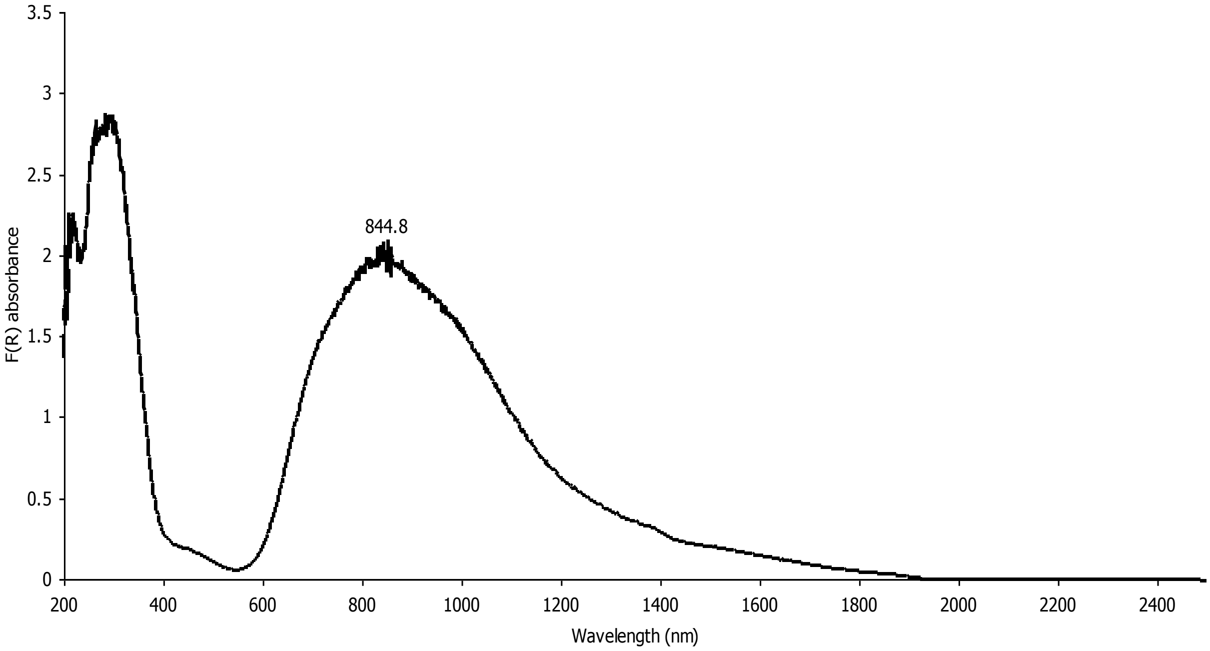

Figure 7-41-UV/Vis/NIR absorbance spectrum of Compound 28

D.2 Iron compounds

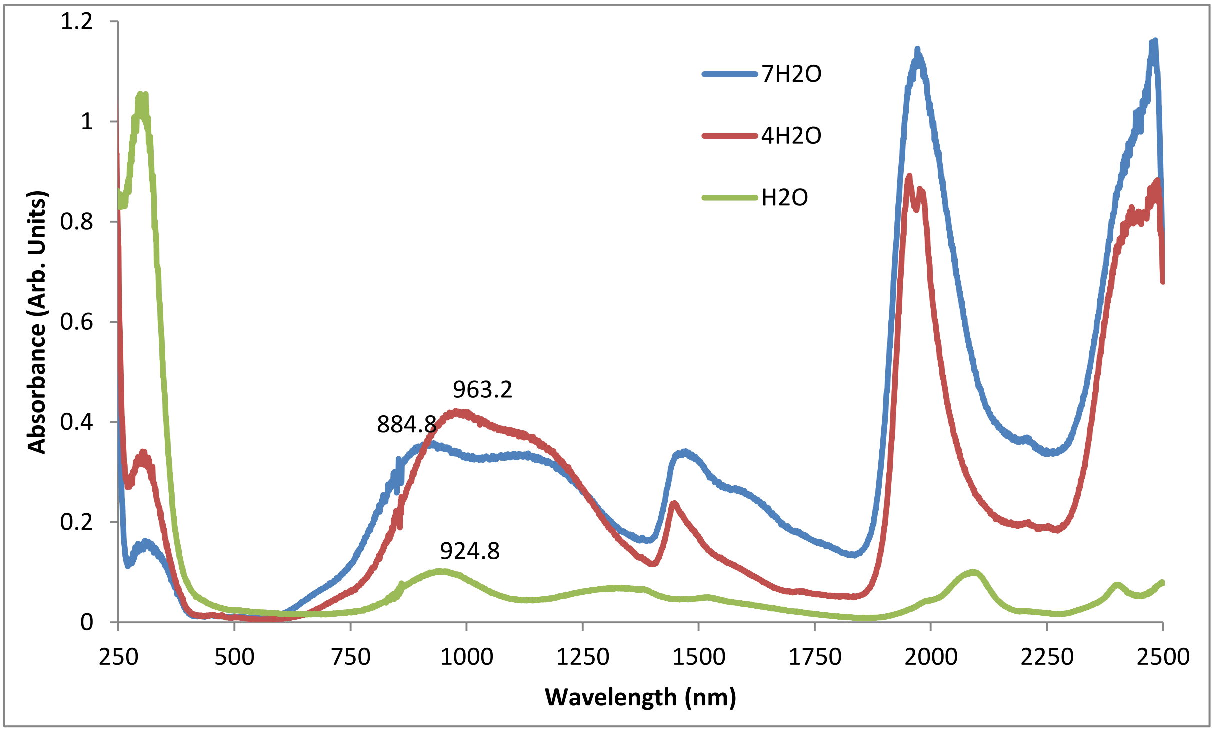

Figure 7-42-UV/Vis/NIR spectra of Compounds 34-36

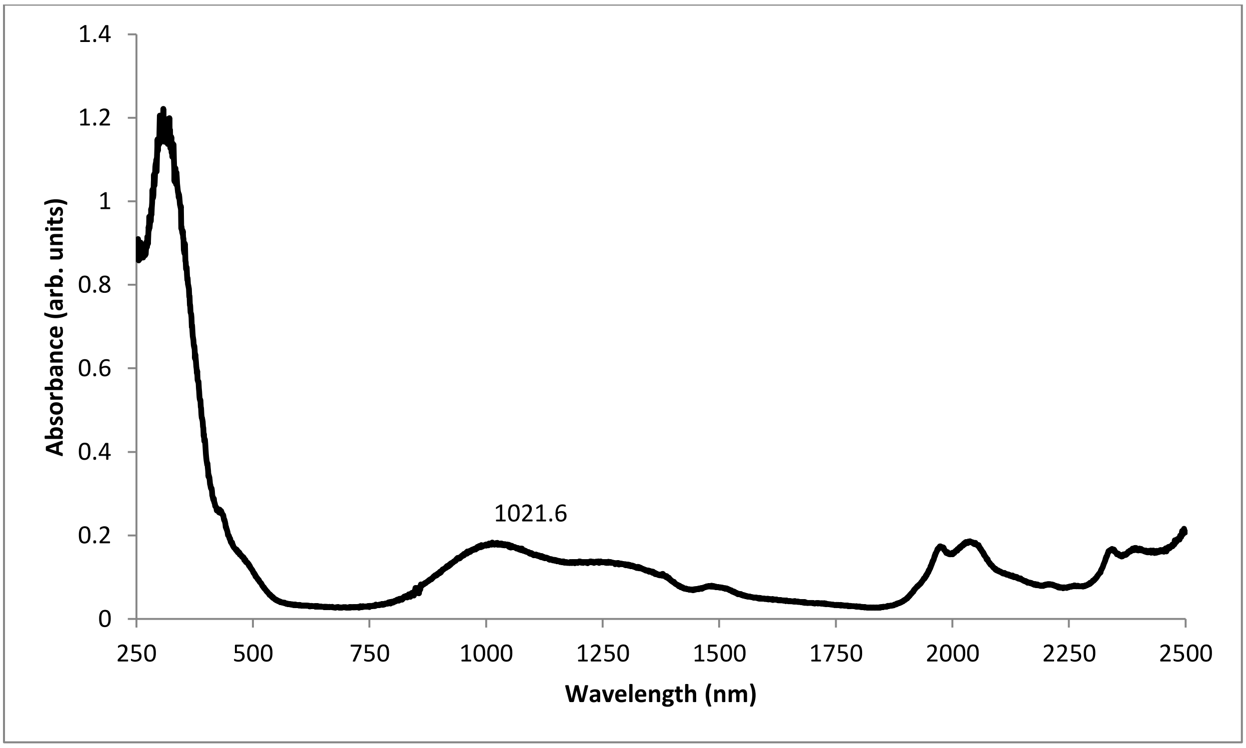

Figure 7-43-UV/Vis/NIR spectrum of Compound 37

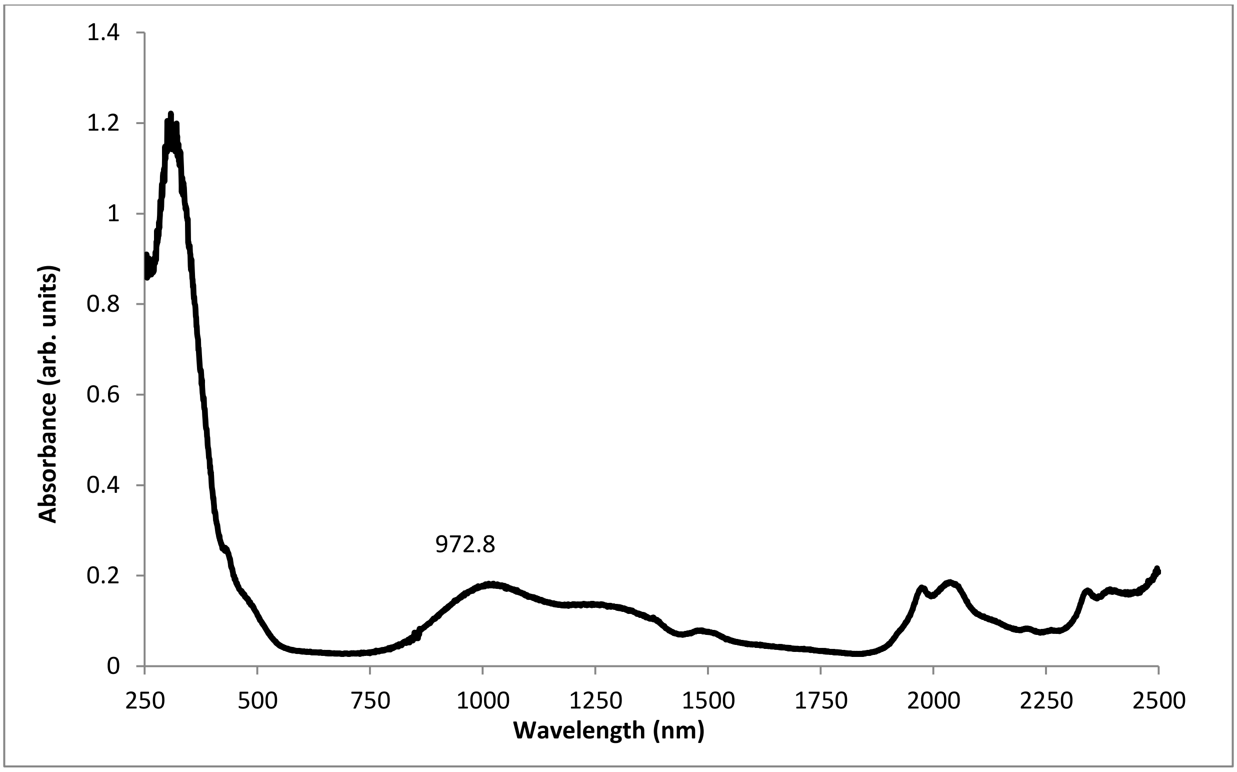

Figure 7-44-UV/Vis/NIR spectrum of Compound 38

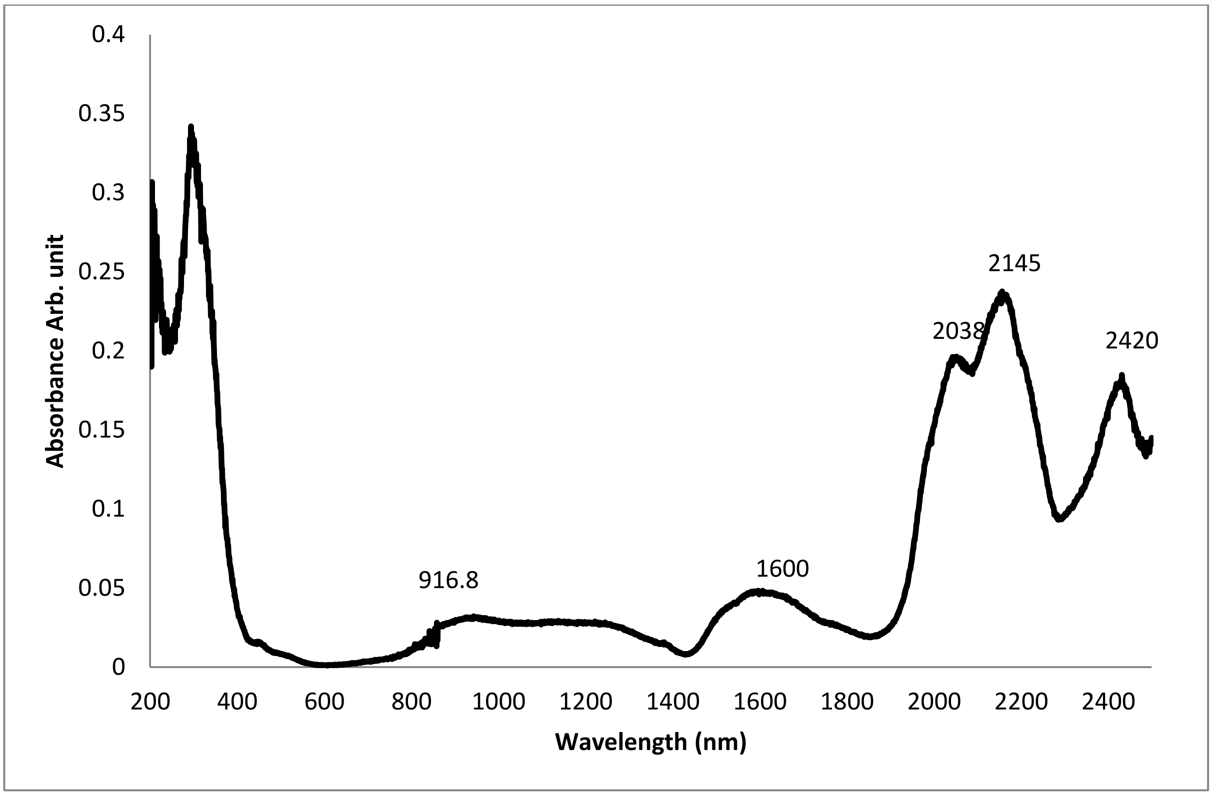

Figure 7-45-UV/Vis/NIR spectrum of Compound 39

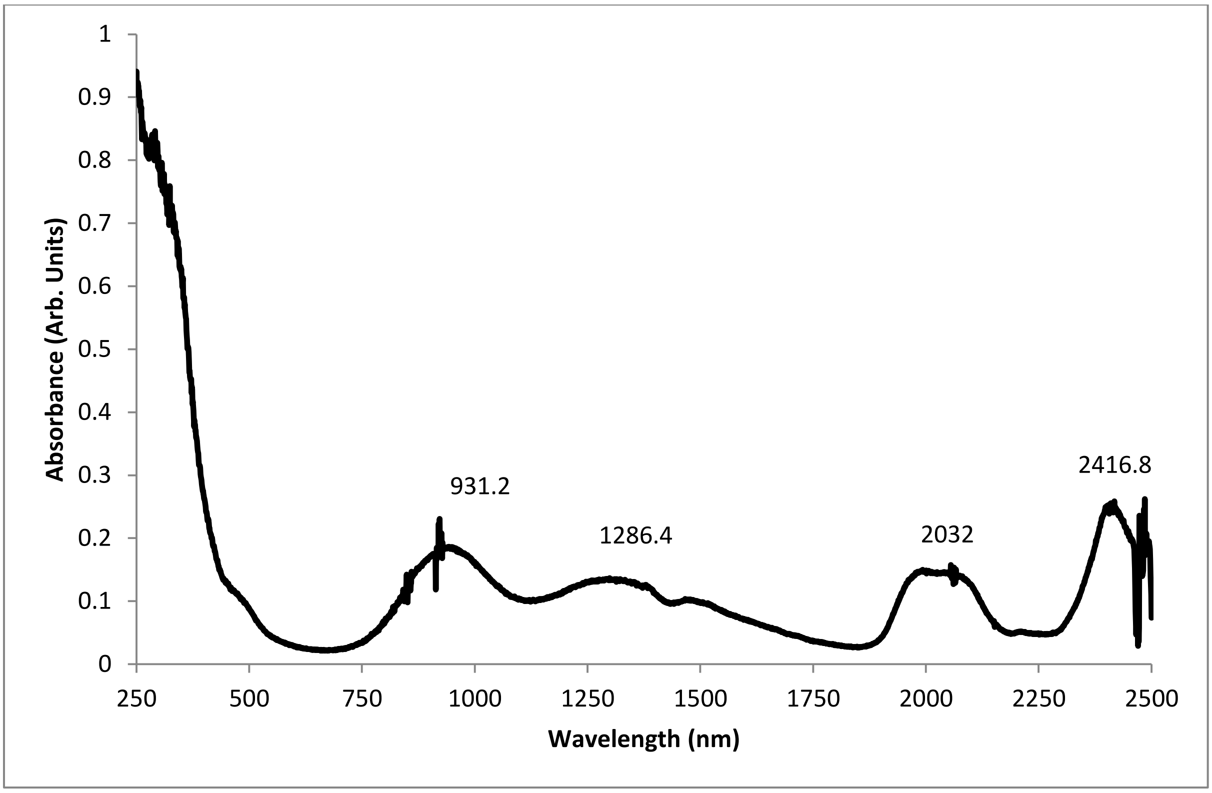

Figure 7-46UV/Vis/NIR absorbance spectrum of Compound 40

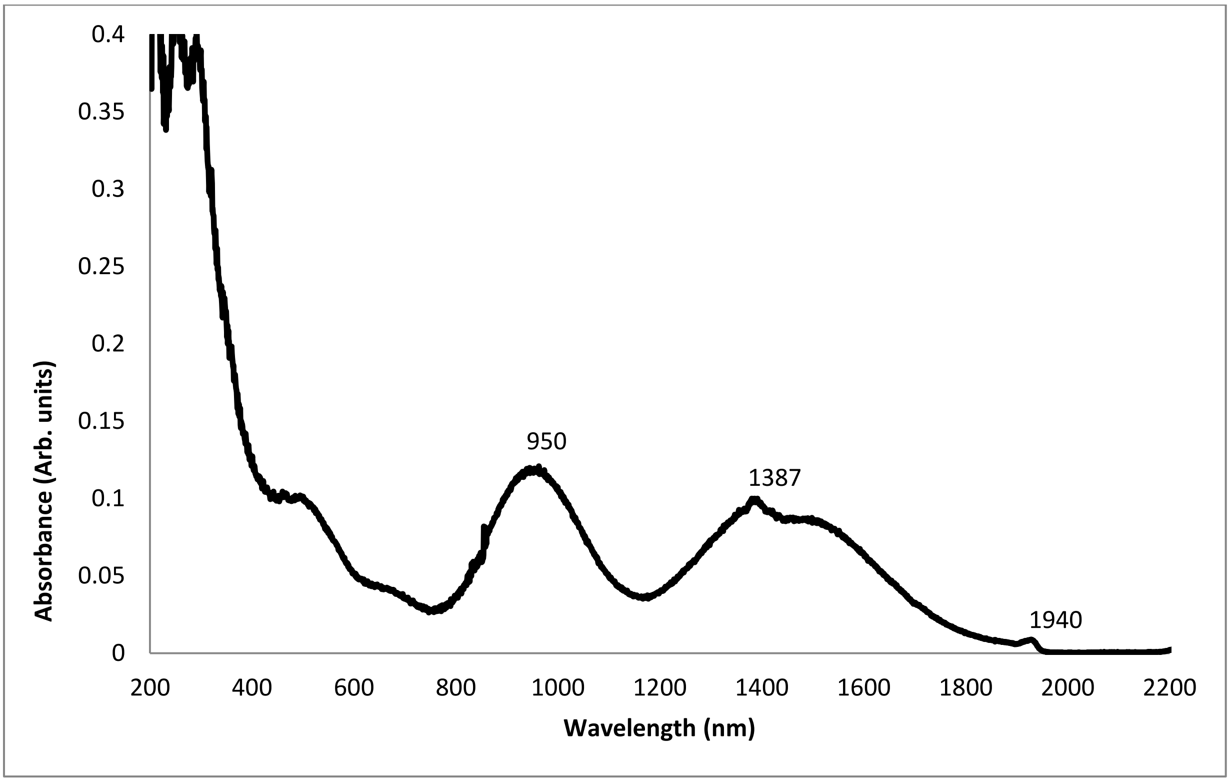

Figure 7-47-UV/Vis/NIR absorbance spectrum of Compound 41

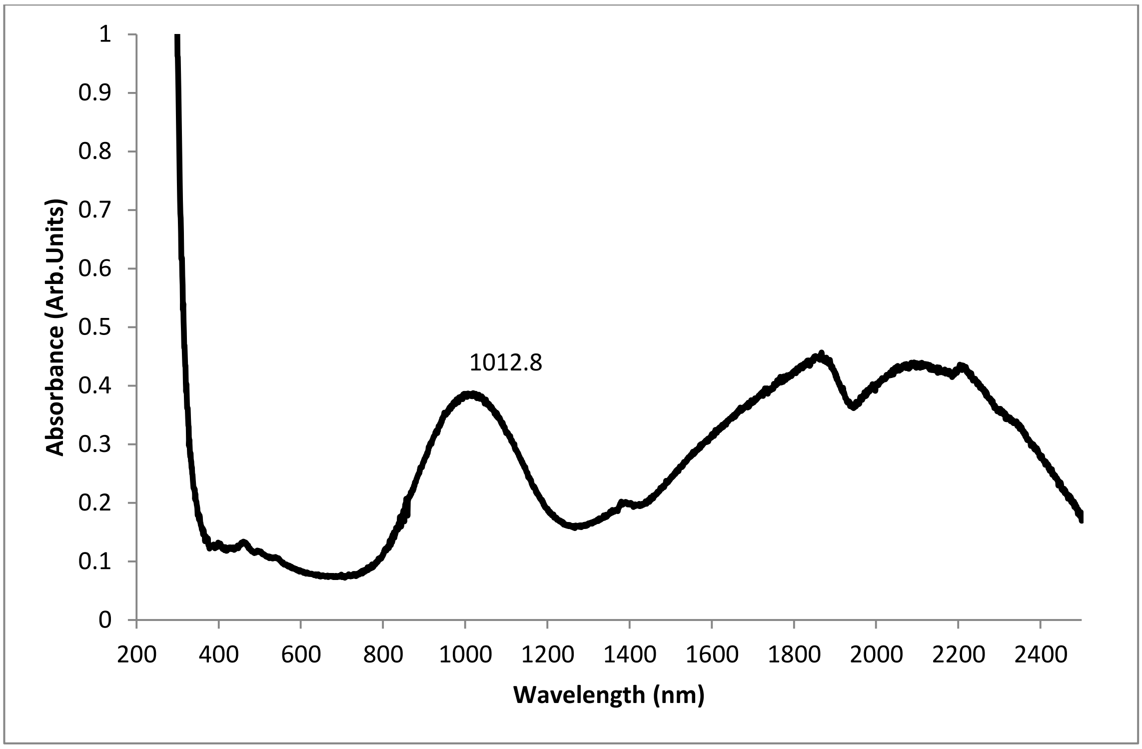

Figure 7-48-UV/Vis/NIR absorbance spectrum of Compound 43

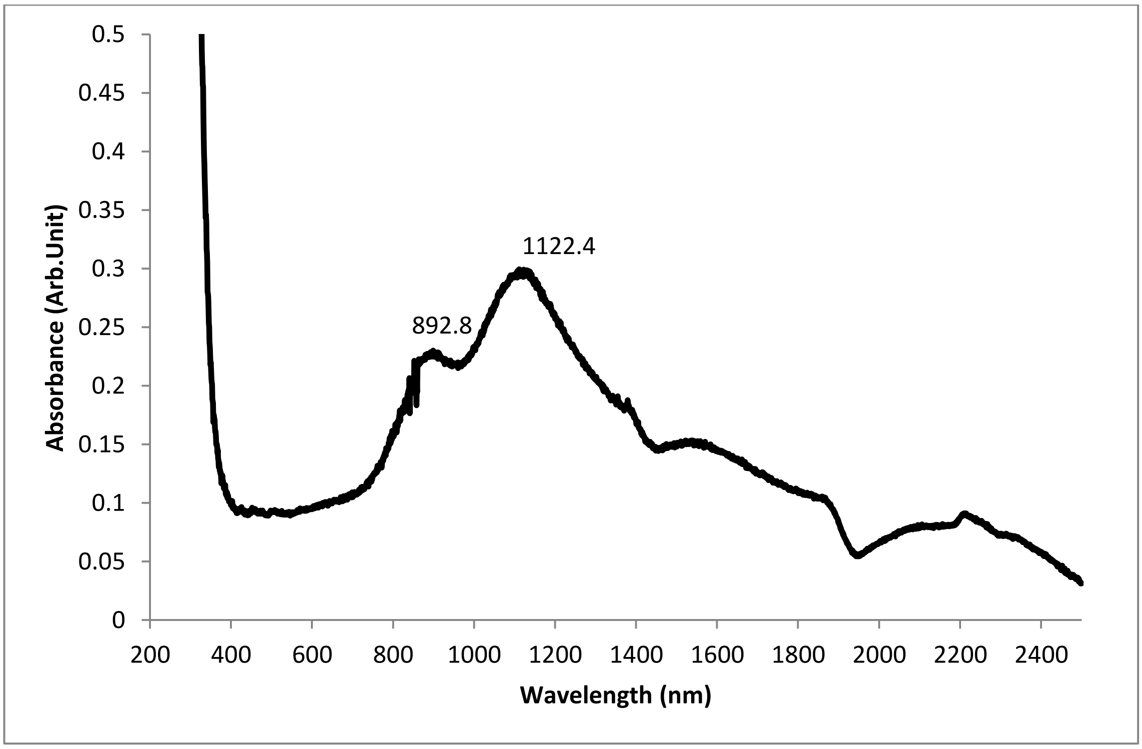

Figure 7-49-UV/Vis/NIR absorbance spectrum of Compound 44

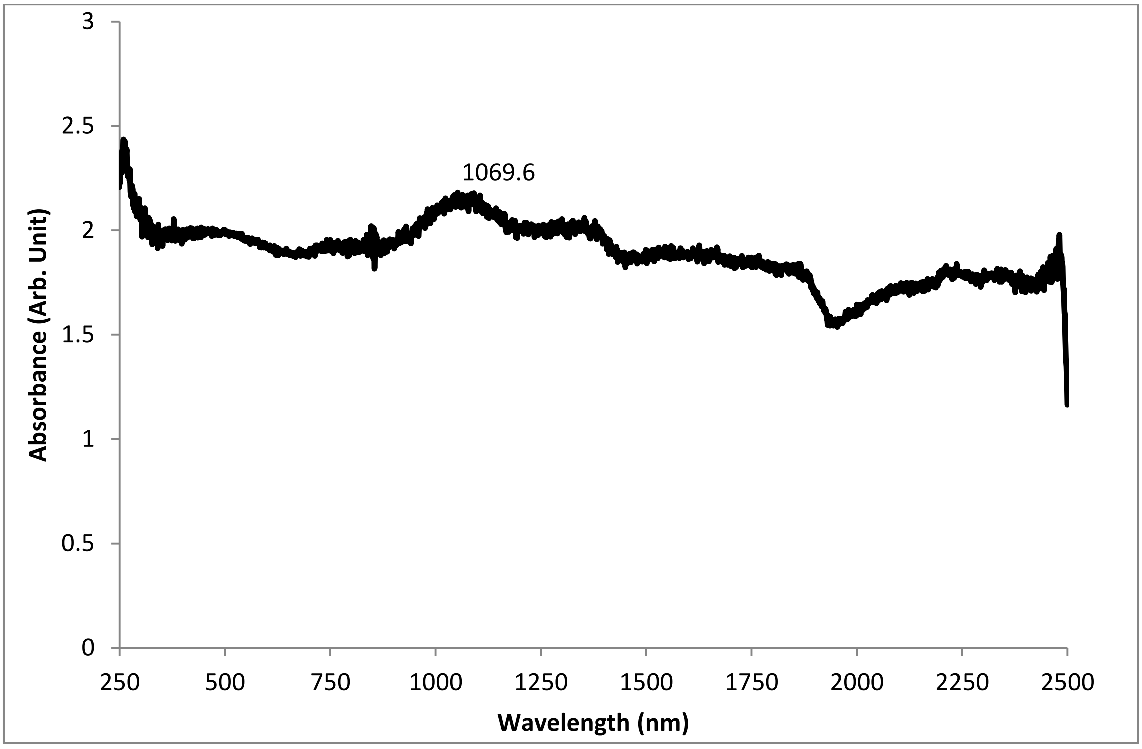

Figure 7-50-UV/Vis/NIR absorbance spectrum of Compound 46